

2015

# Detection of sub-surface stresses in ferromagnetic materials using a new Barkhausen noise method

Orfeas Kypris  
*Iowa State University*

Follow this and additional works at: <https://lib.dr.iastate.edu/etd>

 Part of the [Electrical and Electronics Commons](#), [Materials Science and Engineering Commons](#), [Mechanical Engineering Commons](#), and the [Mechanics of Materials Commons](#)

## Recommended Citation

Kypris, Orfeas, "Detection of sub-surface stresses in ferromagnetic materials using a new Barkhausen noise method" (2015). *Graduate Theses and Dissertations*. 14373.  
<https://lib.dr.iastate.edu/etd/14373>

This Dissertation is brought to you for free and open access by the Iowa State University Capstones, Theses and Dissertations at Iowa State University Digital Repository. It has been accepted for inclusion in Graduate Theses and Dissertations by an authorized administrator of Iowa State University Digital Repository. For more information, please contact [digirep@iastate.edu](mailto:digirep@iastate.edu).

**Detection of sub-surface stresses in ferromagnetic materials using a new  
Barkhausen noise method**

by

**Orfeas Kypris**

A dissertation submitted to the graduate faculty  
in partial fulfillment of the requirements for the degree of  
**DOCTOR OF PHILOSOPHY**

Major: Electrical Engineering

Program of Study Committee:  
David C. Jiles, Major Professor

John P. Basart

Mani Mina

Nicola Bowler

Iver E. Anderson

Meng Lu

Iowa State University

Ames, Iowa

2015

Copyright © Orfeas Kypris, 2015. All rights reserved.

## DEDICATION

This dissertation is lovingly dedicated to my parents, Costas Kypris and Martha Baur. It would not have been possible without their encouragement and love. It is also dedicated to my friends, and to all teachers, formal and informal, that helped shape the person I am today.

*Τὰ πάντα ῥεῖ καὶ οὐδὲν μένει.*

Ἡράκλειτος ὁ Ἐφέσιος (535 π.Χ. – 475 π.Χ.)

*Everything flows and nothing abides.*

Heraclitus of Ephesos (535 B.C. – 475 B.C.)



## TABLE OF CONTENTS

<b>LIST OF TABLES</b> . . . . .	vi
<b>LIST OF FIGURES</b> . . . . .	vii
<b>LIST OF SYMBOLS</b> . . . . .	xvii
<b>ACKNOWLEDGEMENTS</b> . . . . .	xviii
<b>ABSTRACT</b> . . . . .	xix
<b>CHAPTER 1. AIMS OF THE PROJECT</b> . . . . .	1
<b>CHAPTER 2. INTRODUCTION</b> . . . . .	2
2.1 Evaluation of residual stresses . . . . .	2
2.2 Barkhausen noise . . . . .	5
2.2.1 Domain wall motion and Barkhausen noise . . . . .	5
2.2.2 Determination of residual stress from Barkhausen measurements . . . . .	12
<b>CHAPTER 3. THEORETICAL ANALYSIS AND PRELIMINARY RESULTS</b> 17	
3.1 Stress as an effective magnetic field . . . . .	17
3.2 Variation of differential susceptibility and Barkhausen voltage with stress . . . . .	18
3.3 Stochasticity in Barkhausen noise . . . . .	20
3.3.1 Various forms of field $H$ . . . . .	22
3.4 Barkhausen noise in the frequency domain . . . . .	24
3.5 Initial approach to separating emissions from different depths . . . . .	26
3.5.1 Magnetic Barkhausen emissions from a single, uniformly stressed layer . . . . .	28
3.5.2 Magnetic Barkhausen emissions from a combination of two uniformly stressed layers . . . . .	30
3.5.3 Solving for the voltages at the origin of emission . . . . .	34

3.5.4	Shortcomings of this approach . . . . .	39
3.6	Analysis in the frequency domain . . . . .	41
3.6.1	General case - One layer formulation . . . . .	41
3.6.2	Case of constant stress along depth . . . . .	44
3.6.3	Two-layer case . . . . .	46
<b>CHAPTER 4. MEASUREMENTS AND INSTRUMENTATION . . . . .</b>		<b>50</b>
4.1	Experimental procedures . . . . .	50
4.1.1	Inducing uniaxial tensile stress . . . . .	50
4.1.2	Inducing a linear stress-depth gradient . . . . .	54
<b>CHAPTER 5. SIGNAL PROCESSING AND SOFTWARE DEVELOPMENT . . . . .</b>		<b>61</b>
5.1	Signal processing tools . . . . .	61
5.1.1	Mathematical definitions . . . . .	61
5.1.2	Mathematical operations . . . . .	65
5.1.3	Overview of class <i>BarkhausenSignal</i> . . . . .	80
5.1.4	Overview of class <i>BarkhausenExperiment</i> . . . . .	82
5.2	Measurement and instrumentation tools . . . . .	83
<b>CHAPTER 6. RESULTS AND ANALYSIS . . . . .</b>		<b>91</b>
6.1	Excitation amplitude - frequency sweep analysis . . . . .	91
6.2	COMSOL Solid Mechanics Simulation Results . . . . .	95
6.3	Experimental results and analysis . . . . .	101
6.3.1	Time Domain . . . . .	101
6.3.2	Frequency Domain . . . . .	113
6.3.3	Discussion . . . . .	115
<b>CHAPTER 7. CONCLUSION AND FUTURE WORK . . . . .</b>		<b>117</b>
<b>APPENDIX A. ADDITIONAL MATERIAL . . . . .</b>		<b>120</b>
<b>BIBLIOGRAPHY . . . . .</b>		<b>140</b>
<b>LIST OF PUBLICATIONS . . . . .</b>		<b>147</b>

## LIST OF TABLES

Table 3.1	Calibration profile parameters . . . . .	36
Table 4.1	Magnetization conditions for tensile test . . . . .	53
Table 4.2	Magnetization conditions for bending test . . . . .	60
Table 5.1	Simulated annealing algorithm options. . . . .	78
Table A.1	Simulation parameters . . . . .	125
Table A.2	Simulation parameters . . . . .	129

## LIST OF FIGURES

Figure 2.1	(a) Expected stress-depth profile due to shot peening (adapted from <i>Handbook of residual stress and deformation of steel</i> , pg. 348 [1]) (b) Measured stress-depth profiles induced by shot-peening steels of two different compositions [1] . . . . .	3
Figure 2.2	Measurement penetration vs. spatial resolution for various residual stress measurement methods. [2] . . . . .	4
Figure 2.3	Normalised Barkhausen Noise power spectrum [4]. Dotted lines represent computer simulations, while solid lines represent experiment. The experiments were conducted for three different values of $\dot{I}$ , with 1 having the highest value, and 2 the lowest. . . . .	9
Figure 2.4	Barkhausen Noise power maximum vs. field ramp rate [25]. . . . .	10
Figure 2.5	Results from the model for the Barkhausen signal in the zero stress case [27]. . . . .	11
Figure 2.6	RMS Barkhausen noise voltage vs. stress [33]. . . . .	13
Figure 2.7	Barkhausen signal envelope peak $M_{max}$ vs. average compressive stress $\langle \sigma \rangle_{100}$ in a surface layer [31]. . . . .	14
Figure 2.8	Experimental results showing the linear relationship between the reciprocal of the peak Barkhausen Noise voltage and stress [39]. . . . .	16

- Figure 3.1 Effect of eddy current damping on the Barkhausen spectrum. In our model, Barkhausen emissions occurring at an infinitesimally thin region inside a specimen, have a white noise frequency spectrum. The energy in emissions is dissipated due to generation of eddy currents, causing the spectrum to resemble pink noise as the Barkhausen emissions propagate through the material. . . . . 24
- Figure 3.2 Emissions of frequency  $f_a = 0.5$  MHz and  $f_b = 0.1$  MHz originating at depths  $x_a$  and  $x_b$  inside a material of constant permeability and conductivity. Attenuation occurs due to the skin effect described in equation (3.21). The model assumes a sharp cutoff at  $\delta$ , which allows setting cutoff depths to facilitate the separation of emissions. As long as the skin depth of an emission falls between the upper and lower cutoffs of a layer, it is detected within that layer. Attenuation of the amplitude of emissions is represented by fading colour. . . . . 27
- Figure 3.3 Layered specimen considered by the model, where layer boundaries correspond to specific frequencies. Stress is denoted by  $\sigma$ . . . . . 29
- Figure 3.4 Measured voltage from one layer plotted as a function of frequencies  $\omega_0$  (upper cutoff) and  $\omega_1$  (lower cutoff). For this study,  $\rho = 8.93 \times 10^{-8}$   $\Omega/m$ ,  $\mu_r = 50$  and  $V_{orig} = 2\mu V$ . Depth  $x_1$  was set to  $100 \mu m$ . Note that when  $\omega_1 > \omega_0$ , there is no detected voltage. . . . . 30
- Figure 3.5 Contour plot of the measured voltage from one layer, as a function of frequencies  $\omega_0$  (upper cutoff) and  $\omega_1$  (lower cutoff). Voltage values are expressed in  $\mu V$ . Note that when  $\omega_1 > \omega_0$ , there is no detected voltage. 31
- Figure 3.6 Layered specimen considered by the model, where layer boundaries correspond to specific frequencies. Stresses in the first and second layer are denoted by  $\sigma_1$  and  $\sigma_2$  respectively. . . . . 32

- Figure 3.7 Measured voltage from two layers plotted as a function of the lower cutoff frequency  $\omega_2$ . In this plot,  $\omega_0/2\pi = 1$  MHz,  $\omega_1/2\pi = 0.5$  MHz and  $V_{orig2} = 2 \mu\text{V}$ . The value of  $V_{orig1}$  was set to (a)  $1 \mu\text{V}$ , (b)  $2 \mu\text{V}$ , (c)  $3 \mu\text{V}$  and (d)  $4 \mu\text{V}$ . The depths were fixed to  $x_1 = 50 \mu\text{m}$  and  $x_2 = 100 \mu\text{m}$ . . . . . 33
- Figure 3.8 Measured voltage from two layers plotted as a function of frequencies  $\omega_1$  (intermediate cutoff) and  $\omega_2$  (lower cutoff). In this plot,  $\omega_0/2\pi = 1$  MHz,  $V_{orig1} = V_{orig2} = 2 \mu\text{V}$ . The depths were fixed to  $x_1 = 50 \mu\text{m}$  and  $x_2 = 100 \mu\text{m}$ . Note that when  $\omega_1 < \omega_2$ , there is no detected voltage. . . 33
- Figure 3.9 (a) Typical measured Barkhausen noise spectrum, with  $\omega_0$ ,  $\omega_1$ ,  $\omega_2$ , denoting the upper, intermediate and lower cutoff frequencies - these correspond to different depths of sampling (*frequencies not to scale*). The  $\omega_2$  limit can be lowered to  $\omega'_2$  in order to sample deeper regions of the specimen. (b) Ferromagnetic specimen divided in three layers of equal volume, where  $\sigma_1$ ,  $\sigma_2$  and  $\sigma_3$  denote the stress magnitudes in the first, second and third layer respectively. Also  $\bar{\sigma}_{2-3} = \frac{1}{2}(\sigma_2 + \sigma_3)$ . . . . . 35
- Figure 3.10 Experimentally calculated calibration profiles for (a)  $1/V_{orig1}$ , (b)  $1/V_{orig2}$  and (c)  $1/V_{orig2-3}$ , fitted with a linear regression and plotted with 95% confidence intervals. These trends are obtained by filtering the Barkhausen data collected from an ASTM A36 steel specimen under uniaxial tension. In order to produce the calibration profiles, it is assumed that the stress along the measurement direction remains uniform throughout the depth of the specimen. Table 3.1 lists the computed calibration profile parameters. . . . . 37

- Figure 3.11 Conceptual calibration profiles corresponding to specific depths for (a)  $1/V_{orig1}$ , (b)  $1/V_{orig2}$ , and (c)  $1/V_{orig2-3}$ . A specimen of unknown stress state can be assessed by applying (3.26) and (3.27), keeping  $\omega_0$ ,  $\omega_1$  and  $\omega_2$  constant with respect to the calibration stage. The reciprocal value of the measured average Barkhausen emission in the first layer  $1/V_{orig1}$  will then lead to a stress  $\sigma_1$ , via the pre-established linear relationship. In a similar manner, the stress  $\sigma_2$  in the second layer, and the average stress  $\bar{\sigma}_{2-3}$  in the combined second and third layer can be found. . . . . 38
- Figure 3.12 Graphical representation of the model equations. The red and green curves represent the integrals from 0 to  $x_1$  and  $x_1$  to  $x_2$  respectively. The blue curve is a sum of the aforementioned, and represents what is seen at the surface. The curves are all normalized by the maximum value attained by the blue curve, such that their maximum values always sum to 1. . . . . 40
- Figure 3.13 Plot of a stress-depth gradient, with tensile stress at the top surface, monotonically decreasing to a compressive stress at the lower surface. Here,  $x$  indicates distance from the top surface of the specimen. . . . . 42
- Figure 3.14 Effect of slope parameter  $m$  on the Barkhausen spectrum. . . . . 45
- Figure 3.15 Calibration relationship, relating relative permeability and its reciprocal to stress. We set  $a = 2019.620 \text{ Am}^{-1}$ ,  $M_s = 2.485 \times 10^5 \text{ Am}^{-1}$ , and  $\alpha = 1.9119 \times 10^{-2}$ , which are typical values for a soft steel. The values of  $b$  and  $\sigma_{offset}$  were set to  $1 \times 10^{-17} \text{ m}^2 \text{ A}^{-2}$  and  $-800 \text{ MPa}$  respectively. 48
- Figure 3.16 Least-squares fit to simulated Barkhausen spectra, of the model of (3.49) combined with the relationship in (3.51), for different stress magnitudes in the first and second layer. The value of  $b'$ , which quantifies the sensitivity of the sensing element, was set to  $1 \times 10^{-22} \text{ m}^2 \text{ V}^{-2} \text{ A}^{-2}$ . The parameters  $\chi'(0) \cong \mu'_r(0)$ ,  $\rho$  and  $V_{orig}(0)$  were set to 42,  $0.22 \mu\Omega\text{m}$  and 10 V, respectively. The layer thickness  $\Delta x$  was set to  $50 \mu\text{m}$ . Gaussian noise was added to the spectra, to make the modelling more realistic. . . 49

Figure 4.1	Three dimensional visualization of the specimen for tensile testing, manufactured according to the ASTM E8 standard. Sensor indicates where Barkhausen emissions were measured. . . . .	52
Figure 4.2	Experimental setup, showing the grip of the tensile test machine, the A36 test specimen, and the Barkhausen probe kept in a stable position by the clamp. . . . .	53
Figure 4.3	Four-point bender. (a) 3D CAD design, (b) Photograph of manufactured part. . . . .	55
Figure 4.4	Mesh and simulated geometry for the four-point bending experiment for the 1 mm thick specimen. . . . .	58
Figure 4.5	Experimental setup, showing the fixtures of the four-point bender, the A36 test specimen, and the Barkhausen probe kept in a stable position by the customized clamp. . . . .	59
Figure 5.1	Comparison of power spectral density and Fourier magnitude calculations (normalized). . . . .	66
Figure 5.2	Custom designed and built measurement system enclosed in instrument case. . . . .	86
Figure 5.3	Custom measurement system connection diagram. . . . .	87
Figure 5.4	Settings pane on custom acquisition software. . . . .	88
Figure 5.5	Raw signals acquired using the custom acquisition software. . . . .	88
Figure 5.6	Barkhausen signal obtained after filtering the raw $dB/dt$ signal, using the custom acquisition software. . . . .	89
Figure 5.7	Frequency spectrum of Barkhausen signal displayed in Fig. 5.6, obtained using the custom acquisition software. . . . .	89
Figure 5.8	Statistics tab in the custom acquisition software. . . . .	90
Figure 6.1	RMS Barkhausen noise amplitude as a function of excitation voltage and frequency, for specimens of different thickness. The bottom plot shows the coefficient of variation within the first four plots. . . . .	92



Figure 6.2	RMS Barkhausen noise amplitude as a function of excitation voltage and frequency, scaled by excitation frequency $f$ , for specimens of different thickness. The bottom plot shows the coefficient of variation within the first four plots. . . . .	93
Figure 6.3	(a) Geometry of deformed specimen, showing the longitudinal stress at a displacement of 1.2 mm, and (b) stress-depth profile along geometrical center for the 1 mm thick specimen. . . . .	96
Figure 6.4	(a) Geometry of deformed specimen, showing the longitudinal stress at a displacement of 1.2 mm, and (b) stress-depth profile along geometrical center for the 2 mm thick specimen. . . . .	97
Figure 6.5	(a) Geometry of deformed specimen, showing the longitudinal stress at a displacement of 1.2 mm, and (b) stress-depth profile along geometrical center for the 3 mm thick specimen. . . . .	98
Figure 6.6	(a) Geometry of deformed specimen, showing the longitudinal stress at a displacement of 1.2 mm, and (b) stress-depth profile along geometrical center for the 4 mm thick specimen. . . . .	99
Figure 6.7	Slopes of stress-depth profiles $\partial\sigma/\partial x$ along geometrical center for specimens of all thicknesses, plotted against surface stress. . . . .	100
Figure 6.8	Raw Barkhausen waveforms obtained from the 1 mm thick specimen, for different magnitudes of deflection. The custom Barkhausen software is able to calculate ensemble average, waveform envelope (red) and automatically display all waveforms in an experiment, for visual comparison. As can be observed, the peak value increases with magnitude of deflection.	101
Figure 6.9	Raw Barkhausen waveforms obtained from the 1 mm thick specimen, for different magnitudes of deflection. The custom Barkhausen software is able to calculate ensemble average, waveform envelope (red) and automatically display all waveforms in an experiment, for visual comparison. As can be observed, the peak value increases with magnitude of deflection.	102

- Figure 6.10 Raw Barkhausen waveforms obtained from the 1 mm thick specimen, for different magnitudes of deflection. The custom Barkhausen software is able to calculate ensemble average, waveform envelope (red) and automatically display all waveforms in an experiment, for visual comparison. As can be observed, the peak value increases with magnitude of deflection. 103
- Figure 6.11 Raw Barkhausen waveforms obtained from the 1 mm thick specimen, for different magnitudes of deflection. The custom Barkhausen software is able to calculate ensemble average, waveform envelope (red) and automatically display all waveforms in an experiment, for visual comparison. As can be observed, the peak value increases with magnitude of deflection. 104
- Figure 6.12 RMS voltage of (a) 1 mm, (b) 2 mm, (c) 3 mm, (d) 4 mm thick specimen. 105
- Figure 6.13 Peak voltage in the positive part of the magnetizing cycle for (a) 1 mm, (b) 2 mm, (c) 3 mm, (d) 4 mm thick specimen. . . . . 106
- Figure 6.14 Peak voltage in the negative part of the magnetizing cycle for (a) 1 mm, (b) 2 mm, (c) 3 mm, (d) 4 mm thick specimen. . . . . 107
- Figure 6.15 Position of peak voltage in the positive part of the magnetizing cycle for (a) 1 mm, (b) 2 mm, (c) 3 mm, (d) 4 mm thick specimen. . . . . 108
- Figure 6.16 Position of peak voltage in the negative part of the magnetizing cycle for (a) 1 mm, (b) 2 mm, (c) 3 mm, (d) 4 mm thick specimen. . . . . 109
- Figure 6.17 R.M.S. voltage for all specimens, plotted as a function of longitudinal surface stress. . . . . 110
- Figure 6.18 Peak voltage in the positive part of the magnetizing cycle, for all specimens, plotted as a function of longitudinal surface stress. . . . . 110
- Figure 6.19 Peak voltage in the negative part of the magnetizing cycle, for all specimens, plotted as a function of longitudinal surface stress. . . . . 111
- Figure 6.20 Peak position in the positive part of the magnetizing cycle, plotted as a function of longitudinal surface stress. . . . . 111
- Figure 6.21 Peak position in the negative part of the magnetizing cycle, for all specimens, plotted as a function of longitudinal surface stress. . . . . 112

Figure 6.22 Results of fitting parameters  $m$ ,  $\sigma_0$  and  $\zeta$ . The figures (a), (b), (c), and (d) correspond to the 1, 2, 3 and 4 mm specimens respectively. The marked outliers in (d) were not considered in the fitting as they are above 200 MPa and approaching the plastic limit. . . . . 113

Figure 6.23 Typical Barkhausen spectra, obtained by taking the magnitude of the Fourier transform of two Barkhausen bursts (corresponding to a complete magnetizing cycle) and taking the ensemble average of the magnitudes over multiple cycles in multiple trials of the same measurement. The yellow curve is a the result of a 100-point moving average smoothing algorithm (non-parametric), which was calculated for reference purposes. The red curve is the fit of the parametric model of (3.42) to the raw data (blue). . . . . 114

Figure A.1 Equivalent circuits for inductors, including parasitic resistance and capacitance. (a) Circuit for inductor with ferromagnetic core, with resistance  $R_p$  accounting for the hysteretic loss component. (b) Circuit for air-core inductor. . . . . 120

Figure A.2 Equivalent circuit for Barkhausen sensor. . . . . 120

Figure A.3 Equivalent circuits for inductor LCR measurement [59]. . . . . 121

Figure A.4 Impedance criteria [59]. . . . . 121

Figure A.5 Definitions of impedance parameters for series and parallel modes [59]. 122

Figure A.6 Transmission line equivalent circuit [60]. . . . . 123

Figure A.7 Simulation results for (a) 5, (b) 10 and (c) 15 overlapping spectra. As the number of discrete depths is increased (and with it, the number of constituent spectra), the % error in recovering the spectrum intercepts  $V_0$  increases. The matrix becomes singular and impossible to invert (A.7c). This is possibly a result of numerical error, since the concept can be proven correct for a smaller number of distinct curves. . . . . 126

Figure A.8 Simulation results for (a) 5, (a) 10 and (a) 15 overlapping spectra. As the number of layers is increased (and with it, the number of constituent spectra), the % error in recovering the spectrum intercepts  $V_0$  increases. The matrix becomes singular and impossible to invert (Figure A.7c). This is possibly a result of numerical error, since the concept can be proven correct for a smaller number of layers. . . . . 130

Figure A.9 Permeability-stress relationship that was used as an input to the model. 133

Figure A.10 Simulated waveforms at the origin of each layer, for all 5 layers, when all of them are stressed equally (250 MPa). Note that the artificially high amplitude ensures that no significant errors due to rounding occur later on (the waveform was multiplied by an amplification constant). . . . . 134

Figure A.11 Simulated waveforms at the surface, for all 5 layers, when all of them are stressed equally (0 MPa). The most attenuated one is the one corresponding to the fifth layer, situated deeper in the specimen. The apparent shift in the peak position is due to the filter's phase response which causes a phase shift (it looks like the coercive field is changing). . . . . 135

Figure A.12 Simulated waveforms at the surface, for all stresses, in ascending order (0 – 250 MPa). When the waveforms are loaded, they are multiplied by a factor of  $10^{-3}$ . The routine was originally coded like that to convert  $V$  to  $mV$  for data imported from the Stresstech Rollscan. . . . . 137

Figure A.13 FFT of simulated Barkhausen waveform, with smoothed spectrum. In fitting the model, only the mid- to high-frequency range was used, as the low-frequency range contains artifacts from the filter. . . . . 138

Figure A.14 Fit to the model. In fitting the model, only the mid- to high-frequency range was used, as the low-frequency range contains artifacts from the filter. . . . . 138

- Figure A.15 Parameter  $V_0$ , extracted from the fit to the model. For some reason, the parameter is seen to decrease with stress, when it should be increasing. This must be investigated further. Note that there is an outlier at 50 MPa. . . . . 139
- Figure A.16 Parameter  $\zeta$ , extracted from the fit to the model. For the most part, the parameter is seen to increase with stress, suggesting that permeability is increasing with stress, which is what was the input to the model. . . 139

## LIST OF SYMBOLS

Symbol	Units	Description
$x$	m	Layer thickness (or depth of detection).
$\delta$	m	Penetration depth.
$\omega$	rad·s <sup>-1</sup>	Angular frequency.
$f$	Hz	Frequency.
$\rho$	$\Omega \cdot \text{m}$	Electrical resistivity.
$\mu$	H·m <sup>-1</sup>	Magnetic permeability.
$\mu_{eff}$	H·m <sup>-1</sup>	Effective magnetic permeability.
$\zeta$	$\sqrt{S \cdot H} \cdot \text{m}^{-1}$	Barkhausen attenuation constant.
$M$	A·m <sup>-1</sup>	Magnetization.
$H$	A·m <sup>-1</sup>	Magnetic field.
$B$	T	Magnetic flux density.
$\Phi$	Wb	Magnetic flux.
$\langle V_{orig}(\omega) \rangle$	V·Hz <sup>-1</sup>	Mean amplitude spectrum of voltage signal measured in the near vicinity (origin) of a single Barkhausen emission
$V_{att_i}(\omega)$	V·Hz <sup>-1</sup>	Amplitude spectrum of voltage signal measured at some distance away from the point of origin of multiple emissions spanning layer (or depth range) $i$ .
$V_{meas}(\omega)$	V·Hz <sup>-1</sup>	Amplitude spectrum of voltage signal measured by the sensor.

## ACKNOWLEDGEMENTS

First and foremost, I would like to acknowledge my Ph.D. supervisor, Dr. David Jiles, for the academic, moral, and financial support he provided to me over the past four years. Our insightful discussions gave me inspiration and guidance which greatly impacted the outcome of my research. I will always appreciate his encouragement and belief in me.

I would also like to thank my Ph.D. committee, Drs. John Basart, Mani Mina, Iver Anderson, Nicola Bowler and Meng Lu, who patiently attended my examinations, and motivated me to look at my work from different angles by asking a variety of questions. I would like to give special thanks to Dr. Basart, with whom I had very insightful conversations, and who shared with me valuable understanding I could not possibly obtain from a textbook. I would also like to thank him for the opportunity to join him in his jazz group, which provided a wonderful break from late night calculations. Dr. Mina needs to be mentioned for all the interesting discussions we had. Also, Sara K. Harris, who kindly assisted me with organizational matters.

Dr. Ikenna Nlebedim, who co-authored all of the papers I published during my doctorate study, deserves to be mentioned not only for his thorough review of the manuscripts, but also for keeping the soul in me when research results were scarce. Not to forget Dr. Ravi Hadimani, with whom I had a lot of interesting conversations on all sorts of topics. I also enjoyed many discussions with Neelam P. Gaunkar, with whom I co-authored two publications.

I am indebted to all my friends who have supported me over the last few years: Andrey Asadchev, Suffian Khan, Michael Lawrinenko, Jordan Schlak, Ceren Gunsoy, Marius Dragomiroiu, Arunabha M. Roy, and Finn Piatscheck for being my close friends in good and bad times.

## ABSTRACT

In this work, a new, non-destructive method for obtaining stress-depth gradients in ferromagnetic structures was developed, using the information contained within magnetic Barkhausen emissions. A depth- and stress-dependent model for the frequency spectrum of Barkhausen emissions was derived and fitted to measured data obtained from steel samples with controlled stress-depth gradients. To achieve this, a library of signal processing and optimization algorithms was developed, which allowed the analysis of large datasets. To obtain a calibration reference for stress, a number of solid mechanics finite element simulations were carried out. Proof of concept is demonstrated by assuming linear stress-depth gradients and successfully calculating the slopes of those, using a fitting algorithm.



## CHAPTER 1. AIMS OF THE PROJECT

The aims of this project are the following:

- To investigate the possibility of evaluating mechanical stress as a function of depth in ferromagnetic materials using Barkhausen signals.
- To develop a stress dependent model of the Barkhausen effect.
- To formulate a parametric model that relates Barkhausen emissions at their point of origin within the material to their attenuated form at the point of measurement.
- To provide an experimental methodology for conducting the proof of concept.

## CHAPTER 2. INTRODUCTION

### 2.1 Evaluation of residual stresses

Stress is defined as the force per unit area. Applied stress manifests when a component is actively loaded, while residual stress is what remains when that loading is removed. Residual stresses have a "balancing" effect, in the sense that they cancel out over the entire volume of the material.

Consider the example of a shot peening process, where a metallic surface is blasted with small ceramic pellets. Compressive stresses are formed on the surface, in what is essentially a plastic deformation. In order to balance the forces within the entire volume of the specimen, elastic tensile stress forms in the part below the compressed region. The expected stress-depth profile is illustrated in Fig. 2.1a, while the measured stress-depth profiles induced by shot peening in two different hard steels can be seen in Fig. 2.1b.

Residual stresses are typically classified into three different categories, which indicate the length scales over which these stresses manifest. These categories are Type I, II and III [1], and correspond to macro-, micro-<sup>1</sup> and atomic scale residual stresses, respectively. Type I residual stresses, range in the order of millimeters; Type II residual stresses, range in the order of micrometers; Type III residual stresses, range over atomic length scales. The present thesis is addressing the upper end of Type II stresses overlapping with the lower end of the Type I stresses.

A range of measurement techniques, both destructive and non-destructive, may be used to quantify stresses in the aforementioned length scales. Fig. 2.2 provides a visual depiction of the length scales that different methods are suitable for.

---

<sup>1</sup>at the length scale of grains

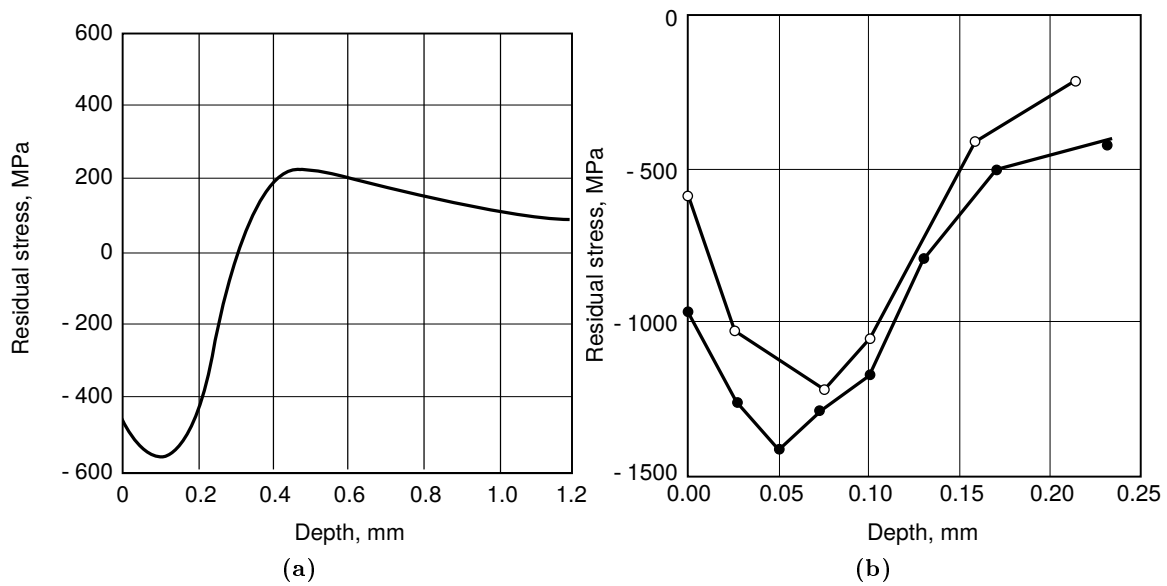


**Figure 2.1:** (a) Expected stress-depth profile due to shot peening (adapted from *Handbook of residual stress and deformation of steel*, pg. 348 [1]) (b) Measured stress-depth profiles induced by shot-peening steels of two different compositions [1]

Currently, x-ray diffraction is used in conjunction with electropolishing (for surface layer removal) to assess the stress-depth profile of shot-peened components. The need to remove surface layers is not there with magnetic techniques, which can be used to probe the near-surface region nondestructively. A common technique within the realm of magnetic nondestructive evaluation methods is Barkhausen noise. The next sections provide the definition of Barkhausen noise, along with the theoretical models developed so far, and an overview of its usage in the field of non-destructive evaluation of steels.

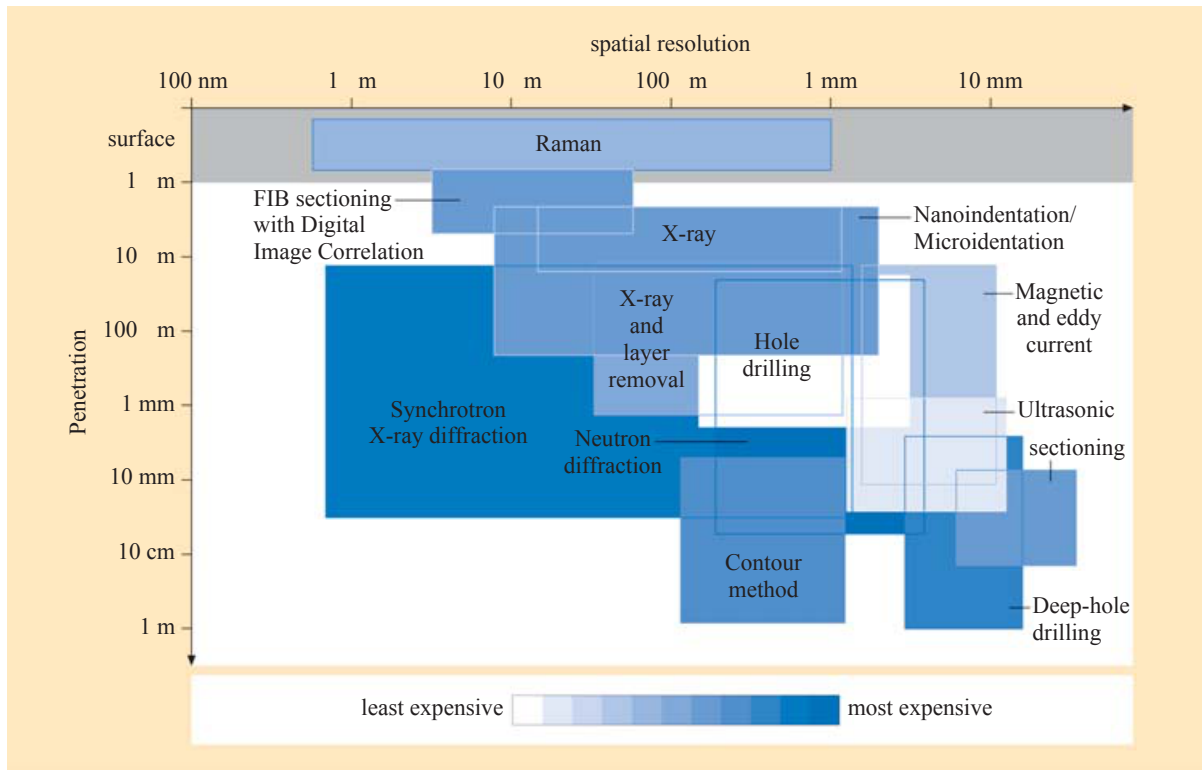


**Figure 2.2:** Measurement penetration vs. spatial resolution for various residual stress measurement methods. [2]

## 2.2 Barkhausen noise

Barkhausen jumps are discontinuous, irreversible changes in magnetization. The voltage induced in a coil due to these discontinuities appears as a noise signal, and is termed the Barkhausen noise, after the discoverer, Heinrich Barkhausen, who noticed a crackling noise while subjecting a ferromagnetic material to an applied field [3]. Over the years, studies have shown that magnetic Barkhausen noise is a rather complex physical process [4, 5, 6, 7]. Its manifestation varies depending on the type of ferromagnetic material, defect/inclusion sizes, frequency of applied magnetic field, as well as thermal effects [8, 9]. The aim of this section is to provide a description of the theoretical models that have been introduced over the years in order to describe Barkhausen noise. It also aims to provide a summary of developments in the context of non-destructive evaluation applications, particularly how measured signals contain information about the stress state of a material.

### 2.2.1 Domain wall motion and Barkhausen noise

Theoretical models of Barkhausen noise are based on domain wall dynamics, and usually attempt to describe a complex physical mechanism in one or two mathematical expressions. This is by no means a trivial task, and all past attempts of modelling Barkhausen activity are lacking in one way or another. Furthermore, Barkhausen activity contains a large stochastic component, which creates ambiguity concerning the choice of statistics that need to be used in describing the phenomenon. The physics community has shown great interest in Barkhausen noise due to the fact that Barkhausen *avalanches* (successive Barkhausen jumps) are fractal in nature and thus exhibit scale-invariance [10, 11, 12, 13, 14, 15, 16, 17, 18, 19]. Despite extensive studies that yielded complicated theories, little has been done towards practical application. In the engineering world, although they are used in the non-destructive evaluation industry, Barkhausen noise techniques still remain much the same after decades of use, as the complexity of the phenomenon hinders understanding. This disconnect between the theoretical and practical realms is what the present work attempts to bridge. The discussion begins with a review of domain wall dynamics, progresses to a description of Barkhausen power spectra, and

ends with a review of models of Barkhausen noise geared towards applications in the field of non-destructive evaluation.

Chikazumi [20] invokes the expression for the coercive field that pins a domain wall, by arguing that the domain wall motion is described by a second order differential equation [21] of the form

$$m_{dw} \frac{d^2x}{dt^2} + \eta \frac{dx}{dt} + \lambda x = \nu H, \quad (2.1)$$

which contains a velocity term  $dx/dt$ , that is dampened by a damping factor,  $\eta$ . In this expression,  $m_{dw}$  is the effective mass of the domain walls,  $d^2x/dt^2$  is the acceleration, and  $\lambda$  is the restoring coefficient that arises due to the internal potential. The force that arises due to the applied field is  $\nu H$ . In the case of an equilibrium, or equivalently, steady-state condition, where  $d^2x/dt^2 = 0$ , the velocity of the domain wall will be given by [7]:

$$v = \frac{\nu}{\eta} \left( H - \frac{\lambda}{\nu} x \right), \quad (2.2)$$

where the term  $\frac{\lambda}{\nu} x$  is equivalent to the local pinning field  $H_c$ . This equation indicates that as the applied field is increased, the velocity of the domain wall progressively decreases, until it is zero, when  $H = H_c$ . The domain wall will undergo acceleration and deceleration, depending on the slope of the internal potential and the local demagnetising field. The internal potential is linked to the pinning field, which is a function of the local pinning site density (dislocations, vacancies, interstitials and regions of second phase material [7]) and is almost impossible to accurately model. It can be approximated, however, by a sinusoidally varying function. This is based on a calculated average over a finite volumetric region, and it is a good illustration of how the domain wall will reach equilibrium at the minima and maxima of the function.

The case of a magnetic thin film with cubic anisotropy incorporates both irreversible rotation due to domain wall motion, as in the previous case, but also reversible motion due to domain rotation, caused by anisotropic effects. The critical field at which a Barkhausen event would happen, is calculated in terms of the anisotropy and spontaneous magnetization by the following equation [7]:

$$H_c \approx \frac{2K}{\mu_0 M_s} \sin(\pi/8) \cos(\pi/4), \quad (2.3)$$

where  $K$  is the anisotropy constant and  $M_s$  is the saturation magnetization. There is a range of critical fields for which Barkhausen events will occur, since there will be domain walls aligned along many different easy axes relative to the direction of the applied field.

Domain wall translation, bending and rotation are processes that are affected by the fluctuation of the internal potential seen by the domain walls. This fluctuation can be described by stochastic equations. Similar to (2.2), Williams, Shockley and Kittel [22] derive that the domain wall velocity is proportional to the the difference between internal magnetic field and pinning field, as in

$$v = \kappa(H - H_c), \quad (2.4)$$

where  $\kappa$  is the mobility of the domain walls, which is defined as the average velocity of the walls per unit magnetic field strength,  $v = \sigma G \dot{\Phi}$ , where  $\sigma$  is the conductivity,  $G$  is a geometrical constant, and  $\dot{\Phi}$  is the rate of change of flux with time. The main contributors to  $H$  are the applied field  $H_a$  and the local magnetostatic fields. It is noteworthy that  $H$  is the total internal field vector, which is the sum of an applied field component  $H_a$  and a demagnetising field  $H_d$ , which arises due to the magnetostatic energy, and is of opposite sign to  $H_a$ , such that

$$H = H_a - H_d, \quad (2.5)$$

where  $H_d = N_d M$ , and  $N_d$  is a geometrical constant. The behaviour of  $H_c$  is stochastic, since the interaction of the domain wall with inhomogeneities in the material is a random process. The input of energy via the applied magnetic field causes the domain wall to move, if its absolute value exceeds that of the local pinning field. The reciprocal of constant  $k$  is the mobility of the domain wall, and has units of velocity per unit magnetic field. This equation is valid only for planar, 180 domain wall motion. It is apparent that modelling domain wall motion is a challenging task, due to the physical system's degree of complexity.

Bertotti et al [5], based on the underlying theory of Williams, Shockley and Kittel, argue that the pinning field is governed by the *Ohrstein-Uhlenbeck process*, quantified by a *Langevin equation* [23]:

$$\frac{dH_p}{d\phi} + \frac{H_p}{\xi} = \frac{dW}{d\phi} \quad (2.6)$$

where  $W(\phi)$  is the Wiener-Levy process, and its derivative,  $dW/d\phi$  is the Gaussian white-noise process. The pinning field  $H_p(\phi)$  quantifies the extent to which inhomogeneities in the lattice pin the domain walls to energetically favourable positions <sup>1</sup>. The correlation length  $\xi$  quantifies the range of interaction between the moving domain wall and the pinning sources. The time-domain equivalent of (3.11) is [23]

$$\frac{dH_p}{dt} + \frac{H_p}{\tau_c} = \frac{dW}{dt} \quad (2.7)$$

where  $\tau_c = \xi/(d\phi/dt)$ . The above formulations were followed by a description of the Barkhausen noise power spectrum, which has the form [4]

$$F(\omega) = 4S\dot{I} \frac{A}{(\sigma G)^2} \frac{\omega^2}{(\omega^2 + \tau^{-2})(\omega^2 + \tau_c^{-2})}. \quad (2.8)$$

The normalised power spectrum was plotted for different magnetization rates (Fig. 2.3).

Sablik [25], based on the stochastic model of Alessandro et al., derives the Barkhausen noise power maximum as a function of magnetising field rate. This study is constrained to a magnetizing field with a constant time derivative, that being a ramp waveform. The power maximum is plotted for a range of field ramp rates  $dH/dt$ . The trend exhibits a non-linear relationship (Fig. 2.4).

---

<sup>1</sup>This model equation applies only to regions of the hysteresis loop where the measured differential permeability  $\mu'_{rmeas}$  can be approximated to be constant, and for  $\mu'_{rmeas} \gg 1$ . This condition holds true for small deviations of  $\mu_0 M = I$  around the coercive point  $H_c$ . The reason for constraining the model around a region of constant permeability is that there, the Barkhausen effect is fairly stationary, in contrast to regions of non-linear permeability, where it is non-stationary [24]. That is because when  $M \approx 0$ , domain wall motion is the governing mechanism, which is relatively well-defined. When  $M$  saturates, domain wall creation and annihilation dominate, those being processes that are more complicated to describe.



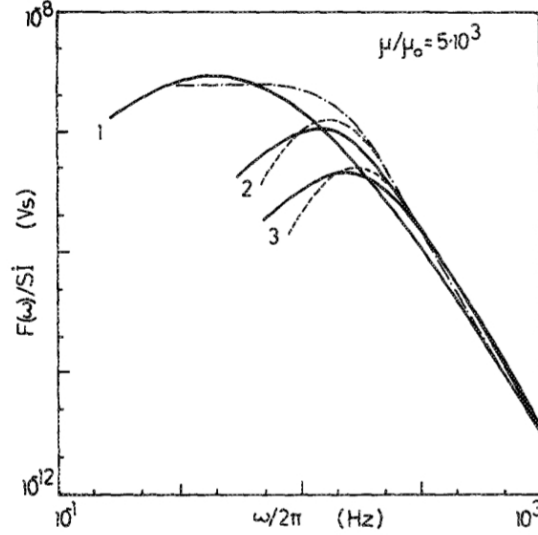


**Figure 2.3:** Normalised Barkhausen Noise power spectrum [4]. Dotted lines represent computer simulations, while solid lines represent experiment. The experiments were conducted for three different values of  $\dot{I}$ , with 1 having the highest value, and 2 the lowest.

Sipahi and Jiles [26], recognized the limitation of Bertotti's approach, and formulated a model that took into account the regions of variable differential permeability, by using the Jiles-Atherton theory of ferromagnetic hysteresis. In their experiments, they measured the count rate  $N$  (number of Barkhausen pulses per magnetizing cycle) as well as the root mean square Barkhausen voltage. One of the key model equations [7], which quantifies the instantaneous Barkhausen voltage  $V_B$  in terms of  $N$  and  $dH/dt$  is

$$V_B = -\mu_0 n A \left( \frac{N d\langle M_{disc} \rangle}{dM_{irr}} + \langle M_{disc} \rangle \frac{dN}{dM_{irr}} \right) \frac{dM_{irr}}{dH} \frac{dH}{dt}, \quad (2.9)$$

and implies that the voltage is linearly dependent on the magnetizing rate. The term  $\frac{d}{dM_{irr}}(N\langle M_{disc} \rangle)$  is defined as  $\gamma$ . This proportionality constant appears in the expression for the Barkhausen *jump sum*  $M_{JS}$ .  $M_{JS}$  quantifies the Barkhausen activity, since it is the product of number of events  $N$  and average event size  $\langle M_{disc} \rangle$ . These two quantities can be determined stochastically from Bertotti's model, while  $dB/dt$  is controlled, and  $dM_{irr}/dt$  is measured from the hysteresis curve. Under certain conditions,  $N$  follows a Poisson distribution. In this theory, the number of events in the present time period affect the number of events in the next time period, as in

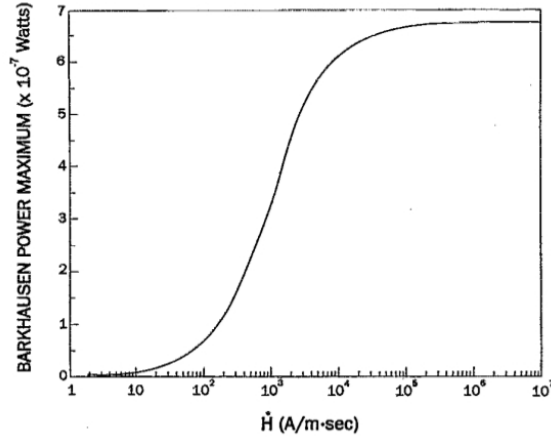


**Figure 2.4:** Barkhausen Noise power maximum vs. field ramp rate [25].

$$N_t = N_{t-1} + \delta_{rand} \sqrt{N_{t-1}}. \quad (2.10)$$

where  $\delta_{rand}$  is a random number that lies within a specific range. The model equation becomes

$$M_{JS}(t_n) = M_{disc} \chi'_{irr} H[N'(t_{n-1} + \delta \sqrt{N'(t_{n-1})})] \quad (2.11)$$

Model results were plotted both for zero stress case (Fig. 2.5), tension and compression.

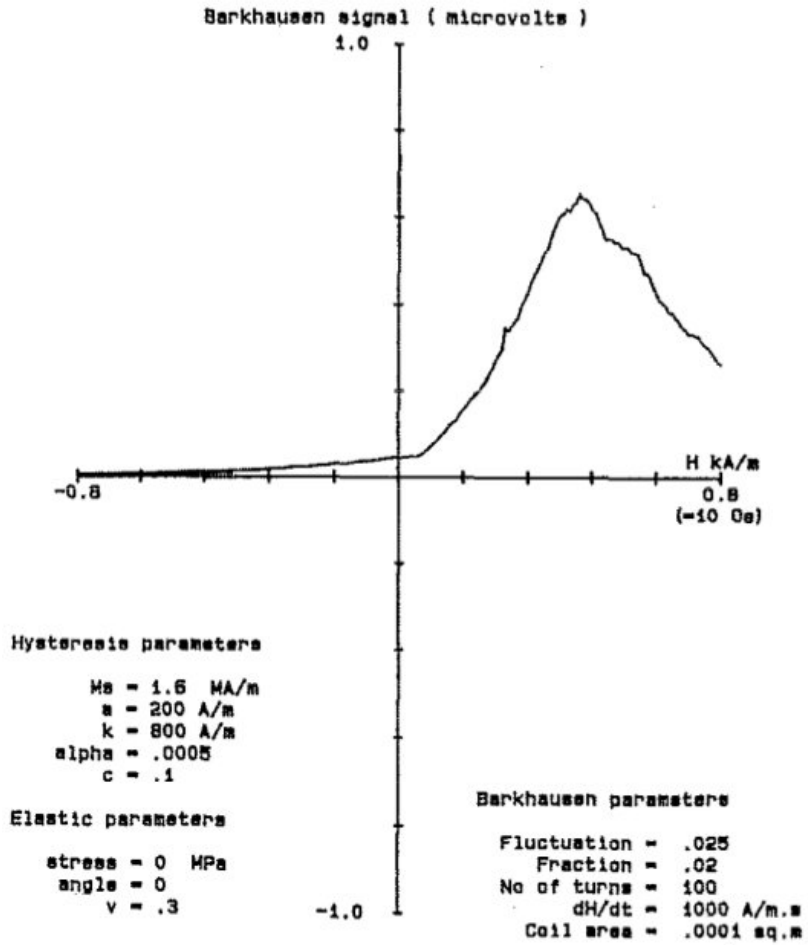


Figure 2.5: Results from the model for the Barkhausen signal in the zero stress case [27].

Some time later, Clatterbuck et. al [28] extended Bertotti's model itself to incorporate hysteresis effects via implementation of the Jiles-Atherton model. The resulting equation was

$$\frac{d\dot{I}_{irr}}{dt} + \frac{\dot{I}_{irr} - \chi'_{irr}\dot{H}_a}{\tau} = -\frac{\chi'_{irr}}{\tau} \frac{dH_c}{dt}. \quad (2.12)$$

Here, the Barkhausen emission signal voltage is expressed in terms of  $I_{irr}$  rather than  $\Phi$ . Also,  $\chi'_{irr}$  and  $H_a$  are functions of time, not constant, as in the original model. Also, the location on the hysteresis curve and the magnetization history both affect the value of  $\tau$ . This modification permits calculation of the Barkhausen signal as a function of stress, frequency and amplitude of applied field.

Sakamoto et al. [6] argued that the RMS voltage induced by a single Barkhausen jump can be modelled as a Gaussian pulse of standard deviation  $\sigma$ , with the reason for choosing a Gaussian shape being the facilitation of mathematical treatment, and not on the grounds of a physical explanation. The expression for a Gaussian pulse at time  $t$  is

$$V(t) = \frac{\Delta\Phi}{\sqrt{2\pi}\sigma} \exp(-(t - t_0)^2/2\sigma^2), \quad (2.13)$$

where  $\Delta\Phi$  is the magnitude of the flux change and at  $t_0$  the gaussian pulse holds a maximum value. These individual RMS pulses can be summed up to give the total induced voltage in a pick up coil.

### 2.2.2 Determination of residual stress from Barkhausen measurements

Magnetic Barkhausen noise is able to provide information about the microstructure of a ferromagnetic material. That is the reason for which it has been extensively used in the non-destructive evaluation of steel components; early diagnosis of fatigue due to time varying mechanical stress is the best way to prevent catastrophic failures. The magnetic Barkhausen noise technique has been proven useful in cases where in-service evaluation of components is required, particularly of the surface and sub-surface conditions. Applied stress as well as residual stress can be evaluated. It has also been shown that the Barkhausen emission is affected by hardness

as well as grinding burns [29], and that through the analysis of the Barkhausen signals, one can distinguish between microstructures, such as pearlitic and bainitic [30].

As discussed previously in this literature review, the nature of Barkhausen emissions is stochastic. Bulk relationships, however, can be deduced by a set of relatively straightforward experiments. Through similar experiments, various authors have plotted applied stress to Barkhausen signal envelope peak [31] also Barkhausen signal envelope RMS value [32] [33], [34], as well as count rate [34].

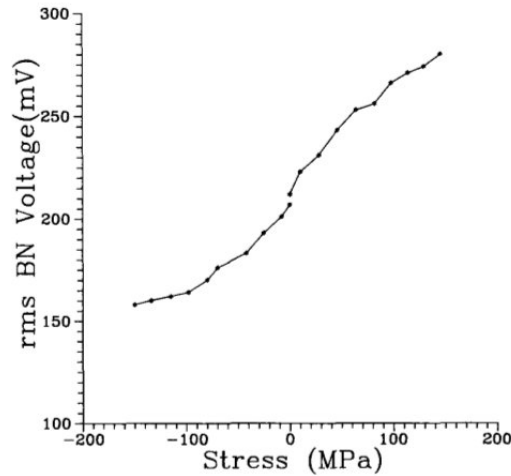


**Figure 2.6:** RMS Barkhausen noise voltage vs. stress [33].

By applying stress within the elastic limit of a semicircular half section of a 9.5 mm thick pipe, Jagadish et al. [33] were able to plot stress vs. the surface Barkhausen noise peak value. In the same study, power spectral and pulse height analyses were also conducted, for both compressive and tensile values of stress. It was found that the number of pulses increased with tensile stress and decreased with compressive stress (Fig. 2.6). This result agrees with Jiles et al. [31], who plotted the relationship between signal envelope peak  $M_{max}$  and compressive stress, finding that the former decreased with increasing compressive stress (Fig. 2.7). The conclusion of this study was that in the case of materials with positive magnetostriction, the Barkhausen signal envelope peak decreases with compression along the direction of the magnetic field and increases with tension along the direction of the magnetic field. Very similar results with the same qualitative explanation were given by Krause et al [35]. Jagadish et al. [33] further observed that stress also affects the pulse height distribution, with the observation being that

the application of tensile stress causes individual Barkhausen events of higher amplitude, while compressive stress gives rise to events of lessened amplitude.

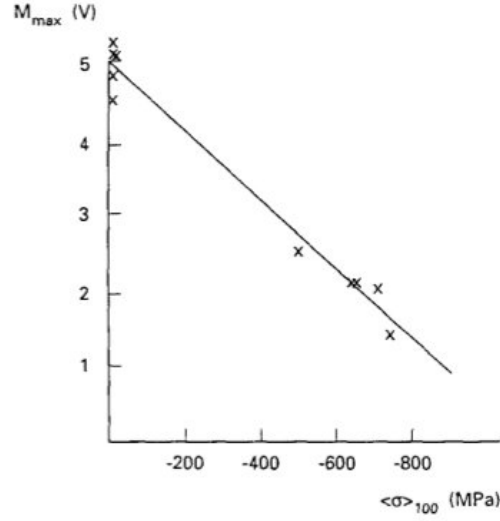


**Figure 2.7:** Barkhausen signal envelope peak  $M_{max}$  vs. average compressive stress  $\langle\sigma\rangle_{100}$  in a surface layer [31].

This observation can be explained qualitatively in terms of the magnetoelastic effect. Applied stress induces stress anisotropy, altering the magnetic permeability. Also, the addition of elastic energy to the lattice facilitates domain wall nucleation, leading to higher number of Barkhausen events in materials with positive magnetostriction. The converse happens in the case of compressive stress.

The previous description is based on the theory of the magnetomechanical effect, which argues that an externally applied stress contributes to the anisotropy energy of the lattice. According to Sablik et al. [36], an applied stress  $\sigma$  can be considered as an equivalent magnetic field  $H_\sigma$  which acts through the magnetostriction  $\lambda_s$ :

$$H_\sigma = \frac{3}{2} \frac{\sigma}{\mu_0} \left( \frac{\partial \lambda}{\partial M} \right)_T \quad (2.14)$$

And as a function of angle  $\theta$ , which is the angle between the direction of stress  $\sigma$  and the direction in which  $H_\sigma$  is measured [37]:

$$H_\sigma = \frac{3}{2} \frac{\sigma}{\mu_0} \left( \frac{\partial \lambda}{\partial M} \right)_T (\cos^2 \theta - \nu \sin^2 \theta) \quad (2.15)$$

At low fields, one can yield the expression for the total field. It is a sum of the magnetic field, the exchange field, and the stress-equivalent field stated above [38]:

$$H_e = H + \alpha M + H_\sigma = H + \alpha M + \frac{3b\sigma}{\mu_0} M (\cos^2 \theta - \nu \sin^2 \theta) \quad (2.16)$$

The anhysteretic magnetization can have the form of a Langevin function, which can incorporate the stress-equivalent field  $H_\sigma$  [38]:

$$M_{an}(H, \sigma) = M_s \left[ \coth \left( \frac{H + H_\sigma + \alpha M}{\alpha} \right) - \frac{\alpha}{H + H_\sigma + \alpha M} \right] \quad (2.17)$$

Mierczak and Jiles [39] recently used the above magnetomechanical relationship to explain a result that relates the reciprocal maximum differential susceptibility at the coercive point, to the reciprocal of the peak Barkhausen Noise amplitude. More specifically, for low field amplitudes where the magnetostriction curve is symmetric the differential susceptibility at the origin of the magnetization curve can be expressed as [40]

$$\frac{1}{\chi'_{max}(0)} - \frac{1}{\chi'_{max}(\sigma)} = \frac{3b\sigma}{\mu_0}. \quad (2.18)$$

Their experimental results (Fig. 2.8) indicated that a relationship of the following form is valid, where  $b'$  absorbs the constant of proportionality between  $\chi'$  and  $V_{meas}$ :

$$\frac{1}{V_{meas}(0)} - \frac{1}{V_{meas}(\sigma)} = \frac{3b'\sigma}{\mu_0}. \quad (2.19)$$

where  $V_{MBN}$  is the peak Barkhausen noise amplitude. This study establishes a linear relationship between the reciprocal of the peak Barkhausen voltage and stress (Fig. 2.8). The constant  $b'$  can only be determined empirically as it is a complicated function of magnetizing frequency and detection frequency.

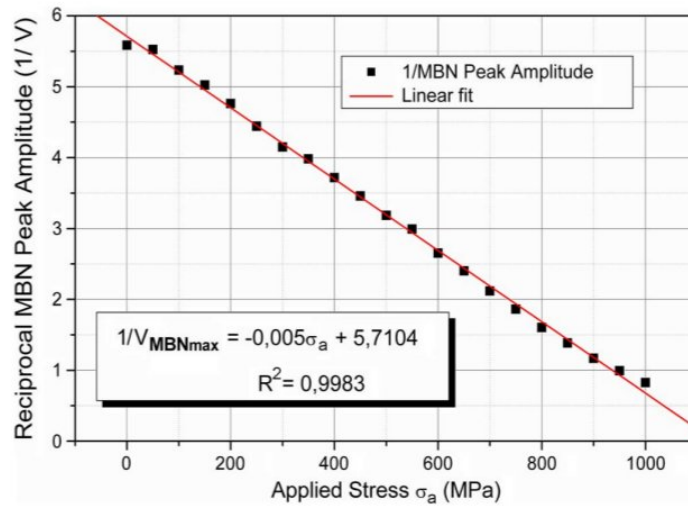


**Figure 2.8:** Experimental results showing the linear relationship between the reciprocal of the peak Barkhausen Noise voltage and stress [39].



## CHAPTER 3. THEORETICAL ANALYSIS AND PRELIMINARY RESULTS

### 3.1 Stress as an effective magnetic field

In the elastic region, a constant applied stress can be represented as an additional magnetic field term  $H_\sigma$ , which is a function of the magnetoelastic energy  $E_\sigma$  and the magnetization  $M$ , such that [41]:

$$H_\sigma = \frac{1}{\mu_0} \frac{\partial E_\sigma}{\partial M}, \quad (3.1)$$

Assuming there are no transverse strains, and assuming the magnetostriction is isotropic, the magnetoelastic energy due to stress has the form [41]

$$E_\sigma = \frac{3}{2} \lambda \sigma \cos^2 \phi, \quad (3.2)$$

where  $\lambda$  is the magnetostriction and  $\phi$  is the angle between the direction of magnetization and the direction of applied stress. The magnetostriction can be expanded into the form  $\lambda \approx bM^2$ , ignoring higher and lower order terms. This implies that the initial region of the  $\lambda - M$  curve can be approximated as parabolic, with  $b$  defined as a second-order coefficient. In general, low carbon steels exhibit low magnetocrystalline anisotropy such that in the presence of applied stress, the stress induced anisotropy dominates. When the field is applied along the direction of stress and assuming that stress is not a function of magnetization, (3.1) reduces to

$$H_\sigma = \frac{3b\sigma M}{\mu_0} \quad (3.3)$$

where  $\sigma$  is the stress amplitude. The magnetization  $M$  is, in strict terms, also a function of stress. However, at relatively small applied stresses and fields, its dependence on stress can

be neglected, such that  $\partial\sigma/\partial M = 0$ . Under the above conditions, it can be seen that the stress-equivalent field  $H_\sigma$  experienced by domains varies linearly with stress.

This effective field term for stress  $H_\sigma$  can then be inserted into the equation for the anhysteretic magnetization  $M_{an}$ :

$$\frac{M_{an}(H)}{M_s} = \coth\left(\frac{H_{app} + \alpha M_{an} + H_\sigma}{a}\right) - \frac{a}{H_{app} + \alpha M_{an} + H_\sigma} \quad (3.4)$$

where  $M_s$  is the saturation magnetization,  $H_{app}$  is the applied field,  $\alpha$  is the mean field coupling term, and  $a$  is a term that quantifies domain wall density in the material. It is possible to use the Taylor series expansion of  $\coth(x)$  at  $x = 0$  to simplify the problem:

$$\coth(x) \approx x^{-1} + \frac{1}{3}x - \dots \quad (3.5)$$

which leads to

$$M_{an}(H) = \frac{M_s \left( H_{app} + \alpha M_{an} + \frac{3b\sigma}{\mu_0} M_s \right)}{3a} \quad (3.6)$$

### 3.2 Variation of differential susceptibility and Barkhausen voltage with stress

From the expression of 3.6, Garikepati et. al [42] derived an equation for the anhysteretic differential susceptibility at the origin  $\chi'_{an}(\sigma)|_{H=0}$ :

$$\chi'_{an}(\sigma)|_{H=0} = \frac{M_s}{3a - \left( \alpha + \frac{3b\sigma}{\mu_0} \right) M_s} \quad (3.7)$$

where  $M_s$  is the saturation magnetization,  $\alpha$  is the coupling coefficient that quantifies the strength of interaction between neighbouring domains,  $b$  is a magnetostrictive coefficient that can be determined experimentally,  $\mu_0$  is the permeability of free space, and  $\sigma$  is the stress. This expression can be rearranged as

$$\frac{1}{\chi'_{an}(0)|_{H=0}} - \frac{1}{\chi'_{an}(\sigma)|_{H=0}} = \frac{3b\sigma}{\mu_0} \quad (3.8)$$

Likewise, at the coercive point  $\chi'_{max} \simeq \chi'_{an}$  so that there is a simple relationship between the peak slope of the magnetization curve and stress:

$$\frac{1}{\chi'_{max}(0)} - \frac{1}{\chi'_{max}(\sigma)} = \frac{3b\sigma}{\mu_0} \quad (3.9)$$

In previous work [39], the voltage peak envelope amplitude,  $V_{MBN,peak}$ , was observed to follow a similar trend as  $\chi'_{max}$  with stress, and thus (3.9) was modified to give

$$\frac{1}{V_{MBN,peak}(0)} - \frac{1}{V_{MBN,peak}(\sigma)} = \frac{3b'\sigma}{\mu_0} \quad (3.10)$$

where  $b'$  is a scaled version of  $b$  found in (3.9).

However, since the Barkhausen signal contains stochastic components, the parameter  $b'$  seen in (3.10) which is proportional to the slope of the line, can only be determined experimentally. Qualitatively, it will depend on the magnetizing frequency and amplitude of the magnetizing field.

It should be noted that the linear relationship that can be established in the low-field, low-stress region, does not hold as the magnitude of stress is increased past the yield point of the material. At the onset of plastic deformation, slip processes form dislocations in the crystal lattice. These, in turn inhibit domain wall motion by increasing the effective field that is needed for domain walls to escape local energy minima thus invalidating the assumption that the stress-induced anisotropy dominates. Thus, in the plastic region the relationship given in (3.10) may not hold. Nevertheless, for the purpose of this study which focuses on the elastic region, the relationship is realistic as the results show. Furthermore, the results of Garikepati et. al [42] experimentally verify that the linear relationship between the reciprocal of the anhysteretic susceptibility at the origin and stress also holds for compressive stress. It is therefore expected that a linear relationship between the reciprocal of the Barkhausen voltage and compressive stress should also hold. However, compressive and plastic stress is outside the scope of the present thesis.

### 3.3 Stochasticity in Barkhausen noise

In a specimen of ferromagnetic material that is magnetised by an applied field, magnetic avalanches of various durations occur at many different depths simultaneously. The stochastic process that governs these discontinuous changes in magnetisation is the *Ohrstein-Uhlenbeck process*, quantified by a *Langevin equation* [23]:

$$\frac{dH_p}{d\phi} + \frac{H_p}{\xi} = \frac{dW}{d\phi} \quad (3.11)$$

where  $W(\phi)$  is the Wiener-Levy process, and its derivative,  $dW/d\phi$  is the Gaussian white-noise process. The pinning field  $H_p(\phi)$  quantifies the extent to which inhomogeneities in the lattice pin the domain walls to energetically favourable positions. The correlation length  $\xi$  quantifies the range of interaction between the moving domain wall and the pinning sources. The time-domain equivalent of (3.11) is [23]

$$\frac{dH_p}{dt} + \frac{H_p}{\tau_c} = \frac{dW}{dt} \quad (3.12)$$

where  $\tau_c = \xi/(d\phi/dt)$ .

At high magnetization rates (typically  $\geq 100$  Hz),  $\tau_c$  becomes small, such that  $H_p \approx dW/dt$ . This implies that at high magnetization rates the pinning field, and consequently the domain wall velocity are governed by a white-noise process. To further clarify what is meant by high magnetization rates, the dimensionless parameter [23]  $c = \tau f$  is invoked, where  $\tau = GS\mu_{irr}/\rho$  and  $f$  is the frequency of the applied field.  $G$  is a constant equal to 0.1356,  $S$  is the cross-sectional area being magnetized,  $\mu_{irr}$  is the irreversible large-scale permeability and  $\rho$  is the electrical resistivity of the specimen. The cross-sectional area can be approximated as  $S = \delta w$ , where  $\delta = \sqrt{\rho/(\pi f \mu_{irr})}$  and is the penetration depth at a certain applied field frequency, and  $w$  is the width of the section. By substitution, we get

$$c = \sqrt{\frac{\mu_{irr} f}{\pi \rho}} G d, \quad (3.13)$$

which for a typical steel resistivity  $\rho = 2.2 \times 10^{-7} \Omega m$ , quasi-static permeability  $\mu_{irr} = 60$ ,  $d = 10$  mm and  $f = 100$  Hz, yields  $c \cong 0.8 \times 10^{-3}$ . In the limit  $c = 0$  and for low applied

field rates [17] (typically in the order of 0.05 Hz) , the power spectrum of Barkhausen emissions resembles that of Brownian noise (with  $P(\omega) \sim \omega^{-2}$ ), while for  $c > 0$ , and for higher applied field rates (typically  $\sim 100 - 1000$  Hz) the power spectrum at the origin of emissions flattens out, and begins to resemble a white noise power spectrum.

The resulting electromagnetic emissions, which diverge outwards from the origin of local magnetisation changes, will have the same statistical properties. This allows us to express the Barkhausen signal at the origin  $V(t)$  as Gaussian white noise of zero mean (the voltage is centered around zero) and variance (the voltage excursion around the mean)  $\sigma^2$ <sup>1</sup>:

$$V(t) \sim \mathcal{N}(0, \sigma^2). \quad (3.14)$$

For steels, the addition of magnetoelastic energy due to stress causes the nucleation of 180 degree domain walls in the direction of applied stress [43]. In materials with positive magnetostriction, an increase in the number of pinned domain walls (caused by elastic stress) leads to an increase in the variance of the noise, owing to the larger number of Barkhausen events occurring on a given time instant. The mean remains at zero, since the net magnetization increase in the specimen is ignored.

---

<sup>1</sup>In Chapter 5 it is shown how the variance mathematically resembles the R.M.S. of the signal.

### 3.3.1 Various forms of field $H$

In ferromagnetic materials the degree of coupling between neighbouring domains is quantified by the mean field coupling coefficient  $\alpha$ . The energy stored between  $N$  neighbouring domains with magnetisation  $m$  is given by

$$E = -\mathbf{m} \cdot \mu_0 \alpha N \mathbf{m}, \quad (3.15)$$

where  $\mu_0$  is the permeability of free space. To model inhomogeneities that impede the domain boundary as it moves, a stochastic pinning field  $H_i \sim \mathcal{N}(0, \sigma^2)$  is introduced, such that the energy stored between the domain and the pinning field is

$$E = -\mu_0 \mathbf{m} \cdot \mathbf{H}_i. \quad (3.16)$$

Finally, the magnetostatic energy in the applied field  $H_a$  is represented by

$$E = -\mu_0 \mathbf{m} \cdot \mathbf{H}_a, \quad (3.17)$$

to yield an expression for the total energy of

$$E = -\mu_0 \mathbf{m} \cdot \mathbf{H}_a - \mathbf{m} \cdot \mu_0 \alpha N \mathbf{m} - \mu_0 \mathbf{m} \cdot \mathbf{H}_i, \quad (3.18)$$

where the first, second and third terms represent the magnetostatic (also known as *Zeeman*), coupling and pinning energies, respectively. Hysteretic behaviour increases with  $\alpha$ , due to the increased coupling between adjacent domains. This is analogous to the snapping mechanism in brittle materials, in that a single domain wall displacement instigates a large avalanche. In models of ferromagnetic hysteresis, a high value for  $\alpha$  is associated with increased switching behaviour, and high permeabilities at the coercive point, a characteristic of hard ferromagnets. Soft ferromagnets, on the contrary, exhibit lower values of permeability at the coercive point, caused by a smaller exchange coupling.

In the presence of dislocations (which may have similar effect on a propagating domain as impurities) caused by lattice straining, domain coupling decreases even further, making the

contribution of  $\alpha$  small enough for the stochastic pinning field term to dominate. Since all other energy terms remain invariant, the free energy term in (3.18) can be expressed as

$$\Delta E = -\mu_0 \mathbf{m} \cdot \mathbf{H}_i. \quad (3.19)$$

Thus, under high applied stresses, the dominating mechanism is  $H_i$ , which can be modeled as white noise with frequency spectrum ranging from  $\sim 20$  kHz (approximate lower cutoff frequency of Barkhausen spectrum) to  $\sim 1.25$  MHz (upper cutoff imposed by measurement system used in this work).

### 3.4 Barkhausen noise in the frequency domain

To examine how the emissions attenuate as they propagate through the material, we take the Fourier transform of the signal  $V(t)$  at the origin. It has been shown previously that the Fourier transform of Gaussian, uncorrelated white noise will have a magnitude that follows the Rayleigh distribution [44]. For mathematical tractability and clarity, we only consider the mean magnitude of the Fourier transform  $\langle V \rangle$ , which is proportional to the standard deviation of the noise. As the emissions propagate, attenuation as a function of frequency causes the higher frequency components to dissipate faster (Fig. 3.1), with the rate of attenuation assumed to be exponential, such that the measured frequency spectrum at the surface, due to one emission, becomes

$$V_{meas}(\omega) = \langle V_{orig} \rangle e^{i\phi} e^{-\gamma(\omega)x}, \quad (3.20)$$

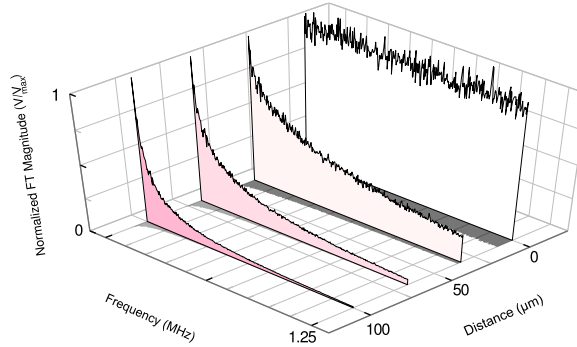


**Figure 3.1:** Effect of eddy current damping on the Barkhausen spectrum. In our model, Barkhausen emissions occurring at an infinitesimally thin region inside a specimen, have a white noise frequency spectrum. The energy in emissions is dissipated due to generation of eddy currents, causing the spectrum to resemble pink noise as the Barkhausen emissions propagate through the material.

where  $\langle V \rangle$  is the expected magnitude of the Fourier transform at the origin,  $\phi$  is the phase of the emission at the point of origin,  $x$  is the distance from the surface to the point of origin of the emission, and  $\gamma(\omega) = \alpha(\omega) + i\beta(\omega)$  is the propagation constant, a function of angular frequency  $\omega$ . Equation (3.20) describes the propagation of a plane wave in an electrically conductive medium; the sensor measures the perpendicular component of the flux density, with unit vector  $\hat{\mathbf{x}}$  normal to the surface. The coefficient  $\alpha(\omega)$  quantifies the rate of attenuation



(in Np/m), while  $\beta(\omega)$  is the phase constant (in rad/m) and defines the rate of phase change as the wave propagates. In conductors,  $\alpha = \beta = \sqrt{\omega\mu_{\text{eff}}/2\rho}$ , where  $\mu_{\text{eff}}$  and  $\rho$  represent the effective magnetic permeability (here we define the effective magnetic permeability as the effective permeability of the magnetic circuit, which includes the test specimen and sensor apparatus) and the electrical resistivity, respectively. For mathematical tractability, we only consider the magnitude of the term  $e^{-\gamma(\omega)x}$  in (3.20), and we take the mean of the phase at the origin (the phase of the Fourier transform of uncorrelated Gaussian noise is uniformly distributed between  $-\pi$  and  $\pi$ , with a mean of zero). We can then write the attenuated amplitude of emission as

$$V_{\text{meas}}(\omega) = \langle V_{\text{orig}} \rangle e^{-\alpha(\omega)x}. \quad (3.21)$$

We assume that the variation of electrical resistivity  $\rho$  with stress is negligible, thus we only consider  $\mu_{\text{eff}}$  and  $\langle V \rangle$  to be functions of stress. Barkhausen jumps occur everywhere inside the specimen, and every depth  $x$  is the point of origin of a Barkhausen spectrum, of the form (3.21). It should be mentioned here that in the following sections,  $\langle V_{\text{orig}} \rangle$  will be denoted as  $V_{\text{orig}}$ .

### 3.5 Initial approach to separating emissions from different depths

The time domain approach where simple time-domain statistics are extracted from the raw measured voltage, is limited. This is due to the fact that these time-domain statistics represent the bulk emission from the material and not specific volumetric regions within it.

The idea of this approach is to transform the measured signal into the frequency domain, remove certain spectral regions through filtering, and revert back to the time domain signal, where certain time domain statistics can be extracted. More specifically, an electromagnetic emission of the type described in (3.21) will be attenuated to  $1/e$  of its amplitude at the origin as it travels a distance  $\delta = 1/\alpha$ , due to eddy current dissipation. It should then be possible to define a "cutoff" distance at which an emission of a certain frequency is assumed to attenuate to zero. To simplify the analysis, it is assumed that each Barkhausen burst is a Dirac delta pulse in the time domain, which in the frequency domain translates to a flat spectrum, like white noise. It is important to note, however, that each frequency component within the burst propagates with its own attenuation constant.

In order to graphically describe the model, an illustration of the solution of the model equations is presented in Fig. 3.2. Consider two different emissions of frequency  $f_a = 0.5$  MHz and  $f_b = 0.1$  MHz (frequencies present in a typical Barkhausen noise spectrum), which occur at depth  $x_a$  and  $x_b$  inside a specimen of constant electrical permeability and constant electrical conductivity. The emission of frequency  $f_a$  will travel a distance  $\delta_a$  before being attenuated to  $1/e$  of its initial amplitude. Its skin depth lies between depths  $x_0$  and  $x_1$ , hence emission  $f_a$  is considered to be present in a Barkhausen measurement band-passed from  $\omega_0$  to  $\omega_1$ . Assuming for the purposes of the analysis that complete attenuation occurs over a propagation depth  $\delta$ , the emission of frequency  $f_b$  will not be present in that measurement. However the emission at frequency  $f_b$  will be present in a measurement band-passed from  $\omega_0$  to  $\omega_2$ .

For a given frequency, emissions originating from regions deeper in the material will arrive at the surface more attenuated than emissions originating from shallower regions. Consequently emissions of relatively high frequency, originating from deep regions of the specimen, do not reach the surface. Hence, it is possible to identify the depth of emission by defining cut-off

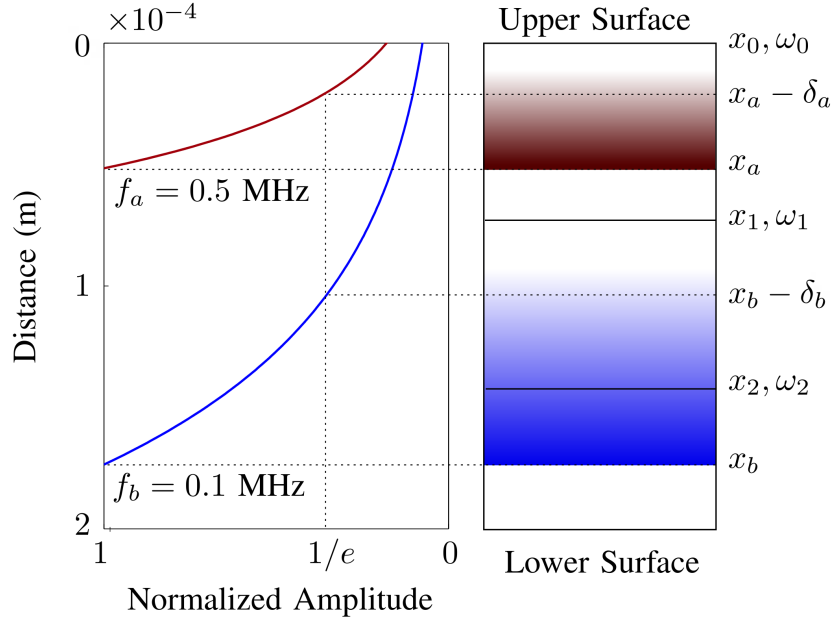


**Figure 3.2:** Emissions of frequency  $f_a = 0.5 \text{ MHz}$  and  $f_b = 0.1 \text{ MHz}$  originating at depths  $x_a$  and  $x_b$  inside a material of constant permeability and conductivity. Attenuation occurs due to the skin effect described in equation (3.21). The model assumes a sharp cutoff at  $\delta$ , which allows setting cutoff depths to facilitate the separation of emissions. As long as the skin depth of an emission falls between the upper and lower cutoffs of a layer, it is detected within that layer. Attenuation of the amplitude of emissions is represented by fading colour.

frequencies for a measurement, which correspond to particular depths. Barkhausen emissions occur at all depths and over a range of different frequencies, and therefore emissions at frequency  $f_b$  can also originate in the region between  $x_0$  and  $x_1$ . Hence, an emission measured at the surface will therefore be a superposition of many different emissions of the same frequency originating at different depths. As a result, to distinguish between the emissions at different depths and construct a stress profile, equation (3.21) alone is not sufficient.

The basic model developed here considers two consecutive layers which have different values of stress. In each of these layers stress is considered to be homogeneous. Barkhausen measurements at the surface are band-pass filtered to retrieve two ranges of signals; one from  $\omega_0$  to  $\omega_1$ , representing emissions from the first layer, and one from  $\omega_0$  to  $\omega_2$  (where  $\omega_2$  is smaller than  $\omega_1$ ), representing emissions from the combined first and second layers. Provided the absolute value of stress in the first layer is known, a set of model equations is used to calculate the stress in the second layer. The signal coming from consecutive layers is found by varying the low frequency cut-off  $\omega_2$  and repeating the procedure. The following sections describe the model equations

which apply to a single uniformly stressed layer of material and two uniformly stressed layers of material. For the sake of clarity, it is important to note that the objective of this methodology is to remove the low frequency part of the emission spectrum originating in the surface layer.

### 3.5.1 Magnetic Barkhausen emissions from a single, uniformly stressed layer

Consider a ferromagnetic slab of finite thickness, relative magnetic permeability  $\mu_r$  and electrical conductivity  $\sigma$  as schematically shown in Fig. 3.3. If Barkhausen emissions of frequency  $\omega_0$  to  $\omega_1$  occur from depth  $x_0$  to depth  $x_1$  into the specimen, and assuming plane wave propagation as well as a white noise spectrum the voltage that is induced in a sense coil located at the surface can be expressed as in equation (3.22) [45, 46]:

$$\begin{aligned} V_{meas}(x_0, x_1, \omega_0, \omega_1) &= \int_{\omega_0}^{\omega_1} \int_{x_0}^{x_1} V_{orig1} e^{-\zeta x \sqrt{\omega}} dx d\omega \\ &= V_{orig1} f(x_0, x_1, \omega_0, \omega_1) \end{aligned} \quad (3.22)$$

where  $\zeta = (2\rho/\mu_0\mu_r)^{1/2}$  and  $V_{orig1}$  is a constant. The function  $f(x_0, x_1, \omega_0, \omega_1)$  is a generalized attenuation function, the ratio of total measured Barkhausen voltage at the surface to the Barkhausen voltage at the point of origin. It is given by

$$\begin{aligned} f(x_0, x_1, \omega_0, \omega_1) &= \frac{2}{\zeta^2} \left[ \frac{1}{x_1} \left( e^{-\zeta x_1 \sqrt{\omega_0}} - e^{-\zeta x_1 \sqrt{\omega_1}} \right) \right. \\ &\quad \left. - \frac{1}{x_0} \left( e^{-\zeta x_0 \sqrt{\omega_0}} - e^{-\zeta x_0 \sqrt{\omega_1}} \right) \right] \end{aligned} \quad (3.23)$$

In the limiting case where  $x_0 = 0$  and emissions from the surface to  $x_1$  are considered, the attenuation function becomes

$$\begin{aligned} f(0, x_1, \omega_0, \omega_1) &= \frac{2}{x_1 \zeta^2} \left[ \left( e^{-x_1 \zeta \sqrt{\omega_0}} - e^{-x_1 \zeta \sqrt{\omega_1}} \right) \right. \\ &\quad \left. + x_1 \zeta (\sqrt{\omega_0} - \sqrt{\omega_1}) \right] \end{aligned} \quad (3.24)$$

The above expression is experimentally verifiable when  $x_1$  is equal to the slab thickness. That is, when emissions from all depths are taken into account. In general, when the slab thickness

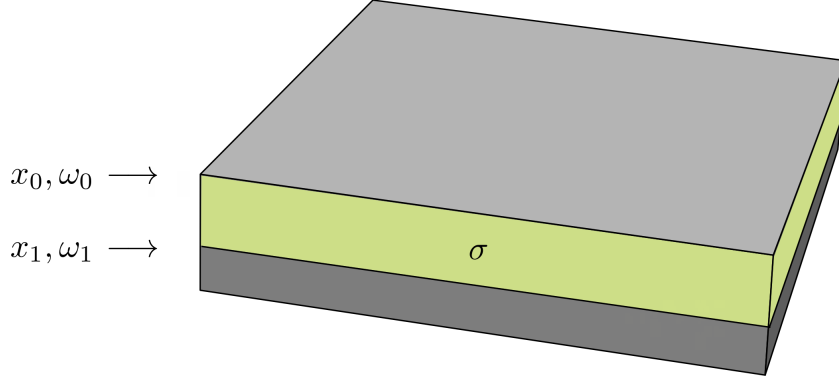


**Figure 3.3:** Layered specimen considered by the model, where layer boundaries correspond to specific frequencies. Stress is denoted by  $\sigma$ .

is greater than  $x_1$  the measured signal at the surface will not only represent the emissions occurring within the interval 0 to  $x_1$  but also emissions in the same frequency range originating at depths beyond  $x_1$ .

Fig. 3.4 is a plot of the voltage given by equation (3.24), where  $\mu_r = 50$ ,  $\rho = 8.93 \times 10^{-8} \Omega/m$  and  $V_{orig} = 2 \mu V$ . In other words, the average Barkhausen emission in the specimen induces a voltage of  $2 \mu V$  in its immediate vicinity. During its propagation towards the surface, the induced voltage is attenuated exponentially as determined by the term  $\zeta$ . For this plot,  $x_1 = 100 \mu m$ , which is also the thickness of the specimen. The frequency cut-offs  $\omega_0/2\pi$  and  $\omega_1/2\pi$  are each varied from 30 kHz to 1 MHz, which correspond to penetration depths  $\delta$  of  $\sim 122 \mu m$  and  $\sim 21 \mu m$  for a material of the given resistivity and permeability. Having established a constant thickness and varying the frequency limits  $\omega_0$  and  $\omega_1$ , a non-linear trend is apparent.

Fig. 3.5 is a contour plot of the measured voltage from one layer, plotted as a function of the two cutoff frequencies. It can be seen that the peak voltage is  $\sim 400 \mu V$ . Since  $\omega_1$  and  $\omega_0$  were defined as the lower and upper cutoff frequencies respectively, values of  $V_{meas}$  for which  $\omega_1 > \omega_0$  can be ignored for the purposes of this model. Hence, they were omitted from both plots.

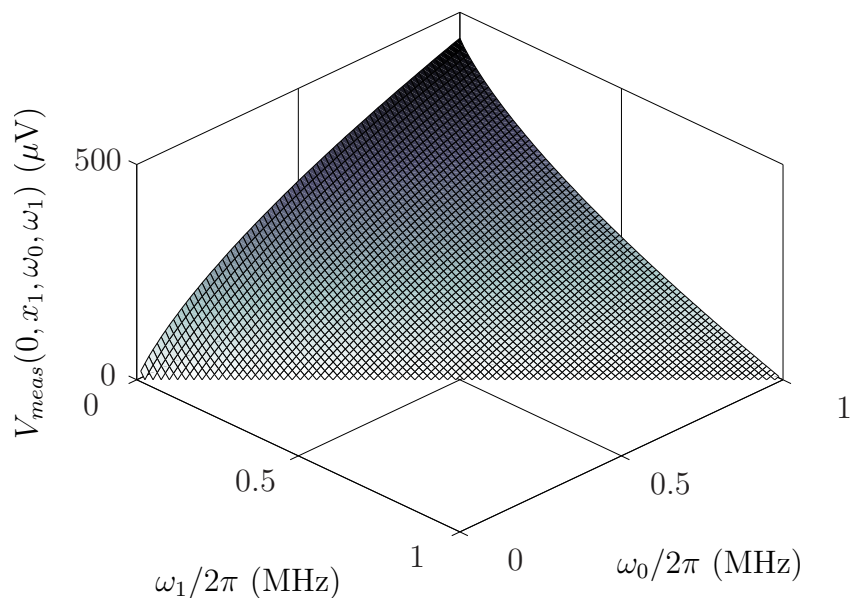


**Figure 3.4:** Measured voltage from one layer plotted as a function of frequencies  $\omega_0$  (upper cutoff) and  $\omega_1$  (lower cutoff). For this study,  $\rho = 8.93 \times 10^{-8} \Omega/m$ ,  $\mu_r = 50$  and  $V_{orig} = 2\mu V$ . Depth  $x_1$  was set to  $100 \mu m$ . Note that when  $\omega_1 > \omega_0$ , there is no detected voltage.

### 3.5.2 Magnetic Barkhausen emissions from a combination of two uniformly stressed layers

In order to produce a stress depth profile where stress takes on different values with depth, it is necessary to consider the test specimen divided into more than one region, as would be practically expected. A second layer which extends deeper into the specimen has to be considered. However, if the average stresses in the first and second layer are different, the Barkhausen emission amplitudes at their origin will also be different. Then this can be used to determine the difference in stress between the two layers if it is possible to distinguish between emissions from different depths (Fig. 3.6).

Consequently,  $V_{orig1}$  and  $V_{orig2}$  are defined as the amplitude of emission at the origin for the first and second layer respectively. The expression that takes into account emissions from both is equation (3.25) [46]

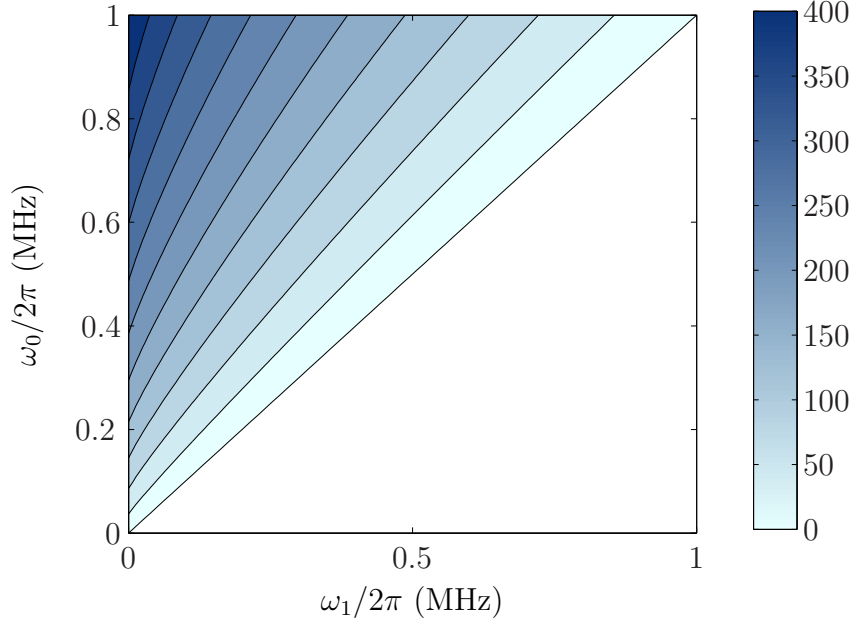


**Figure 3.5:** Contour plot of the measured voltage from one layer, as a function of frequencies  $\omega_0$  (upper cutoff) and  $\omega_1$  (lower cutoff). Voltage values are expressed in  $\mu\text{V}$ . Note that when  $\omega_1 > \omega_0$ , there is no detected voltage.

$$\begin{aligned}
 V_{meas}(0, x_1, x_2, \omega_0, \omega_1, \omega_2) = & \\
 & V_{meas}(0, x_1, \omega_0, \omega_2) \left( 1 + \frac{f(0, x_1, \omega_1, \omega_2)}{f(0, x_1, \omega_0, \omega_1)} \right) \\
 & + V_{orig2} f(x_1, x_2, \omega_1, \omega_2)
 \end{aligned} \tag{3.25}$$

The first term on the right hand side contains the attenuation ratio  $f(0, x_1, \omega_1, \omega_2)/f(0, x_1, \omega_0, \omega_1)$  which normalizes for emissions in the  $\omega_2, \omega_1$  range coming from the first layer. The second term contains the quantity of interest,  $V_{orig2}$  (from which the stress in the second layer can be determined) multiplied by the attenuation function.

To examine the effect of varying  $V_{orig1}$  relative to  $V_{orig2}$ , equation (3.25) was plotted for  $V_{orig1}$  at 1, 2, 3 and 4  $\mu\text{V}$ , while keeping  $V_{orig2}$  constant at 2  $\mu\text{V}$ . In Fig. 3.7 the measured voltage is plotted as a function of  $\omega_2$ , with  $\omega_1 = 0.5$  MHz and  $\omega_0 = 1$  MHz being held constant. Fig. 3.7 shows that as the value of  $V_{orig1}$  is increased, there is a corresponding increase in the peak value of the measured voltage. It can be seen that when  $V_{orig1} = V_{orig2} = 2$   $\mu\text{V}$ , the peak voltage is  $\sim 400$   $\mu\text{V}$ .

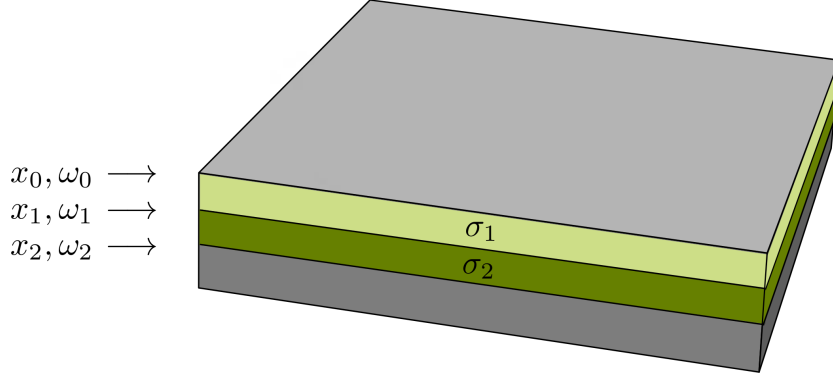


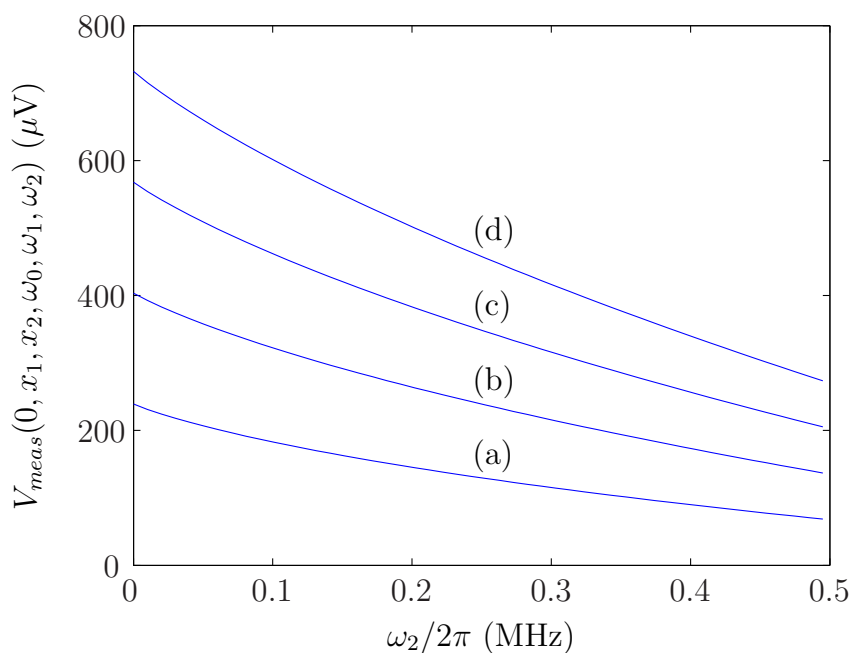
**Figure 3.6:** Layered specimen considered by the model, where layer boundaries correspond to specific frequencies. Stresses in the first and second layer are denoted by  $\sigma_1$  and  $\sigma_2$  respectively.

In Fig. 3.8, the measured voltage is plotted as a function of  $\omega_2$  and  $\omega_1$ . Having set  $\omega_0 = 1$  MHz, and both  $V_{orig1}$  and  $V_{orig2}$  at  $2 \mu\text{V}$ , it can be seen that the effect of varying  $\omega_1$  is not significant and can be ignored in this case. Again, values of  $V_{meas}$  that do not satisfy the condition  $\omega_2 < \omega_1$  can be ignored, so they were omitted in both plots.

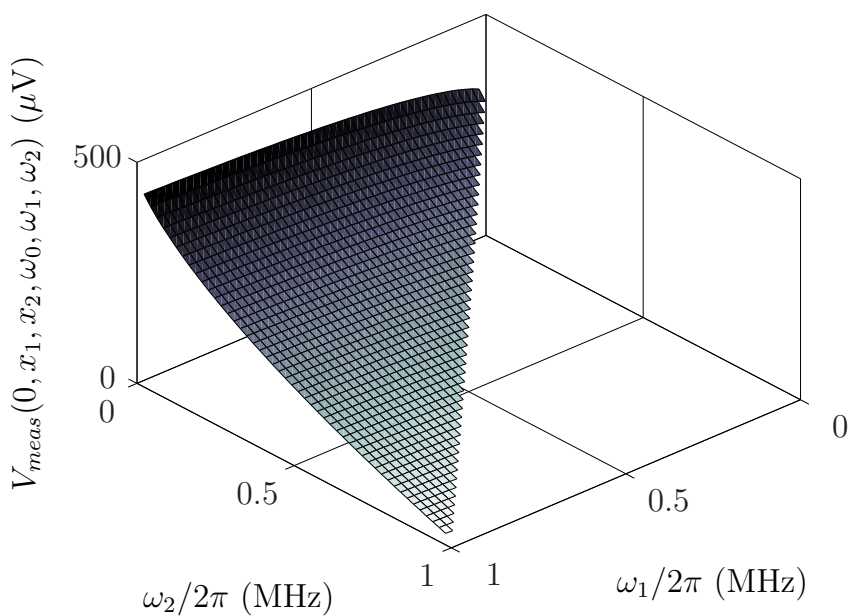
It can be seen that the measured voltage increases as the frequency span increases, for both the one- and the two layer cases. In particular, the peak voltage reaches  $\sim 400 \mu\text{V}$ , for a specimen of  $100 \mu\text{m}$  thickness,  $\mu_r = 50$ ,  $\rho = 8.93 \times 10^{-8} \Omega/\text{m}$ , having considered emissions of a frequency range of 30 kHz to 1 MHz. Comparison of the peak voltages of Fig. 3.5 and Fig. 3.7 yields the observation that when  $V_{orig1} = V_{orig2} = 2 \mu\text{V}$ , and the upper and lower cut-off frequencies and depths are identical, the structure can be considered as only consisting of one layer with  $V_{orig2} = 2 \mu\text{V}$ . This result can be further generalized to arrive to the conclusion that when emission amplitudes at the origin of different consecutive layers are identical and the cutoff frequencies are identical, the structure can then be approximated as having a single layer.

Fig. 3.9 illustrates the concept of a layered specimen, and how sampling different parts of the Barkhausen frequency spectrum translates into sampling different depth ranges.





**Figure 3.7:** Measured voltage from two layers plotted as a function of the lower cutoff frequency  $\omega_2$ . In this plot,  $\omega_0/2\pi = 1$  MHz,  $\omega_1/2\pi = 0.5$  MHz and  $V_{orig2} = 2 \mu\text{V}$ . The value of  $V_{orig1}$  was set to (a)  $1 \mu\text{V}$ , (b)  $2 \mu\text{V}$ , (c)  $3 \mu\text{V}$  and (d)  $4 \mu\text{V}$ . The depths were fixed to  $x_1 = 50 \mu\text{m}$  and  $x_2 = 100 \mu\text{m}$ .



**Figure 3.8:** Measured voltage from two layers plotted as a function of frequencies  $\omega_1$  (intermediate cutoff) and  $\omega_2$  (lower cutoff). In this plot,  $\omega_0/2\pi = 1$  MHz,  $V_{orig1} = V_{orig2} = 2 \mu\text{V}$ . The depths were fixed to  $x_1 = 50 \mu\text{m}$  and  $x_2 = 100 \mu\text{m}$ . Note that when  $\omega_1 < \omega_2$ , there is no detected voltage.

### 3.5.3 Solving for the voltages at the origin of emission

To determine stress it is necessary to determine the Barkhausen voltage at the point of origin of the emission. Both  $V_{meas}(0, x_1, \omega_0, \omega_1)$  and  $V_{meas}(0, x_1, x_2, \omega_0, \omega_1, \omega_2)$  are experimentally measurable quantities, which correspond to two filtered versions of the measured Barkhausen signal, one band-passed from  $\omega_0$  to  $\omega_1$  and the other band-passed from  $\omega_0$  to  $\omega_2$ , as seen in Fig. 3.9. However, the voltage emanating from the second layer cannot be directly measured because emissions of the same frequency may occur in different depths, making it impossible to identify the depth of emission simply by filtering the measured signal. Nevertheless, the value of  $V_{orig2}$  can be calculated by subtracting a normalized version of the first layer voltage  $V_{meas}(0, x_1, \omega_0, \omega_1)$  from the combined layer voltage  $V_{meas}(0, x_1, x_2, \omega_0, \omega_1, \omega_2)$  and by solving for  $V_{orig2}$ .

The depth-profiling model considers complete attenuation at the skin depth, such that when the lower cutoff frequency is decreased, more material volume is sampled and more Barkhausen emissions are taken into account. The voltage of a single Barkhausen emission  $V_{orig1}$  can be solved for by rearranging (3.22), such that:

$$V_{orig1} = \frac{V_{meas}(0, x_1, \omega_0, \omega_1)}{f(0, x_1, \omega_0, \omega_1)}. \quad (3.26)$$

Similarly, (3.25) can be rearranged to yield the average amplitude of a Barkhausen emission in the second layer  $V_{orig2}$ , such that

$$V_{orig2} = \frac{1}{f(x_1, x_2, \omega_1, \omega_2)} \left( V_{meas}(0, x_1, x_2, \omega_0, \omega_1, \omega_2) - V_{meas}(0, x_1, \omega_0, \omega_1) \left( 1 + \frac{f(0, x_1, \omega_1, \omega_2)}{f(0, x_1, \omega_0, \omega_1)} \right) \right) \quad (3.27)$$

Once the probing depths and corresponding frequencies are calculated, the attenuation functions can be evaluated, and  $V_{meas}(0, x_1, \omega_0, \omega_1)$  as well as  $V_{meas}(0, x_1, x_2, \omega_0, \omega_1, \omega_2)$  can be obtained by filtering the original Barkhausen signal accordingly. Thus,  $V_{orig1}$  and  $V_{orig2}$  can be obtained by applying (3.26) and (3.27) respectively. These two separate quantities correspond to the first and second layer in the specimen.

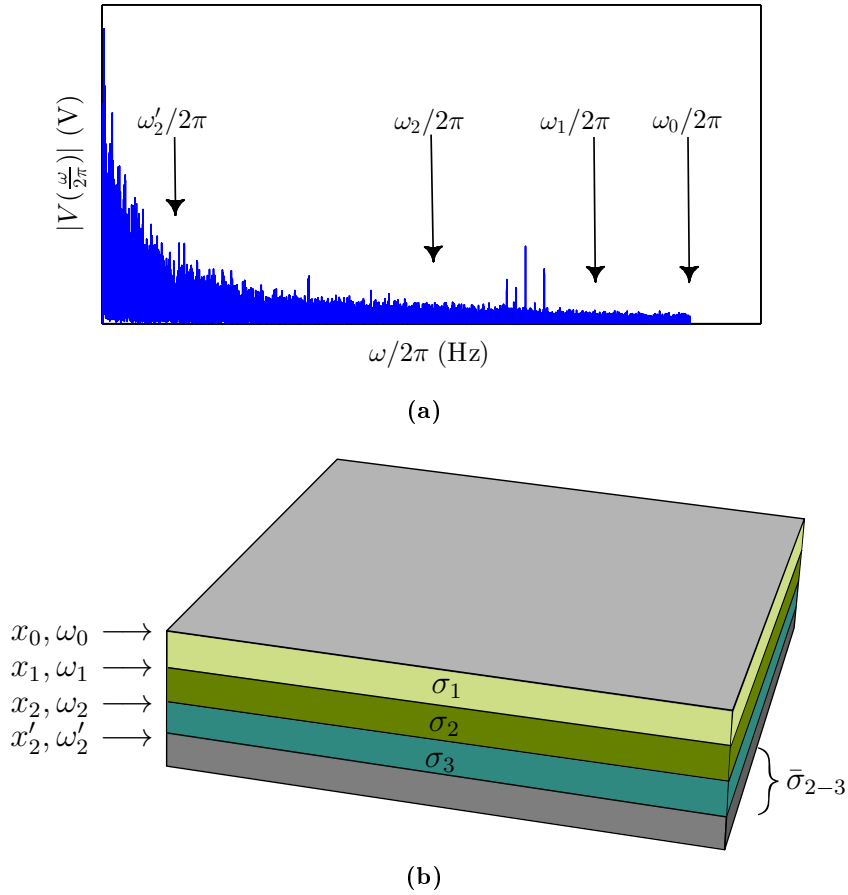


**Figure 3.9:** (a) Typical measured Barkhausen noise spectrum, with  $\omega_0$ ,  $\omega_1$ ,  $\omega_2$ , denoting the upper, intermediate and lower cutoff frequencies - these correspond to different depths of sampling (*frequencies not to scale*). The  $\omega_2$  limit can be lowered to  $\omega'_2$  in order to sample deeper regions of the specimen. (b) Ferromagnetic specimen divided in three layers of equal volume, where  $\sigma_1$ ,  $\sigma_2$  and  $\sigma_3$  denote the stress magnitudes in the first, second and third layer respectively. Also  $\bar{\sigma}_{2-3} = \frac{1}{2}(\sigma_2 + \sigma_3)$ .

In order to create a calibration profile it is necessary to start with an unstressed specimen of the material under examination. This will serve as a reference, for which the stress-voltage relationship at different depths can be determined. By applying a uniform uniaxial tensile stress, measuring the amplitude of Barkhausen emissions, and using (3.26) and (3.27),  $1/V_{orig}$  corresponding to each depth range can be plotted versus stress. It is expected that since the stress in the reference specimen is uniform,  $V_{orig1} = V_{orig2} = V_{orig2-n}$ . This will be true provided that the model assumptions are correct, namely that the Barkhausen frequency spectrum at the origin is white and that a sharp frequency cutoff can be used to discriminate between different depths. To the extent that these assumptions are invalid, the calibration curves will not coincide, and will each be characterized by a different offset and slope, like in the results of Fig. 3.10. Fig. 3.10 shows the reciprocal of the average Barkhausen emission voltage for each layer, plotted against uniaxial engineering stress. The fact that the calibration profile for  $V_{orig1}$  does not coincide with that of  $V_{orig2}$  and  $V_{orig2-3}$ , indicates that the Barkhausen spectrum at the origin is either not white at the higher end of the frequency spectrum or that the assumption of a sharp cutoff are invalid. It should be noted that the intercepts and slopes are also expected to vary with magnetizing frequency, which should not happen in an all-inclusive theory.

**Table 3.1:** Calibration profile parameters

Profile	Depth span ( $\mu m$ )	$b'$ ( $msA^{-1}N^{-1}$ )	Adj. $R^2$
$\frac{1}{V_{orig1}}$	0-60	$-9.22 \times 10^{-13}$	0.98
$\frac{1}{V_{orig2}}$	60-120	$-8.95 \times 10^{-14}$	0.97
$\frac{1}{V_{orig2-3}}$	60-180	$-1.27 \times 10^{-13}$	0.96

After the calibration profile is created, a specimen of the same composition and unknown stress state can be evaluated. This is done by conducting a Barkhausen measurement and by applying (3.26) and (3.27) to compute the Barkhausen peak envelope voltages in the first and second layer. Using the calibration profile, the stress in each layer can subsequently be obtained. By decreasing the lower detection frequency from  $\omega_2$  to  $\omega'_2$  in (3.27), the average stress magnitude  $\bar{\sigma}_{2-3}$  in the combined second and third layer can be determined, provided the calibration profile for  $1/V_{orig2-3}$  exists. Fig. 3.11 illustrates this concept.

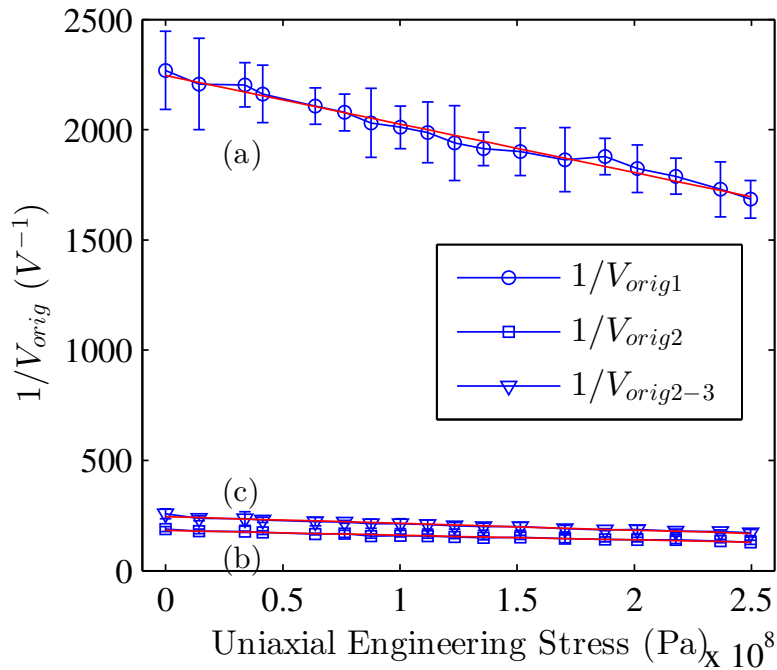


**Figure 3.10:** Experimentally calculated calibration profiles for (a)  $1/V_{orig1}$ , (b)  $1/V_{orig2}$  and (c)  $1/V_{orig2-3}$ , fitted with a linear regression and plotted with 95% confidence intervals. These trends are obtained by filtering the Barkhausen data collected from an ASTM A36 steel specimen under uniaxial tension. In order to produce the calibration profiles, it is assumed that the stress along the measurement direction remains uniform throughout the depth of the specimen. Table 3.1 lists the computed calibration profile parameters.

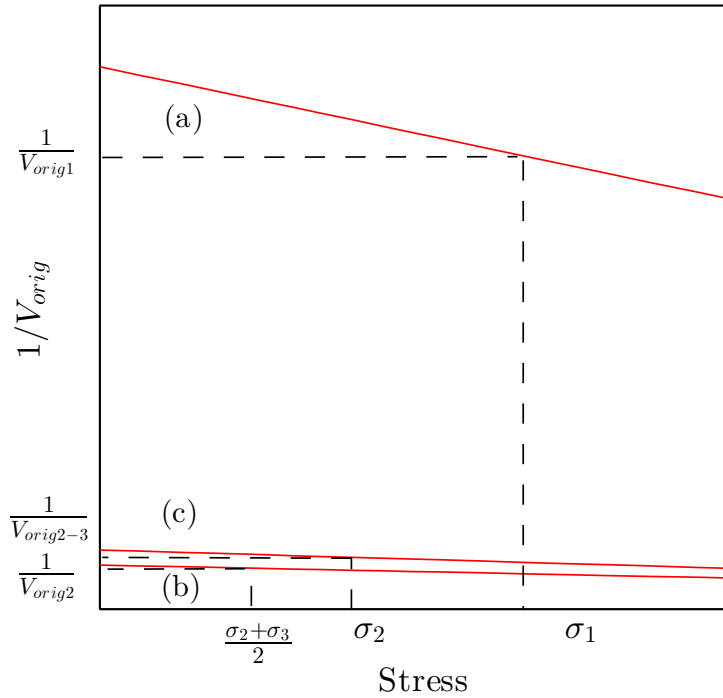


**Figure 3.11:** Conceptual calibration profiles corresponding to specific depths for (a)  $1/V_{orig1}$ , (b)  $1/V_{orig2}$ , and (c)  $1/V_{orig2-3}$ . A specimen of unknown stress state can be assessed by applying (3.26) and (3.27), keeping  $\omega_0$ ,  $\omega_1$  and  $\omega_2$  constant with respect to the calibration stage. The reciprocal value of the measured average Barkhausen emission in the first layer  $1/V_{orig1}$  will then lead to a stress  $\sigma_1$ , via the pre-established linear relationship. In a similar manner, the stress  $\sigma_2$  in the second layer, and the average stress  $\bar{\sigma}_{2-3}$  in the combined second and third layer can be found.

### 3.5.4 Shortcomings of this approach

Evaluating the integrals that represent the emission frequency spectra originating in the first and second layers of material, we obtain

$$\int_0^{x_1} e^{-\zeta x \sqrt{\omega}} dx = \frac{1}{\zeta \sqrt{\omega}} \left( 1 - e^{-\zeta x_1 \sqrt{\omega}} \right) \quad (3.28)$$

and

$$\int_{x_1}^{x_2} e^{-\zeta x \sqrt{\omega}} dx = \frac{1}{\zeta \sqrt{\omega}} \left( e^{-\zeta x_1 \sqrt{\omega}} - e^{-\zeta x_2 \sqrt{\omega}} \right), \quad (3.29)$$

respectively (note that we have assumed  $V_{orig} = 1$  and independent of frequency). An interactive GUI was written in Matlab to plot these, in order to graphically visualize the model assumptions and evaluate them.

- The assumption of a sharp frequency "cutoff" is unrealistic, and implies that the signal emanating from the second layer can be ignored in the first frequency range (where the signal is filtered from  $\omega_0$  to  $\omega_1$ ). By visual inspection of Figure 3.12, one can see that this is a severe approximation, as the measured signal comprises at least 20 percent of the second layer emissions.
- The second assumption, which is an inherent assumption (and not explicitly stated) in this model, is that each spectral component carries stress information, and that we do not need to look at the spectrum in its entirety. But by piecewise considering the spectrum we are omitting information, since the Barkhausen spectra from all depths completely overlap to produce the measured signal at the surface. This assumption is strongly coupled to the first.
- The third assumption is that we can take an inverse Fourier transform to revert back to the time domain signal and measure the peak amplitude. This method is inherently flawed: we are not consistent with our choice of parameters that describe the signal as we switch between time and frequency domains. Essentially, we are assuming that  $V_{peak}$

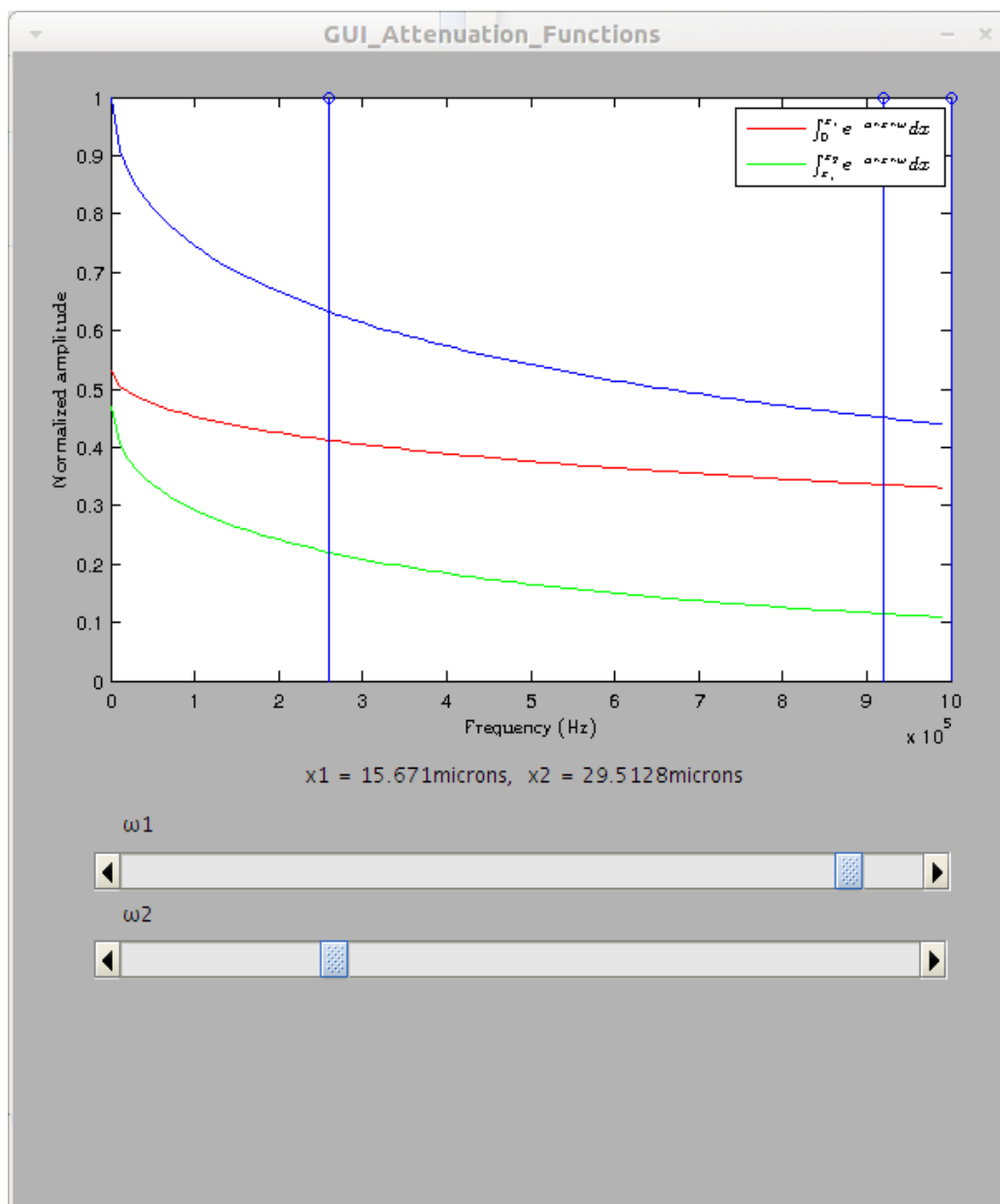


**Figure 3.12:** Graphical representation of the model equations. The red and green curves represent the integrals from 0 to  $x_1$  and  $x_1$  to  $x_2$  respectively. The blue curve is a sum of the aforementioned, and represents what is seen at the surface. The curves are all normalized by the maximum value attained by the blue curve, such that their maximum values always sum to 1.



of a single sinusoid is qualitatively and quantitatively equivalent to  $V_{peak}$  of a wideband signal, which is not true.

### 3.6 Analysis in the frequency domain

Given the shortcomings that were described in the previous section, we found that a re-evaluation of the model was necessary. More specifically, the "sharp cutoff" assumption which lead to the windowed spectrum approach was abandoned, to give way to a methodology where the entire spectrum is considered at once.

This is in some way a transition from a semi-parametric to a parametric approach. In the former, which is a time- and frequency-domain hybrid, a moving average smoothing algorithm was used to obtain a scalar value ( $V_{peak}$ ) from a measured time series, after making some assumptions about the underlying nature of the physical process (white noise assumption, exponential attenuation). In the latter, which is a purely frequency-domain approach, a model with a number of parameters is derived, and that model is fitted to the experimental data, in order to obtain an estimate of those parameters. Both approaches have their merits and disadvantages, so it was considered necessary to address both for the sake of completeness.

For example, a method that employs non-parametric statistics could be trained against known methods to yield the desired result, without knowledge of the underlying physical process. This may restrict the model to a very specific case. On the other hand, a parametric method may provide useful insight into the underlying mechanism, but can omit important features that allow the model to describe special cases. In other words, the former may be limited by its specificity, while the latter may be too general.

The following sections present the derivation of a multi-parameter model for the Barkhausen spectrum, both for the general case, as well as for more specific cases.

#### 3.6.1 General case - One layer formulation

Suppose that the longitudinal (parallel to the surface) component of stress in a ferromagnetic specimen varies linearly with depth. An adequate expression to describe this variation would be the following:

$$\sigma(x) = mx + \sigma_0, \quad (3.30)$$

where  $\sigma(x)$  is the longitudinal component of stress, as a function of depth  $x$ ,  $m$  is the slope of the stress-depth gradient, and  $\sigma_0$  is the stress at the surface, when  $x = 0$ . A visual representation of this can be seen in Fig. 3.13.

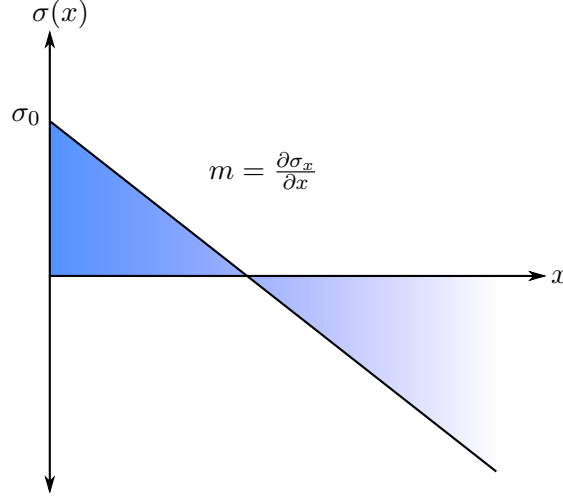


**Figure 3.13:** Plot of a stress-depth gradient, with tensile stress at the top surface, monotonically decreasing to a compressive stress at the lower surface. Here,  $x$  indicates distance from the top surface of the specimen.

From theory and previous experimental results [39, 47], we know that <sup>1</sup>

$$\frac{1}{V_{orig}(0)} - \frac{1}{V_{orig}(\sigma)} = \frac{3b'\sigma}{\mu_0} \quad (3.31)$$

where  $V(\sigma)$  and  $V(0)$  are the Barkhausen voltage amplitude at the origin under stress and no stress respectively,  $b'$  is a modified magnetostrictive constant and  $\mu_0$  is the magnetic permeability of free space.

For small magnitudes of stress, we can approximate (3.31) by its Taylor series expansion around  $\sigma = 0$  (equivalently referred to as Maclaurin series). Solving for  $V(\sigma)$ :

$$V(\sigma) = \frac{1}{\frac{1}{V(0)} - \frac{3b'\sigma}{\mu_0}} \quad (3.32)$$

<sup>1</sup>This formulation follows from (2.19) which was also shown to be valid in [47]. However, here it is assumed that this relationship also holds for  $V_{orig}$ , which is necessary to proceed in the derivation.

Then,

$$V(\sigma) \cong V(0) + \frac{dV(0)}{d\sigma}\sigma + O(h^2), \quad (3.33)$$

and since

$$\frac{dV(\sigma)}{d\sigma} = \frac{3b'}{\mu_0} \left( \frac{1}{V(0)} - \frac{3b'\sigma}{\mu_0} \right)^{-2} \quad (3.34)$$

it follows that

$$\frac{dV(0)}{d\sigma} = \frac{3b'V^2(0)}{\mu_0} \quad (3.35)$$

and we conclude that to a first order approximation, the voltage  $V(\sigma)$  is proportional to stress  $\sigma$ :

$$V(\sigma) = V(0) + \frac{3b'V^2(0)}{\mu_0}\sigma + O(h^2). \quad (3.36)$$

Since  $V(\sigma) \propto \sigma$ , and the stress-depth profile is linear, such that  $\sigma \propto x$ , it follows that  $V(x) \propto x$ . In other words, a change along depth in the longitudinal stress, will also result in a change of the Barkhausen emission amplitude as a function of depth. If the stress gradient is linear (i.e. stress depth profile resulting from four point-bending or approximate stress depth profile resulting from shot peening), the following equation can be used to quantify the change of Barkhausen amplitude at the origin with depth:

$$V(x) = a(mx + \sigma_0) \quad (3.37)$$

Now, the measured Barkhausen spectrum at the surface will depend on the aforementioned stress-depth profile. We can express the measured Barkhausen frequency spectrum  $V_{meas}$  as the following depth integral:

$$V_{meas}(\omega) = \int_0^{x_{max}} V(x)e^{-\zeta x\sqrt{\omega}} dx \quad (3.38)$$

$$= a \int_0^{x_{max}} (mx + \sigma_0)e^{-\zeta x\sqrt{\omega}} dx \quad (3.39)$$

$$= am \int_0^{x_{max}} xe^{-\zeta x\sqrt{\omega}} dx + a\sigma_0 \int_0^{x_{max}} e^{-\zeta x\sqrt{\omega}} dx \quad (3.40)$$

$$= -am \left[ \frac{1}{\zeta^2 \omega} \left( e^{-\zeta x_{max}\sqrt{\omega}} (\zeta x_{max}\sqrt{\omega} + 1) - 1 \right) \right] \quad (3.41)$$

$$- a\sigma_0 \left[ \frac{1}{\zeta\sqrt{\omega}} \left( e^{-\zeta x_{max}\sqrt{\omega}} - 1 \right) \right] \quad (3.42)$$

where  $\zeta$  is the attenuation constant with units  $\sqrt{SH}/m$ , a function of magnetic permeability and electrical conductivity,  $\omega$  is the angular frequency. Parameter  $m$ , being the stress-depth gradient, has units of Pa/m. Parameter  $\sigma_0$ , has units of Pa, and can be thought of as the surface stress. Now, since the units of  $V_{meas}(\omega)$  are  $V/Hz$  (resulting from Fourier transforming a time domain voltage waveform), the scaling coefficient must carry the units of  $V \cdot Pa^{-1} \cdot Hz^{-1} \cdot m^{-1}$ . The parameter  $a$  can thus be thought of as a magnetomechanical scaling coefficient, relating a stress gradient to Barkhausen voltage in the frequency domain.

The parameter  $am$  is equivalent to  $V_{orig}$  in case of bending (which can be noted as  $V_{orig}|_{\frac{d\sigma}{dx} \neq 0}$ ), and the parameter  $a\sigma_0$  is equivalent to  $V_{orig}$  in case of uniaxial tensile stress (noted as  $V_{orig}|_{\frac{d\sigma}{dx} = 0}$ ). For brevity, these two can be substituted by  $V_{orig,b}$  and  $V_{orig,t}$ . The effect of  $m$  on the spectrum can be seen in Fig. 3.14.

### 3.6.2 Case of constant stress along depth

When uniaxial tensile stress is applied to a specimen, such that the stress along depth is invariant, the slope parameter  $m$  will be zero, reducing (3.42) to:

$$V_{meas}(\omega) = V_{orig,t} \left[ \frac{1}{\zeta\sqrt{\omega}} \left( 1 - e^{-\zeta x\sqrt{\omega}} \right) \right] \quad (3.43)$$

It can be shown, that in the limit of  $\omega \rightarrow 0$ , the equation of 3.42 converges to  $V_{orig}x$ , showing that the signal is a linear combination of signals coming from all depths:

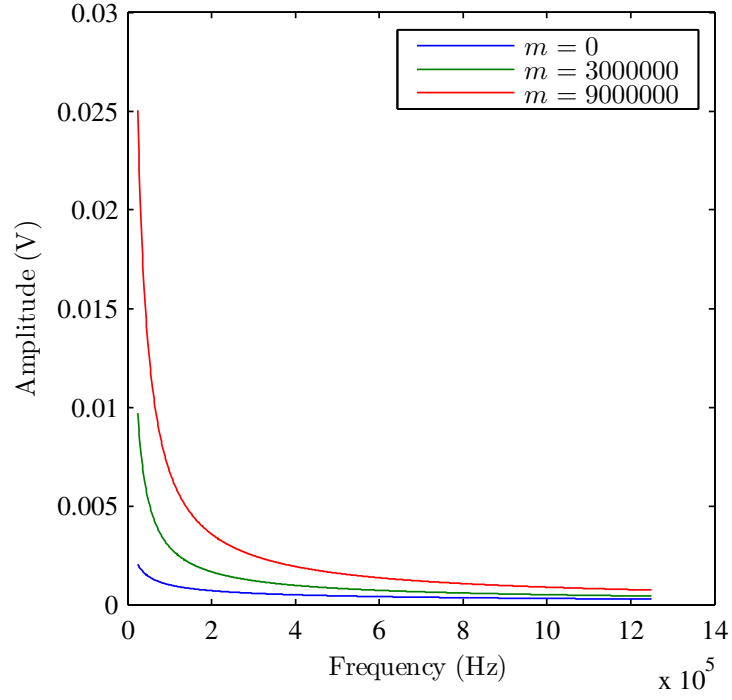


**Figure 3.14:** Effect of slope parameter  $m$  on the Barkhausen spectrum.

$$\lim_{\omega \rightarrow 0} V_{meas} = V_{orig,t} \lim_{\omega \rightarrow 0} \left( \frac{1 - e^{-\zeta\sqrt{\omega}x}}{\zeta\sqrt{\omega}} \right) \quad (3.44)$$

$$= V_{orig,t} \lim_{\omega \rightarrow 0} \left( \frac{\frac{d}{d\omega}(1 - e^{-\zeta\sqrt{\omega}x})}{\frac{d}{d\omega}(\zeta\sqrt{\omega})} \right) \quad (3.45)$$

$$= V_{orig,t} x \quad (3.46)$$

### 3.6.3 Two-layer case

#### 3.6.3.1 Coupled $V$ and $\zeta$

Since multiple emissions occur in a layer, by taking the integral over a certain depth range, the combined spectra of all emissions within that range are considered. That gives  $V_{att1}(\omega)$  as the component of the signal detected at the surface [48, 49]:

$$\begin{aligned} V_{att1}(\omega) &= V_{orig1} \int_{x_0}^{x_1} e^{-\zeta_1 x \sqrt{\omega}} dx \\ &= -\frac{V_{orig1}}{\zeta_1 \sqrt{\omega}} \left( e^{-\zeta_1 x_1 \sqrt{\omega}} - e^{-\zeta_1 x_0 \sqrt{\omega}} \right) \end{aligned} \quad (3.47)$$

Similarly, for emissions originating in the second layer:

$$\begin{aligned} V_{att2}(\omega) &= V_{orig2} \int_{x_1}^{x_2} e^{-\sqrt{\omega}(\zeta_2(x-\Delta x) + \zeta_1 \Delta x)} dx \\ &= -\frac{V_{orig2}}{\zeta_2 \sqrt{\omega}} \left( e^{-\sqrt{\omega}(\zeta_2 x_2 - (\zeta_2 - \zeta_1) \Delta x)} \right. \\ &\quad \left. - e^{-\sqrt{\omega}(\zeta_2 x_1 - (\zeta_2 - \zeta_1) \Delta x)} \right) \end{aligned} \quad (3.48)$$

It should be noted that in this treatment, two different values of attenuation coefficient  $\zeta$  have been assumed, one for each layer, which also implies that emissions attenuate at a different rates in each layer; this has been taken into account in the above equations. Uncorrelated white noise has a uniformly distributed phase between  $-\pi$  and  $\pi$ ; we can therefore use the assumption that at the origin the phase is zero (mean value) such that, since the phase velocity is assumed to be independent of frequency, the resulting phase at the surface is also zero, leading to only constructive interference when all attenuated spectra are summed. By summing the emissions in separate layers, we are also implicitly assuming that they are statistically independent. This summation yields the measured spectrum at the surface  $V_{meas}(\omega)$ , such that:

$$V_{meas}(\omega) = \sum_i V_{att_i}(\omega), \quad (3.49)$$

where  $V_{att_i}$  is the Barkhausen signal from the  $i$ th layer. One can retrieve the stress state of the material, by fitting the above expression to Barkhausen spectra measured at the surface of a specimen, and extracting the value of stress-related parameters  $\zeta$  and  $V_{orig}$ . With this

approach, for  $n$  total layers, one obtains  $2n$  parameters. It is possible to reduce the number of fitting parameters by incorporating a Barkhausen-stress calibration relationship [39, 47] into our model for the spectrum.

It was shown previously [42] that the reciprocal of the peak differential susceptibility  $1/\chi'$  varies linearly with stress, as shown by (3.9). Also, in previous work [39], the voltage peak envelope amplitude,  $V_{MBN,peak}$ , was observed to follow a similar trend as  $\chi'_{max}$  with stress, and thus (3.9) was modified to give (3.10). Unlike  $b$ , which can be determined via a quasi-static magnetostriction measurement,  $b'$ , the modified coefficient depends on the frequency of magnetization, strength of magnetizing field and sensitivity of the Barkhausen probe, and is thus not easily determinable.

By dividing (2.18) by (2.19), we yield

$$\frac{\frac{1}{\chi'(0)} - \frac{1}{\chi'(\sigma)}}{\frac{1}{V_{orig}(0)} - \frac{1}{V_{orig}(\sigma)}} = \frac{b}{b'} \quad (3.50)$$

Solving for  $V_{orig}(0)$  yields

$$V_{orig}(\sigma) = -\frac{b}{b'} \frac{1}{\frac{1}{\chi'(0)} - \frac{1}{\chi'(\sigma)} - \frac{b}{b'} \frac{1}{V_{orig}(0)}}, \quad (3.51)$$

where  $b$ ,  $\chi'(0)$  and  $V_{orig}(0)$  can be experimentally determined. The susceptibility at some value of unknown stress  $\chi'(\sigma)$  is related to  $\mu_r$  and  $\zeta$  such that

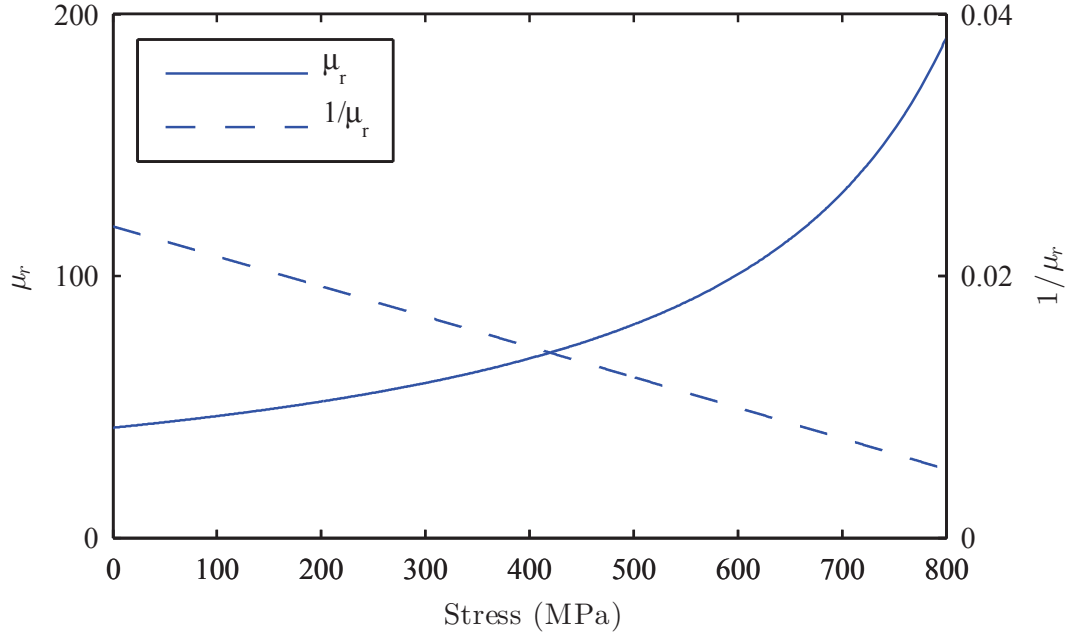
$$\chi'(\sigma) \cong \mu'_r(\sigma) = 2\rho\zeta^2(\sigma)/\mu_0 \quad (3.52)$$

By substituting (3.51) into (3.47) and (3.48) (and consequently (3.49)), we are reducing the number of fitting parameters from  $2n$  to  $n + 1$ .

To establish a relationship between stress and relative permeability, an extension to the theory of ferromagnetic hysteresis [42] was used:

$$\mu_r \cong \chi = \frac{M_s}{3a - \left( \alpha + \frac{3b(\sigma + \sigma_{offset})}{\mu_0} \right) M_s}, \quad (3.53)$$

where  $a$  is a parameter which characterizes the shape of the anhysteretic magnetization,  $\alpha$  is a mean field term that quantifies interdomain coupling,  $\sigma$  is the stress present in the sample and

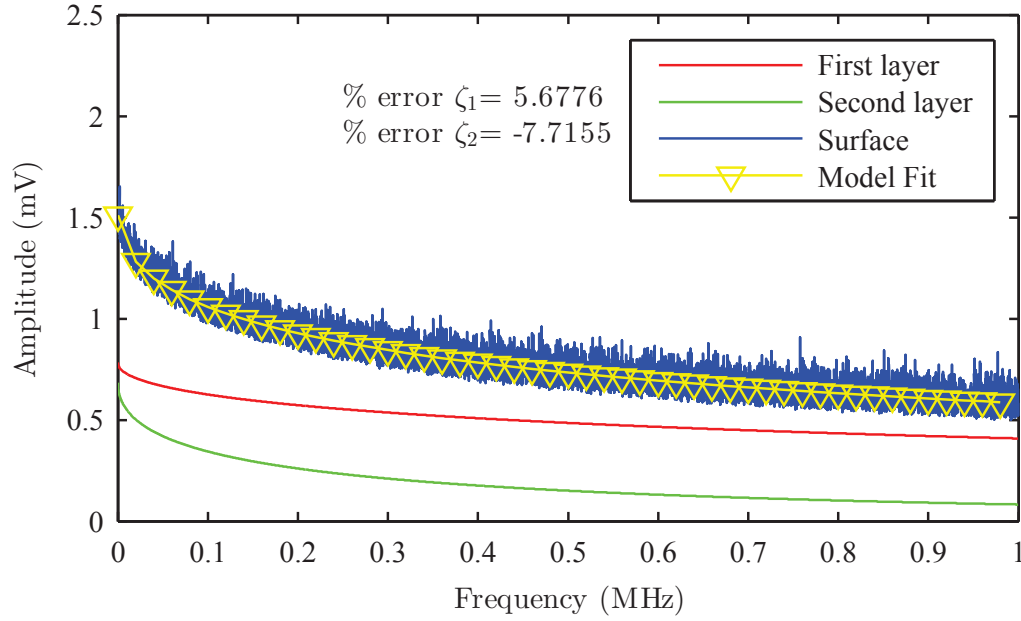
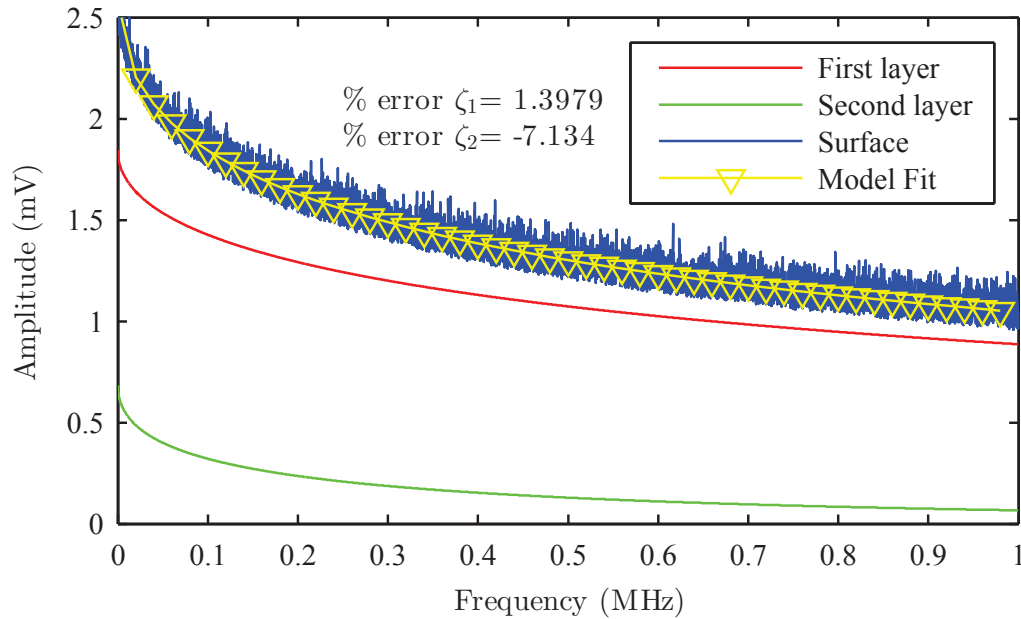


**Figure 3.15:** Calibration relationship, relating relative permeability and its reciprocal to stress. We set  $a = 2019.620 \text{ Am}^{-1}$ ,  $M_s = 2.485 \times 10^5 \text{ Am}^{-1}$ , and  $\alpha = 1.9119 \times 10^{-2}$ , which are typical values for a soft steel. The values of  $b$  and  $\sigma_{offset}$  were set to  $1 \times 10^{-17} \text{ m}^2\text{A}^{-2}$  and  $-800 \text{ MPa}$  respectively.

$M_s$  is the saturation magnetization. Plots of  $\mu_r$  and its reciprocal versus stress can be seen in Fig. 3.15.

To simulate non-uniform strain, each layer was assigned a different value of stress, by modulating the value of the differential permeability and thus the parameter  $\zeta$ , which was defined in the Theory section. Different values of stress lead to different y-axis intercepts and spectrum shapes, as shown in Fig. 3.16. To simulate a practical measurement and thus make the treatment more realistic, random Gaussian noise was added to the simulated spectra. A least squares algorithm was used to obtain the estimates  $\hat{\zeta}_1$  and  $\hat{\zeta}_2$ , from which the stress can be calculated, using the linear relationship shown in Fig. 3.15.



(a)  $\sigma_1 = 200\text{MPa}$ ,  $\sigma_2 = 150\text{MPa}$ (b)  $\sigma_1 = 400\text{MPa}$ ,  $\sigma_2 = 150\text{MPa}$ 

**Figure 3.16:** Least-squares fit to simulated Barkhausen spectra, of the model of (3.49) combined with the relationship in (3.51), for different stress magnitudes in the first and second layer. The value of  $b'$ , which quantifies the sensitivity of the sensing element, was set to  $1 \times 10^{-22} \text{ m}^2 \text{ V}^{-2} \text{ A}^{-2}$ . The parameters  $\chi'(0) \cong \mu_r'(0)$ ,  $\rho$  and  $V_{orig}(0)$  were set to 42,  $0.22 \mu\Omega\text{m}$  and 10 V, respectively. The layer thickness  $\Delta x$  was set to  $50 \mu\text{m}$ . Gaussian noise was added to the spectra, to make the modelling more realistic.

## CHAPTER 4. MEASUREMENTS AND INSTRUMENTATION

### 4.1 Experimental procedures

This section describes the experimental procedures that were used to validate the theory presented in Chapter 3. Measurements were repeated several times to ensure that experimental conditions were as consistent as possible.

#### 4.1.1 Inducing uniaxial tensile stress

##### 4.1.1.1 Experimental procedure

The first step in detecting stress variations along depth is to calibrate against a known stress-depth profile. The simplest type of stress-depth profile is one where stress is constant along depth. This can be obtained by subjecting a specimen to uniaxial stress. This specimen must be manufactured according to the ASTM standard for tensile testing [50], which is designed such that upon tension stress is concentrated in the central region of the specimen (gauge section) where ultimately the fracture occurs.

During the tensile test, the control parameter is force, which is applied using a pneumatic system, and the state variable is extension, which is measured using an extensometer. Strain is then measured using the following formula [51]:

$$\varepsilon = \frac{\Delta L}{L_0} = \frac{L - L_0}{L_0} \quad (4.1)$$

where  $L_0$  is the original length of the specimen,  $L$  is the final length, and  $\Delta L$  is the extension.

For this experiment, stress is referred to as  $\sigma$ , without a subscript denoting direction, as it is implied that stress is measured along the direction of strain. However, the distinction between

two types of stress must be made: true and engineering stress. True stress can be calculated by the following formula:

$$\sigma_{true} = \frac{F}{A(\varepsilon)} \quad (4.2)$$

where  $F$  is the force applied along the direction of strain and  $A(\varepsilon)$  is the cross-sectional area of the specimen as a function of strain. As volume of the specimen must be conserved, elongation of the specimen results in the reduction of cross-sectional area. This is commonly referred to as the *Poisson* effect, with Poisson's ratio  $\nu$  being a measure of this effect. Engineering stress is given by [51]

$$\sigma_{eng} = \frac{F}{A} \quad (4.3)$$

where  $A$  is the cross sectional area of the unstressed specimen and is taken to be a constant throughout the experiment. For the purposes of this experiment, engineering stress was deemed to be an adequate measure.

It is assumed here that the material is linear, elastic and isotropic. The stress that is applied is uniaxial (or plane), which leads to the following elastic relationship [51]:

$$\epsilon_x = \frac{\sigma_x}{E} \quad (4.4)$$

where  $E$  is the Young's modulus (or elastic modulus),  $\epsilon_x$  and  $\sigma_x$  are the strain and stress along  $x$ -axis, respectively.

#### 4.1.1.2 Design and manufacture of ASTM specimen

In order to manufacture an ASTM E8 standard "dogbone" specimen for tensile testing, a bar of hot rolled ASTM A36 steel was machined along the rolling direction. The specimen has a thickness of 6.5 mm, width of 12.7 mm and gauge length of 26.5 mm. A three-dimensional model with the placement of the sensor can be seen in Fig. 4.1.

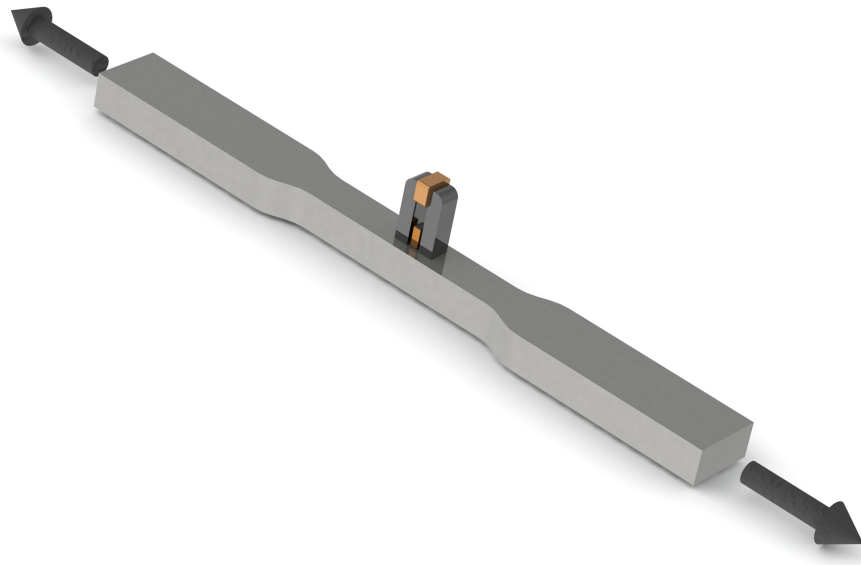


**Figure 4.1:** Three dimensional visualization of the specimen for tensile testing, manufactured according to the ASTM E8 standard. Sensor indicates where Barkhausen emissions were measured.

#### 4.1.1.3 Experimental procedure

The specimen was subjected to uniaxial tension at a deformation rate of 3 mm/min, using an Instron 5969 tensile test machine. The specimen was magnetized with a Barkhausen probe consisting of a magnetizing coil wound around a ferritic C-core electromagnet with cross-sectional area of 25.6 mm<sup>2</sup> (8 mm × 3.2 mm), and a sensing coil wound around a ferritic cuboid with cross-sectional area of 3.6 mm<sup>2</sup> (3 mm × 1.2 mm) positioned between the electromagnet poles, and picking up the perpendicular component of the flux density from the specimen. The measurement was paused every ~ 1000 N of load, in order to collect Barkhausen data along the direction of stress, with the probe positioned as pictured in Figure 4.2. The Barkhausen

**Table 4.1:** Magnetization conditions for tensile test

Magnetizing Voltage	1 V
Magnetizing Frequency	100 Hz
Sampling Frequency	2.5 MHz
Bursts	10
Filter Low	95 kHz
Filter High	1.25 MHz
Smoothing	10

equipment settings can be seen in Table 4.1. The maximum applied magnetic field was 0.5 kA/m, measured between the poles of the electromagnet. A total of five equally spaced measurements were carried out for each value of stress, with every trial containing 10 Barkhausen bursts. Because the specimen underwent small amount of relaxation every time the tensile test was paused, the ensemble average of the waveforms obtained over that relaxation period was taken and these were plotted against the stress. The specimen was brought to fracture.



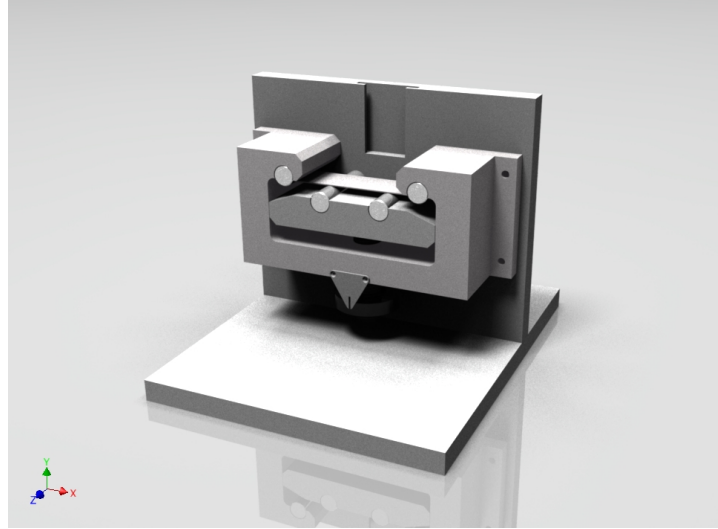
**Figure 4.2:** Experimental setup, showing the grip of the tensile test machine, the A36 test specimen, and the Barkhausen probe kept in a stable position by the clamp.

### 4.1.2 Inducing a linear stress-depth gradient

In order to induce a variation of stress with depth, a specimen can be subjected to four-point bending. Four-point bending is used to apply bending moment on a specimen and establish a linear stress-depth profile, ranging from tensile stress at the top surface to compressive stress at the bottom surface, such as the one depicted in Fig. 3.13.

#### 4.1.2.1 Design and manufacture of four-point bending device

For the purposes of this experiment, a four-point bending apparatus was designed and manufactured. The apparatus was designed in the software packages DS SolidWorks and Autodesk Inventor. A three-dimensional model and the manufactured part can be seen in Fig. 4.3. The main body is composed of high strength aluminium (3070), and the cylindrical fixtures are ceramic. The platform holding the lower two fixtures is displaced by means of a bolt, which if rotated for a full 360 degrees produces a 1/8" deflection upwards. This can be measured indirectly by reading the rotation in degrees on the dial and then converting to vertical deflection, or directly by means of the digital extensometer. The Barkhausen sensor can be stabilized by means of a mount with one degree of freedom, which can move along the direction of deflection.



(a)



(b)

**Figure 4.3:** Four-point bender. (a) 3D CAD design, (b) Photograph of manufactured part.

#### 4.1.2.2 Solid mechanics simulation of four-point bending

In order to obtain the stress-depth profile, a simulation in COMSOL Multiphysics was carried out. The geometry was imported from the CAD model of the four-point bender. Two materials were used in the model, namely ASTM A36 steel (for the specimen) and alumina (for the ceramic fixtures). A custom mesh was created, to accommodate the need for a fine mesh in the volumetric region of the specimen where the stress-depth gradient is established. The COMSOL solid mechanics module was used to perform the simulation. Given all the initial and boundary conditions, the solver computes the gradient of the displacement  $\mathbf{u} = [u \ v \ w]^T$ , denoted as [52]:

$$\nabla \mathbf{u} = \begin{bmatrix} \frac{\partial u}{\partial X} & \frac{\partial u}{\partial Y} & \frac{\partial u}{\partial Z} \\ \frac{\partial v}{\partial X} & \frac{\partial v}{\partial Y} & \frac{\partial v}{\partial Z} \\ \frac{\partial w}{\partial X} & \frac{\partial w}{\partial Y} & \frac{\partial w}{\partial Z} \end{bmatrix} \quad (4.5)$$

where  $X, Y, Z$  are the material coordinates. From the above, the Lagrangian strain tensor  $\epsilon$  is calculated, via

$$\epsilon \approx \frac{1}{2} (\nabla \mathbf{u} + \nabla \mathbf{u}^T). \quad (4.6)$$

The above is an approximation of the Lagrangian strain tensor, as the second-order terms can be neglected, as a consequence of assuming infinitesimal deformation of a continuum body. The linear strain tensor (also termed Cauchy strain tensor) is expressed as

$$\epsilon = \begin{bmatrix} \epsilon_x & \epsilon_{xy} & \epsilon_{xz} \\ \epsilon_{yx} & \epsilon_y & \epsilon_{yz} \\ \epsilon_{zx} & \epsilon_{zy} & \epsilon_z \end{bmatrix}. \quad (4.7)$$

Strains with single subscripts denote principal strains, and double subscripts denote shear strains, also commonly written as  $\gamma_{ij}$ . When there is symmetry, arising from isotropy in material properties,  $\gamma_{ij} = \gamma_{jj}$ . The specimen and fixtures were specified as linear isotropic elastic materials, and the latter were also given the property of *nearly incompressible material*, as the



hardness of the ceramic material far surpasses that of steel. In a linear isotropic elastic material, the constitutive equations which relate stresses to strains, otherwise referred to as generalized Hooke's law, are the following [51]:

$$\sigma_x = \frac{E}{(1 + \nu)(1 - 2\nu)} [(1 - \nu)\epsilon_x + \nu(\epsilon_y + \epsilon_z) - (1 + \nu)(\alpha\Delta T)] \quad (4.8)$$

$$\sigma_y = \frac{E}{(1 + \nu)(1 - 2\nu)} [(1 - \nu)\epsilon_y + \nu(\epsilon_z + \epsilon_x) - (1 + \nu)(\alpha\Delta T)] \quad (4.9)$$

$$\sigma_z = \frac{E}{(1 + \nu)(1 - 2\nu)} [(1 - \nu)\epsilon_z + \nu(\epsilon_x + \epsilon_y) - (1 + \nu)(\alpha\Delta T)] \quad (4.10)$$

$$(4.11)$$

and

$$\sigma_{xy} = G\epsilon_{xy} \quad (4.12)$$

$$\sigma_{yz} = G\epsilon_{yz} \quad (4.13)$$

$$\sigma_{zx} = G\epsilon_{zx} \quad (4.14)$$

where  $E$  is Young's modulus (or modulus of elasticity) which is a scalar (due to the isotropy condition),  $\nu$  is Poisson's ratio (scalar), and  $\epsilon_i$  and  $\sigma_i$  are the principal strain and stress components respectively.  $G$  represents the shear modulus of elasticity,  $\epsilon_{ij}$  represent shear strains, and  $\sigma_{ij}$  are the shear stresses, commonly denoted as  $\tau_{ij}$  since they reflect torques. Note that these equations are the more general form of (4.4) for uniaxial (or plane) stress-strain relationship, which only defines this relationship normal to the plane on which the stress is applied. The Cauchy stress tensor is expressed as:

$$\sigma = \begin{bmatrix} \sigma_x & \sigma_{xy} & \sigma_{xz} \\ \sigma_{yx} & \sigma_y & \sigma_{yz} \\ \sigma_{zx} & \sigma_{zy} & \sigma_z \end{bmatrix} \quad (4.15)$$

This is a symmetric tensor, as angular momentum is balanced, meaning that  $\sigma_{ij} = \sigma_{ji}$ . This has the physical consequence of the objects remaining at rest.

The bottom two fixtures and the specimen were assigned a *free* condition (which implies that no constraints or loads acting on the boundaries), and given a prescribed displacement upwards, which assigns the displacement vector  $v$  a finite value for each run. The upper two fixtures were given a *fixed* constraint, which constrains the displacement vectors  $u$ ,  $v$ , and  $w$  to be zero in all directions. The simulation was parametrically swept, such that the solver runs multiple times, each time for a different amount of prescribed displacement. A stationary, direct solver was used to solve the problem. A similar simulation was set up for a specimen of smaller thickness. The meshes for both specimens and a preview of the simulation results, visualizing the principal stress component in the  $x$  direction can be seen in Figs. 4.4a and 4.4b (complete set of results are presented in Chapter 6).

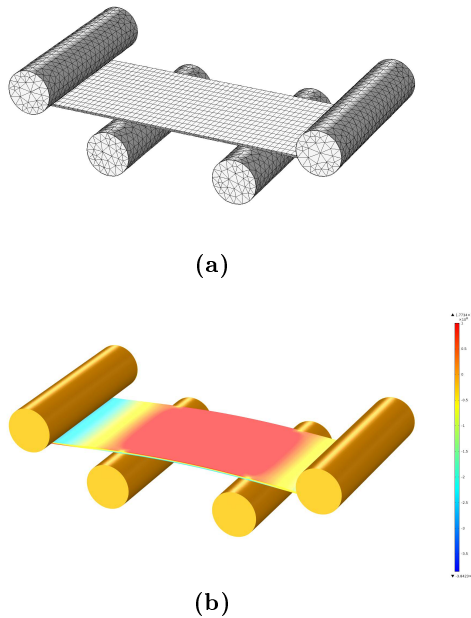


**Figure 4.4:** Mesh and simulated geometry for the four-point bending experiment for the 1 mm thick specimen.

#### 4.1.2.3 Experimental procedure

In order to relieve any residual stresses which may have been present due to rolling, the block of A36 steel was first heat treated at 922 K for 2 hours and then slow cooled over 8 hours. The individual specimens were then extracted from the main block via electric discharge machining (EDM).

Each specimen was positioned on the platform of the four-point bender and the platform was displaced to secure the specimen in a stable position. A total of three measurement trials were carried out for each value of deflection, with every trial containing 10 Barkhausen bursts. The measurement settings are listed in Table 4.2. In total, the specimen was deflected 18 times, each time by 10 degrees of rotation, or equivalently  $\sim 0.088$  mm of vertical displacement. The specimen was taken beyond the yield limit, but not stressed enough for it to fracture. The specimen was not deflected further, as there were concerns of the surface curvature adversely affecting the specimen-sensor coupling.

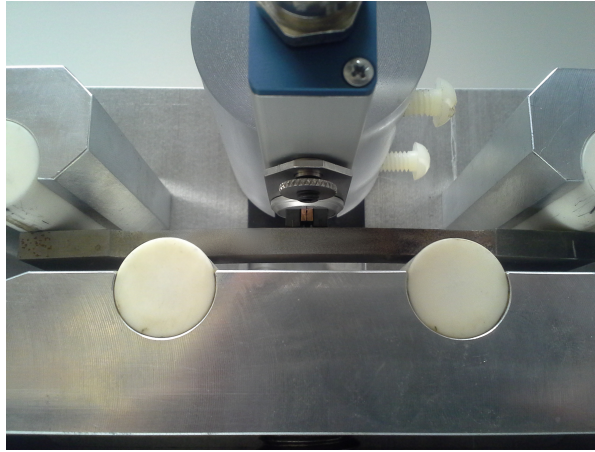


**Figure 4.5:** Experimental setup, showing the fixtures of the four-point bender, the A36 test specimen, and the Barkhausen probe kept in a stable position by the customized clamp.

**Table 4.2:** Magnetization conditions for bending test

Magnetizing Voltage	1,3,5,7 V
Magnetizing Frequency	20,60,100,140,180,220 Hz
Sampling Frequency	2.5 MHz
Bursts	10
Filter Low	95 kHz
Filter High	1.25 MHz
Smoothing	10

## CHAPTER 5. SIGNAL PROCESSING AND SOFTWARE DEVELOPMENT

### 5.1 Signal processing tools

Custom tools were written to facilitate the analysis and visualization of measured Barkhausen signals. The software was written using MATLAB®(2012a, The MathWorks, Natick, MA, USA). The backbone of the software resides in the class *BarkhausenSignal.m*, which bundles up two main features needed to effectively process a measured signal: 1) properties that describe the signal, and 2) functions that operate on the signal. This programming paradigm is commonly referred to as *object-oriented* programming, where a *class* (containing properties and functions) can be instantiated in the form of an *object*. This lends to the user a capability of instantiating many distinct objects belonging to the same class and storing them in memory and/or on disk. Objects of type *BarkhausenSignal* are designed to store a Barkhausen waveform and various time- and frequency-domain statistics, as well as the functions needed to derive these statistics from the waveform.

What follows is meant to provide an overview of the significant properties and functions employed in the designed classes, while omitting redundant ones. Describing the intricate details of designing a class is beyond the scope of the present thesis.

#### 5.1.1 Mathematical definitions

Before advancing to a description of the mathematical operations performed by the software, it is necessary to provide a definition of the Barkhausen signal in terms of its statistical properties.

The long-range structure of a magnetic material gives rise to its bulk behaviour (M-H loop),

which can be defined as deterministic. The short-range structure is responsible for random fluctuations in measurements, which is reflected in Barkhausen signals. While their time series contain a deterministic component, they are predominantly stochastic, as they largely depend on fine microstructural variations.

Inspection of the long-range features of a Barkhausen signal, such as the envelope shape, can provide information relating to the macroscopic stress state within the material <sup>1</sup>. On the other hand, measures like the pulse height distribution, are more representative of microscopic features like grain size.

When driving the material with an alternating field (of sinusoidal or triangular shape) at a high rate of magnetization, a periodicity can be seen in the measured Barkhausen signal. It will be seen in the next subsections that it can be classified as a cyclostationary process.

#### 5.1.1.1 Stationarity

A stationary process is formally defined as [53]

$$f_{x(t_1)}(\alpha) = f_{x(t_2)}(\alpha) \quad (5.1)$$

and a process that exhibits stationarity in the wide-sense is defined as [53]

$$E[x(t_1)] = E[x(t_2)] \quad (5.2)$$

and

$$\text{Cov}[x(t_1), x(t_2)] = \text{Cov}[x(t_1), x(t_1 + \tau)] \quad (5.3)$$

where  $\tau$  is the time difference between successive values in the time series. In simple terms, (5.2) states that given multiple observations of the stochastic function  $x(t)$ , the amplitude at time  $t_1$  is on average equal to the amplitude at time  $t_2$ . An example of that would be the steady sound created by a stream of water given constant conditions (the mean and covariance do not change with time).

<sup>1</sup>This occurs because the Barkhausen envelope is highly correlated with the differential magnetic susceptibility, whose shape depends on the stress state of the material.

### 5.1.1.2 Cyclostationarity

In the case of Barkhausen noise, however, there is periodicity - one can clearly see periodic peaks and troughs in the signal; we can express this periodicity as  $N$  interleaved stationary processes, where  $N$  is the number of data points in the time series. From this it follows that in a cyclostationary process, the probability distribution (or in this case, voltage amplitude distribution) of the points in the time series varies periodically with time. In other words, the mean and covariance vary periodically with time.

A process  $x(t)$  is wide-sense first order cyclostationary, if [53]

$$E[x(t)] = E[x(t + lP)] \quad (5.4)$$

where  $l$  is an integer and  $P$  is the period. Consider a white noise process (which is stationary in the wide sense) with normally distributed amplitude of mean zero and variance  $\sigma^2$  distributed as  $\sim \mathcal{N}(0, \sigma^2)$ . A deterministic term which represents the differential susceptibility as a function of time  $\chi'(t)$  (under the action of an applied field) is multiplied with  $V(t)$ , thereby lending it periodicity:

$$V_{BN} = \chi'(t)V(t) = \frac{dM}{dH} V(t) = \frac{dM}{dt} \frac{dt}{dH} V(t) \quad (5.5)$$

In other words,  $\chi'$  modulates the white noise term  $V(t)$ . This is the simplest model of a Barkhausen signal in the time domain. For the purposes of mathematical tractability, we are ignoring any attenuation effects which the signal undergoes while propagating through the material (see Chapter 3 for such treatment). The term  $dM/dt$  contains the deterministic, bulk variation of magnetization with time,  $dH/dt$  is the rate of change of applied field with time and lends periodicity to  $V_{BN}$ , and  $V(t)$  is the stochastic term. Overall, modulated signals such as the one described in (5.5) are cyclostationary processes.

### 5.1.1.3 Autocorrelation

The autocorrelation function is defined as [53]

$$R_{ff}(\tau) = \lim_{T \rightarrow \infty} \frac{1}{T} \int_0^T f(t + \tau) f^*(t) dt \quad (5.6)$$

If a signal is second order cyclostationary it has a periodic autocorrelation function. Periodicity in the autocorrelation function is formally expressed as [53]

$$R_{ff}(t, \tau) = R_{ff}(t + T, \tau) \quad (5.7)$$

where  $T$  is the period over which the function repeats itself. In strict terms, the Fourier transform of a wide sense stationary stochastic signal does not exist, since such a signal has infinite energy. However, the autocorrelation function asymptotically approaches zero (which makes it an energy signal), and its Fourier transform exists. The Fourier transform of the autocorrelation function is called the power spectral density function,  $S(f)$  [53]:

$$S(f) = \sum_{k=-\infty}^{\infty} R(k) e^{-j\omega k T} \quad (5.8)$$

Although in strict mathematical terms the Fourier transform of a cyclostationary signal does not exist, the assumptions that were used to derive the physical model of Barkhausen emissions (outlined in Chapter 3) naturally lead to an expression for the frequency spectrum of Barkhausen noise at the surface, and not the power spectral density. It must be mentioned here that the above definitions were included for completeness, to demonstrate awareness of the mathematically rigorous way of handling the signal processing aspect of the problem and to highlight possible future routes for improving the signal processing methods presented in this chapter. The power spectral density was calculated for some datasets, and compared with the Fourier voltage spectrum in order to reassure that the main features (i.e. spectral shape) are present in both cases. The comparison was qualitative in some aspects, as the two methods yield different units ( $\text{W}\cdot\text{Hz}^{-1}$  vs.  $\text{V}\cdot\text{Hz}^{-1}$ ). The Fourier method was deemed to be more appropriate for the following reasons, in descending order of importance:

- The power spectral density was calculated in MATLAB via the Welch method, and then converted into an amplitude spectrum. The result was reasonably close to that obtained from the FFT method (Fig. 5.1).



- The assumptions that were used to derive the physical model of Barkhausen emissions (outlined in Chapter 3) naturally lead to an expression for the frequency spectrum of Barkhausen noise at the surface, and not the power spectral density, which is not as mathematically tractable.
- The probability of error increases with the number of calculations. Obtaining the Fourier spectrum directly from a time series is therefore computationally less risky.
- The number of data points in each time series was in the millions, which reduces the uncertainty in calculating the Fourier spectrum.
- The region of interest in the spectrum is at the low frequency end, where uncertainty is less than that at the high end.

## 5.1.2 Mathematical operations

### 5.1.2.1 Envelope calculation

In order to calculate the envelope of a Barkhausen waveform, a smoothing algorithm is used, which calculates the moving (or running) average of the Barkhausen time series. This operation can be described by the following formula:

$$V_i = \frac{\sum_{j=i-k}^{i-1} V_j + V_i + \sum_{j=i+k}^{i+1} V_j}{k+1} \quad (5.9)$$

for  $k = 2n - 1$ , where  $n$  is a non-zero, positive integer. Parameter  $k = 1$  designates the order of the moving average operation.

Since the Barkhausen signal is centered and somewhat symmetric around zero<sup>1</sup>, the moving average of the time series would fluctuate around zero, as positive and negative amplitude would eliminate each other. To calculate the envelope, the negative values are negated, thus eliminating the negative part of the signal. A moving average calculation is performed on the

<sup>1</sup>The mean of the time series approaches zero as the DC component of the  $dB/dt$  waveform is removed by high-pass filtering, to obtain the Barkhausen signal.

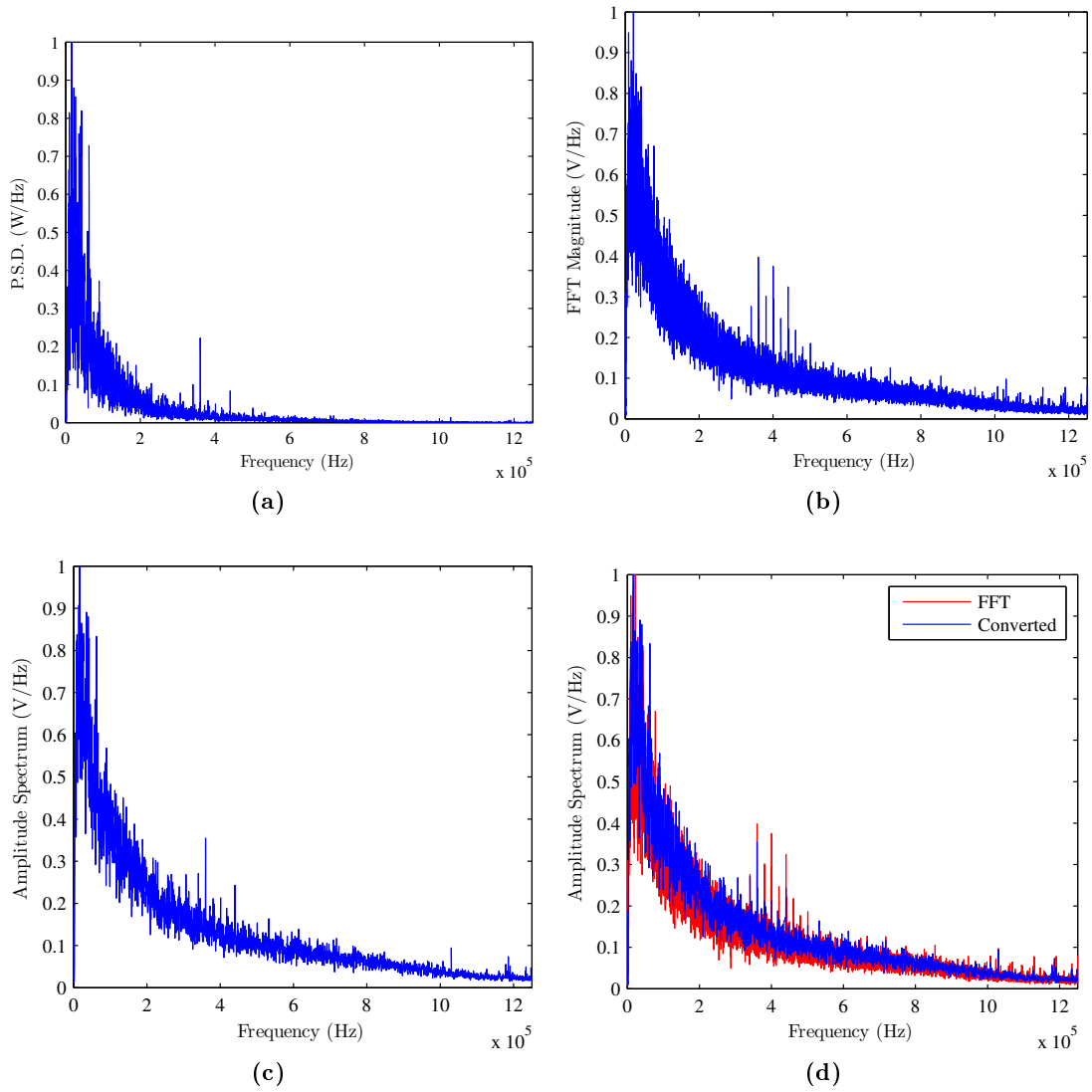


**Figure 5.1:** Comparison of power spectral density and Fourier magnitude calculations (normalized).

resultant time series. This is then multiplied by a heuristically determined scaling factor, which levels the envelope. This scaling factor has remained constant throughout all analyses.

### 5.1.2.2 Peak calculation

The peak calculation algorithm that was written takes advantage of the fact that for any smooth, univariate function, when the first derivative is zero it means that a stationary point has occurred. This can be either a maximum, a minimum or a point of inflection. However, since the envelope only exists for positive values,  $dV/dt = 0$  will mean that at that point, a peak occurs. It is then straightforward to calculate the peak position by querying the array index of the peak value.

### 5.1.2.3 Root mean square calculation

The continuous-time representation of the root mean square (RMS) voltage of a signal is defined as [53]:

$$V_{RMS} = \sqrt{\frac{1}{b-a} \int_a^b [f(t)]^2 dt} \quad (5.10)$$

where  $a \leq t \leq b$  and  $f(t)$  is a smooth and continuous function of  $t$  in the interval  $[a, b]$ . When dealing with digitized measurements, the discrete-time version of the same expression is employed:

$$V_{RMS} = \sqrt{\frac{1}{N} \sum_{i=1}^N V_i^2} \quad (5.11)$$

where  $V_i$  are the discrete measurement samples and  $N$  is the number of samples. This equation is analogous to the expression for the standard deviation of a time series (or population) when the mean of the data set is zero, such that [53]

$$\sigma = \sqrt{\frac{1}{N} \sum_{i=1}^N (X_i - \mu)^2} \quad (5.12)$$

$$= \sqrt{\frac{1}{N} \sum_{i=1}^N X_i^2} \quad (5.13)$$

In the case of Barkhausen time series, the condition of  $\mu = 0$  is true, and the standard deviation of the dataset can be computed instead.

#### 5.1.2.4 Power calculation

The energy of a real, continuous-time signal can be calculated using the following formula [53]:

$$E = \int_{-\infty}^{\infty} V^2(t) dt \quad (5.14)$$

and the power

$$P = \lim_{T \rightarrow \infty} \frac{1}{T} \int_{-T/2}^{T/2} V^2(t) dt \quad (5.15)$$

Their discrete time representations will be [53]

$$E = \sum_{i=-\infty}^{\infty} V_i^2 \quad (5.16)$$

and

$$P = \lim_{N \rightarrow \infty} \frac{1}{2N+1} \sum_{i=-N}^N V_i^2 \quad (5.17)$$

respectively. An energy signal satisfies the condition  $E < \infty$  (meaning it has finite energy), and a power signal satisfies the condition  $0 < P < \infty$  (meaning it has finite power). The Barkhausen signal can be classified as a power signal, as the energy is infinite (if we keep magnetizing the material sinusoidally we will keep measuring Barkhausen emissions) and the power is finite and non-zero.

### 5.1.2.5 Calculation of pulse height distribution

The sudden displacement of a domain wall gives rise to a change of flux over time, which in turn induces a voltage in the sensing coil. This voltage can be shown to be proportional to the velocity of the domain wall. According to Faraday's law of induction, the measured voltage  $V(t)$  can be shown to be proportional to the rate of change of magnetization  $dM(t)/dt$ :

$$V \propto \frac{dM}{dt}. \quad (5.18)$$

The quantity  $dM/dt$  can be expressed as

$$\frac{dM}{dt} = \frac{dM}{dx} \frac{dx}{dt}, \quad (5.19)$$

where  $dx/dt$  is the velocity of the domain wall. Assuming  $dM/dx$  is a constant (meaning magnetization does not vary spatially, which is true over small distances), this proves that the voltage is proportional to the velocity of the domain wall. In a practical situation, where a multitude of domain walls are displaced over different locations within the material, the measured signal is composed of microsecond pulses, which are the superposition (whether constructive or destructive) of these induced pulses. The pulses seen at the point of measurement come in a variety of durations and amplitudes. Even though it is non-trivial to spatially locate and separate individual pulses in the time-domain, the signal can be high-pass filtered to only keep the surface emissions, and calculate the distribution of amplitudes and durations of the resulting pulses.

This is implemented by specifying a noise floor and tracing the excursions of the signal above and below this threshold voltage. The duration of a Barkhausen pulse, or avalanche will be equal to the time it takes for the measured voltage to intersect the noise floor, and its amplitude will be the maximum voltage reached during that excursion. The algorithm scans through the Barkhausen signal and plots a distribution of durations and amplitudes.

Typically, plastic deformation increases the number of low amplitude pulses (due to the increased dislocation density), while when under elastic deformation an increased pulse amplitude is observed (as domain walls travel larger distances in the absence of dislocations).

### 5.1.2.6 Calculation of Fourier Transform

The Fourier transform of a voltage signal  $V(t)$  of finite energy is defined as [53]

$$\mathcal{F}(\omega) = \int_{-\infty}^{\infty} V(t)e^{-j\omega t} dt \quad (5.20)$$

where  $t$  denotes the time variable and  $\omega$  denotes angular frequency. The Fourier transform is essentially the inner product of a function with an orthonormal basis set, which allows expressing any periodic function in terms of a Fourier series, which is a sum of sinusoids of different frequencies and amplitudes. The Fourier basis set is defined as [53]

$$\Phi_m(t) = e^{jm\omega_0 t} \quad \text{for} \quad -\infty \leq m \leq \infty \quad \text{and} \quad \omega_0 = \frac{2\pi}{P} \quad (5.21)$$

A property of this basis set is its orthonormality, which means that the inner product of two set functions  $\langle \Phi_m, \Phi_n \rangle$  is non-zero when  $m = n$  and zero otherwise. In the process of expressing a time signal in terms of its Fourier components (which are complex sinusoids), one obtains the coefficients (or amplitudes)  $z_m$  for each sinusoid:

$$z_m = \frac{1}{P} \int_0^P V(t)\Phi_m^*(t) dt \quad (5.22)$$

where  $P$  is the period of the signal. After calculating  $z_m$  for  $-\infty \leq m \leq \infty$ , the voltage  $V(t)$  can be expressed as:

$$V(t) = \sum_{m=-\infty}^{\infty} z_m \Phi_m(t) \quad (5.23)$$

It is important to note that in the case of Barkhausen signals, it is almost imperative to obtain a multitude of observations to then calculate the ensemble average. However, something that is not readily obvious, is the order of operations, which matters when the operations are not associative. More specifically, both the Fourier transform and the expectation of a signal are linear operations and therefore associative. Thus, the following holds true:

$$\mathcal{F}\{E[V_i(t)]\} = E[\mathcal{F}\{V_i(t)\}] \quad (5.24)$$

However, since the model for the Barkhausen frequency spectrum only takes into account the magnitude of the Fourier transform,  $|\mathcal{F}(\omega)|$ , we have to consider the case where the magnitude is taken before or after averaging the observations. In the former case, the following relationship holds true:

$$E[|\mathcal{F}\{V_i(t)\}|] = E[|F_i(\omega)|] \neq |\mathcal{F}\{E[V_i(t)]\}| \quad (5.25)$$

In fact, it was shown in practice that it is better to take the expectation of the magnitude spectra, rather than the expectation of the time series. The resulting magnitude spectra are smoother, due to the fact that before averaging the phase information is omitted.

### 5.1.2.7 Finite Impulse Response (FIR) filtering

Filtering is central to the idea of depth profiling. Whereas digital filtering was not employed in the later stages of this project (as the idea prevailed that the entire frequency spectrum contains extractable depth information), in the first approach, where the high-frequency part of the signals were isolated, it was necessary to process the signals using a high-pass filter.

While analog systems have an infinite impulse response, the discrete nature of digital systems limits them to a finite impulse response (FIR). The impulse response of a filter in the discrete frequency (or  $z$ -) domain is denoted as  $H(z)$ , which can be defined as the ratio of the output  $Y(z)$  to the input  $X(z)$ :

$$H(z) = \frac{Y(z)}{X(z)} \quad (5.26)$$

In the MATLAB implementation, the filter design toolbox was used to programmatically create filter objects that can operate on time series. Four types of filter were created, namely low-pass, band-pass, high-pass, and arbitrary frequency response. A notable point is that the order of the filter increases as the roll-off (distance between stop and pass frequencies) becomes steeper. This, in turn, increases the size of the filter object in memory, slows down computations, and sometimes leads to spurious results. That is the reason why the roll-off was set to increase linearly as a function of passband frequency, such that

$$kF_{pass} = |F_{pass} - F_{stop}| \quad (5.27)$$

where  $k$  is an arbitrary constant. This safety mechanism guarantees that the filtering algorithm does not terminate unexpectedly, or causes the operating system to crash.

### 5.1.2.8 Simulated Annealing

In assessing the predictive capability of a theoretical model, comparison with real world data is necessary. Fitting the model to a set of experimental data is performed in the hopes of observing a deterministic variation of the model parameter(s) in response to a control variable. This is usually done by calculating the forward model with a given set of initial parameter values, and minimizing the objective (or cost) function with respect to those parameters, and subject to constraints on those parameters. A typical optimization problem can be written as [54]:

$$\min_{x \in \mathbb{R}^n} f(x) \quad \text{subject to} \quad \begin{cases} c_i(x) = 0, & i \in \mathcal{E} \\ c_i(x) \leq 0, & i \in \mathcal{I}. \end{cases} \quad (5.28)$$

where  $x$  is the vector variables (or unknowns, or parameters),  $f$  is the function to be minimized, and  $c$  is the constraint vector, which specifies the constraints that are imposed on the parameters. For the situation addressed in this thesis, the simplest form of the optimization problem will look as follows:

$$\min_{V_{orig}, \zeta} V_{meas}(\omega; V_{orig}, \zeta) \quad \text{subject to} \quad \begin{cases} V_{orig} > 0, \\ \zeta > 0. \end{cases} \quad (5.29)$$

Depending on the model formulation, more parameters other than just  $V_{orig}$  and  $\zeta$  can be included in the optimization (which will become obvious in later chapters). In the case of convex functions, which only contain one stationary point, this is rather trivial, since a local minimum must also be a global minimum. For non-convex, non-linear objective functions, the problem becomes more difficult, as the objective function will contain multiple minima, of



which only one can be the global one. There are multiple methods that can be used to estimate parameters from a given set of data. One of those is the least squares method, which can be used to solve both linear and non-linear problems. In this method, the goal is to minimize the sum of squares of residuals. The residuals are defined as the difference between the measured data  $y_j$  and the forward-model calculated data  $V_{meas}$  over a set of frequencies  $\omega_j \in [0, \infty)$  for given parameters  $V_{orig}$  and  $\zeta$ .

$$r_j(V_{orig}, \zeta) = y_j - V_{meas}(\omega_j; V_{orig}, \zeta), \quad j = 1, \dots, m \quad (5.30)$$

Minimizing the sum of squares of residuals can be expressed as

$$\min_{\substack{V_{orig} \in \mathbb{R} \\ \zeta \in \mathbb{R}}} f(V_{orig}, \zeta) = \sum_{i=1}^m r_i^2(V_{orig}, \zeta). \quad (5.31)$$

While this method of obtaining parameter estimates yields good results for certain problems, there are some drawbacks. Least squares optimization is unconstrained, which may lead to unrealistic parameter estimates. Also, the chance of getting "trapped" in a local minimum (rather than a global minimum) is high.

Simulated annealing [55] provides a better alternative to optimizing functions with multiple local minima, as it does not rely on computing derivatives numerically. It depends on a scheme which accepts or rejects function evaluations on a probabilistic basis, which drives it uphill and downhill from local minima until it converges to the global minimum. While computationally it is not as efficient, the initial values provided to the algorithm have little influence on the end result, and thus alleviate the need for manually restarting the algorithm with different inputs, like in the case of least squares. It is used extensively to optimize non-convex, non-linear objective functions and has been proven superior to the genetic algorithm [55] in solving certain problems. In the case of this research, the primary reason for using it is the large Barkhausen data sets that were collected and the immense number of function evaluations needed; a least squares algorithm would require manually restarting the algorithm multiple times.

Given two initial input values, say  $V_{orig}$  and  $\zeta$ , an objective function evaluation  $f(V_{orig}, \zeta)$  is made. Next, the algorithm chooses two new parameter values  $V'_{orig}$   $\zeta'$ , based on the following

condition:

$$V'_{orig} = V_{orig} + r \cdot v_{V_{orig}} \quad (5.32)$$

$$\zeta' = \zeta + r \cdot v_{\zeta} \quad (5.33)$$

where  $r \sim \mathcal{U}(-1, 1)$  and  $v_{V_{orig}}$  and  $v_{\zeta}$  are the step lengths for each parameter. If the condition

$$f(V'_{orig}, \zeta') < f(V_{orig}, \zeta) \quad (5.34)$$

is true, the algorithm accepts the new function evaluation  $f(V'_{orig}, \zeta')$  as the best answer, and the algorithm proceeds downhill. If the above condition is not true, the algorithm uses a probabilistic criterion, named the Metropolis criterion, to decide whether or not to accept the new function evaluation. The probability

$$p = \exp((f(V'_{orig}, \zeta') - f(V_{orig}, \zeta))/T) \quad (5.35)$$

is computed, where  $T$  is the annealing temperature<sup>1</sup>. If  $p$  is greater than  $p' \sim \mathcal{U}(0, 1)$ , the new parameters are accepted. It can be seen that the probability of acceptance depends on both the distance  $f(V'_{orig}, \zeta') - f(V_{orig}, \zeta)$  and the annealing temperature  $T$ . As more parameter values are accepted, their associated step lengths increase, in order to sample a larger region of the parameter space. This also reduces the temperature such that the new temperature

$$T' = r_T T \quad (5.36)$$

where  $r_T \sim \mathcal{U}(0, 1)$ . As the temperature decreases, uphill moves are less frequent, which also reduces the step lengths by rejecting more and more function evaluations.

There are a number of criteria that one can choose to terminate the algorithm with. In the MATLAB @implementation, the user can specify the total number of function evaluations, the

<sup>1</sup>This naming convention derives from the of annealing a metal, where the temperature is decreased slowly, to allow the material to reach its minimum energy state and not get trapped in metastable states, which are the physical analogue to local minima in an optimization problem.

objective function tolerance, as well as the difference between successive function evaluations. These require careful selection (and generosity, in the case of number of function evaluations), which comes from experience in handling a particular type of objective function. If the number of total function evaluations is too low, the algorithm may never get enough time to reach the global minimum; the more local minima, the more function evaluations it usually requires. Similarly, if the objective function tolerance is set too high, the algorithm may terminate prematurely. Now, the difference between successive function evaluations is a delicate criterion. In some ways it is a safety net, which compensates for the case of never reaching the global minimum (which is not a rare scenario). If the difference between, say, 5 best function evaluations is really small, the algorithm terminates. While there could possibly be a better value, it may not be reachable within a realistic timeframe. These criteria were experimented with multiple times, until the algorithm seemed to converge reasonably fast (within approximately 4000 function evaluations), with a low objective function tolerance and low difference between successive function evaluations.

Since simulated annealing is a stochastic fitting algorithm, it was deemed necessary to run the algorithm 30 times for each dataset (minimum number of samples to yield a normally distributed set, according to the Central Limit theorem [56]), of which the mean is then taken. Since the Barkhausen data set contains a large stochastic component, and the algorithm is also stochastic, it is expected that the variance of results is relatively large. The mean, however, should follow a clear enough trend to prove that the model is capable of extracting depth-dependent information.

#### **5.1.2.9 Summary of Barkhausen signal analysis**

The signal analysis algorithm entails several stages, which can be grouped as below:

- Data loading stage (initiated by running script)
  1. Specify path to .txt files containing Barkhausen data
  2. Specify magnetization parameters (magnetization frequency and amplitude)

### 3. Specify control parameter (i.e. stress or magnitude of deflection)

```
ControlParameterBkhExplmm_Pa = ControlParameter_SurfStress_new(1,:);
BkhExplmm_Pa_3V_100Hz = BarkhausenExperiment('path/to/file/3V_100Hz', ...
    ControlParameterBkhExplmm_Pa, 'Longitudinal Surface Stress (Pa)', [8 3], [4
20 2.5e6]);
BkhExplmm_Pa_3V_100Hz.LoadAverageDataFiles;
```

- Signal processing stage

By default, upon creation of every BarkhausenSignal object, the following commands are executed:

```
BkhSignal.ComputeEnvelope('Raw.allcycles') % Computes the envelope of the waveform
BkhSignal.ComputePeakStats('Raw.allcycles') % Computes peak locations and amplitudes
BkhSignal.ComputeRMS('Raw') % Computes R.M.S. voltage
BkhSignal.ComputePower('Raw') % Computes signal power
BkhSignal.ComputePHD('Raw') % Computes the pulse height distribution
BkhSignal.ComputeFFT('Raw.allcycles') % Computes the Fast Fourier transform
BkhSignal.ComputeWindowedFFT() % Computes the Fast Fourier transform using window
```

The following command has to be manually entered by the user, and will calculate the time domain statistics of the created experiment.

```
BkhExplmm_Pa_3V_100Hz.PopulateExpStats('Raw');
```

- Visualization stage (optional)

A variety of automated plotting functions were written to facilitate fast visualization of results in the time- and frequency domain. Their use is optional but highly recommended prior to performing further analysis, as they can provide useful information regarding the validity of results.

```

BkhExplmm_Pa_3V_100Hz.Plot('Raw.RMS')
BkhExplmm_Pa_3V_100Hz.Plot('Raw.NPeak')
BkhExplmm_Pa_3V_100Hz.Plot('Raw.PPeak')
BkhExplmm_Pa_3V_100Hz.Plot('Raw.PPeakPos')
BkhExplmm_Pa_3V_100Hz.Plot('Raw.NPeakPos')
BkhExplmm_Pa_3V_100Hz.Plot('Raw.Power')
BkhExplmm_Pa_3V_100Hz.Plot('Raw.Spectrum')

```

*Raw* can be substituted with *Proc*, to display the above plots but for the processed (filtered) signals.

- Model fitting stage

In the model fitting stage, the simulated annealing algorithm within the *BarkhausenExperiment* class is invoked, and after each iteration of the parameter extraction process, the parameter estimates are stored in a multidimensional array. There are two renditions of the model that are used to analyze the data, which are outlined in the next subsection.

#### 5.1.2.10 Analysis configurations

##### Analysis of frequency domain data using $m$ parameter method

In summary, in this method the model of (3.43), which assumes a stress gradient along depth, is fitted to Barkhausen frequency spectra, for many different magnitudes of deflection and observing the change of the fitted parameters  $m$ ,  $\sigma_0$  and  $\zeta$  as a function of longitudinal surface stress, for all four specimens. The algorithm was incorporated into the developed MATLAB libraries, and comprises of the following main steps:

1. Load measurements and obtain ensemble average of multiple measurement trials for each magnitude of deflection, using class *BarkhausenExperiment.m*.
2. Calculate FFT of entire time domain waveform resulting from the ensemble average.
3. Configure algorithm options prior to computation:

```
Params = [2 2 10;... % Data option
```

```

1 1 1;...      % a
0+sqrt(10^16)*rand(1) -10^8 10^8;...      % m
500 + sqrt(500)*rand(1) - 0 1000;...      % sigma_0
500 + sqrt(500)*rand(1) - 0 1000;...      % zeta
0 0 0;...      % k
depth depth depth] % x_max

```

The first line, first entry indicates which version of the Fourier transform is to be used (windowed - 1 or full time series - 2<sup>1</sup>), while the second and third entries can be used to exclude a given percentage of the frequency spectrum from the lower and higher ends, respectively. This is useful if there is a low or high-frequency region where it is known there is a lot of external interference which the model does not explain.

Lines 2 to 7 correspond to parameters  $a$ ,  $m$ ,  $\sigma_0$ ,  $\zeta$ ,  $k^2$ , and  $x_{max}$ . The three entries correspond to initial value, lower and upper bounds, respectively. As can be seen, all parameters were allowed to vary, except for  $k$ , and the detection depth  $x_{max}$  (which has to be specified). The algorithm options are summarized in Table 5.1.

**Table 5.1:** Simulated annealing algorithm options.

Parameter	Initial Value	Lower Bound	Upper Bound
$m$	$\mathcal{N}(0, 10^{16})$	$-10^8$	$10^8$
$a$	1	1	1
$\sigma_0$	$\mathcal{N}(750, 250^2)$	500	1000
$\zeta$	$\mathcal{N}(750, 250^2)$	500	1000

Initial parameter values are randomized, to avoid correlations in the results. Command `rand(1)` returns random variable  $X$  drawn from the pseudorandom distribution  $\mathcal{N} \sim (0, 1)$ . It is possible to use the lower and upper bounds,  $b_L$  and  $b_U$ , to denote that the initial value input should be bounded such that the upper and lower bounds,  $b_U$  and  $b_L$ , are one standard deviation away from the mean, or initial value  $a$ :

<sup>1</sup>The windowed Fourier transform only uses data points around the peak of the waveform, where permeability approaches that of the coercive point in the B-H loop

<sup>2</sup>Parameter  $k$  lends a  $1/\omega^k$  dependence to the spectrum; this was only used in measurements when the rest of the model (multi-exponential form) did not seem to explain the results well. It was not used in this case, thus it was set to 0.

$$a \pm b = \left( b_L + \frac{b_U - b_L}{2} \right) \pm \frac{b_U - b_L}{2} \quad (5.37)$$

We then can modify the standard normal distribution ( $X$ ) to obtain the needed distribution  $Y \sim \mathcal{N}(a, b^2)$ , which will be symmetric and centered between the parameter bounds. Its mean will be:

$$\mathbb{E}(Y) = \mathbb{E}(a + bX) = \mathbb{E}(a) + \mathbb{E}(bX) = a + b\mathbb{E}(X) = a \quad (5.38)$$

and its variance will be:

$$\text{Var}(Y) = \text{Var}(a + bX) = \text{Var}(a) + \text{Var}(bX) = b^2 \text{Var}(X) = b^2 \quad (5.39)$$

Thus, for setting the bounds to  $\pm 10^8$  for parameter  $m$ , we yield  $a = 0$  and  $b = 10^8$ , thus the third line (bounds for  $m$ ), as seen above, will read:

```
0+10^16*rand(1) -10^8 10^8; ... % m
```

The data option is set to "full", meaning that the the frequency spectrum is calculated from the entire dataset (using a rectangular window), while 2% and 10% of the data are removed from the beginning and end of the frequency spectrum, respectively.

4. Obtain parameter estimates for  $m$ ,  $\sigma_0$  and  $\zeta$  via the simulated annealing algorithm . The algorithm options can be seen below:

```
options = saoptimset('InitialTemperature', 1000, 'ReannealInterval', 80, ...
'AnnealingFcn', @annealingfast, 'TolFun', 1e-1, 'ObjectiveLimit', 1e-2);
```

These options are explained as follows: Option *InitialTemperature* provides the initial temperature to the algorithm. Option *ReannealInterval* resets the temperature to a higher value (in order to escape local minima) within a set time. Option *AnnealingFcn* specifies

the type of probability function to use. Option *TolFun* will stop the algorithm if the average change in function evaluations is smaller than the function tolerance. Option *ObjectiveLimit* will stop the algorithm if the objective function value is equal or less than that.

5. Iterate through step 4, 30 times. Save values in matrix  $\mathbf{A}_{mnp}$ , where  $m$  denotes number of parameters,  $n$  denotes number of deflections,  $p$  denotes iteration number.
6. Obtain mean of  $\mathbf{A}_{mnp}$  along dimension  $p$ , thus reducing it to  $\mathbf{A}_{mn}$ .
7. Plot  $m$ ,  $\sigma_0$  and  $\zeta$  vs. longitudinal surface stress.

### 5.1.3 Overview of class *BarkhausenSignal*

The class *BarkhausenSignal* stores and operates on a single Barkhausen time-series, of arbitrary number of cycles, excitation frequency and field, and sampling frequency. This class was designed primarily to organize waveform statistics hierarchically. The aforementioned properties need to be specified upon calling the class constructor, along with the path to the .txt file containing the time series. After an instance of the class is created, a number of statistics, such as envelope, envelope peak, pulse height distribution, power and RMS, as well as frequency spectrum are automatically calculated and ready to be visualized. In addition, the user can also call a function to filter the time series using filters of different impulse responses. Upon calling this function, the aforementioned signal properties are re-calculated and stored in different variables, which allows the user to easily go back and compare filtered to unfiltered results. This functionality is implemented by the following class methods:

#### **ComputeEnvelope**

Computes the envelope for either the raw signal, ensemble average of the signal, or processed (filtered) version of the ensemble average.

#### **ComputeAverage**

Computes the ensemble average of the signal over N cycles.



**ComputePeakStats**

Computes the peak values from the envelope of either the raw signal, ensemble average of the signal, or processed (filtered) version of the ensemble average.

**ComputeFFT**

Computes the FFT for either either the raw signal, ensemble average of the signal, or processed (filtered) version of the ensemble average.

**ComputeWindowedFFT**

Computes the windowed FFT (using a Hamming window) for either the ensemble average of the signal, or processed (filtered) version of the ensemble average.

**ComputeRMS**

Computes the signal RMS for either the ensemble average of the signal, or processed (filtered) version of the ensemble average

**ComputePower**

Computes the signal power for either the ensemble average of the signal, or processed (filtered) version of the ensemble average.

**ComputePHD**

Computes the pulse height distribution of the time domain signal.

**BandPassFilter**

Band-pass filters the raw signal given the filtering parameters.

**HighPassFilter**

High-pass filters the raw signal given the filtering parameters.

**ExponentialFilter**

Filters the raw signal using a filter of decaying exponential frequency response.

#### 5.1.4 Overview of class *BarkhausenExperiment*

In addition to the class *BarkhausenSignal*, which was designed to store a single time-series, a separate class was written, *BarkhausenExperiment*, which can be used to analyze multiple measurements simultaneously. It uses the concept of an object array, in that every instance of class *BarkhausenExperiment* contains an array of *BarkhausenSignal* objects. This class facilitates analysis of controlled experiments, where the objective is to observe the change of a state variable in response to some control variable. To construct an instance of class *BarkhausenExperiment*, it is necessary to provide the values for the control variable. This could be uniaxial stress, magnitude of bending, or even a microstructural parameter, such as grain size. The number of measurements, which is another input, has to be equal to the times the control variable was varied, while the number of measurement trials represents how many times each measurement was repeated. It is imperative that the number of trials, cycles in each time series, excitation frequency and field, as well as sampling frequency are the same for all measurements in one instance of *BarkhausenExperiment*, such that the control variable is the only independent variable.

Using this class, one is able to carry out signal processing operations on multiple Barkhausen waveforms at once. This could be the filtering of an entire set of measurements and plotting the mean peak value, or pulse height distribution, versus stress. For certain statistics (such as RMS and peak value) it is also possible to plot confidence intervals.

A function central to this class is the implementation of the simulated annealing algorithm. The function can be called from an external script that iterates through the parameter of interest (such as depth), running the simulated annealing algorithm with a different input each time. The end result can be a plot of fitted parameter (such as  $V_1$ ) versus depth (computational control parameter), for different values of stress (experimental control parameter).

#### **LoadDataFiles**

Individually loads all the specified time series into an object array. For example, an experiment consisting of 18 measurements of 5 trials each, would be loaded as 90 distinct time series.

**LoadAverageDataFiles**

Loads the specified time series, and computes the ensemble average (in the time domain and frequency domain separately), for each measurement. For example, an experiment consisting of 18 measurements of 5 trials each, would be loaded as 18 distinct time series representing ensemble averages.

**PopulateExpStats**

Computes statistical parameters (mean and standard deviation) of time domain properties.

**HighPassFilter**

High-pass filters all measurements at once, using the specified filter characteristics.

**FitOneLayerModel**

Fits the one layer model to all measurements and returns a matrix with parameter estimates.

**FitTwoLayerModel**

Fits the two layer model to all measurements and returns a matrix with parameter estimates.

**PlotOptimResults**

Plots the optimization results.

**Plot**

Plots time- and frequency-domain statistics versus control parameter, for all measurements.

## 5.2 Measurement and instrumentation tools

While the signal processing operations were performed within the MATLAB® programming environment, the hardware interfacing and signal acquisition was accomplished using LabVIEW® (National Instruments, Austin, TX, USA). LabVIEW (Laboratory Virtual Instrument Engineering Workbench) is a development environment which is commonly used for system design.

The programming language that LabVIEW uses, "G", is a dataflow programming language, where code execution happens from left to right, and is routed virtual wires, or nodes, which serves as connections between functional blocks. The built-in ability of parallel processing, multiplexing and interfacing with a multitude of commercial instrumentation are the main strengths of LabVIEW.

A typical subroutine is termed a *VI*. A *VI* encompasses a front-panel, which serves as a graphical user interface. This contains indicators (which monitor results) and controls (which allow the user to input information). The *VI* also encompasses a block diagram, which contains the source code; controls and indicators on the front panel appear as source and sink terminals on the block diagram, respectively. A *VI* can be run as a stand-alone entity (as it contains a user interface), or used as a subroutine in the block diagram of another program, with input and output connections defined by the connector pane.

While for very simple acquisition and visualization operations LabVIEW code is easy to create and maintain, for larger and more complicated projects programs quickly become messy and unreadable. This is especially true if best programming practices are not followed. This is why the functional requirements of the software were examined carefully, in order to use specify a suitable software architecture and employ the minimum amount of complexity needed. The software was built on a *state machine* architecture, which is ideal for acquiring a finite number of samples (as opposed to continuous measurement). After an signal acquisition is performed, the acquired data is sent to a MathScript node that invokes MATLAB, which then performs the signal processing using the class *Inputsignal.m* which was written specifically for interaction with LabVIEW, and which was the basis of class *BarkhausenSignal.m*. Subsequently, the results are returned and visualized in LabVIEW. In this way, the software was broken down into two separate entities, making use of the benefits of both programming environments, and keeping complexity to a minimum.

In the state machine architecture, the basic block diagram (LabVIEW code) is a while loop (which loops indefinitely until the user terminates it) containing a case structure which is controlled by buttons on the graphical user interface and executes functions on demand. The software can perform the following main functions:

- “Acquire” button: Acquires a measurement, and automatically saves a MATLAB (.mat) file on location ‘C:/temp/acquiredSignal’, with file name equal to the measurement ID displayed in entry on left of table.
- “Save” button: Saves the current Barkhausen measurement in .mat (MATLAB) format at the location specified by the user. The user has the option to select any measurement from the table by clicking on the measurements from the table
- “Load” button : Loads a previously saved (measurement file) .mat file into the current session.
- “Clear” button: Clears every measurement from the tables and also the graphs from the front panel.
- “Analyze” button: Filters an existing measurement according to selected high-pass cutoff frequency in the settings panel. To use this function, open the settings panel (see next sections) and change to the desired cutoff frequency. Then click OK. To analyze using the newly selected settings, simply click on the “Analyze” button. The peak amplitude and other statistics of the measurement should now change, and this change can be seen in the statistics table on the last tab.
- “Copy Graph” button: Copies the currently opened graph in .bmp format and saves it in file location specified by the user.
- “Export” button: Exports the present measurement data into a .txt format (containing the data along with the acquisition settings) in the file location specified by the user.
- “Exit” button : Stops the currently running VI.

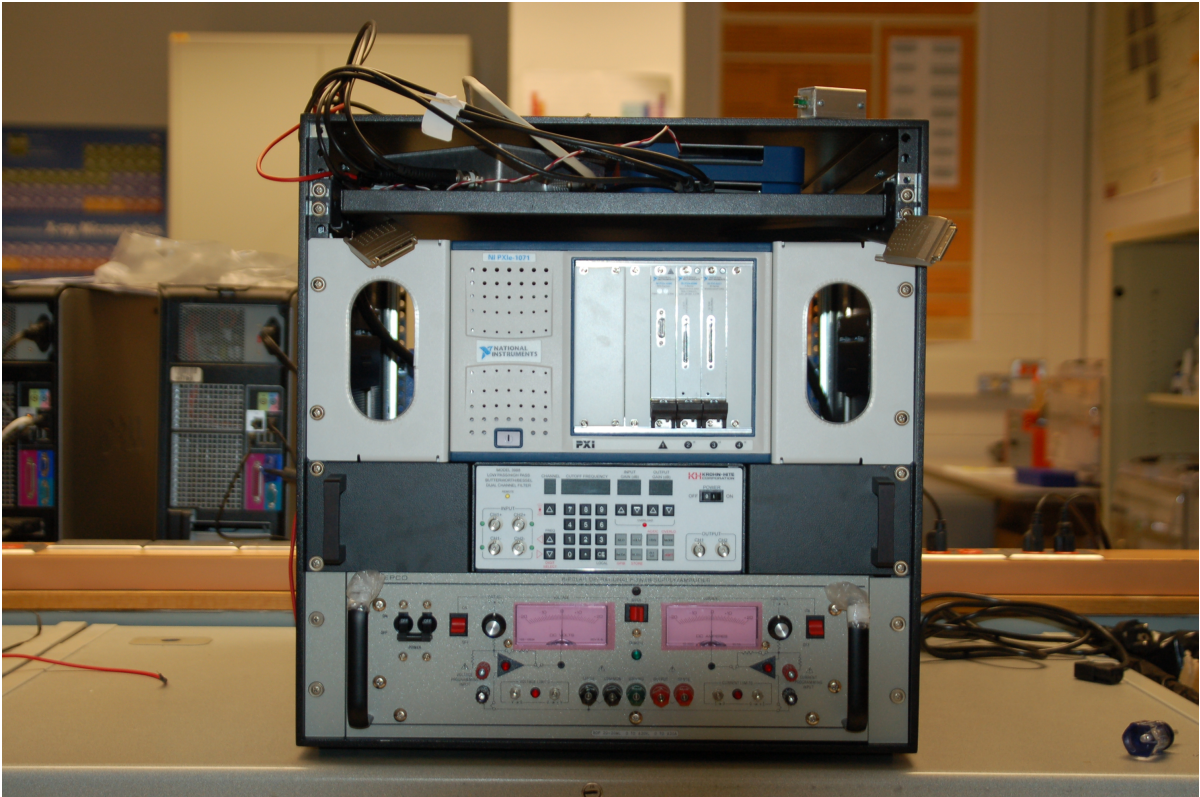


**Figure 5.2:** Custom designed and built measurement system enclosed in instrument case.

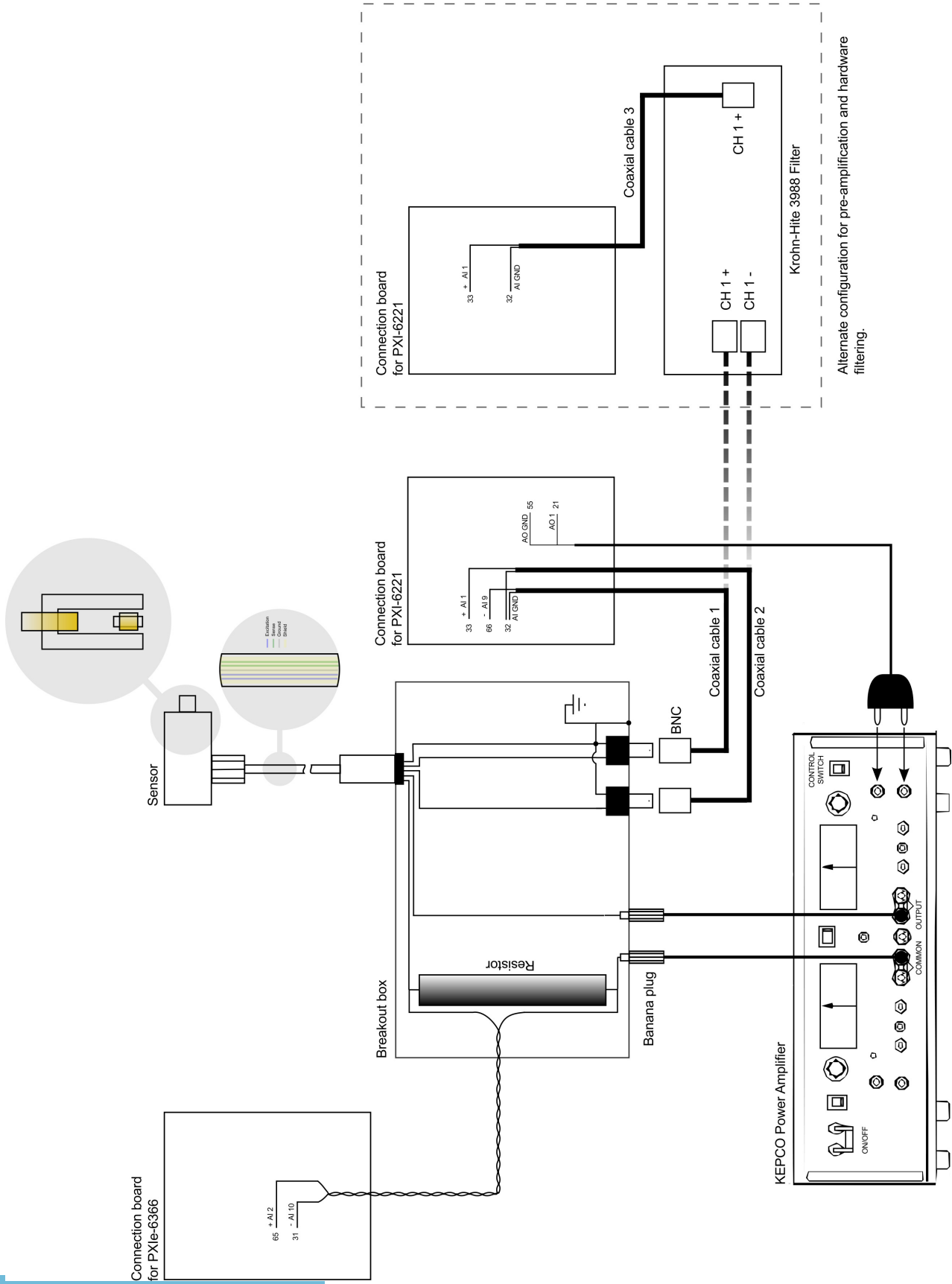


Figure 5.3: Custom measurement system connection diagram.

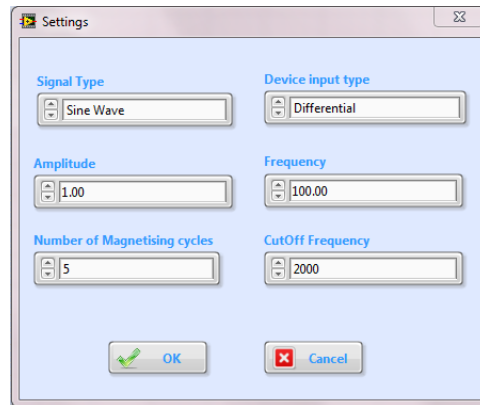


Figure 5.4: Settings pane on custom acquisition software.

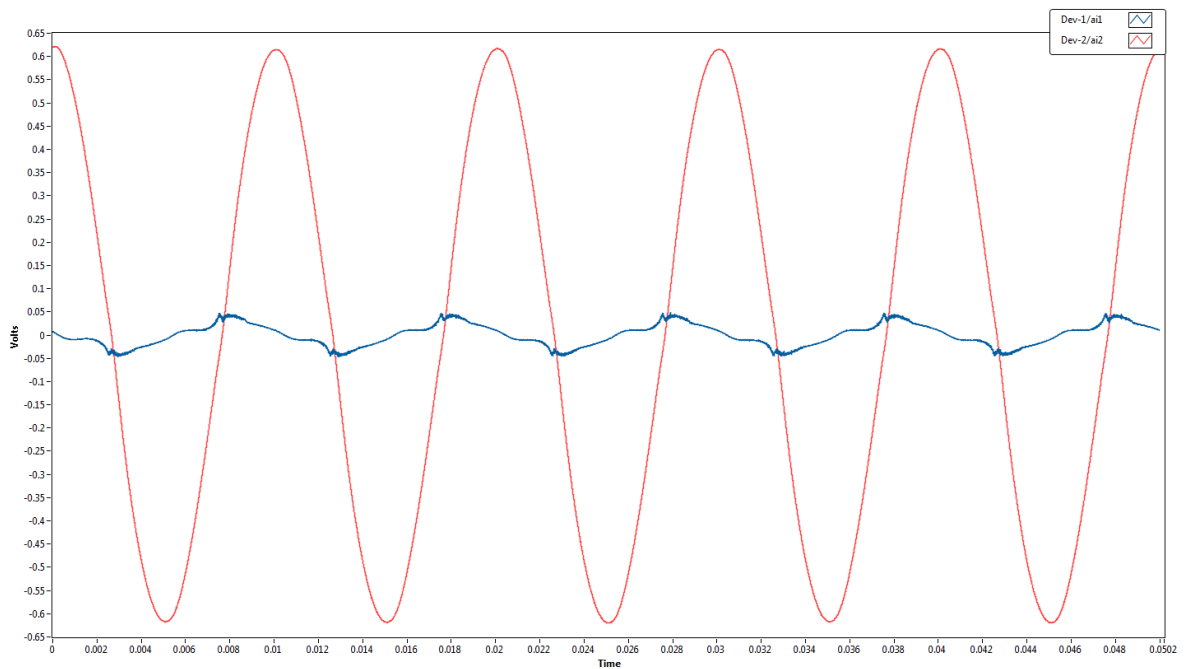
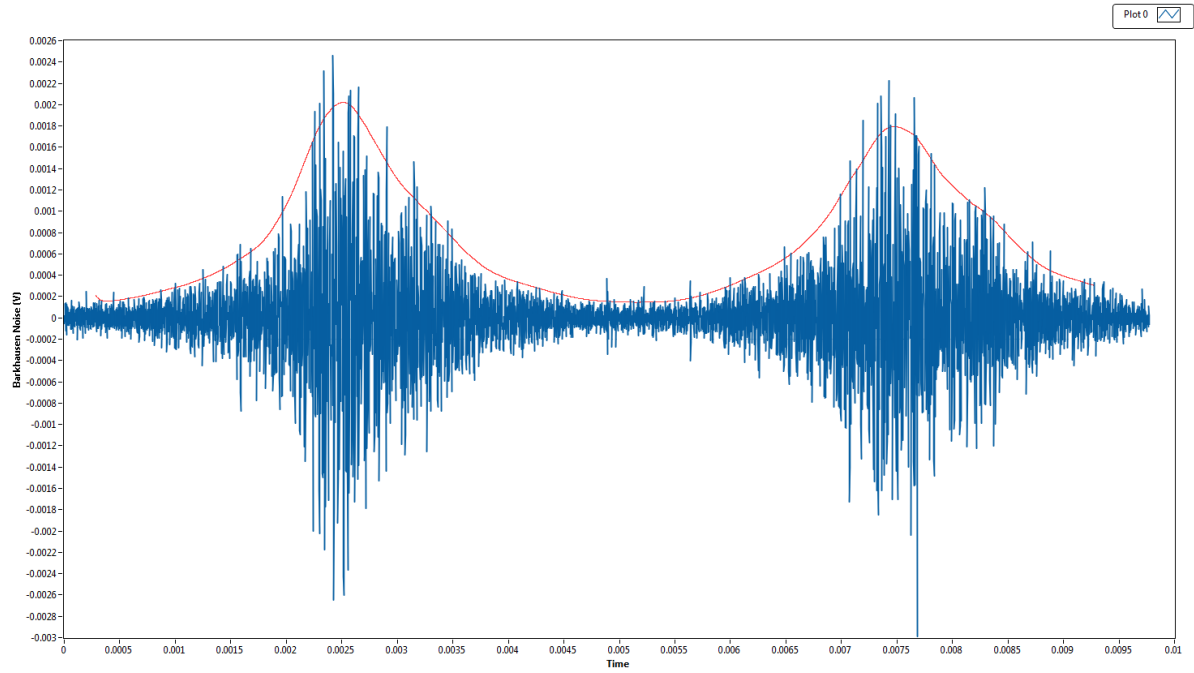
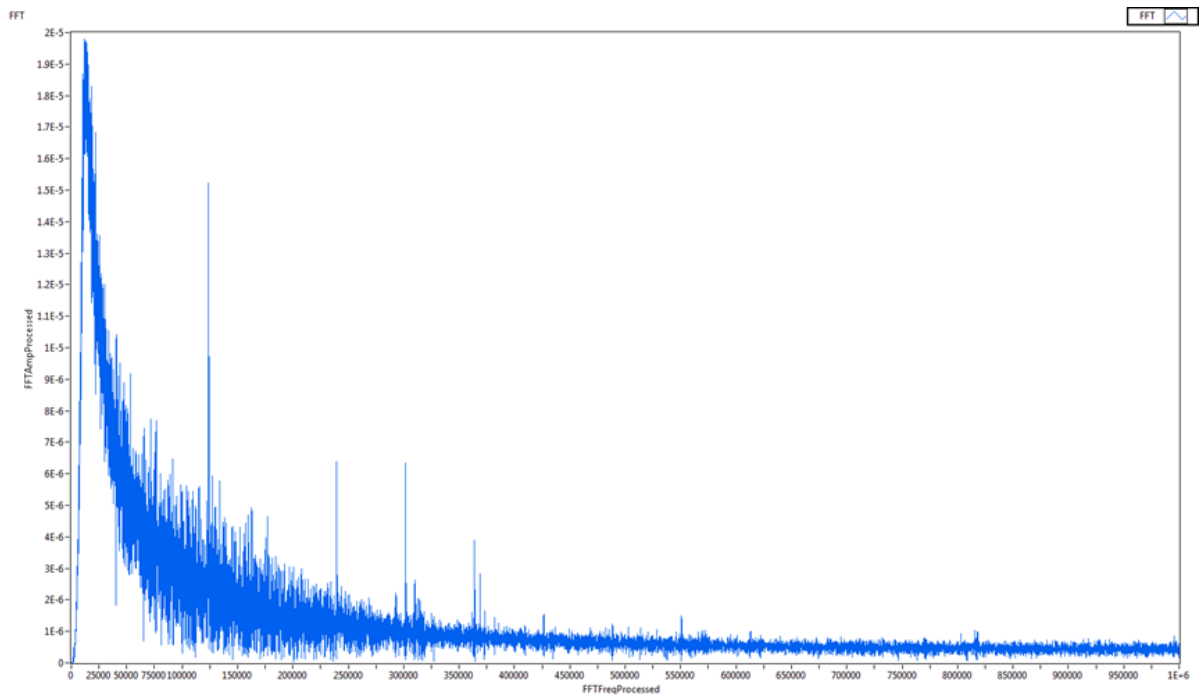


Figure 5.5: Raw signals acquired using the custom acquisition software.





**Figure 5.6:** Barkhausen signal obtained after filtering the raw  $dB/dt$  signal, using the custom acquisition software.



**Figure 5.7:** Frequency spectrum of Barkhausen signal displayed in Fig. 5.6, obtained using the custom acquisition software.



## CHAPTER 6. RESULTS AND ANALYSIS

### 6.1 Excitation amplitude - frequency sweep analysis

From the excitation - frequency sweep it is possible to obtain additional information which can help decide under which settings the subsequent measurements can be performed. Fig. 6.1 shows the RMS Barkhausen noise amplitude as a function of excitation voltage and frequency.

The Barkhausen voltage  $V(t)$  is proportional to time derivative of the flux crossing the cross-sectional area of the sensing coil  $d\Phi(t)/dt$ . Assuming that the  $d\Phi(t)/dt$  waveform is not saturated, meaning there are no harmonic components, we can write

$$V(t) \propto -\frac{d\Phi(t)}{dt} \propto -\omega\Phi e^{j(\omega t + \phi)} \quad (6.1)$$

Therefore, to obtain the flux crossing the coil, we can simply scale  $V(\omega)$  by  $1/f$ , where  $f = \omega/2\pi$ . This will rule out Faraday's law contribution to the signal and will reveal how the frequency affects the depth of penetration. Clearly, from examination of Fig. 6.2 it is obvious that increasing the frequency decreases the amount of flux crossing the coil, meaning that a smaller volume of the sample is excited due to the skin effect. Of course, from this plot it is not possible to tell which depth signals originate from, but it provides a good qualitative validation of basic physical principles that we expect to govern this process. Figure 6.2 shows  $V(\omega)$  divided by  $1/f$ .

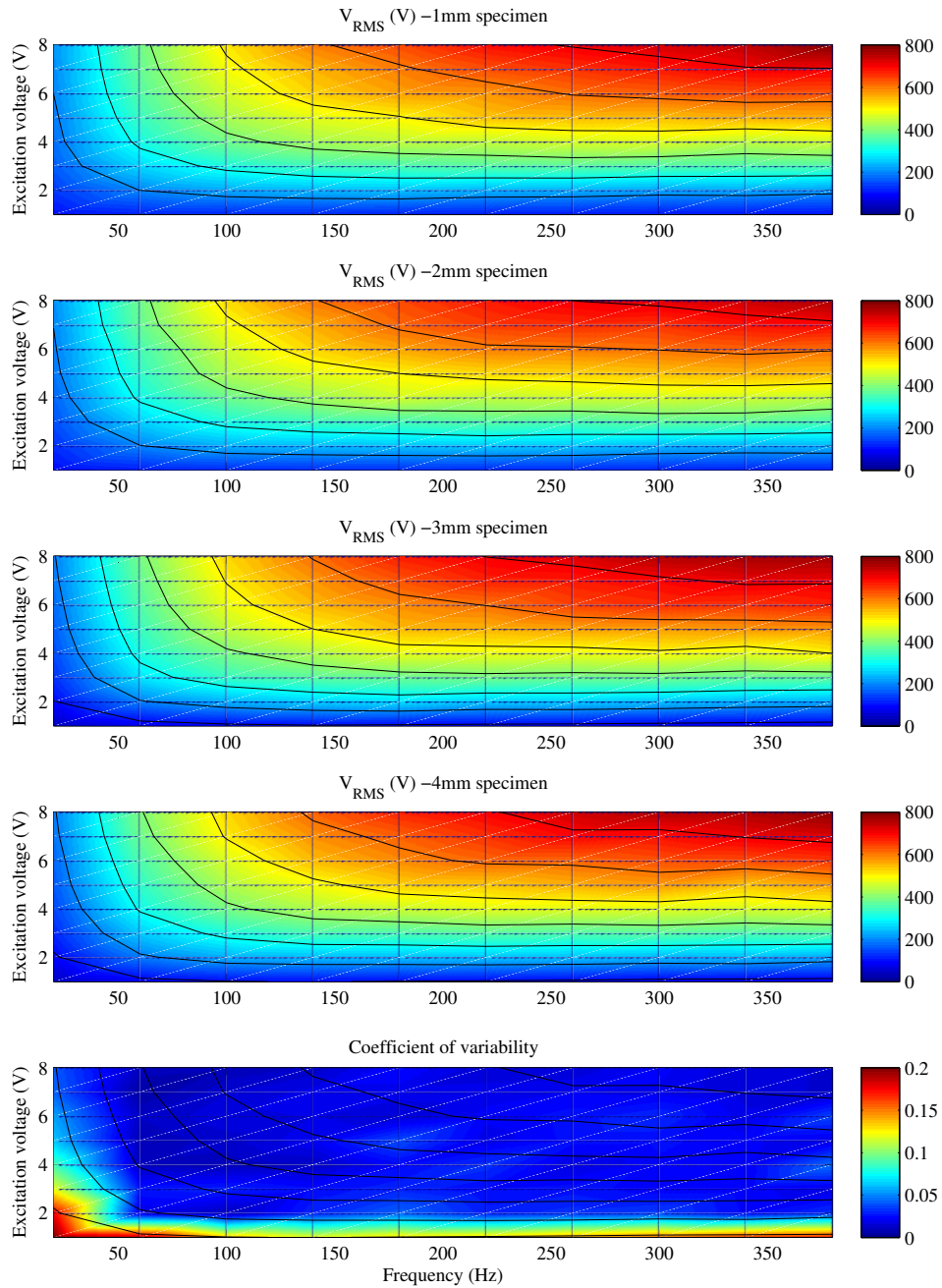


**Figure 6.1:** RMS Barkhausen noise amplitude as a function of excitation voltage and frequency, for specimens of different thickness. The bottom plot shows the coefficient of variability within the first four plots.

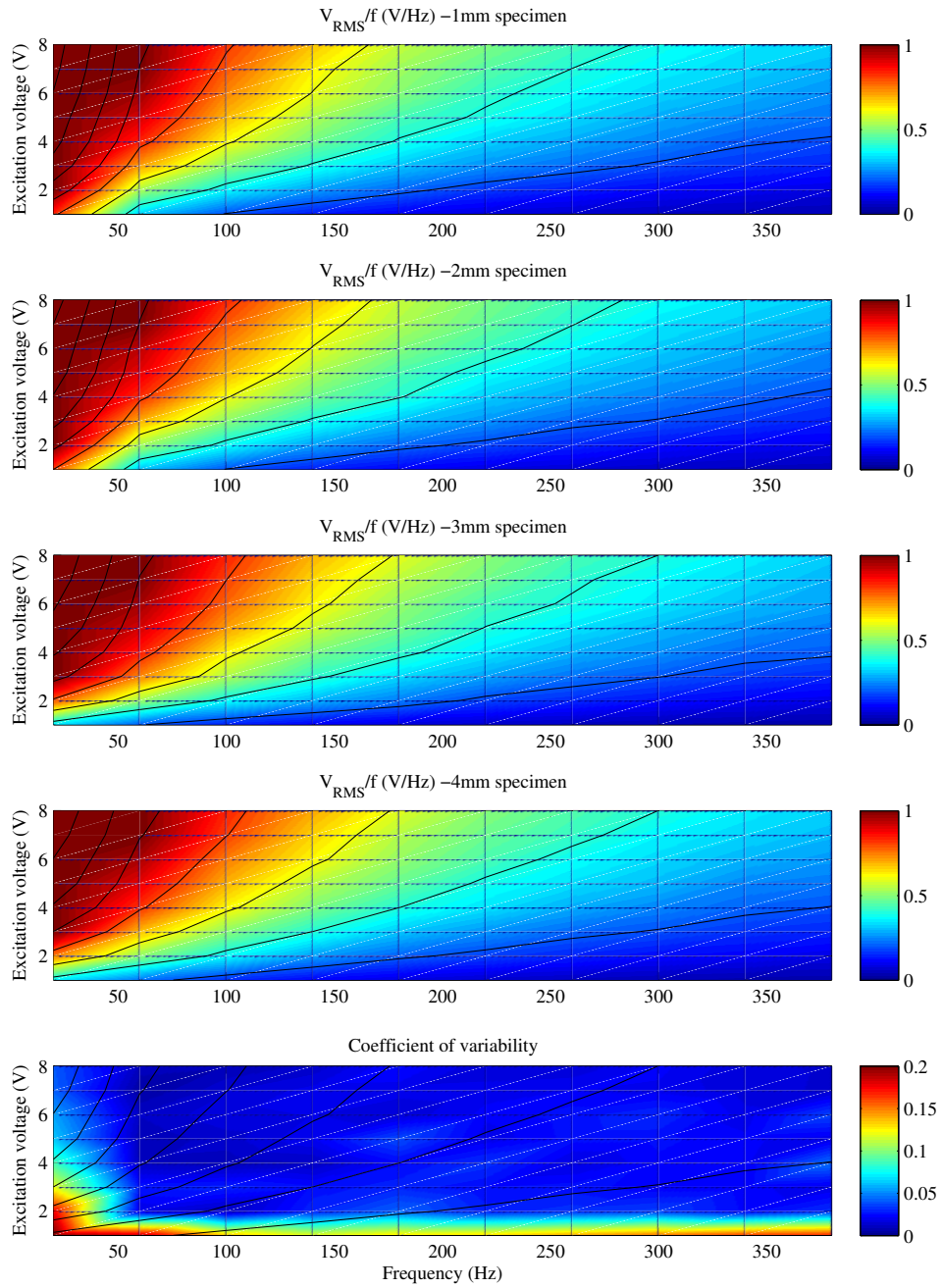


**Figure 6.2:** RMS Barkhausen noise amplitude as a function of excitation voltage and frequency, scaled by excitation frequency  $f$ , for specimens of different thickness. The bottom plot shows the coefficient of variability within the first four plots.

It is important to mention that the  $d\Phi(t)/dt$  waveform is spectrally rich as it contains contributions from  $dM(t)/dt$  (which contains the Barkhausen signal), therefore scaling  $V(t)$  by  $\omega$  assumes that the RMS Barkhausen is only a function of magnetizing frequency and that magnetizing frequency simply scales the entire spectrum (at least within the range presented here).

A way to make use of the multitude of information in Figs. 6.1 and 6.2 is by examining the coefficient of variability plot. The coefficient of variation [57] is defined as the ratio of standard deviation to the mean:

$$C.V. = \frac{\sqrt{\text{Var}(X)}}{E(X)} \quad (6.2)$$

The coefficient of variation is useful in comparing random variables, as it is dimensionless. A high C.V. indicates that the variability in the data is high, and that the associated measurements may not be reliable. A quick look at the bottom plots of Figs. 6.1 and 6.2 shows that the latter is true for low excitation voltages and especially at the lower end of excitation frequency. In order to rule out effects of changing sample thickness as much as possible, a MATLAB code was written, which searched for the point of minimum variability in the amplitude of the Barkhausen signal in the time domain (as a function of both amplitude and frequency of excitation) and reported the associated excitation parameters. By applying this code to the data of Figs. 6.1 and 6.2 it was found that the point with the least coefficient of variation was at 3 V and 100 Hz. While this result represents the data collected in the unstressed condition, it should also apply to the stressed condition, since thickness is the only parameter that will significantly affect the coefficient of variability at one point in the f-V plane.

Thus, given that the specimens are composed of the same material and in an unstressed state, it means that at this measurement point one has isolated the effects of sample thickness on the excitation signal. This allows one to proceed with applying stress while carrying out Barkhausen measurements with these measurement settings. From this analysis, it was concluded that the measurement settings which satisfy these above conditions were  $f = 100$  Hz, and  $V_m = 3$  V. Measurements with these settings can thus be used in the frequency domain analysis, in order to observe how the model parameters vary with stress.

## 6.2 COMSOL Solid Mechanics Simulation Results

The results obtained from the COMSOL solid mechanics simulation can be seen in the plots of Figs. 6.3, 6.4, 6.5, and 6.6. In order to compare the above results on an equal basis,  $\partial\sigma/\partial x$  for each stress-depth profile was calculated, and plotted against surface stress. As can be seen from Fig. 6.7, in the case of the 1 mm specimen it is possible to achieve a steep stress-depth gradient over a small range of stress magnitudes. In the case of the 4 mm specimen, to achieve a steep gradient one has to achieve a significantly higher surface stress. Thus, more work is required to achieve the same gradient in a thick specimen than in a thin one. This distinction will prove useful in calibrating the Barkhausen data.

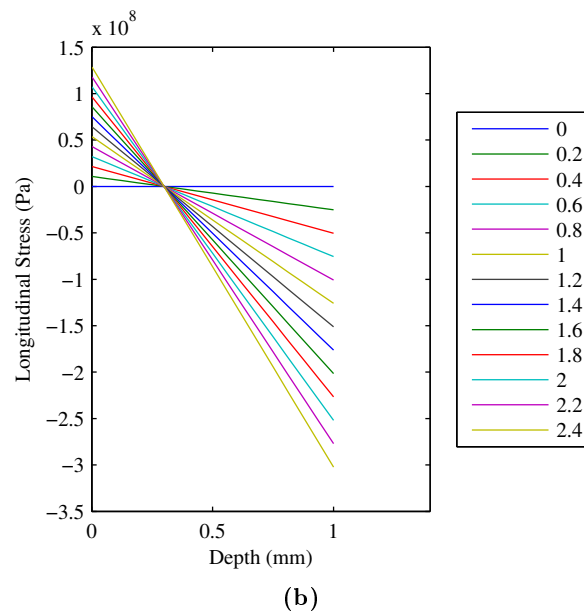
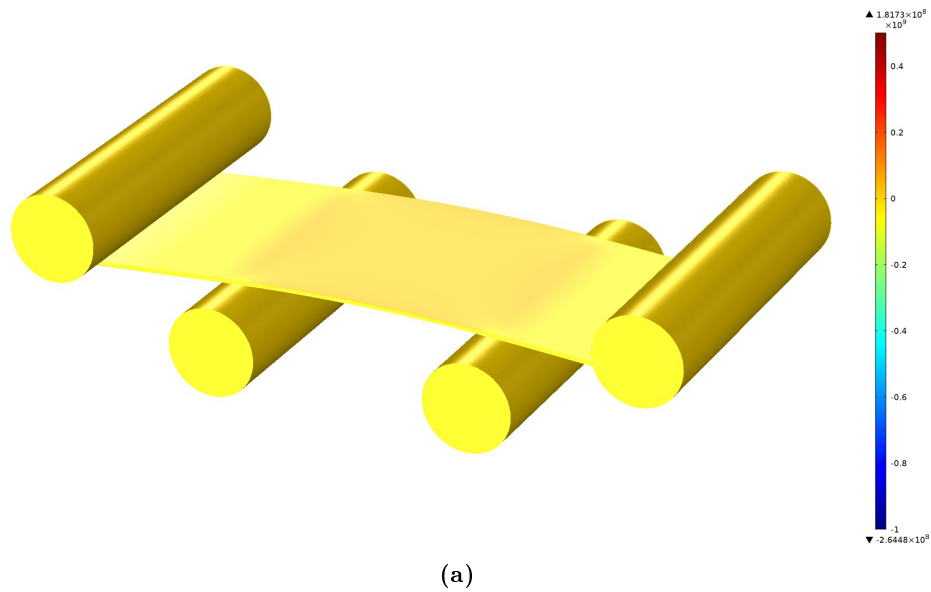


**Figure 6.3:** (a) Geometry of deformed specimen, showing the longitudinal stress at a displacement of 1.2 mm, and (b) stress-depth profile along geometrical center for the 1 mm thick specimen.



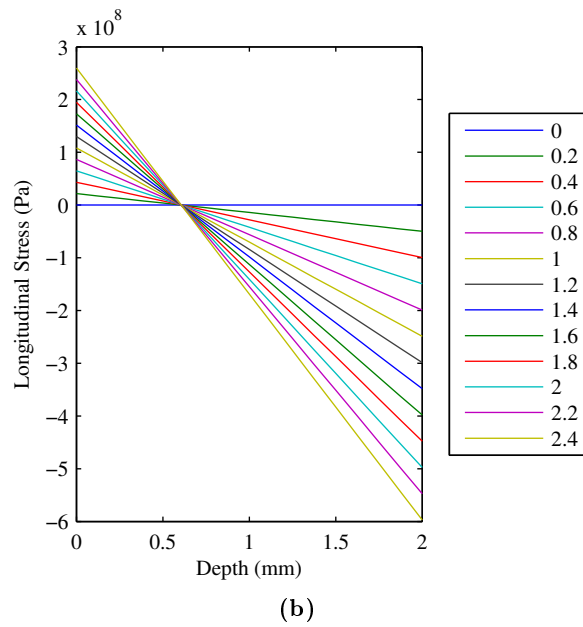
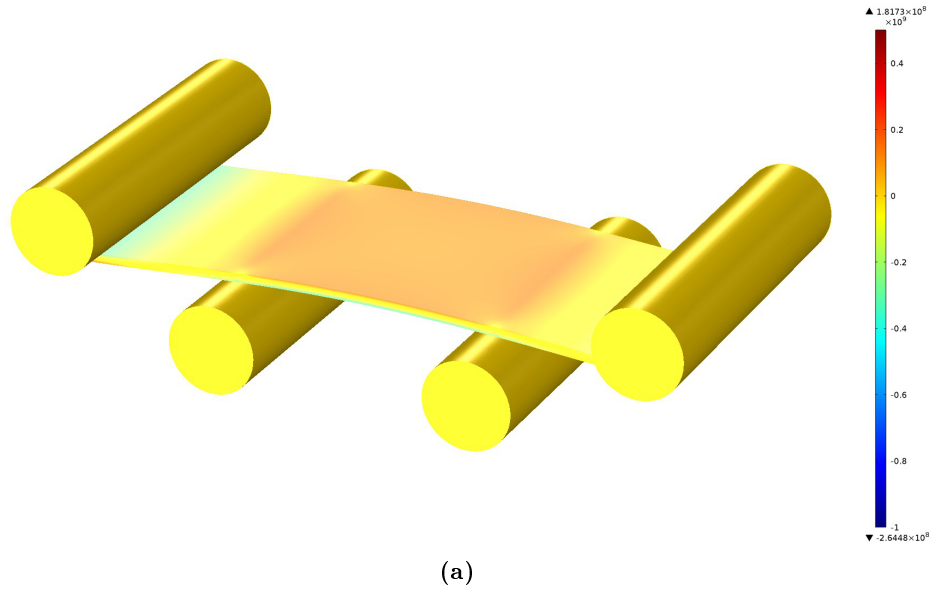


**Figure 6.4:** (a) Geometry of deformed specimen, showing the longitudinal stress at a displacement of 1.2 mm, and (b) stress-depth profile along geometrical center for the 2 mm thick specimen.

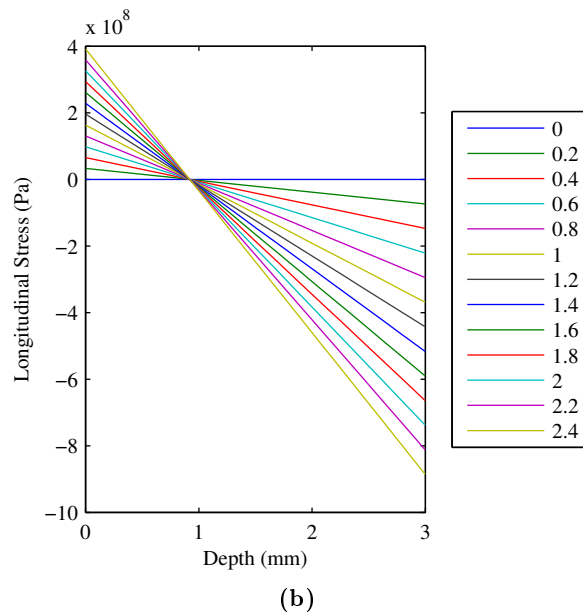
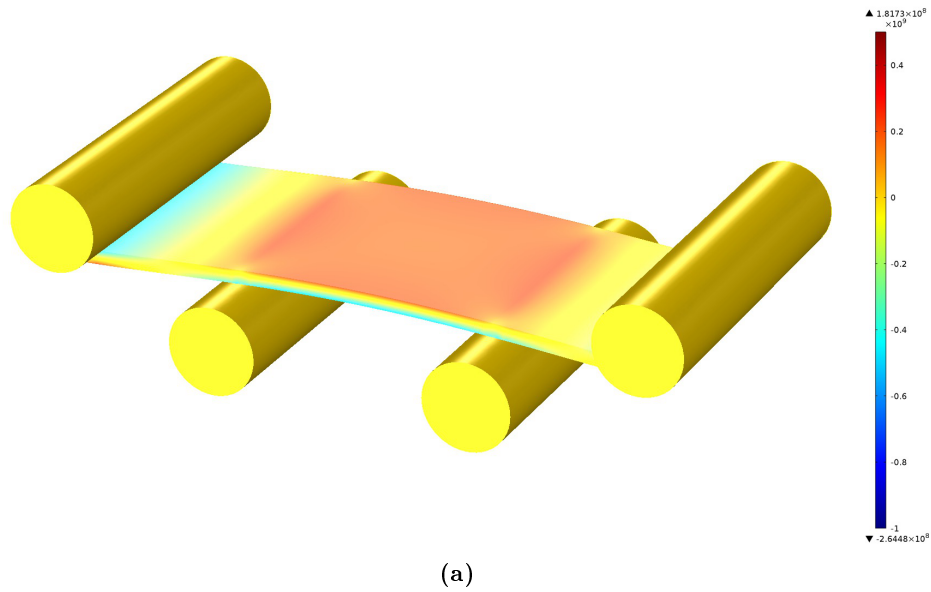


**Figure 6.5:** (a) Geometry of deformed specimen, showing the longitudinal stress at a displacement of 1.2 mm, and (b) stress-depth profile along geometrical center for the 3 mm thick specimen.

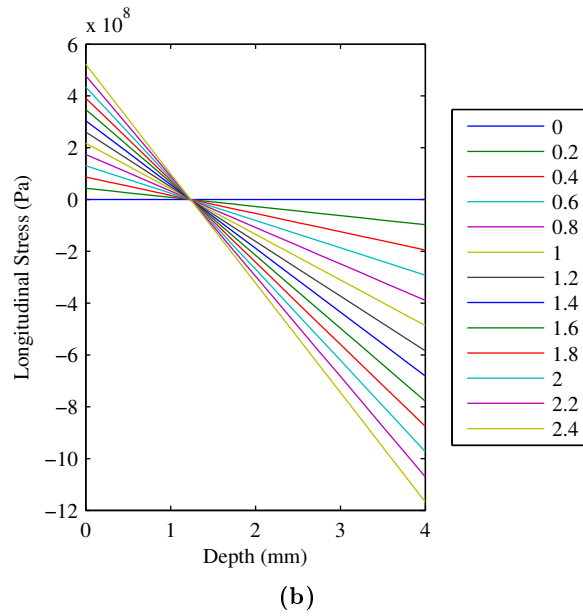
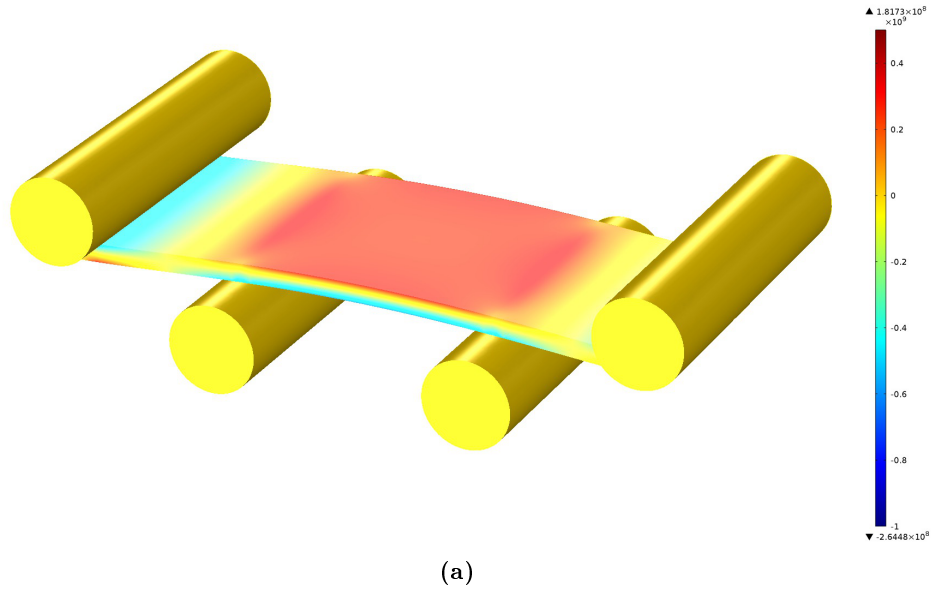


**Figure 6.6:** (a) Geometry of deformed specimen, showing the longitudinal stress at a displacement of 1.2 mm, and (b) stress-depth profile along geometrical center for the 4 mm thick specimen.

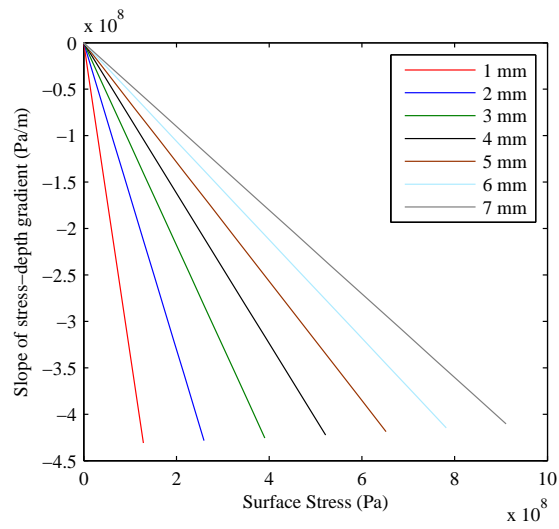


**Figure 6.7:** Slopes of stress-depth profiles  $\partial\sigma/\partial x$  along geometrical center for specimens of all thicknesses, plotted against surface stress.

## 6.3 Experimental results and analysis

### 6.3.1 Time Domain

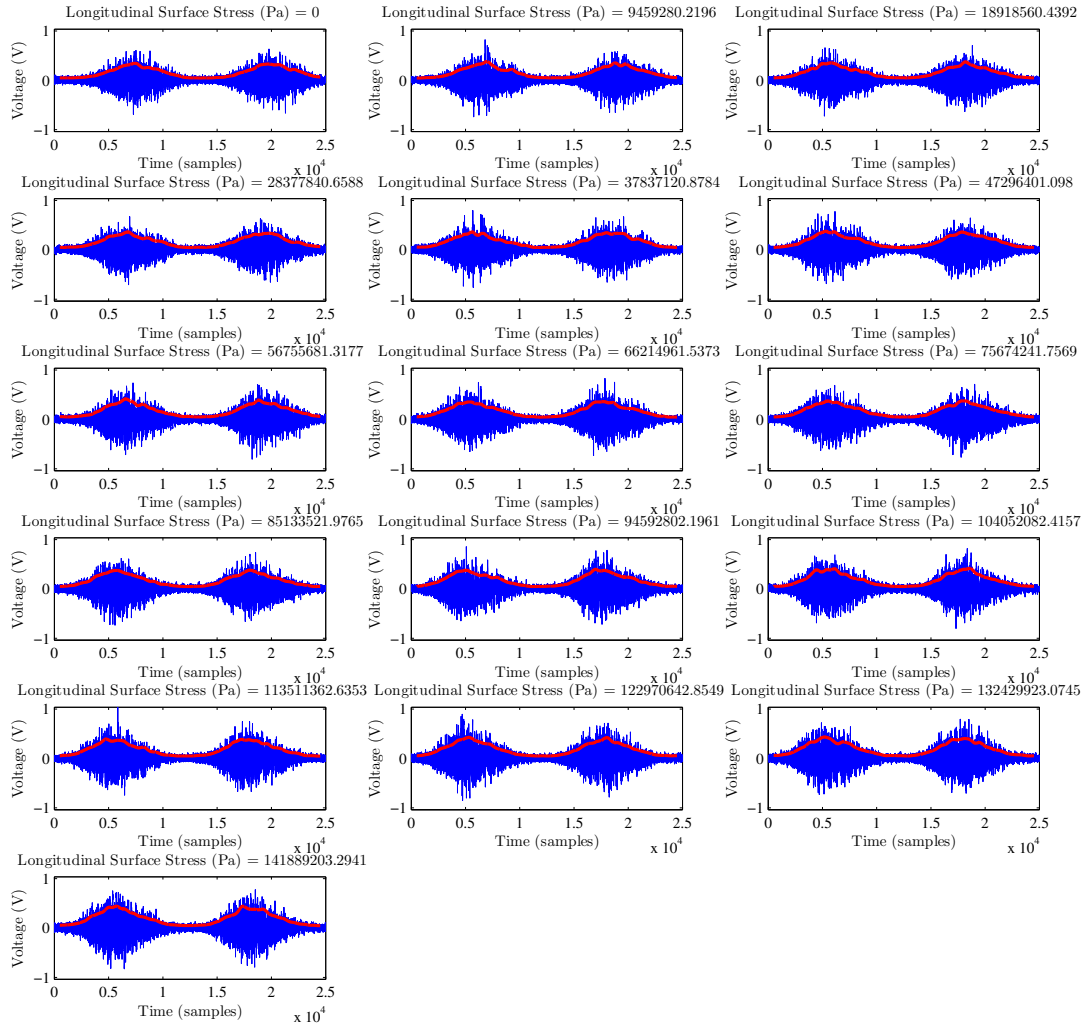


**Figure 6.8:** Raw Barkhausen waveforms obtained from the 1 mm thick specimen, for different magnitudes of deflection. The custom Barkhausen software is able to calculate ensemble average, waveform envelope (red) and automatically display all waveforms in an experiment, for visual comparison. As can be observed, the peak value increases with magnitude of deflection.

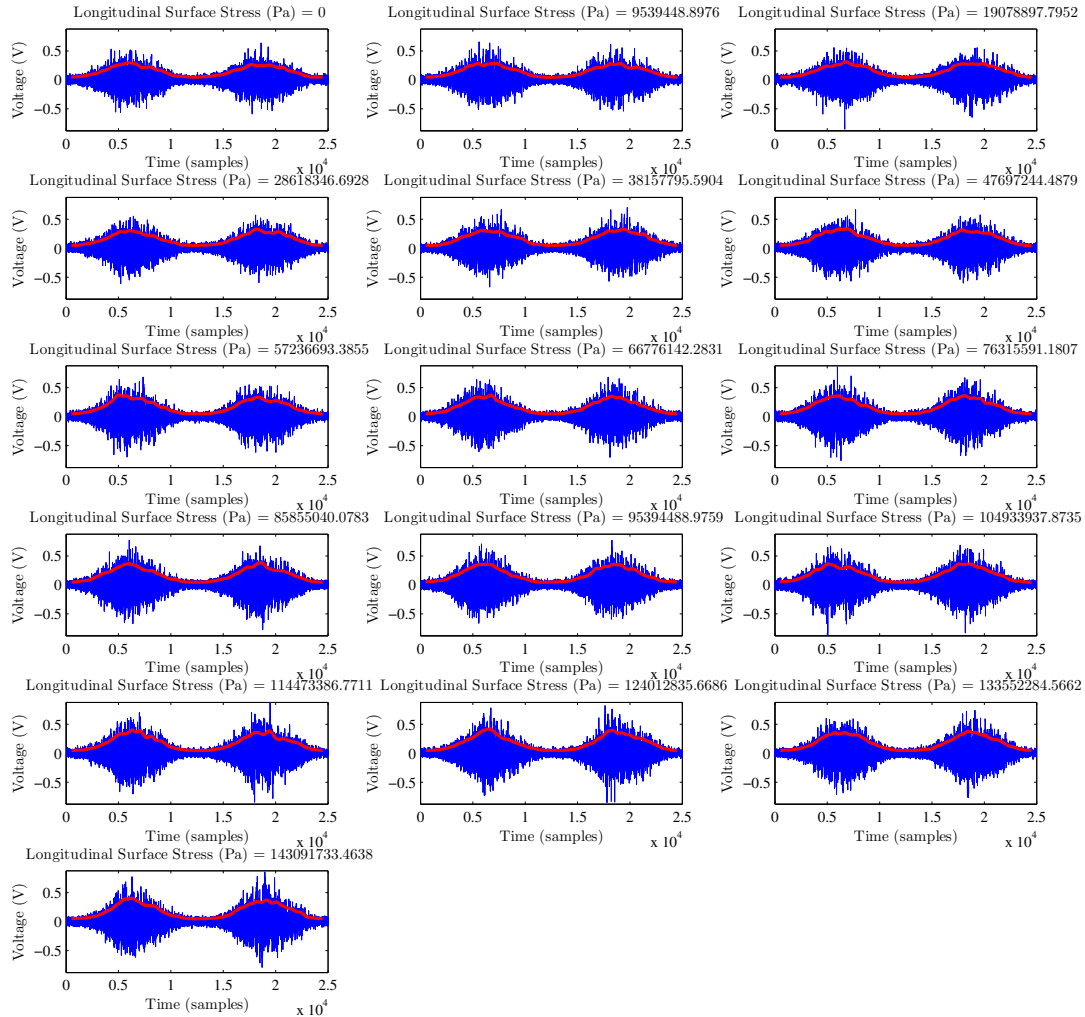


**Figure 6.9:** Raw Barkhausen waveforms obtained from the 1 mm thick specimen, for different magnitudes of deflection. The custom Barkhausen software is able to calculate ensemble average, waveform envelope (red) and automatically display all waveforms in an experiment, for visual comparison. As can be observed, the peak value increases with magnitude of deflection.

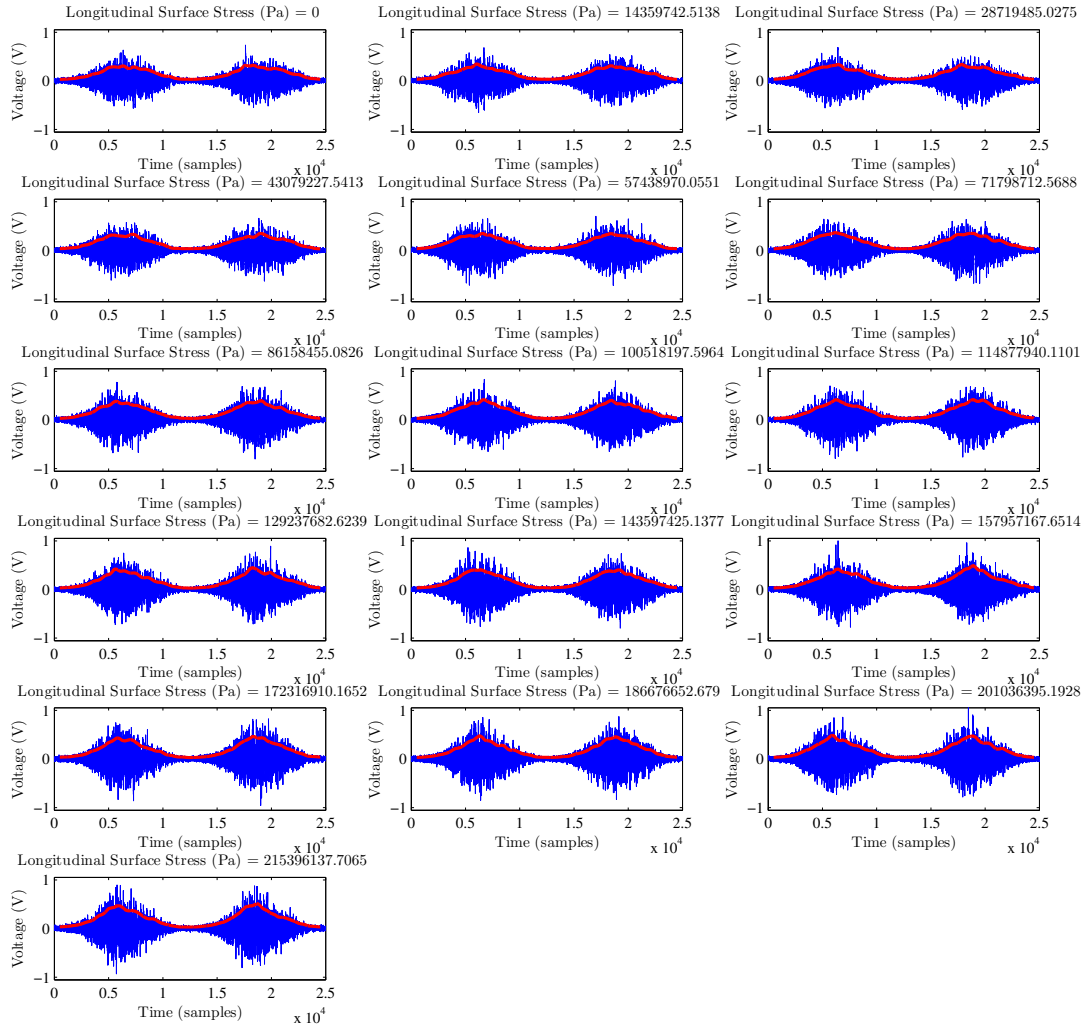


**Figure 6.10:** Raw Barkhausen waveforms obtained from the 1 mm thick specimen, for different magnitudes of deflection. The custom Barkhausen software is able to calculate ensemble average, waveform envelope (red) and automatically display all waveforms in an experiment, for visual comparison. As can be observed, the peak value increases with magnitude of deflection.

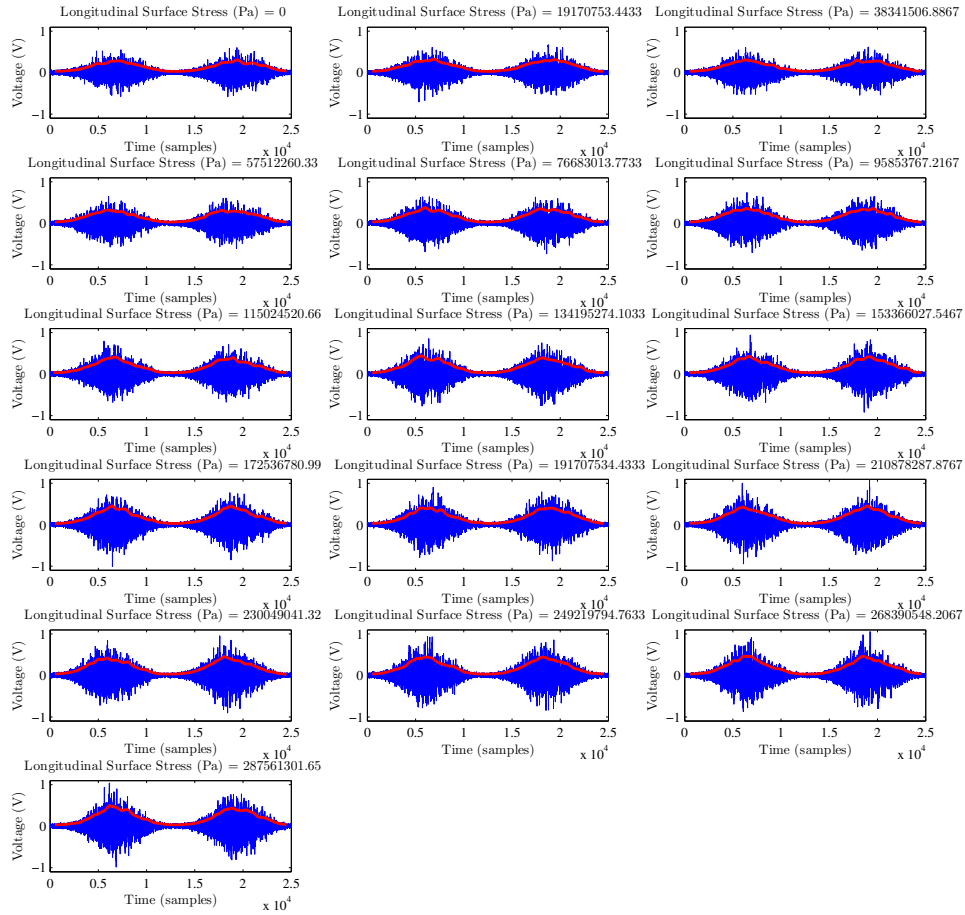


**Figure 6.11:** Raw Barkhausen waveforms obtained from the 1 mm thick specimen, for different magnitudes of deflection. The custom Barkhausen software is able to calculate ensemble average, waveform envelope (red) and automatically display all waveforms in an experiment, for visual comparison. As can be observed, the peak value increases with magnitude of deflection.



### 6.3.1.1 Time Domain Statistics

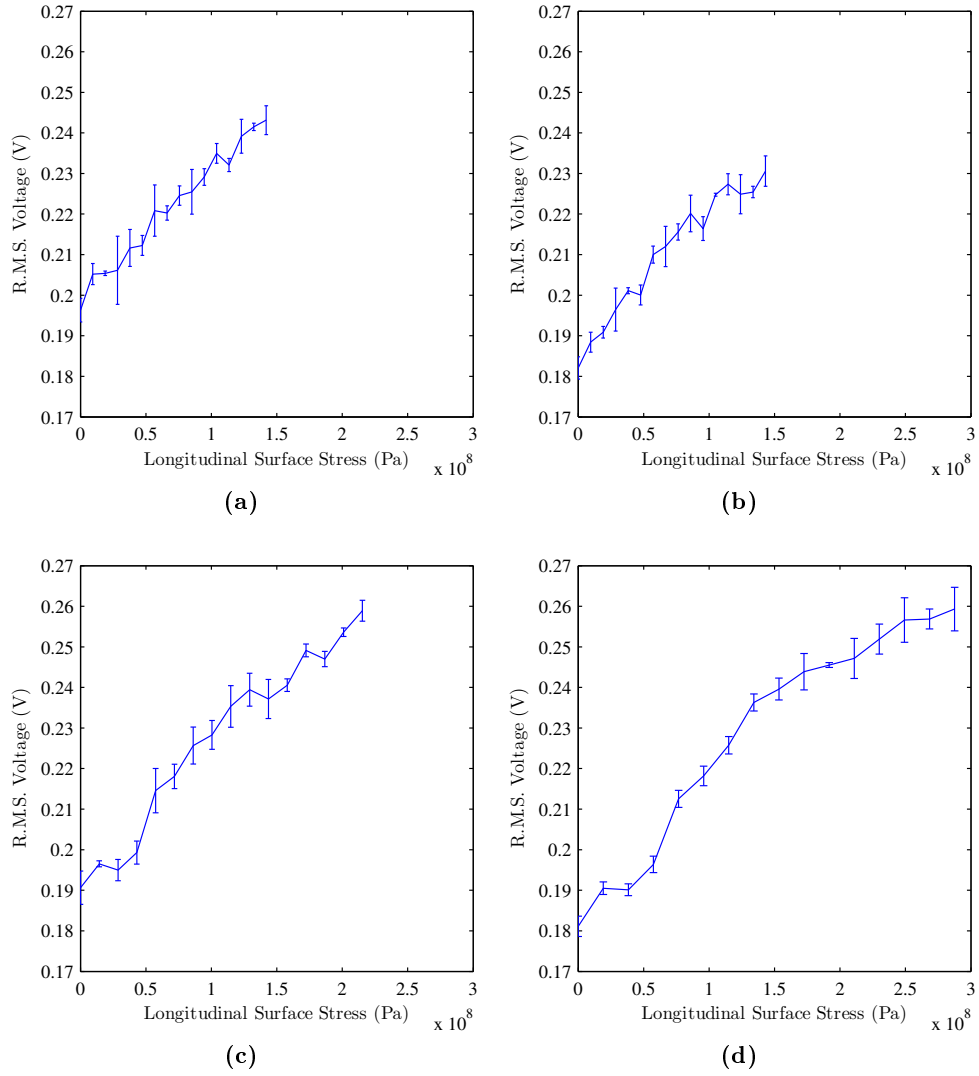
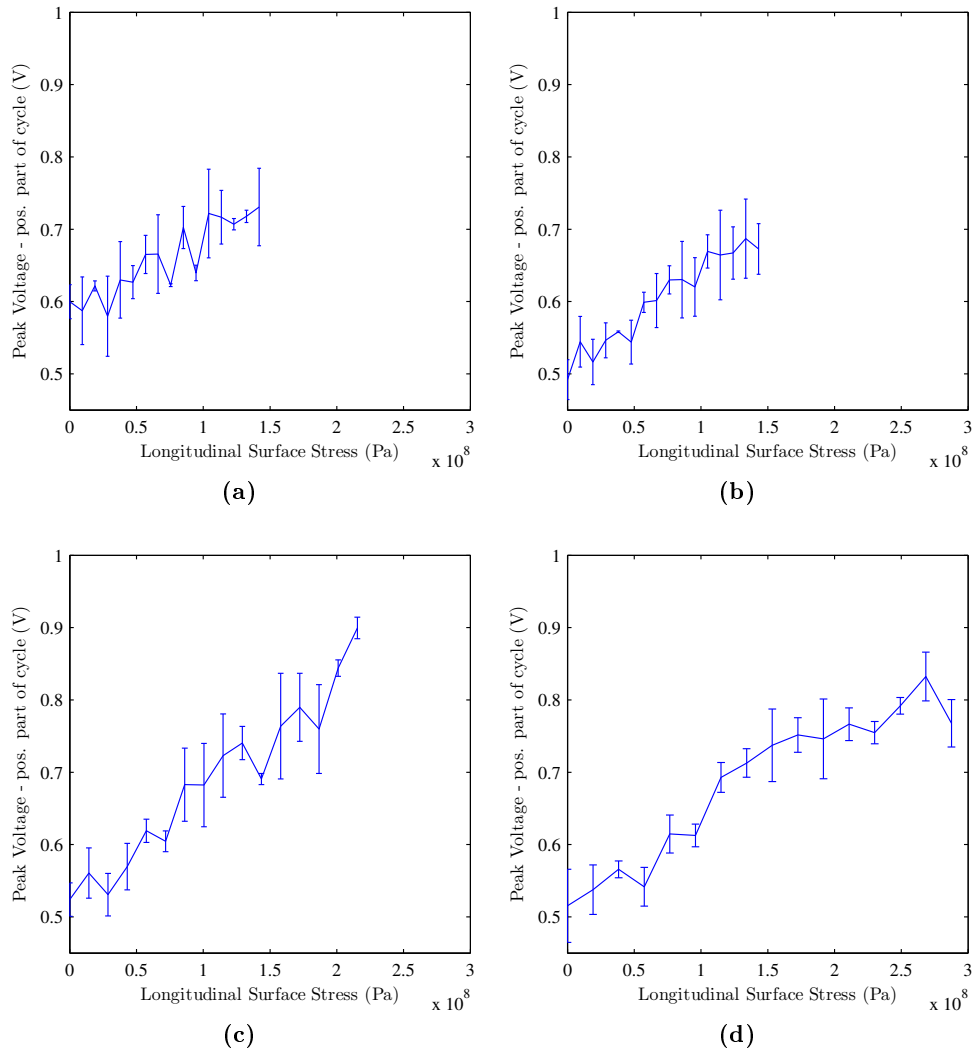
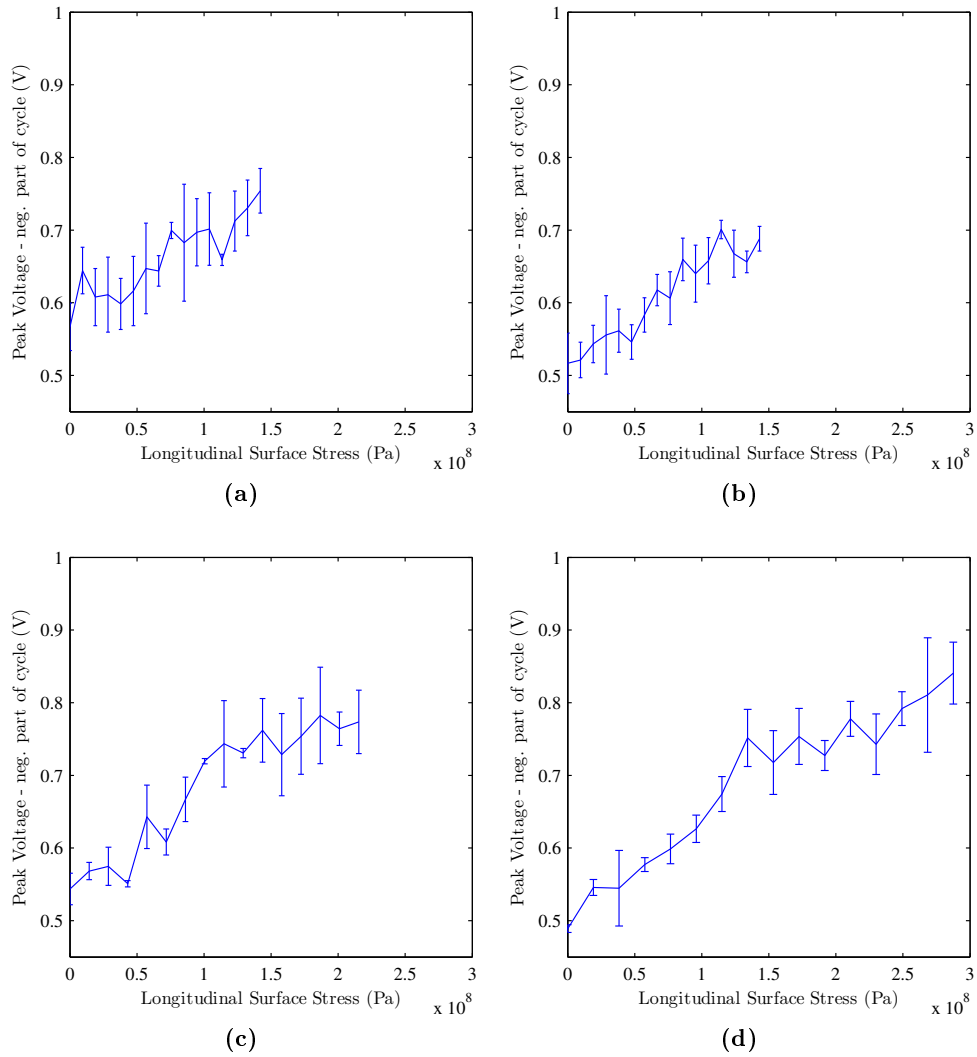


Figure 6.12: RMS voltage of (a) 1 mm, (b) 2 mm, (c) 3 mm, (d) 4 mm thick specimen.



**Figure 6.13:** Peak voltage in the positive part of the magnetizing cycle for (a) 1 mm, (b) 2 mm, (c) 3 mm, (d) 4 mm thick specimen.



**Figure 6.14:** Peak voltage in the negative part of the magnetizing cycle for (a) 1 mm, (b) 2 mm, (c) 3 mm, (d) 4 mm thick specimen.

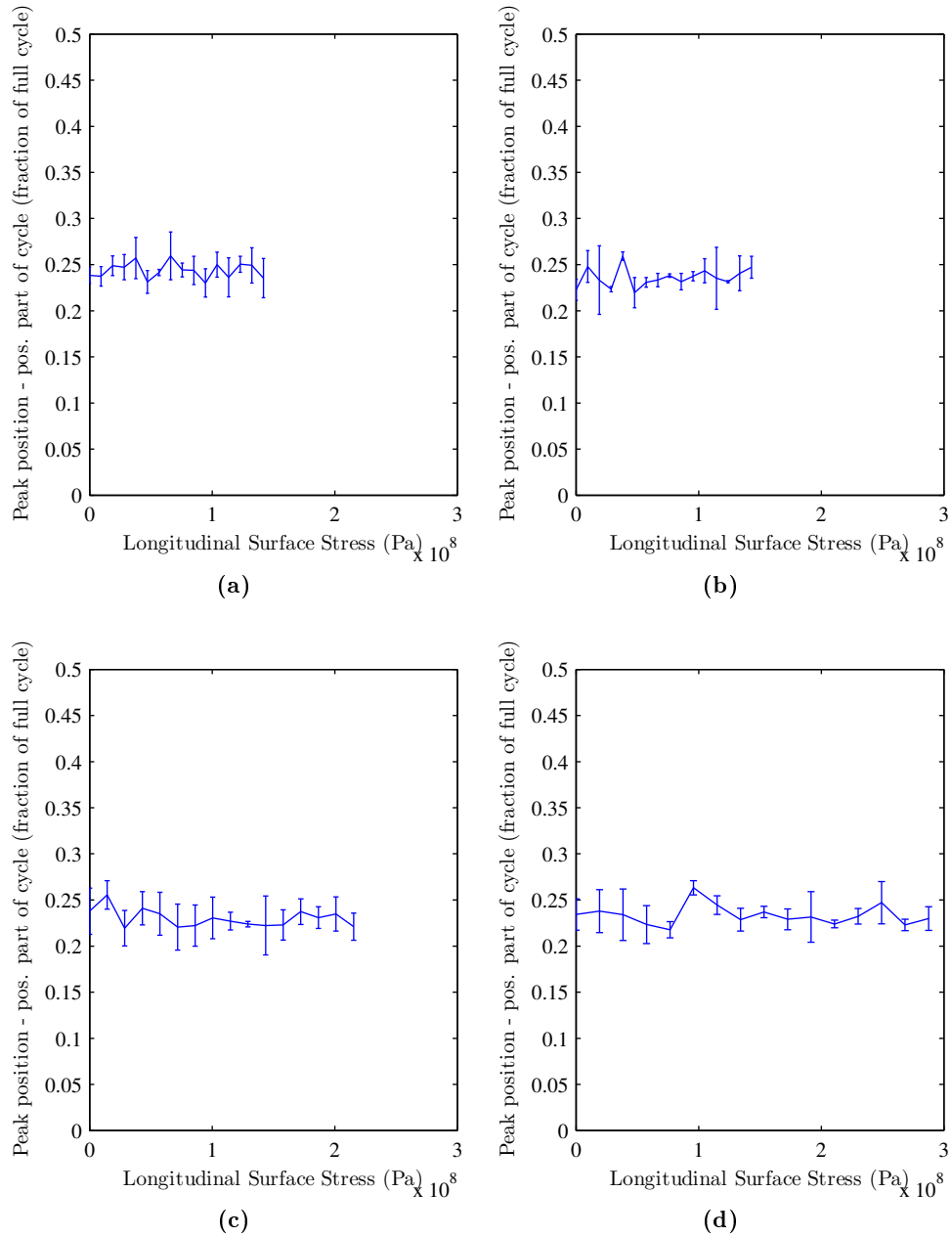


**Figure 6.15:** Position of peak voltage in the positive part of the magnetizing cycle for (a) 1 mm, (b) 2 mm, (c) 3 mm, (d) 4 mm thick specimen.

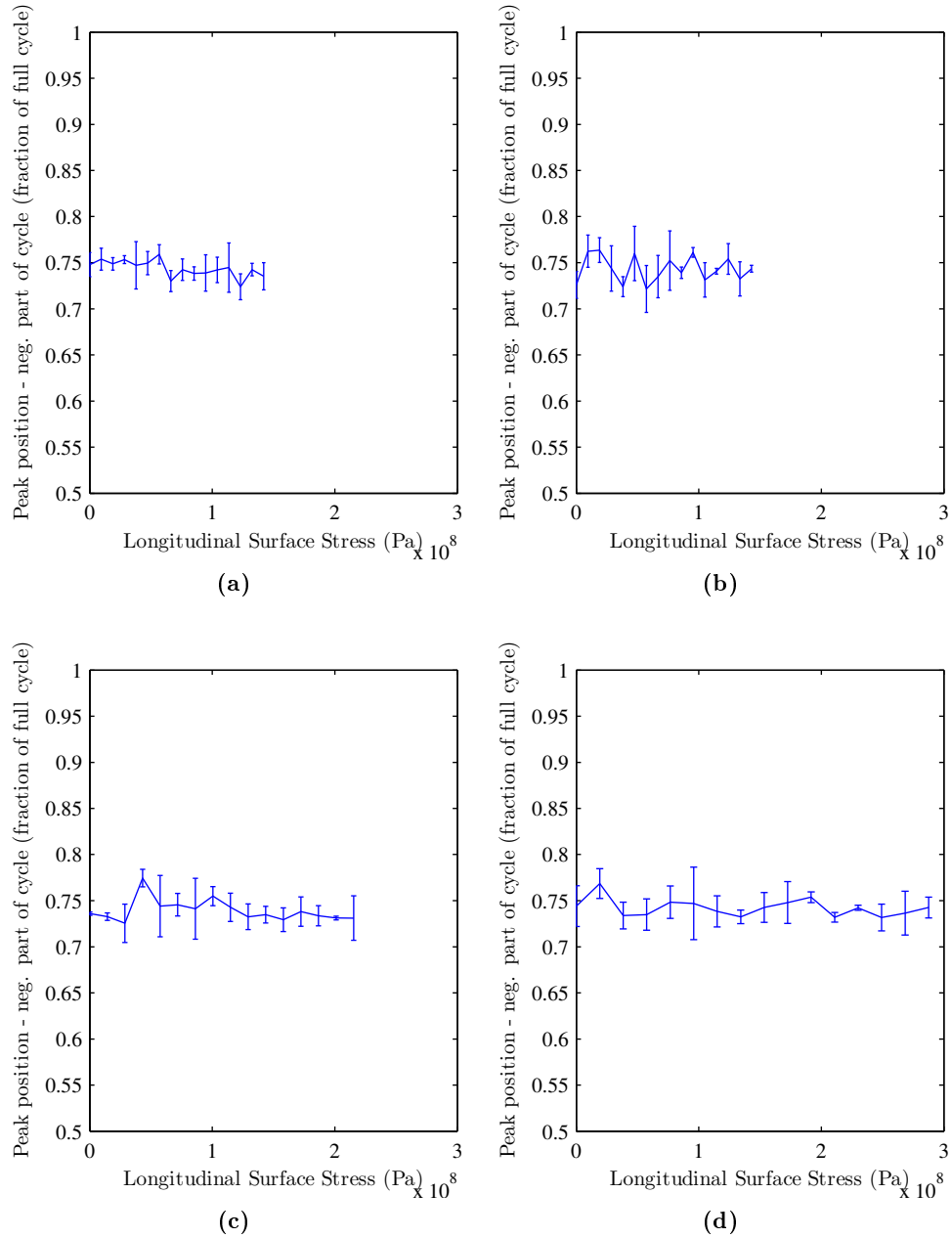


**Figure 6.16:** Position of peak voltage in the negative part of the magnetizing cycle for (a) 1 mm, (b) 2 mm, (c) 3 mm, (d) 4 mm thick specimen.

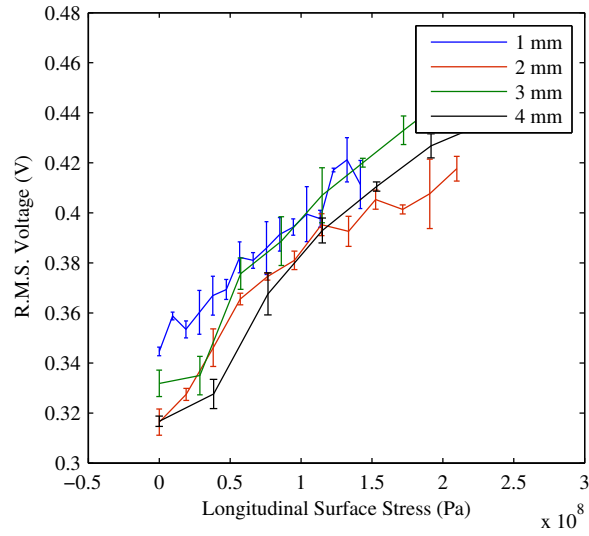


**Figure 6.17:** R.M.S. voltage for all specimens, plotted as a function of longitudinal surface stress.

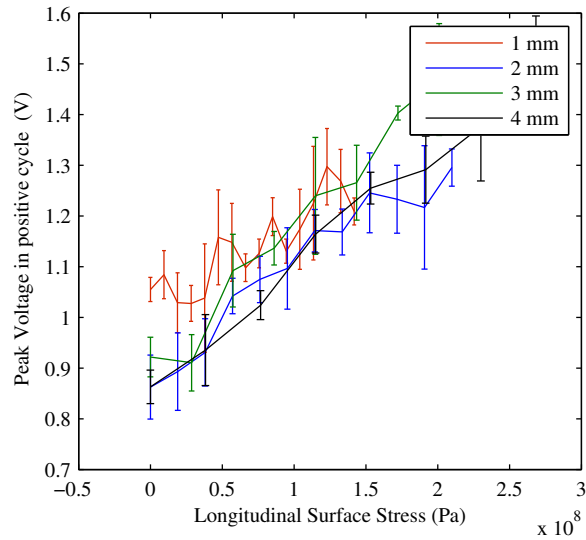


**Figure 6.18:** Peak voltage in the positive part of the magnetizing cycle, for all specimens, plotted as a function of longitudinal surface stress.

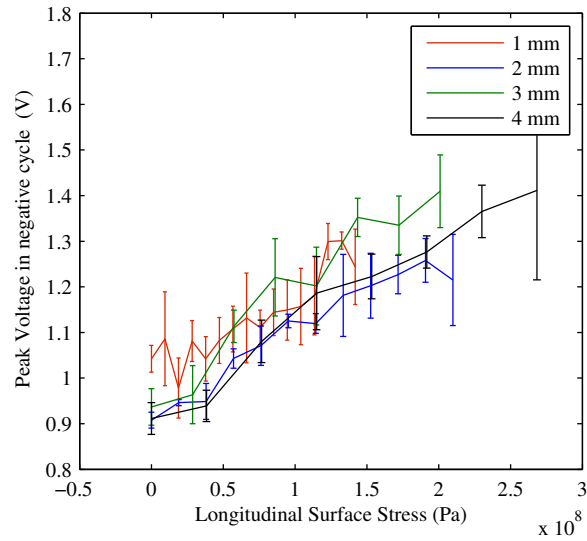


**Figure 6.19:** Peak voltage in the negative part of the magnetizing cycle, for all specimens, plotted as a function of longitudinal surface stress.

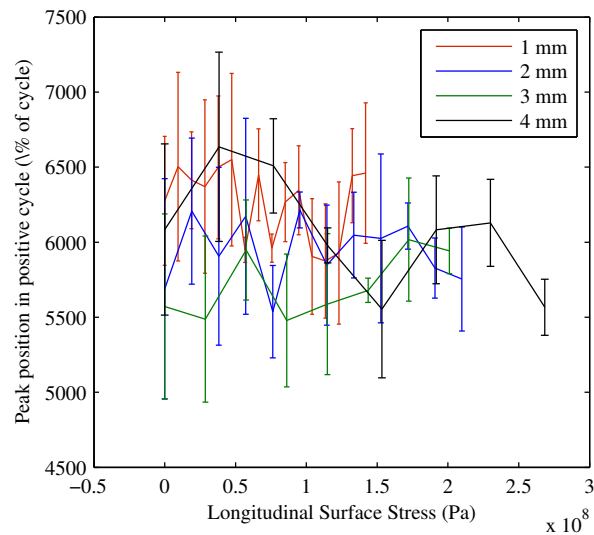


**Figure 6.20:** Peak position in the positive part of the magnetizing cycle, plotted as a function of longitudinal surface stress.

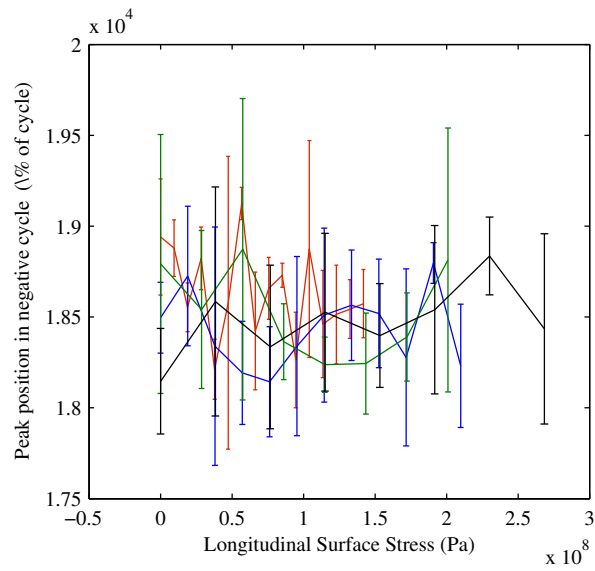


**Figure 6.21:** Peak position in the negative part of the magnetizing cycle, for all specimens, plotted as a function of longitudinal surface stress.



## 6.3.2 Frequency Domain

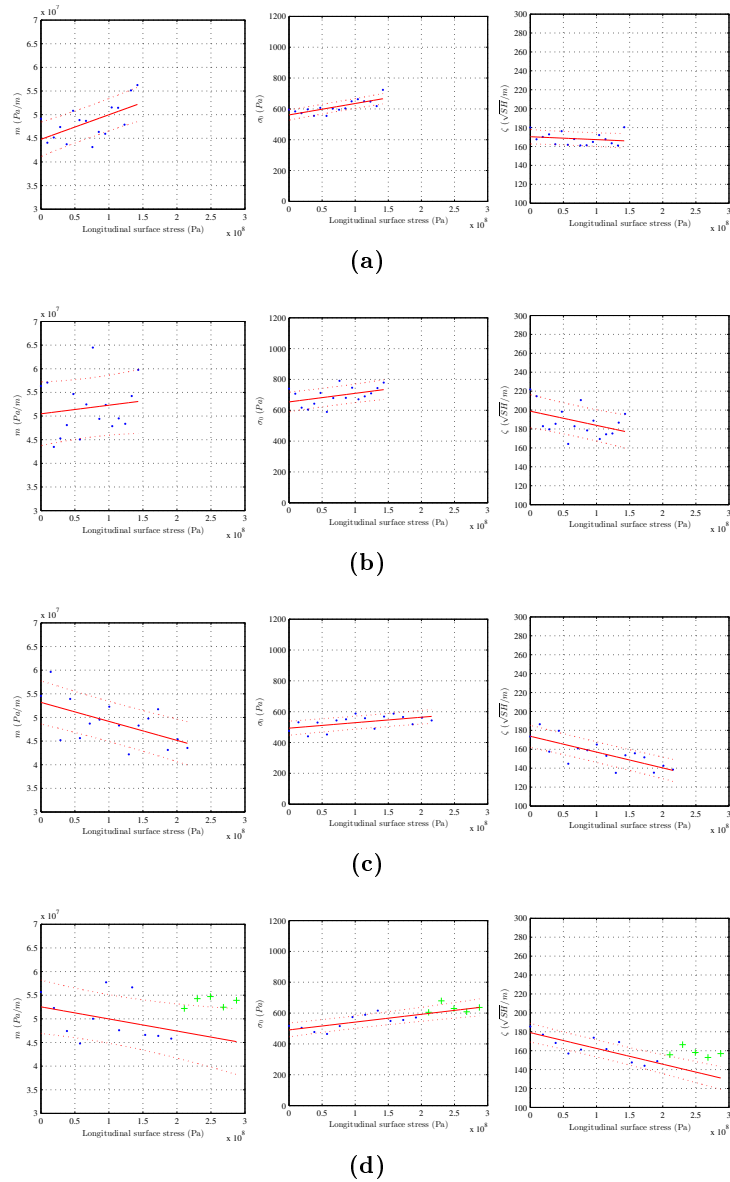


**Figure 6.22:** Results of fitting parameters  $m$ ,  $\sigma_0$  and  $\zeta$ . The figures (a), (b), (c), and (d) correspond to the 1, 2, 3 and 4 mm specimens respectively. The marked outliers in (d) were not considered in the fitting as they are above 200 MPa and approaching the plastic limit.

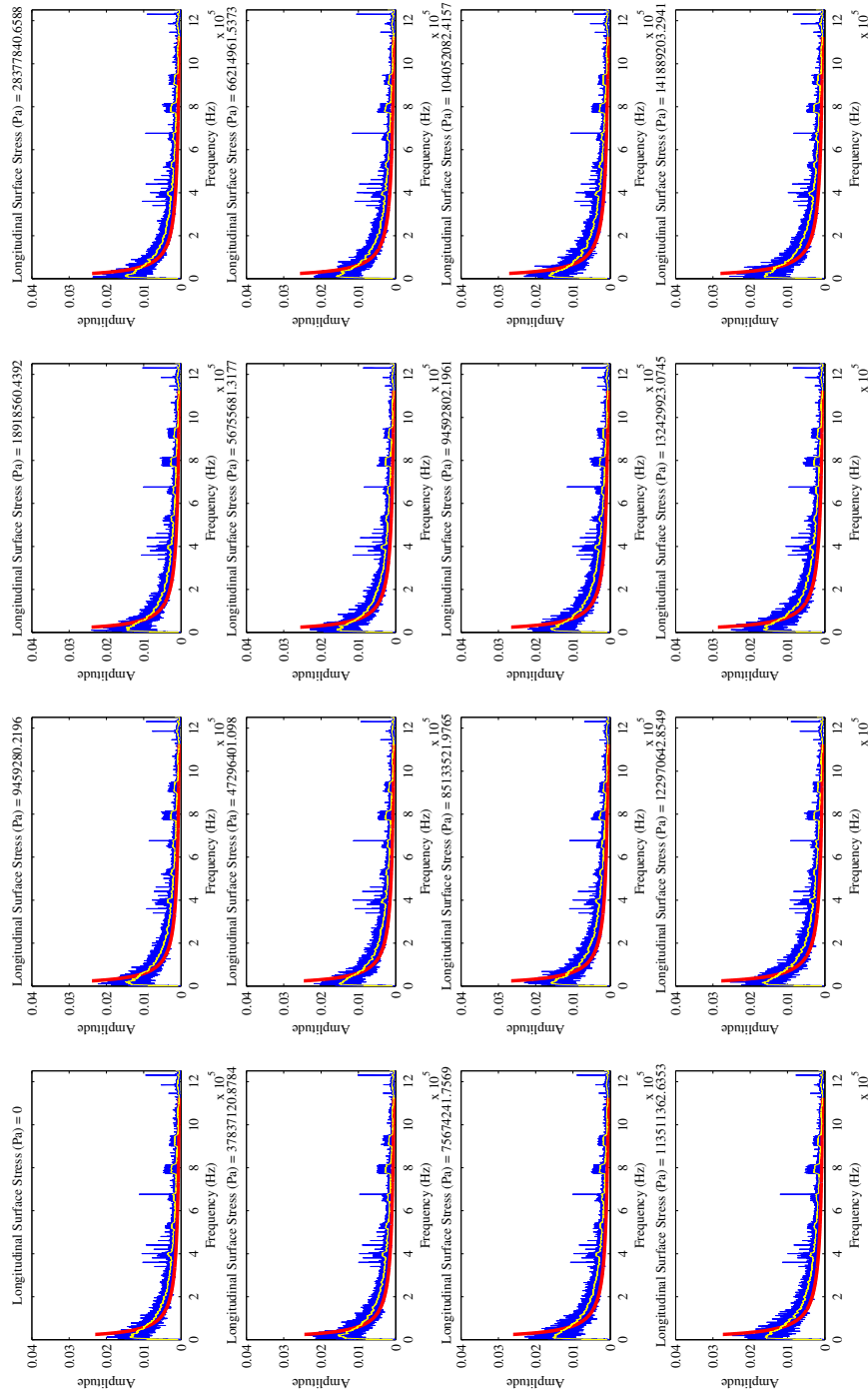


**Figure 6-23:** Typical Barkhausen spectra, obtained by taking the magnitude of the Fourier transform of two Barkhausen bursts (corresponding to a complete magnetizing cycle) and taking the ensemble average of the magnitudes over multiple trials of the same measurement. The yellow curve is a the result of a 100-point moving average smoothing algorithm (non-parametric), which was calculated for reference purposes. The red curve is the fit of the parametric model of (3.42) to the raw data (blue).

### 6.3.3 Discussion

#### 6.3.3.1 Time Domain

The plots of Fig. 6.12 indicate that on average, R.M.S. Barkhausen voltage increases with tensile elastic stress in materials such as steel with positive magnetostriction. While the rate of change of  $V_{RMS}$  with stress,  $\partial V_{RMS}/\partial\sigma$  is approximately equal for all specimens,  $V_{RMS}(\sigma = 0)$  varies, fluctuating from 0.18 V to 0.2 V; there is no clear variation with sample thickness, at least not a monotonic one. Given that a change in sample thickness brings about redistribution of the magnetic flux within the specimen, the excitation field at every different point within the sample may also change. The 1 mm specimen displays a higher Barkhausen amplitude, which is possibly a result of constraining the same magnetic flux to a smaller area, thereby increasing the total flux density flowing through that area, leading to more Barkhausen activity in that volumetric region.

By layering all the curves on one plot (Fig. 6.17), and comparing the 1 mm and 4 mm specimens, one can see that the Barkhausen amplitude in the region 0 – 150 MPa is different for  $\sigma = 0$  but starts to converge as the magnitude of bending is increased. For thicker specimens, the stress-depth gradient increases faster with bending magnitude, and since the RMS voltage represents a combination of depths, the effect of increasing stress in sub-surface regions is also seen.

Similar behaviour is observed in the plots of Figs. 6.13 and 6.14. An important observation to make is that in Figs. 6.16 and 6.15 the peak position slightly varies, depending on which part of the magnetizing cycle it occurs in. This can be explained by an asymmetry in the magnetization loop, which is determined by the magnetization history of the material.

#### 6.3.3.2 Frequency Domain

Fig. 6.23 indicates that even though the model for the Barkhausen frequency spectrum is based on first order approximations, it follows a monotonic decreasing and asymptotic trend with frequency, similar to the measured frequency spectrum. Fig. 6.22 indicates that the model has explanatory power, as the parameters change as a function of magnitude of bending.

- $\sigma_0$

The surface stress parameter  $\sigma_0$  is seen to increase with longitudinal surface stress, which is expected in the case of all specimens. Even though the units of the two axes are the same, this is because the scaling parameter  $a$  (of units V/Pa) has been omitted, and assumed to be equal to 1.

- $\zeta$

The parameter  $\zeta$  follows a decreasing trend, which according to the model theory indicates that the attenuation experienced by the Barkhausen emissions on their way to the surface is decreased. This has been seen before in the case of the constant stress along depth, where this parameter was not related to the permeability  $\mu$ , but to an effective permeability  $\mu_{eff}$ . This is necessary, as previous results indicate that permeability increases with tensile stress in a material with positive magnetostriction.

- $m$

The parameter  $m$  displays interesting behaviour. As mentioned before,  $m$  should be proportional to the stress-depth gradient and should therefore be negative, with increasing magnitude in the negative direction as a result of a bending moment being applied to the specimen. However, obtaining strictly negative values  $m$  with trends whose slopes correspond to Fig. 6.7 would be a matter of calibration, as it is the case with most Barkhausen parameters. However, this is thought to be a calibration issue; the desired feature is a monotonic variation in the slope of  $m$  vs. bending magnitude (or surface stress, its normalized equivalent). The slope of the trend changes significantly with changing specimen thickness; it goes from positive for the 1 mm specimen, to negative for the 4 mm specimen.

An important matter to note is the parameter bounds. These, if changed, can produce different results; this is a result of the system not being uniquely constrained. Actually, it is rarely the case that physical systems have unique solutions. It is necessary to manually constrain the solution using specific parameter bounds, since there may be no unique solution.

## CHAPTER 7. CONCLUSION AND FUTURE WORK

In this research, we developed a new model and signal processing technique to extract depth-dependent stress information from magnetic materials, by interpreting the information contained in Barkhausen signals. The ability of the model to extract depth-dependent information has been demonstrated by developing a parametric model that describes the frequency spectrum of Barkhausen emissions, as measured by an inductive Barkhausen sensor.

In the initial approach to the problem, a time-frequency method was developed [48, 49], where frequency- and time-domain data was used interchangeably to extract depth-dependent stress information. More specifically, the measured voltage signals were high-pass filtered at different cutoff frequencies in order to isolate the emissions in different volumetric regions within the specimen, followed by envelope peak detection in order to correlate the amplitude of those emissions with stress. The structure of the model implied the use of time domain statistics (peak), which made necessary the assumption that sharp cutoff of a signal occurs at the skin depth; the latter, combined with the inability to construct a universal stress-voltage calibration curve for all depths, partly invalidated the model and steered the research into a different direction, in which only frequency domain information was used.

The first stage of development of the frequency domain model focused on describing the Barkhausen frequency spectrum of a uniaxially stressed specimen [58]. Two stress-related parameters were used to express the Barkhausen frequency spectrum integrated over a depth range below the surface. The results showed correlation between stress and these two parameters, of which one is proportional to average Barkhausen activity at each infinitesimal depth, and the other controls the decay of the spectrum with frequency. This model, having the ability to describe uniaxial stress (the longitudinal component of which remains constant as depth is traversed) in the frequency domain can be used as a calibration for evaluating the stress-depth

gradient.

The second stage of development of the frequency domain model focused on describing the Barkhausen frequency spectrum of specimens with stress-depth gradients. In this case, three stress-related parameters (two of which were incorporated in the previous model) were used to express the Barkhausen frequency spectrum integrated over a depth range below the surface. The new parameter was used to describe the slope of the stress-depth gradient. The results showed correlation between stress due to bending (which induced a linear stress-depth gradient) and the three model parameters.

Since this is an interdisciplinary research, future work may follow different routes. Also, the same interdisciplinary nature of the present work prevented delving very deeply into some aspects. While certain ideas were explored, they were not deemed to be a priority and their in-depth analysis was discontinued shortly after their inception. Of course, they may become part of future research; for this reason, they are being presented in the following list, as well as in the Appendix.

- From the materials viewpoint, a steel with higher magnetostriction would possibly increase the quality of fit of the slopes seen in Fig. 6.22, as more Barkhausen activity would occur for the same magnitude of bending, leading to a higher signal-to-noise ratio.
- From the measurement viewpoint, an important contribution to the measured spectrum is the sensor frequency response. While the sensor is perceived as a constant when conducting a set of measurements, its frequency spectrum is nevertheless part of the measurement, such that the total measured spectrum is a linear combination of the Barkhausen spectrum originating in the material, and the frequency spectrum of the Barkhausen noise originating in the sensing ferrite itself as well as some resonance due to sensing coil, which is essentially the LRC circuit:

$$V_{meas}(\omega) = V_{MBN,material}(\omega) + V_{MBN,sensor}(\omega) + V_{circuit}(\omega) \quad (7.1)$$

A more in depth analysis of the sensor frequency response is presented in the Appendix.

- Another possibility, relating to the measurement, would be a sensor array configuration, where measurements are conducted by an array of sensors in response to excitation by a single electromagnet. In other applications, such as ultrasonics, the deterministic nature of signals allows the exploitation of the signal phase to spatially locate defects within a material (i.e. phased arrays). The present Barkhausen model can be extended to incorporate a phase parameter, which implies there the phase velocity is a function of frequency, giving rise to dispersion.
- It would be interesting to explore the problem from a linear algebra perspective, where a system of linear equations  $\mathbf{Ax} = \mathbf{b}$  is set up to represent the problem. This would provide more insight in terms of when the linear system yields no solution, one solution, or infinite solutions. This is partly explored in the Appendix.

## APPENDIX A. ADDITIONAL MATERIAL

### Estimating the sensor circuit frequency response

The objective of this section is to provide a framework for estimating frequency response of an inductive sensor that is used for Barkhausen measurements. The transfer function includes the sensing coil circuit in combination with the transmission line.

- Coil circuit:

The band of the Barkhausen frequency spectrum we are interested in measuring, does not extend beyond 2 MHz. This range is well below the series resonant frequency (where  $X_L = X_C$ ) for most inductors, so the three element inductor models of Fig. A.1 should suffice. The equivalent circuit for an inductor with an initial current through it, is a series voltage source, as in Fig. A.2. This is our model of the Barkhausen sensor.

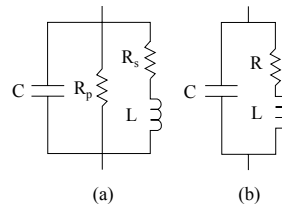


**Figure A.1:** Equivalent circuits for inductors, including parasitic resistance and capacitance. (a) Circuit for inductor with ferromagnetic core, with resistance  $R_p$  accounting for the hysteretic loss component. (b) Circuit for air-core inductor.

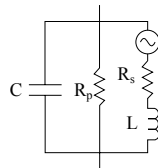


**Figure A.2:** Equivalent circuit for Barkhausen sensor.

The following conventions will be used:



$$X_L = \omega L \tag{A.1}$$

and

$$X_C = \frac{1}{\omega C} \tag{A.2}$$

The transfer function ( $V_o/V_i$ ) will be:

$$\frac{V_o}{V_i} = \frac{\frac{-jX_C R_p}{R_p - jX_C}}{R_s + jX_L - \frac{jX_C R_p}{R_p - jX_C}} \tag{A.3}$$

An LCR meter can be used to characterize the sensor circuit. There are two modes of impedance measurement, one for series and one for parallel equivalent circuits, as depicted in Fig. A.3. Since we are operating within RF frequencies, but below 100 MHz, the medium impedance case applies best, as seen in Fig. A.4, such that the parallel circuit model can be used, as previously stated.

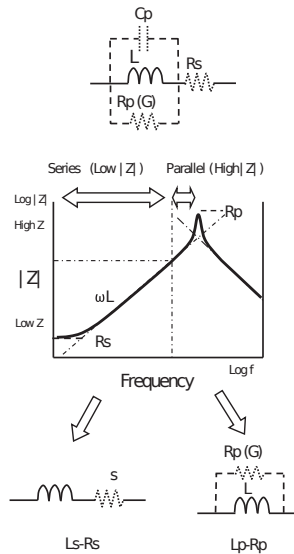


**Figure A.3:** Equivalent circuits for inductor LCR measurement [59].

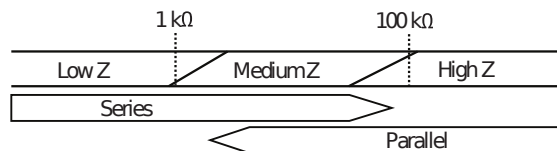


**Figure A.4:** Impedance criteria [59].

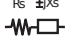

The input impedance will be equal to

$$Z_{in} = \frac{(R_s + jX_L) \left( \frac{-jX_C R_p}{R_p - jX_C} \right)}{R_s + jX_L - \frac{-jX_C R_p}{R_p - jX_C}} \quad (\text{A.4})$$

And the input admittance is defined as

$$Y_{in} = \frac{1}{Z_{in}} = G + jB \quad (\text{A.5})$$

The input admittance can be measured by using an LCR meter. The latter should be set to parallel mode. The auto balancing bridge method should be used [59]. After having measured the admittance, individual circuit component values can be deduced by using the relationships in Fig. A.5. Note that in the parallel case, sometimes  $R_s$  is taken to be zero.

Series mode	Parallel mode
 $ Z  = \sqrt{R_s^2 + X_s^2}$ $q = \tan^{-1}(X_s / R_s)$	 $ Y  = \sqrt{G_p^2 + B_p^2}$ $q = \tan^{-1}(B_p / G_p)$
Rs: Series resistance Xs: Series reactance ( $X_L = \omega L_s$ , $X_C = -1/(\omega C_s)$ ) Ls: Series inductance ( $=X_L / \omega$ ) Cs: Series capacitance ( $=-1/(\omega X_C)$ ) D: Dissipation factor ( $=R_s / X_s = R_s / (\omega L_s)$ or $\omega C_s R_s$ ) Q: Quality factor ( $=X_s / R_s = \omega L_s / R_s$ or $1/(\omega C_s R_s)$ )	Gp: Parallel conductance ( $=1/R_p$ ) Bp: Parallel susceptance ( $B_c = \omega C_p$ , $B_L = -1/(\omega L_p)$ ) Lp: Parallel inductance ( $=-1/(\omega B_L)$ ) Cp: Parallel capacitance ( $=B_c / \omega$ ) D: Dissipation factor ( $=G_p / B_p = G_p / (\omega C_p)$ $=1/(\omega C_p R_p)$ or $\omega L_p G_p = \omega L_p / R_p$ ) Q: Quality factor ( $=B_p / G_p = \omega C_p / G_p$ $=\omega C_p R_p$ or $1/(\omega L_p G_p) = R_p / (\omega L_p)$ )

**Figure A.5:** Definitions of impedance parameters for series and parallel modes [59].

After component values have been calculated at multiple frequencies between  $\sim 10$  kHz and 2 MHz, provided that in this range they remain relatively constant, they can be substituted into (A.3) and the frequency response of the sensor circuit can be plotted.

- Transmission line circuit:

The equivalent circuit of a twisted pair wire transmission line is usually modelled as in Fig. A.6:

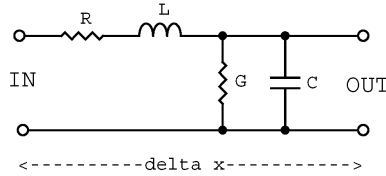


**Figure A.6:** Transmission line equivalent circuit [60].

The quantities  $R$ ,  $L$ ,  $C$  and  $G$  are per unit length, since the above model is a lumped representation. By inspection of the cable datasheet, these quantities can be obtained.

- Loading circuit:

In the case of the Stresstech® device, it is not possible to easily obtain this information, as the technology is proprietary. For our custom made Barkhausen measurement system however, it is easier to obtain this information. More specifically, the NI X-series 6366 device, which digitizes the Barkhausen signal, has an input impedance of  $100\text{ G}\Omega$  in parallel with a  $10\text{ pF}$  capacitance, from AI+ to ground, and the same from AI- to ground (information obtained from the NI X-Series 6366 manual). In differential mode, the input impedance is approximately  $Z/2$ .

It can be seen that obtaining the "true" frequency spectrum of the Barkhausen emissions, meaning the spectrum of the Barkhausen activity after accounting for measurement artifacts, is non-trivial. However, in this research it was assumed that as long as the measurement system remains a constant, knowledge of the exact frequency spectrum of the system is not crucial.

### Separating emissions emanating from $N$ discrete depths

This section takes a linear algebra approach to the inverse problem of separating Barkhausen spectra, by beginning with a very simple model. To start off, we will assume that Barkhausen emissions occur at two discrete distances from the point of measurement,  $x_1$  and  $x_2$ . Assuming flat emission spectra at the origin (white noise), the resulting frequency spectrum at the point of measurement will be

$$V_i(\omega) = V_1 f(x_1, \omega) + V_2 f(x_2, \omega) \quad (\text{A.6})$$

where  $f(x, \omega) = e^{-\zeta x \sqrt{\omega}}$ . If  $x_1$  and  $x_2$  are known, and we are considering only two frequencies in the spectrum, a system of linear equations can be set up in order to determine  $V_1$  and  $V_2$ , such that

$$V_i(\omega) = V_1 f(x_1, \omega) + V_2 f(x_2, \omega) \quad (\text{A.7})$$

$$\begin{bmatrix} V_i(1) \\ V_i(2) \end{bmatrix} = \begin{bmatrix} f(x_1, 1) & f(x_2, 1) \\ f(x_1, 2) & f(x_2, 2) \end{bmatrix} \begin{bmatrix} V_1 \\ V_2 \end{bmatrix}, \quad (\text{A.8})$$

in which system

$$\begin{vmatrix} f(x_1, 1) & f(x_2, 1) \\ f(x_1, 2) & f(x_2, 2) \end{vmatrix} = (e^{-\zeta x_1} e^{-\zeta x_2 \sqrt{2}}) - (e^{-\zeta x_1 \sqrt{2}} e^{-\zeta x_2}) \neq 0 \quad (\text{A.9})$$

meaning that the matrix is non-singular (and therefore invertible), such that

$$\begin{bmatrix} V_1 \\ V_2 \end{bmatrix} = \begin{bmatrix} f(x_1, 1) & f(x_2, 1) \\ f(x_1, 2) & f(x_2, 2) \end{bmatrix}^{-1} \begin{bmatrix} V_i(1) \\ V_i(2) \end{bmatrix}. \quad (\text{A.10})$$

For an arbitrary number of constituent spectra, the system of equations will be

$$V_i(\omega) = \sum_{i=0}^N V_i f(x_i, \omega) \quad (\text{A.11})$$

and the corresponding solution given by

$$\begin{bmatrix} V_1 \\ V_2 \\ \vdots \\ V_i \end{bmatrix} = \begin{bmatrix} f(x_1, 1) & f(x_2, 1) & \dots & f(x_i, 1) \\ f(x_1, 2) & f(x_2, 2) & \dots & f(x_i, 2) \\ \vdots & \vdots & \ddots & \vdots \\ f(x_1, \omega_N) & f(x_2, \omega_N) & \dots & f(x_i, \omega_N) \end{bmatrix}^{-1} \begin{bmatrix} V_t(1) \\ V_t(2) \\ \vdots \\ V_t(\omega_N) \end{bmatrix} \quad (\text{A.12})$$

where  $\omega_N$  is the Nyquist frequency. As long as there are  $N$  equations and  $N$  unknowns, yielding an  $N \times N$  coefficient matrix, this system will have a unique solution. A simulation was constructed to simulate white noise signals attenuated exponentially as they travel to the surface. The procedure comprised of the following steps:

1. Simulation of exponentially attenuating white noise spectra, that add up at the point of measurement to produce the measured spectrum. Variation of the amplitude of the spectrum at the origin for each depth of emission, in order to simulate the effect of stress. The simulation parameters can be seen in Table A.1.
2. Usage of the system of equations in (A.12) to calculate the spectrum amplitudes  $V_1, V_2, \dots, V_i$ .

**Table A.1:** Simulation parameters

No. of discrete depths	5, 10 and 15
Separation	20 $\mu m$
$\zeta$	$\sim 13 \sqrt{SH}/m$
$V_i$ profile	Increasing amplitude (span of 10 V)
Start frequency	100 kHz
Stop frequency	1000 kHz
Frequency spacing	5, 10 and 15 linear steps

The result of the simulation can be seen in Figure A.7.

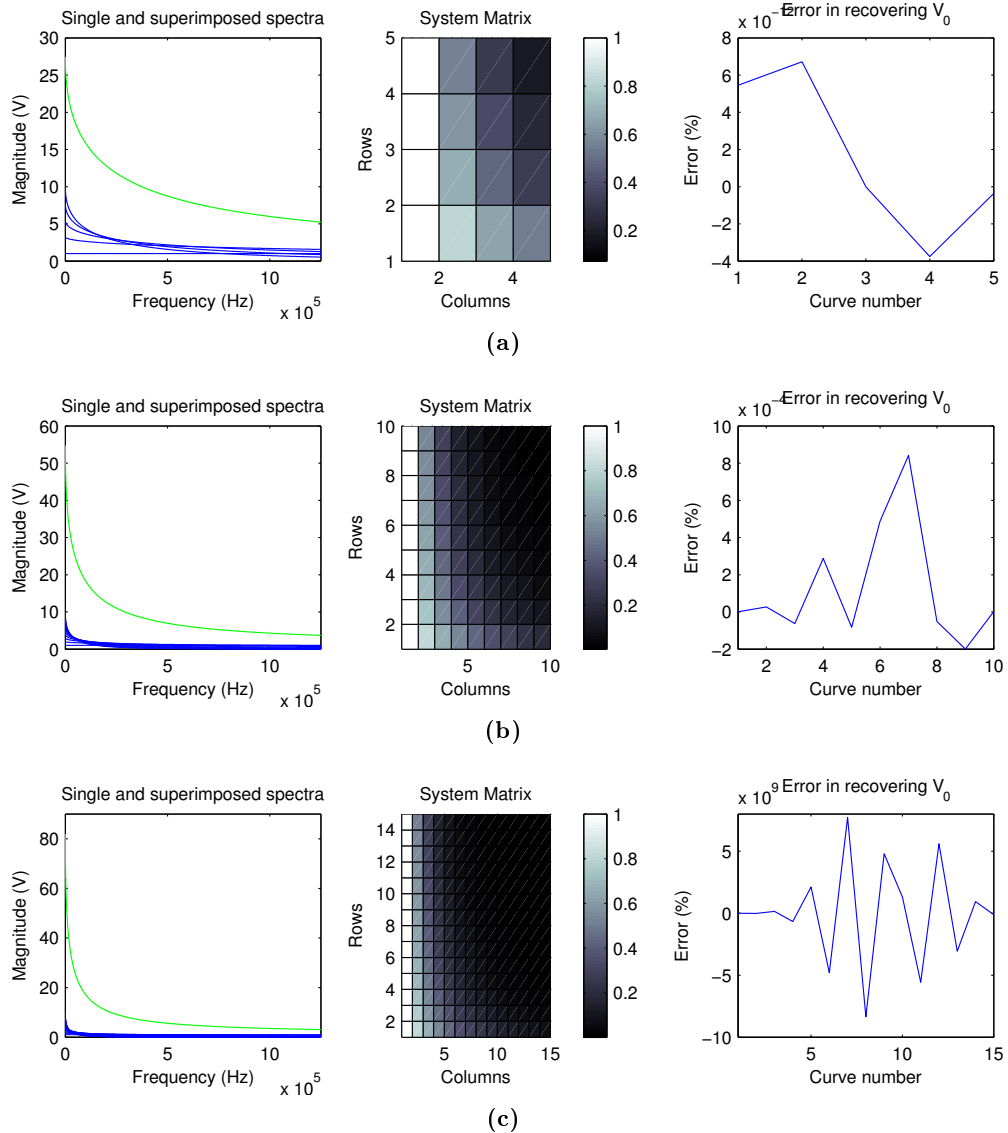


**Figure A.7:** Simulation results for (a) 5, (b) 10 and (c) 15 overlapping spectra. As the number of discrete depths is increased (and with it, the number of constituent spectra), the % error in recovering the spectrum intercepts  $V_0$  increases. The matrix becomes singular and impossible to invert (A.7c). This is possibly a result of numerical error, since the concept can be proven correct for a smaller number of distinct curves.

### Solution for system with $N$ depth spans, each from $x_i$ to $x_{i+1}$

This approach is more realistic, since in practice Barkhausen emissions occur over depth spans, and not just at infinitesimal depths. Consider an array of discrete depths  $x_i$ , and an integral from  $x_i$  to  $x_{i+1}$ , as in Equation A.13:

$$f(x_i, x_{i+1}, \omega) = \frac{1}{\zeta\sqrt{\omega}} \left( e^{-\zeta x_i \sqrt{\omega}} - e^{-\zeta x_{i+1} \sqrt{\omega}} \right), \quad (\text{A.13})$$

The magnitude of the Fourier transform,  $V_t(\omega)$ , of the signal at the surface of the specimen can be described in terms of a sum of signals with spectra  $V_i(\omega)$  emanating from different layers:

$$V_t(\omega) = \sum_{i=0}^N V_i(\omega) f(x_i, x_{i+1}, \omega) \quad (\text{A.14})$$

For simplicity, suppose that each layer is equally stressed (as in the tensile test) and the spectra are independent of frequency, such that  $V_i(\omega) = V_i$  and  $V_1 = V_2 = \dots = V_N = V$ . Then,

$$V = \frac{V_t(\omega)}{\sum_{i=0}^N f(x_i, x_{i+1}, \omega)} \quad (\text{A.15})$$

Since  $V_t(\omega)$  can be experimentally measured, and we can evaluate  $f(x_i, x_{i+1}, \omega)$  after substituting for  $x_i$ , we can obtain  $V$ . This is pretty straightforward and can be used in a calibration procedure where all layers are equally stressed.

However, in the case where  $V_1 \neq V_2 \neq \dots \neq V_N$ , the situation becomes more complicated. We do not longer know how much each layer contributes to the measured spectrum, as is the case with emissions from a discrete number of layers, where all layers are stressed to a different magnitude. Again, we can set up a system of simultaneous equations and solve the problem numerically:

$$\begin{bmatrix} V_t(1) \\ V_t(2) \\ \vdots \\ V_t(\omega_N) \end{bmatrix} = \begin{bmatrix} f(x_1, x_2, 1) & f(x_2, x_3, 1) & \dots & f(x_i, x_{i+1}, 1) \\ f(x_1, x_2, 2) & f(x_2, x_3, 2) & \dots & f(x_i, x_{i+1}, 2) \\ \vdots & \vdots & \ddots & \vdots \\ f(x_1, x_2, \omega_N) & f(x_2, x_3, \omega_N) & \dots & f(x_i, x_{i+1}, \omega_N) \end{bmatrix} \times \begin{bmatrix} V_1 \\ V_2 \\ \dots \\ V_i \end{bmatrix} \quad (\text{A.16})$$

where the signal frequency spectrum at the origin  $V_1, V_2, \dots, V_i$  is independent of frequency, but can be also expressed as a function of frequency. Also, it is important to note that the frequencies chosen do not necessarily have to be ascending in steps of one. In fact, it is more robust to have them ascend in larger steps, such that a bigger span of frequencies is considered. What is important is that the number of equations is equal to the number of unknowns. It is good to summarize the assumptions taken in this approach:

- We assume that the spectrum shape is independent of stress. In previous work [33, 61, 62] it is shown that the power spectrum shape and voltage distribution are dependent on stress. A point the aforementioned references all have in common is that the analysis is made in terms of what is measured at the surface. It is not obvious of how the spectra add up to produce the spectrum at the surface, an issue to which the solution would be central to solving the overall depth-profiling problem. According to Durin et al. [61], stress affects the parameter  $v_0$  appearing in the expression for the voltage distribution:

$$P(v) \sim v^{-(1-c)} e^{-v/v_0}, \quad (\text{A.17})$$

where  $c$  is a dimensionless parameter proportional to the magnetizing field rate. Jagadish et al. [33] present power spectra that change with stress, but their shape does not seem to change with stress.

- Although the permeability is a function of stress, we assume that the attenuation constant  $\zeta$  responsible for preferential attenuation of the emission spectra (which is dependent on permeability) is independent of stress. This assumption is essential, otherwise the solution would have to contain a number of unknown terms and would make the problem highly non-linear and difficult to solve.
- We assume that the signal is real (not complex), and therefore does not contain phase information. This greatly simplifies the analysis procedure. We treat the signal only in terms of attenuation in amplitude and we ignore dispersive effects. Ignoring the phase is a reasonable assumption, since all Barkhausen events occur randomly.



A simulation was constructed, to simulate white noise signals attenuated exponentially as they travel to the surface. The procedure comprised of the following steps:

1. Simulation of exponentially attenuating white noise spectra emanating from a span of depths that add up at the surface to produce the measured spectrum. Vary the amplitude of the spectrum at the origin for each layer, to simulate the effect of stress. The simulation parameters can be seen in Table A.1.
2. Use the system of equations in (A.16) to calculate the spectrum amplitudes  $V_1, V_2, \dots, V_i$ .

**Table A.2:** Simulation parameters

No. of layers	5, 10 and 15
Separation	20 $\mu m$
$\zeta$	$\sim 13 \sqrt{SH}/m$
$V_i$ profile	Increasing amplitude (span of 10 V)
Start frequency	100 kHz
Stop frequency	1000 kHz
Frequency spacing	5, 10 and 15 linear steps

The result of the simulation can be seen in Figure A.8.

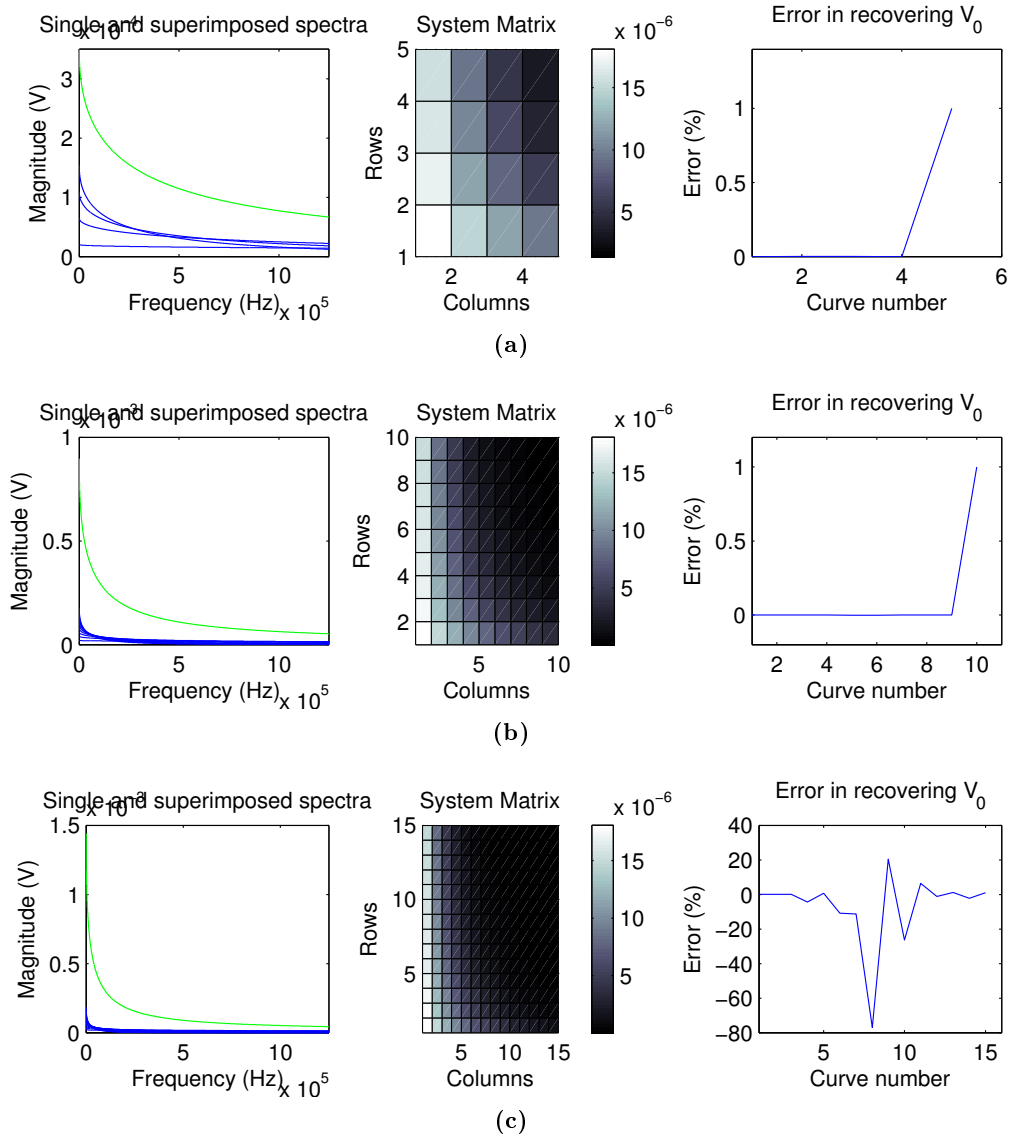


**Figure A.8:** Simulation results for (a) 5, (a) 10 and (a) 15 overlapping spectra. As the number of layers is increased (and with it, the number of constituent spectra), the % error in recovering the spectrum intercepts  $V_0$  increases. The matrix becomes singular and impossible to invert (Figure A.7c). This is possibly a result of numerical error, since the concept can be proven correct for a smaller number of layers.

## Time-frequency domain simulation of Barkhausen noise

In this section, a "calibration" measurement is simulated (in which all layers are equally stressed) in order to shed more light on whether some of our assumptions about the nature of Barkhausen signals are valid.

### Assumptions:

- Barkhausen information propagates in the form of plane waves and thus attenuates exponentially with frequency and distance, such that the measured signal at the surface due to one emission is

$$V = V_0 e^{-\zeta(\sigma)x} \quad (\text{A.18})$$

where  $\zeta$  is the absorption coefficient and is dependent on stress (as it depends on permeability) but assumed independent of frequency. In this treatment we ignore the phase of emissions.

- The amplitude of the emission at the origin can be approximated as a dirac delta function  $\delta(t)$ . In the frequency domain, this corresponds to a flat spectrum, which is also true for white noise.
- The mean amplitude of emission at the origin,  $V_0$  is stress dependent. Also,  $\mu$  is stress dependent.
- The Barkhausen signal measured at the surface is a linear combination of Barkhausen signals emanating from multiple volumetric regions within the specimen, such that

$$V_{meas}(t) = \sum_i V_{t_i}(\omega) \quad (\text{A.19})$$

and

$$V_{meas}(\omega) = \sum_i V_{att_i}(\omega) \quad (\text{A.20})$$

where  $V_{att_i}$  is the Barkhausen signal emanating from the  $i$ th layer, attenuated as it propagates towards the surface. Also,  $V_{att_i}$  can be obtained by integrating over a depth  $\Delta x$ .

$$V_{att_i}(\omega) = V_{orig} \int_{i\Delta x}^{(i+1)\Delta x} e^{-\sqrt{\frac{\omega\mu(\sigma)}{2\rho}}x} dx \quad (\text{A.21})$$

It can be shown, that in the limit of  $\omega \rightarrow 0$ , the equation of 3.29 converges to  $V_{orig}x$ , validating our assumption that the signal is a linear combination of signals coming from all depths:

$$\lim_{\omega \rightarrow 0} V_{att} = V_{orig} \lim_{\omega \rightarrow 0} \left( \frac{1 - e^{-\zeta\sqrt{\omega}x}}{\zeta\sqrt{\omega}} \right) \quad (\text{A.22})$$

$$= V_{orig} \lim_{\omega \rightarrow 0} \left( \frac{\frac{d}{d\omega}(1 - e^{-\zeta\sqrt{\omega}x})}{\frac{d}{d\omega}(\zeta\sqrt{\omega})} \right) \quad (\text{A.23})$$

$$= V_{orig}x \quad (\text{A.24})$$

- The signals corresponding to each layer are statistically independent from each other (hence the simple summation to yield the measured signal at the surface).
- The applied field has a low enough frequency, such that it can be essentially considered constant over the volumetric region that we are considering. In fact, a wave of frequency 100 Hz will have a skin depth of approx. 2.8 mm in a material of permeability 70 and conductivity 4.5 MS/m. The maximum analysis depth of 0.1 mm corresponds to approx 3.6% of that.
- The Barkhausen frequency spectrum can be described by white noise at the point of its origin. This implies that that past and future points in the time series are statistically uncorrelated. Physically, this implies that the local magnetization state being independent from neighbouring regions (i.e. only short range correlations exist).

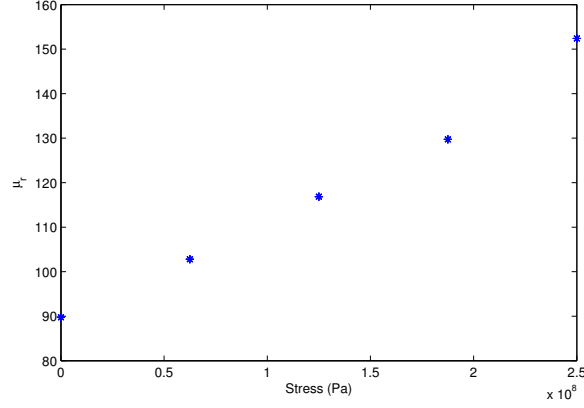


**Figure A.9:** Permeability-stress relationship that was used as an input to the model.

#### Method:

- The stress-dependent JA model was used to produce an  $M - H$  hysteresis loop. From that, the susceptibility was given a time dependence by specifying a an applied field rate  $dH/dt$ :

$$\chi'(t) = \frac{dM(\sigma)}{dH} = \frac{dM(\sigma)}{dt} \frac{dt}{dH} \quad (\text{A.25})$$

The selection of certain hysteresis and magnetostrictive parameters resulted in the permeability-stress relationship seen in Fig. A.9.

- A white noise signal  $W(t)$  was modulated by the diff. susceptibility in the time domain, to produce the signal that corresponds to the  $i$ th layer (Fig. A.10):

$$V_{orig_i}(t) = \chi'_i(t)W(t) = \frac{dM(\sigma_i)}{dH}W(t) \quad (\text{A.26})$$

- To simulate the effect of the material on the propagation of Barkhausen emissions originating in each discrete depth  $i\Delta x$ , the signals were convolved with the impulse response  $h_i(t)$  of the material (which depends on permeability and therefore stress), such that the measured voltage at the surface can be expressed as

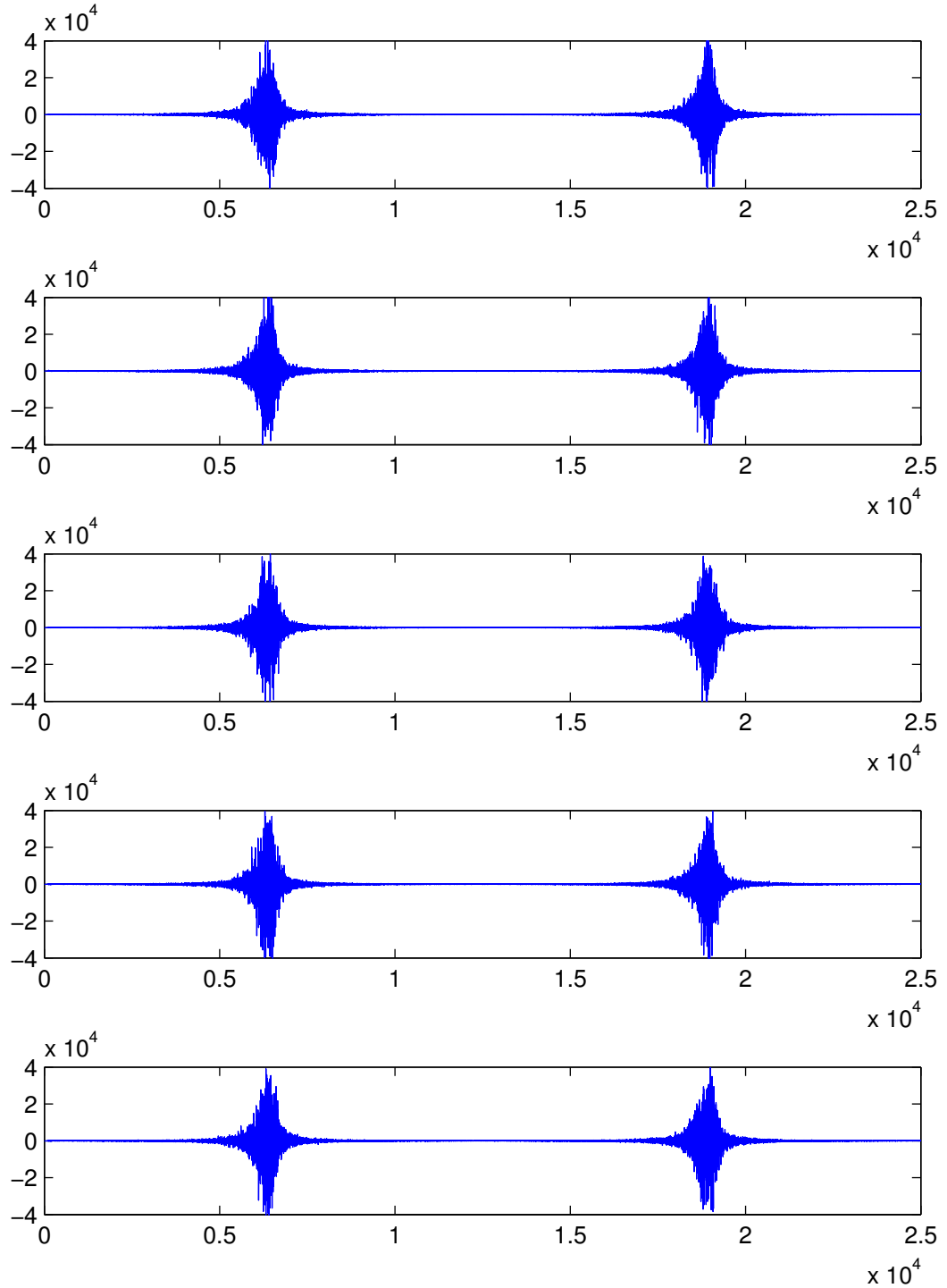


**Figure A.10:** Simulated waveforms at the origin of each layer, for all 5 layers, when all of them are stressed equally (250 MPa). Note that the artificially high amplitude ensures that no significant errors due to rounding occur later on (the waveform was multiplied by an amplification constant).

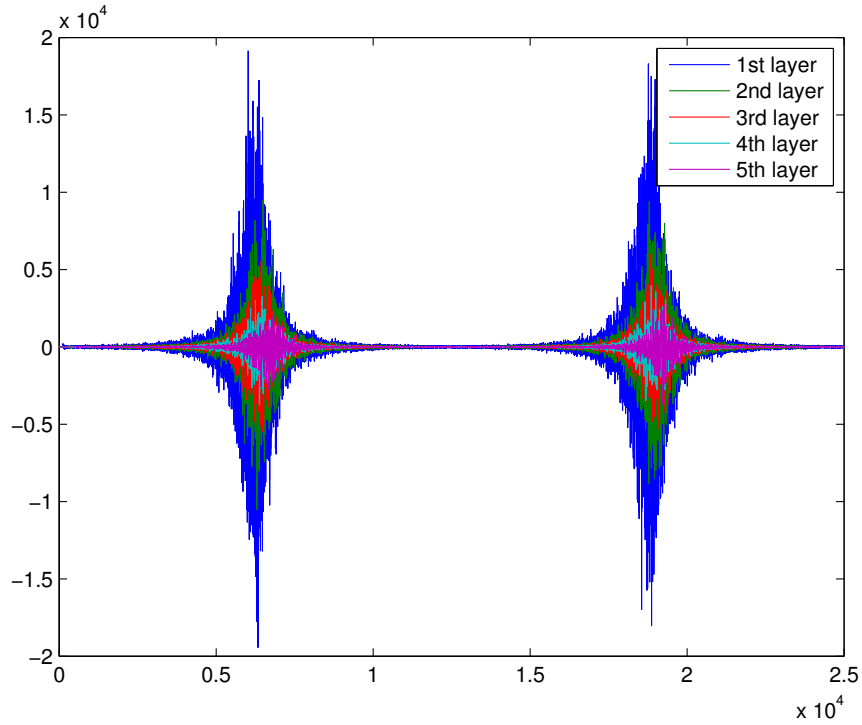


**Figure A.11:** Simulated waveforms at the surface, for all 5 layers, when all of them are stressed equally (0 MPa). The most attenuated one is the one corresponding to the fifth layer, situated deeper in the specimen. The apparent shift in the peak position is due to the filter's phase response which causes a phase shift (it looks like the coercive field is changing).

$$\begin{aligned}
 V_{meas}(t) &= \sum_i V_{att_i}(t) \\
 &= \sum_i V_{orig_i}(t) * h_i(t) \\
 &= \int_{-\infty}^t \sum_i V_{orig_i}(t) \delta(t - \zeta(\sigma)(i\Delta x)) dt
 \end{aligned}$$

where  $\zeta(\sigma)$  is the propagation constant introduced previously, which causes attenuation of the signal with frequency and distance. The mean depth of each layer was used as an input to the filter. Figure A.11 shows what happens to the waveforms when they are attenuated by the filter.

- A total of 5 distinct stress magnitudes were used, with each surface measurement waveform containing a total of 5 layer contributions. The resulting waveforms were saved on disk,

for later use.

- The resulting surface waveforms were loaded from file into memory, and into a custom written software module, which facilitates the loading and analysis of a series of Barkhausen measurements. The loaded surface waveforms can be seen in Figure A.12.

A windowed FFT of the signals near the coercive point was taken and a smoothing operation was performed to reduce random noise. Finally, the model equation of 3.29 was fitted to the data. An example spectrum can be seen in Fig. A.13.

The fit of the Barkhausen spectra (obtained by taking the FFT of the simulated waveforms) to the model can be seen in Fig. A.14. Results of parameter extraction can be seen in Figs. A.15 and A.16.



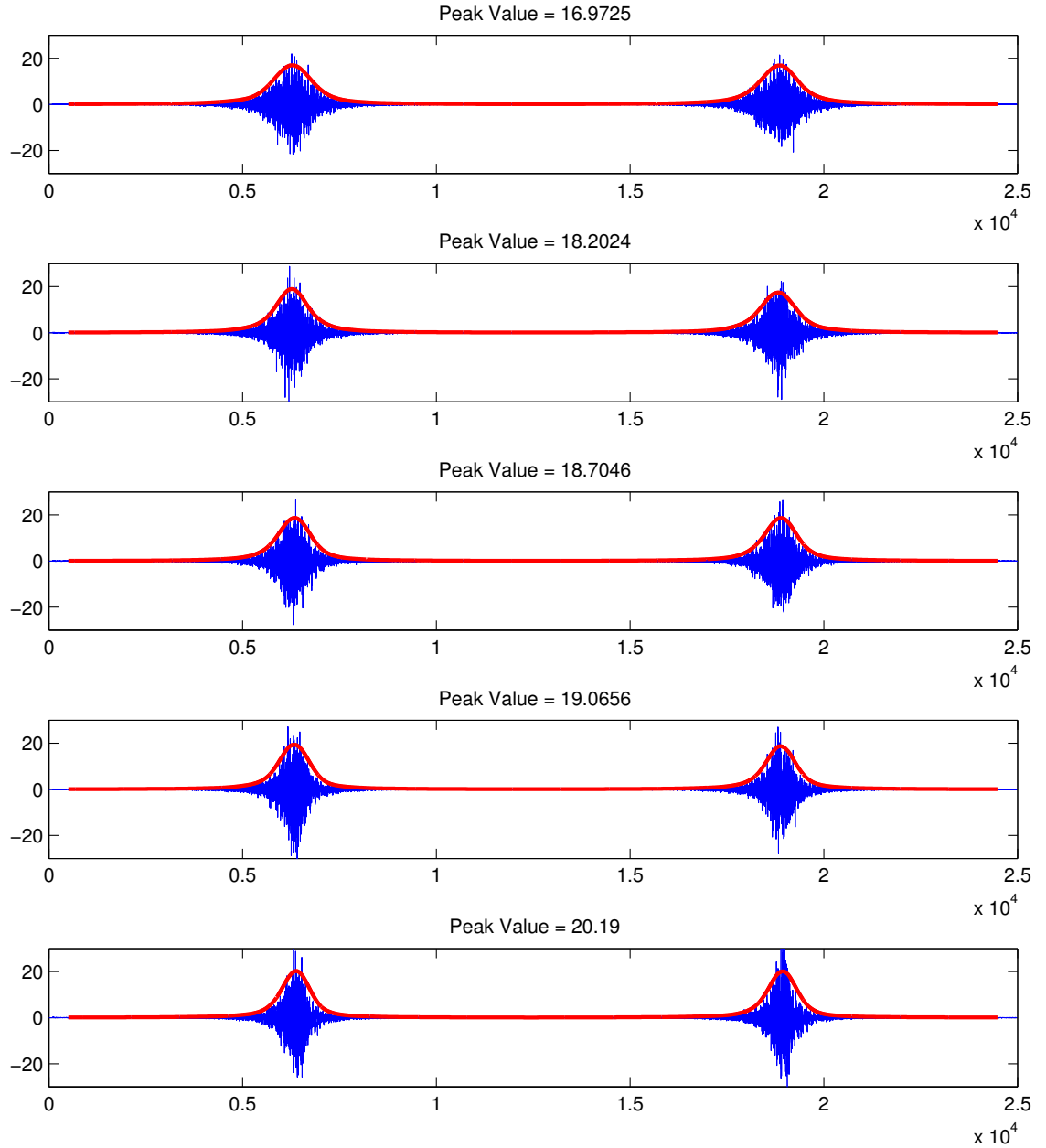


**Figure A.12:** Simulated waveforms at the surface, for all stresses, in ascending order (0 – 250 MPa). When the waveforms are loaded, they are multiplied by a factor of  $10^{-3}$ . The routine was originally coded like that to convert  $V$  to  $mV$  for data imported from the Stresstech Rollscan.

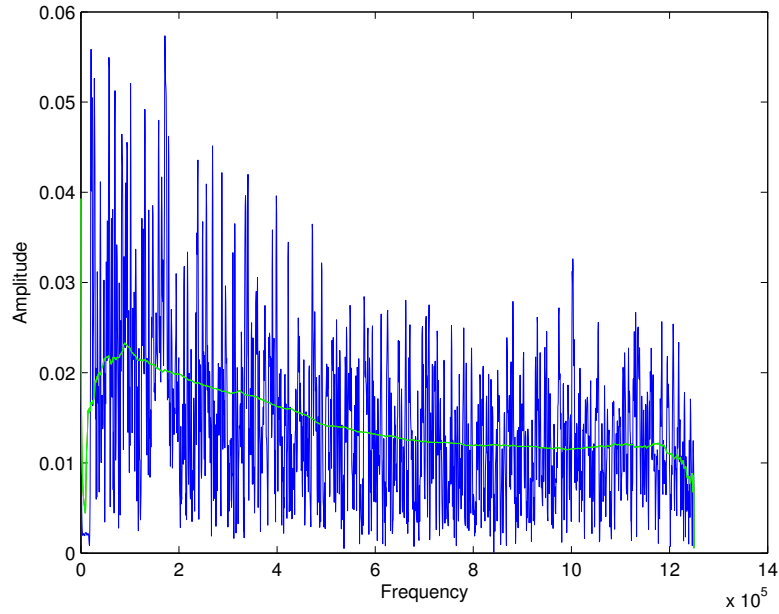


**Figure A.13:** FFT of simulated Barkhausen waveform, with smoothed spectrum. In fitting the model, only the mid- to high-frequency range was used, as the low-frequency range contains artifacts from the filter.

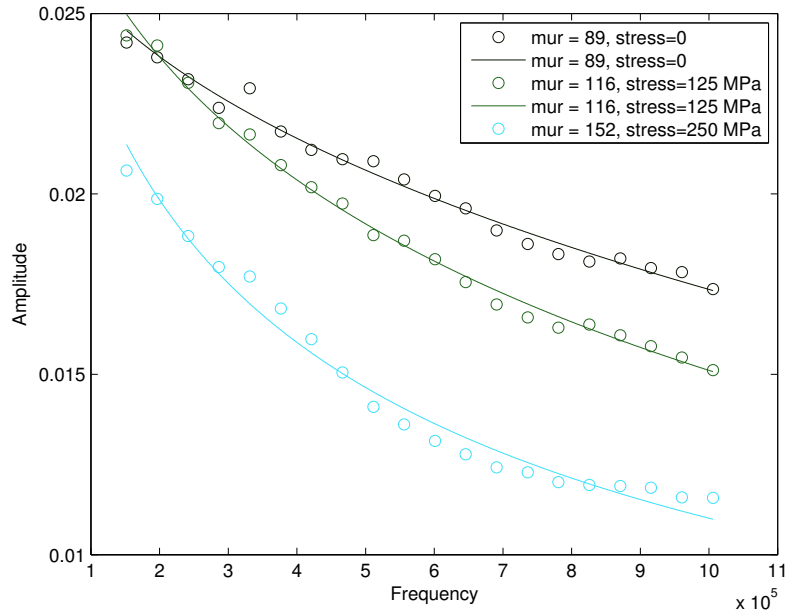


**Figure A.14:** Fit to the model. In fitting the model, only the mid- to high-frequency range was used, as the low-frequency range contains artifacts from the filter.

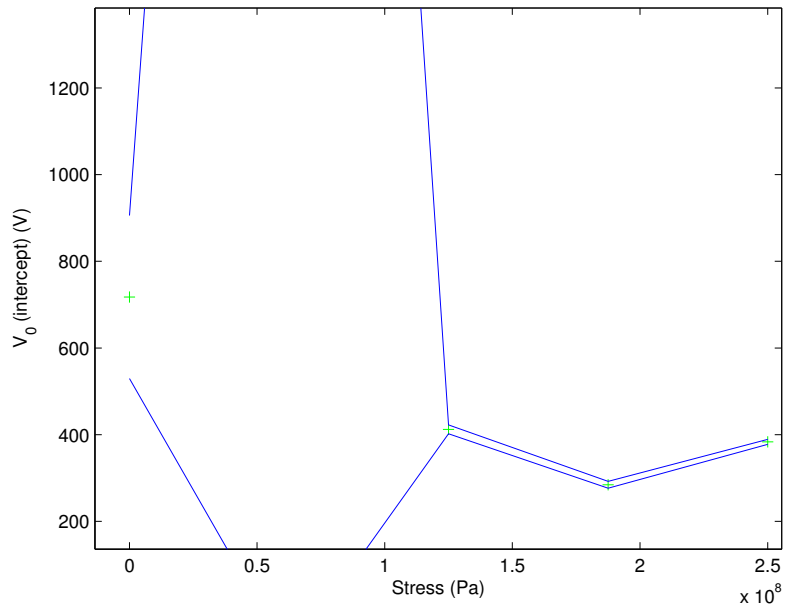


**Figure A.15:** Parameter  $V_0$ , extracted from the fit to the model. For some reason, the parameter is seen to decrease with stress, when it should be increasing. This must be investigated further. Note that there is an outlier at 50 MPa.

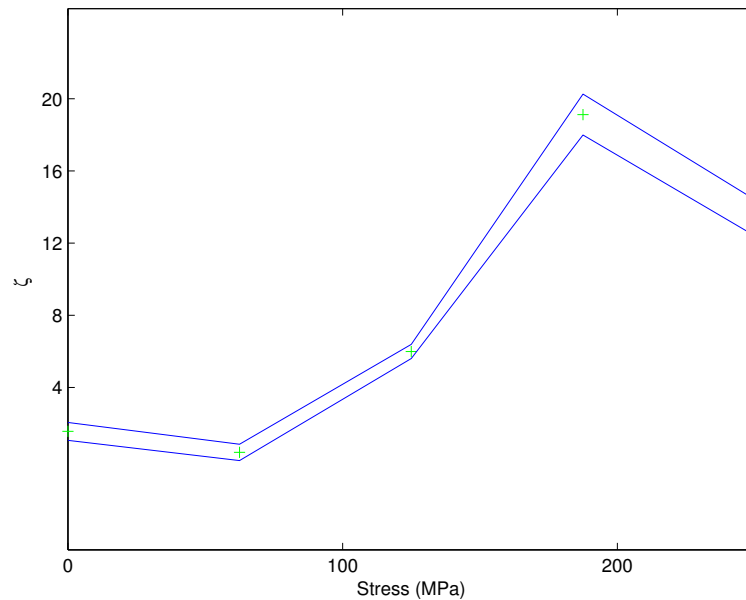


**Figure A.16:** Parameter  $\zeta$ , extracted from the fit to the model. For the most part, the parameter is seen to increase with stress, suggesting that permeability is increasing with stress, which is what was the input to the model.

## BIBLIOGRAPHY

- [1] G. E. Totten, M. A. H. Howes, and T. Inoue, *Handbook of residual stress and deformation of steel*. Materials Park and OH: ASM International, 2002. (cited on p. vii, 2, 3)
- [2] G. S. Schajer, *Practical residual stress measurement methods*. Wiley, New York, 2013. (cited on p. vii, 4)
- [3] H. Barkhausen, "Rauschen der ferromagnetischen materialen," *Phys. Zeitschrift*, vol. 20, pp. 401–403, 1919. (cited on p. 5)
- [4] B. Alessandro, C. Beatrice, G. Bertotti, and A. Montorsi, "Domain-wall dynamics and Barkhausen effect in metallic ferromagnetic materials. II. Experiments," *Journal of Applied Physics*, vol. 68, no. 6, p. 2908, 1990. (cited on p. vii, 5, 8, 9)
- [5] —, "Domain-wall dynamics and Barkhausen effect in metallic ferromagnetic materials. I. Theory," *Journal of Applied Physics*, vol. 68, no. 6, pp. 2901–2907, 1990. (cited on p. 5, 8)
- [6] H. Sakamoto, M. Okada, and M. Homma, "Theoretical analysis of Barkhausen noise in carbon steels," *IEEE Transactions on Magnetics*, vol. 23, no. 5, pp. 2236–2238, 1987. (cited on p. 5, 12)
- [7] D. Jiles, "Dynamics of domain magnetization and the Barkhausen effect," *Czechoslovak Journal of Physics*, vol. 50, no. 8, pp. 893–924, 2000. (cited on p. 5, 6, 9)
- [8] R. Ranjan, D. C. Jiles, O. Buck, and R. B. Thompson, "Grain size measurement using magnetic and acoustic Barkhausen noise," *Journal of Applied Physics*, vol. 61, no. 8, p. 3199, 1987. (cited on p. 5)

- [9] D. C. Jiles and S. Hariharan, “Interpretation of the magnetization mechanism in Terfenol-D using Barkhausen pulse-height analysis and irreversible magnetostriction,” *Journal of Applied Physics*, vol. 67, no. 9, pp. 5013–5015, 1990. (cited on p. 5)
- [10] G. Durin and S. Zapperi, “Scaling exponents for Barkhausen avalanches in polycrystalline and amorphous ferromagnets,” *Physical Review Letters*, vol. 84, no. 20, pp. 4705–4708, 2000. (cited on p. 5)
- [11] P. J. Cote and L. V. Meisel, “Self-organized criticality and the Barkhausen effect,” *Physical Review Letters*, vol. 67, no. 10, pp. 1334–1337, 1991. (cited on p. 5)
- [12] A. Baldassarri, F. Colaioni, and C. Castellano, “Average shape of a fluctuation: universality in excursions of stochastic processes,” *Physical Review Letters*, vol. 90, no. 6, p. 060601, 2003. (cited on p. 5)
- [13] O. Narayan, “Self-similar Barkhausen noise in magnetic domain wall motion,” *Physical Review Letters*, vol. 77, no. 18, pp. 3855–3857, 1996. (cited on p. 5)
- [14] E. Puppini, S. Ricci, and L. Callegaro, “Barkhausen jumps in a magnetic microstructure,” *Applied Physics Letters*, vol. 76, no. 17, p. 2418, 2000. (cited on p. 5)
- [15] E. Puppini, “Statistical properties of Barkhausen noise in thin Fe films,” *Physical Review Letters*, vol. 84, no. 23, pp. 5415–5418, 2000. (cited on p. 5)
- [16] K.-S. Ryu, H. Akinaga, and S.-C. Shin, “Tunable scaling behaviour observed in Barkhausen criticality of a ferromagnetic film,” *Nature Physics*, vol. 3, no. 8, pp. 547–550, 2007. (cited on p. 5)
- [17] S. Papanikolaou, F. Bohn, R. L. Sommer, G. Durin, S. Zapperi, and J. P. Sethna, “Universality beyond power laws and the average avalanche shape,” *Nature Physics*, vol. 7, no. 4, pp. 316–320, 2011. (cited on p. 5, 21)
- [18] A. Schwarz, M. Liebmann, U. Kaiser, R. Wiesendanger, T. Noh, and D. Kim, “Visualization of the Barkhausen Effect by Magnetic Force Microscopy,” *Physical Review Letters*, vol. 92, no. 7, 2004. (cited on p. 5)

- [19] D.-H. Kim, S.-B. Choe, and S.-C. Shin, "Direct Observation of Barkhausen Avalanche in Co Thin Films," *Physical Review Letters*, vol. 90, no. 8, 2003. (cited on p. 5)
- [20] S. Chikazumi and S. Charap, "Physics of magnetism," 1964. (cited on p. 6)
- [21] W. Döring, "über die Trägheit der Wände zwischen Weißschen Bezirken," *Zeitschrift Naturforschung Teil A*, vol. 3, p. 373, 1948. (cited on p. 6)
- [22] H. J. Williams, W. Shockley, and C. Kittel, "Studies of the propagation velocity of a ferromagnetic domain boundary," *Physical Review*, vol. 80, no. 6, p. 1090, 1950. (cited on p. 7)
- [23] G. Bertotti, *Hysteresis in magnetism: For physicists, materials scientists and engineers*, ser. Electromagnetism. San Diego and Calif. [u.a.]: Acad. Press, 1998. (cited on p. 8, 20)
- [24] B. Alessandro, C. Beatrice, G. Bertotti, and A. Montorsi, "Phenomenology and interpretation of the Barkhausen effect in ferromagnetic materials (invited)," *Journal of Applied Physics*, vol. 64, no. 10, p. 5355, 1988. (cited on p. 8)
- [25] M. J. Sablik, "A model for the Barkhausen noise power as a function of applied magnetic field and stress," *Journal of Applied Physics*, vol. 74, no. 9, p. 5898, 1993. (cited on p. vii, 8, 10)
- [26] L. B. Sipahi, D. C. Jiles, and D. Chandler, "Comprehensive analysis of Barkhausen emission spectra using pulse height analysis, frequency spectrum, and pulse wave form analysis," *Journal of Applied Physics*, vol. 73, no. 10, pp. 5623–5625, 1993. (cited on p. 9)
- [27] D. C. Jiles, L. B. Sipahi, and G. Williams, "Modeling of micromagnetic Barkhausen activity using a stochastic process extension to the theory of hysteresis," *Journal of Applied Physics*, vol. 73, no. 10, p. 5830, 1993. (cited on p. vii, 11)
- [28] D. M. Clatterbuck, "Modeling of the magnetic Barkhausen effect," in *AIP Conference Proceedings*. AIP, 2000, pp. 1533–1540. (cited on p. 12)

- [29] R. Rautioaho, P. Karjalainen, and M. Moilanen, "Improvement of the Barkhausen noise method for stress evaluation," *Journal of Magnetism and Magnetic Materials*, vol. 73, no. 1, pp. 96–102, 1988. (cited on p. 13)
- [30] A. Mitra, Govindaraju, and D. C. Jiles, "Influence of microstructure on micromagnetic Barkhausen emissions in AISI 4140 steel," *IEEE Transactions on Magnetics*, vol. 31, no. 6, pp. 4053–4055, 1995. (cited on p. 13)
- [31] D. C. Jiles, "Frequency dependence of hysteresis curves in conducting magnetic materials," *Journal of Applied Physics*, vol. 76, no. 10, pp. 5849–5855, 1994. (cited on p. vii, 13, 14)
- [32] M. Vashista and S. Paul, "Novel processing of Barkhausen noise signal for assessment of residual stress in surface ground components exhibiting poor magnetic response," *Journal of Magnetism and Magnetic Materials*, 2011. (cited on p. 13)
- [33] C. Jagadish, L. Clapham, and D. L. Atherton, "Influence of uniaxial elastic stress on power spectrum and pulse height distribution of surface Barkhausen noise in pipeline steel," *IEEE Transactions on Magnetics*, vol. 26, no. 3, pp. 1160–1163, 2002. (cited on p. vii, 13, 128)
- [34] A. Mitra, L. B. Sipahi, Govindaraju, D. C. Jiles, and V. R. Ramanan, "Effects of tensile stress on magnetic Barkhausen emissions in amorphous Fe<sub>80</sub>Si<sub>20</sub>B alloy," *Journal of Magnetism and Magnetic Materials*, vol. 153, no. 1, pp. 231–234, 1996. (cited on p. 13)
- [35] T. W. Krause, A. Pattantyus, and D. L. Atherton, "Investigation of strain dependent magnetic Barkhausen noise in steel," *IEEE Transactions on Magnetics*, vol. 31, no. 6, pp. 3376–3378, 2002. (cited on p. 13)
- [36] M. J. Sablik, G. L. Burkhardt, H. Kwun, and D. C. Jiles, "A model for the effect of stress on the low-frequency harmonic content of the magnetic induction in ferromagnetic materials," *Journal of Applied Physics*, vol. 63, no. 8, pp. 3930–3932, 1988. (cited on p. 14)
- [37] M. J. Sablik, S. W. Rubin, L. A. Riley, D. C. Jiles, D. A. Kaminski, and S. B. Biner, "A model for hysteretic magnetic properties under the application of noncoaxial stress and field," *Journal of Applied Physics*, vol. 74, no. 1, p. 480, 1993. (cited on p. 14)

- [38] D. C. Jiles and J. B. Thoelke, "Magnetization and Magnetostriction in Terbium–Dysprosium–Iron Alloys," *physica status solidi (a)*, vol. 147, no. 2, pp. 535–551, 1995. (cited on p. 15)
- [39] L. Mierczak, D. C. Jiles, and G. Fantoni, "A New Method for Evaluation of Mechanical Stress Using the Reciprocal Amplitude of Magnetic Barkhausen Noise," *IEEE Transactions on Magnetics*, vol. 47, no. 2, pp. 459–465, 2011. (cited on p. vii, 15, 16, 19, 42, 47)
- [40] D. C. Jiles, "The effect of compressive plastic deformation on the magnetic properties of AISI 4130 steels with various microstructures," *Journal of Physics D: Applied Physics*, vol. 21, p. 1196, 1988. (cited on p. 15)
- [41] B. D. Cullity and C. D. Graham, *Introduction to magnetic materials*. Wiley-IEEE Press, 2008. (cited on p. 17)
- [42] P. Garikepati, T. T. Chang, and D. C. Jiles, "Theory of ferromagnetic hysteresis: evaluation of stress from hysteresis curves," *IEEE Transactions on Magnetics*, vol. 24, no. 6, pp. 2922–2924, 1988. (cited on p. 18, 19, 47)
- [43] C. G. Stefanita, L. Clapham, and D. L. Atherton, "Subtle changes in magnetic Barkhausen noise before the macroscopic elastic limit," *Journal of materials science*, vol. 35, no. 11, pp. 2675–2681, 2000. (cited on p. 21)
- [44] M. Richards, "The Discrete-Time Fourier Transform and Discrete Fourier Transform of Windowed Stationary White Noise," 2007. (cited on p. 24)
- [45] O. Kypris, I. C. Nlebedim, and D. C. Jiles, "Mapping Stress as a Function of Depth at the Surface of Steel Structures Using a Frequency Dependent Magnetic Barkhausen Noise Technique," *Magnetics, IEEE Transactions on*, vol. 48, no. 11, pp. 4428–4431, 2012. (cited on p. 28)
- [46] L. Mierczak, Y. Melikhov, and D. Jiles, "Determining Residual Stress Depth Profiles using the Magnetic Barkhausen Effect," *IEEE Transactions on Magnetics*, p. 1, 2014. (cited on p. 28, 30)



- [47] O. Kypris, I. C. Nlebedim, and D. C. Jiles, “A New Method for Obtaining Stress-Depth Calibration Profiles for Non-Destructive Evaluation Using a Frequency-Dependent Model of Barkhausen Emissions,” *Magnetics, IEEE Transactions on*, vol. 49, no. 7, pp. 3893–3896, 2013. (cited on p. 42, 47)
- [48] —, “Mapping Stress as a Function of Depth at the Surface of Steel Structures Using a Frequency Dependent Magnetic Barkhausen Noise Technique,” *IEEE Transactions on Magnetics*, vol. 48, no. 11, pp. 4428–4431, 2012. (cited on p. 46, 117)
- [49] —, “Experimental Verification of the Linear Relationship Between Stress and the Reciprocal of the Peak Barkhausen Voltage in ASTM A36 Steel,” *Magnetics, IEEE Transactions on*, vol. 49, no. 7, pp. 4148–4151, 2013. (cited on p. 46, 117)
- [50] Astm E8, “Standard test methods for tensile testing of metallic materials,” *Annual book of ASTM standards*, vol. 3, 1997. (cited on p. 50)
- [51] R. R. Craig, *Mechanics of materials*, 3rd ed. Hoboken and NJ: Wiley, 2011. (cited on p. 50, 51, 57)
- [52] Comsol, “Multiphysics Reference Guide for COMSOL 4.2,” 2011. (cited on p. 56)
- [53] R. Shiavi, *Introduction to applied statistical signal analysis: Guide to biomedical and electrical engineering applications*, 3rd ed. Amsterdam and Boston: Elsevier Academic Press, 2007. (cited on p. 62, 63, 64, 67, 68, 70)
- [54] J. Nocedal and S. J. Wright, *Numerical optimization*, 2nd ed., ser. Springer series in operations research and financial engineering. New York: Springer, 2006. (cited on p. 72)
- [55] W. L. Goffe, G. D. Ferrier, and J. Rogers, “Global optimization of statistical functions with simulated annealing,” *Journal of Econometrics*, vol. 60, no. 1-2, pp. 65–99, 1994. (cited on p. 73)
- [56] I. Miller, M. Miller, and J. E. Freund, *John E. Freund’s mathematical statistics with applications*, 8th ed. Boston: Pearson, 2014. (cited on p. 75)

- [57] C. E. Brown, "Coefficient of Variation," in *Applied Multivariate Statistics in Geohydrology and Related Sciences*, C. E. Brown, Ed. Berlin and Heidelberg: Springer Berlin Heidelberg, 1998, pp. 155–157. (cited on p. 94)
- [58] O. Kypris, I. C. Nlebedim, and D. C. Jiles, "Barkhausen spectroscopy: Non-destructive characterization of magnetic materials as a function of depth," *Journal of Applied Physics*, vol. 115, no. 17, p. 17E305, 2014. (cited on p. 117)
- [59] Agilent Technologies, "Agilent Impedance Measurement Handbook: A guide to measurement technology and techniques." (cited on p. xiv, 121, 122)
- [60] R. Lao, "The Twisted-Pair Telephone Transmission Line," *High Frequency Electronics*, 2002. (cited on p. xiv, 123)
- [61] G. Durin and S. Zapperi, "Barkhausen noise in soft amorphous magnetic materials under applied stress," *Journal of Applied Physics*, vol. 85, no. 8, p. 5196, 1999. (cited on p. 128)
- [62] A. J. Birkett, W. D. Corner, B. K. Tanner, and S. M. Thompson, "Influence of plastic deformation on Barkhausen power spectra in steels," *Journal of Physics D: Applied Physics*, vol. 22, p. 1240, 1989. (cited on p. 128)

## LIST OF PUBLICATIONS

- [1] **Kypris, O**, I. Nlebedim, and D. Jiles, “Experimental Verification of the Linear Relationship Between Stress and the Reciprocal of the Peak Barkhausen Voltage in ASTM A36 Steel,” *IEEE Transactions on Magnetics*, vol. 49, no. 7, pp. 4148–4151, 2013.
- [2] —, “Mapping Stress as a Function of Depth at the Surface of Steel Structures Using a Frequency Dependent Magnetic Barkhausen Noise Technique,” *IEEE Transactions on Magnetics*, vol. 48, no. 11, pp. 4428–4431, 2012.
- [3] —, “A New Method for Obtaining Stress-Depth Calibration Profiles for Non-Destructive Evaluation Using a Frequency-Dependent Model of Barkhausen Emissions,” *IEEE Transactions on Magnetics*, vol. 49, no. 7, pp. 3893–3896, 2013.
- [4] —, “A model for the Barkhausen frequency spectrum as a function of applied stress,” *Journal of Applied Physics*, vol. 115, no. 8, p. 083906, 2014.
- [5] —, “Barkhausen spectroscopy: Non-destructive characterization of magnetic materials as a function of depth,” *Journal of Applied Physics*, vol. 115, no. 17, p. 17E305, 2014.
- [6] N. P. Gaunkar, **Kypris, O**, I. Nlebedim, and D. Jiles, “Optimization of sensor design for Barkhausen noise measurement using finite element analysis,” *Journal of Applied Physics*, vol. 115, no. 17, p. 17E512, 2014.
- [7] —, “Analysis of Barkhausen Noise Emissions and Magnetic Hysteresis in Multi-Phase Magnetic Materials,” *IEEE Transactions on Magnetics*, vol. 50, no. 11, pp. 1–4, Nov 2014.

# Experimental Verification of the Linear Relationship Between Stress and the Reciprocal of the Peak Barkhausen Voltage in ASTM A36 Steel

O. Kypris<sup>1</sup>, I. C. Nlebedim<sup>1,2</sup>, and D. C. Jiles<sup>1,2</sup>, *Fellow, IEEE*

<sup>1</sup> Department of Electrical and Computer Engineering, Iowa State University, Ames, IA 50011 USA

<sup>2</sup> Ames Laboratory, US DOE, Ames, IA 50011 USA

This study presents an experimental validation of a model theory for determining the relationship between a nondestructive measurement parameter and a property of interest. It was found that the reciprocal of the peak envelope amplitude of the Barkhausen emission voltage follows a linear relationship with stress. A linear relationship between stress and the reciprocal of the root mean square voltage was also obtained. These observations represent an important step towards improving the use of Barkhausen signals for magnetic non-destructive evaluation of stress as a function of depth in ferromagnetic load bearing structures.

**Index Terms**—Barkhausen effect, magnetic Barkhausen noise, nondestructive evaluation, nondestructive testing, stress depth profiling.

## I. INTRODUCTION

DISCONTINUOUS changes in magnetization result in Barkhausen signals, which can be detected by a search coil on the surface of the material subject to magnetization. The Barkhausen signal amplitude and spectrum varies depending on the type of ferromagnetic material, the stress state, defect/inclusion sizes and microstructure [1]–[6]. Barkhausen signal analysis is used as a tool for nondestructive evaluation for assessing residual surface stresses in load-bearing components, especially steel parts. However, the absence of an underlying theory that describes the variation of a measurable Barkhausen parameter (such as the voltage peak envelope amplitude) with stress, has made the evaluation process until now highly dependent on empirical data.

In general, it is accepted that for materials with positive magnetostriction, the peak amplitude of the Barkhausen signal increases with applied tensile stress in the elastic region. In recent research it was shown that under uniaxial tension the reciprocal of the peak envelope amplitude of the magnetic Barkhausen noise signal ( $1/V_{peak}$ ) follows a linear relationship with stress ( $\sigma$ ) [7], [8]. This relationship resembles that of the anhysteretic differential susceptibility at the origin  $\chi'_{an}|_{H=0}$  with stress, as presented by Garikepati *et al.* [9].

In previous studies [7]–[9], 32CDV13, SAE 9310, AISI 4130, and RAEX400 steels were used. It is important to verify that the relationship is more general and holds for steels of other compositions and properties. This study aims at validating the linear relationship between  $1/V_{peak}$  and  $\sigma$  in A36 steel so that it can later be incorporated into a technique for mapping stress as a function of depth in ferromagnetic structures [10]. A36 steel is widely used for load-bearing parts. It is elastic ( $\sim 200$  GPa), it exhibits high yield- and ultimate tensile strengths ( $\sim 250$  MPa and  $\sim 450$ – $550$  MPa respectively), and it offers high performance at minimum cost, which gives it important uses in many

industries, including the construction, industrial, marine, transport and military sectors.

In the present study, a uniaxial tensile test was conducted on an A36 steel sample, while an inductive probe measured the Barkhausen emissions corresponding to a range of stresses. The waveform data were then analyzed using a customized Matlab routine and the reciprocal of the peak envelope amplitude, as well as the root mean square (RMS) of the magnetic Barkhausen signal were plotted against the engineering stress.

## II. THEORY

Garikepati *et al.* [9] presented an expression for the stress dependence of the anhysteretic differential susceptibility at the origin  $\chi'_{an}|_{H=0}$  of the form

$$\chi'_{an}(\sigma)|_{H=0} = \frac{M_s}{3\alpha - \left(\alpha + \frac{3b\sigma}{\mu_0}\right) M_s} \quad (1)$$

where  $M_s$  is the saturation magnetization,  $\alpha$  is the coupling coefficient that quantifies the strength of interaction between neighbouring domains,  $b$  is a magnetostrictive coefficient that can be determined experimentally,  $\mu_0$  is the permeability of free space, and  $\sigma$  is the stress. This expression can be rewritten as

$$\frac{1}{\chi'_{an}(0)|_{H=0}} - \frac{1}{\chi'_{an}(\sigma)|_{H=0}} = \frac{3b\sigma}{\mu_0} \quad (2)$$

Likewise, at the coercive point  $\chi'_{max} \simeq \chi'_{an}$  so that there is a simple relationship between the peak slope of the magnetization curve and stress

$$\frac{1}{\chi'_{max}(0)} - \frac{1}{\chi'_{max}(\sigma)} = \frac{3b\sigma}{\mu_0} \quad (3)$$

In previous work [7], the voltage peak envelope amplitude was observed to follow a similar trend with stress, and thus (3) was modified to give

$$\frac{1}{V_{MBN,peak}(0)} - \frac{1}{V_{MBN,peak}(\sigma)} = \frac{3b'\sigma}{\mu_0} \quad (4)$$

where  $b'$  is a scaled version of  $b$  found in (3).

Manuscript received November 05, 2012; accepted December 06, 2012. Date of current version July 15, 2013. Corresponding author: O. Kypris (e-mail: kypris@iastate.edu).

Color versions of one or more of the figures in this paper are available online at <http://ieeexplore.ieee.org>.

Digital Object Identifier 10.1109/TMAG.2012.2234728

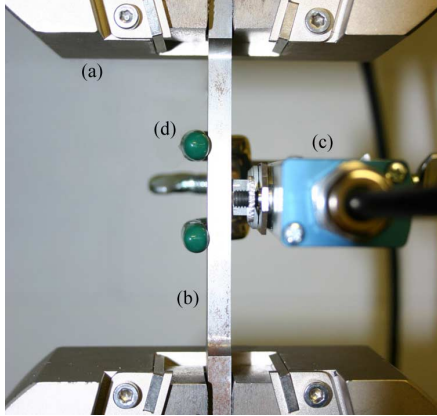


Fig. 1. Experimental setup, where (a) is the grip of the tensile test machine, (b) is the A36 test specimen, (c) is the Barkhausen probe, and (d) is the clamp.

### III. EXPERIMENTAL DETAILS

#### A. Uniaxial Tensile Test

A bar of hot rolled ASTM A36 steel was machined along the rolling direction to produce an ASTM E8 standard “dog-bone” specimen for tensile testing. The specimen has a thickness of 6.5 mm, width of 12.7 mm and gauge length of 26.5 mm. It was subjected to uniaxial tension at a deformation rate of 3 mm/min, using an Instron 5969 tensile test machine. The specimen was magnetized with a Barkhausen probe consisting of a magnetizing coil wound around a ferritic C-core electromagnet with cross-sectional area of 25.6 mm<sup>2</sup> (8 mm × 3.2 mm), and a sensing coil wound around a ferritic cuboid with cross-sectional area of 3.6 mm<sup>2</sup> (3 mm × 1.2 mm) positioned between the electromagnet poles, and picking up the perpendicular component of the flux density from the specimen. The measurement was paused every ~1000 N of load, in order to collect Barkhausen data along the direction of stress, with the probe positioned as pictured in Fig. 1. The Barkhausen waveforms were measured at a sampling rate of 2.5 MHz, while magnetizing the specimen at a rate of 100 Hz with maximum applied magnetic field of 0.5 kA/m measured between the poles of the electromagnet. A total of five equally spaced measurements were carried out for each value of stress, with every trial containing 10 Barkhausen bursts. Because the specimen underwent small amount of relaxation every time the tensile test was paused, to obtain the Barkhausen signals the waveforms were averaged over that relaxation period and these were plotted against the stress.

#### B. Post-Processing

To analyze the Barkhausen data, a customized object-oriented Matlab signal processing program was used. In order to only consider the surface component of the Barkhausen emissions, the waveforms were high-pass filtered at the frequency which corresponds to a skin depth  $\delta$  of 100  $\mu\text{m}$ , using the well known skin-depth relation

$$\delta = \sqrt{\frac{2\rho}{\omega\mu}} \quad (5)$$

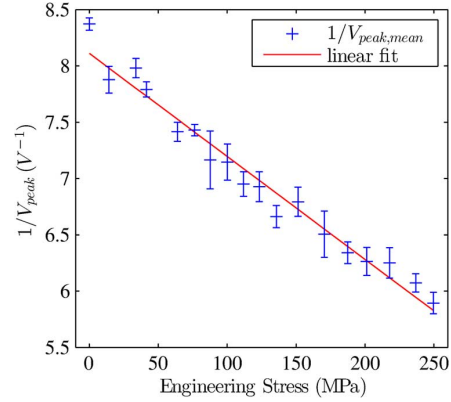


Fig. 2. Variation of the mean reciprocal peak envelope voltage amplitude with applied uniaxial stress, plotted with 95% confidence intervals. The signals were high-pass filtered such that the peak voltage corresponds to the average of the Barkhausen emissions over the nearest 100  $\mu\text{m}$  from the surface. From a linear regression,  $b' = -3.99 \times 10^{-15} \text{ msA}^{-1} \text{ N}^{-1}$ , with an adjusted  $R^2$  value of 0.9678.

where  $\rho$  and  $\mu = \mu_0\mu_r$  are the dc resistivity and dc permeability of the sample, and  $\omega = 2\pi f$  is the angular frequency of the Barkhausen emission. A four-point dc conductivity measurement and a quasi-static  $B - H$  measurement preceded the Barkhausen experiment, in order to obtain the values needed to determine the high-pass cut-off frequency. During the Barkhausen experiment, the specimen was not magnetically saturated, thus the value of the differential permeability at the coercive point  $\mu'_r|_{H=H_c}$  was used.

In order to obtain the envelopes from the Barkhausen waveforms, a customized triangular moving average routine was written in Matlab. It performs two successive simple moving average calculations, such that the end result is smoother. The envelope smoothness is defined by the combined number of data points before and after the current data point. The procedure used 2000 over a total number of 25 000 data points contained in each magnetizing cycle. Using the calculated envelopes, the peak amplitudes were calculated for both the positive and negative parts of the magnetizing cycles, then averaged to produce the mean. Calculation of the RMS values was also performed.

### IV. RESULTS AND DISCUSSION

Figs. 2 and 3 show the variation of the reciprocal peak envelope voltage and the reciprocal of the RMS voltage corresponding to the first 100  $\mu\text{m}$  of depth from the surface of the specimen. At a relative permeability  $\mu_r = 62$  and resistivity  $\rho = 0.231 \mu\Omega\text{m}$ , 100  $\mu\text{m}$  from the surface corresponds to a cutoff frequency of ~95 kHz. It can be seen that the result obtained in the present study is in good agreement with the model equation presented in (4). This is important because it demonstrates the relationship between a nondestructive measurement parameter (Barkhausen signal) and a property of interest (stress). This result can be incorporated in a model procedure for the depth profiling of stress using a frequency dependent Barkhausen signal technique.

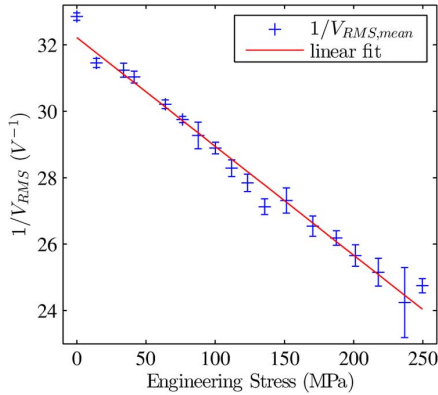


Fig. 3. Variation of the mean reciprocal RMS voltage with applied uniaxial stress, plotted with 95% confidence intervals. The signals were high-pass filtered such that the RMS voltage corresponds to the average of the Barkhausen emissions over the nearest  $100 \mu\text{m}$  from the surface. From a linear regression,  $b' = -1.38 \times 10^{-14} \text{ msA}^{-1} \text{ N}^{-1}$ , with an adjusted  $R^2$  value of 0.9833.

Comparing both results, the variability of the quantity  $1/V_{RMS}$  is less than that of  $1/V_{peak}$ . This can be attributed to the computational method used to obtain those quantities.  $1/V_{peak}$  is a measure of a single point on the voltage envelope curve and is more prone to localized voltage fluctuations, which may be a result of fluctuations in the Barkhausen signal. Furthermore, the smoothness of the voltage envelope curve is highly dependent on the smoothing parameter, which is determined heuristically. On the other hand, the computation of the RMS voltage relies on a well-defined mathematical formula which brings increased repeatability.

Furthermore, it is worth noting that a lower absolute value of  $b'$  is observed in the peak data of Fig. 2 as compared to the RMS data of Fig. 3. This suggests that the reciprocal of the RMS voltage is more responsive to changes in stress. This can be of use in practical stress detection applications, where high sensitivity is vital.

Some of the variability in the voltage can also be accounted for by the relaxation between successive Barkhausen measurements, which reduced the Barkhausen signal amplitude as the specimen relaxed. Overall, the fit of the experimental results to the theoretical model was very good and this is a strong indication of the validity of the model. However, the consideration of higher order terms in the relationship between magnetostriction  $\lambda$  and magnetization  $M$  may be considered in future work, to account for any nonlinear variation in the experimental data.

An extension to the theory of ferromagnetic hysteresis can be used to help explain the experimental result. In the elastic region, a constant applied stress can be represented as an additional magnetic field term  $H_\sigma$ , which is a function of the magnetoelastic energy  $E_\sigma$  and the magnetization  $M$ , such that

$$H_\sigma = \frac{1}{\mu_0} \frac{\partial E_\sigma}{\partial M}. \quad (6)$$

Assuming there are no transverse strains, the magnetoelastic energy due to stress is

$$E_\sigma = \frac{3}{2} \lambda \sigma \cos^2 \phi \quad (7)$$

where  $\lambda$  is the magnetostriction and  $\phi$  is the angle between the direction of magnetization and the direction of applied stress. In general, low carbon steels exhibit reduced magnetocrystalline anisotropy. In the presence of applied stress, the stress induced anisotropy dominates. When the field is applied along the direction of stress, (6) reduces to

$$H_\sigma = \frac{3b\sigma M}{\mu_0} \quad (8)$$

where  $\sigma$  is the stress amplitude. The magnetization  $M$  is, in strict terms, also a function of stress. However, at relatively small applied stresses and fields, its dependence on stress can be neglected. The initial region of the  $\lambda - M$  curve can therefore be approximated as parabolic, with  $b$  defined as a second-order magnetostriction coefficient, such that  $\lambda = bM^2$ . It can be seen that the stress-equivalent field  $H_\sigma$  experienced by domains varies linearly with stress, and by examination of Figs. 2 and 3, so does the reciprocal of the Barkhausen voltage. However, since the Barkhausen signal contains stochastic components, the parameter  $b'$  seen in (4) which is proportional to the slope of the line, can only be determined experimentally. Qualitatively, it will depend on the magnetizing frequency and amplitude of the magnetizing field.

It should be noted that the linear relationship that can be established in the low-field, low-stress region, does not hold as the magnitude of stress is increased past the yield point of the material. At the onset of plastic deformation, slip processes form dislocations in the crystal lattice. These, in turn inhibit domain wall motion by increasing the effective field that is needed for domain walls to escape local energy minima and thus invalidating the assumption that the stress-induced anisotropy dominates. Thus, in the plastic region the relationship given in (4) may not hold. Nevertheless, for the purpose of this study which focuses on the elastic region, the relationship is realistic as the results show. Furthermore, the results of Garikepati *et al.* [9] experimentally verify that the linear relationship between the reciprocal of the anhysteretic susceptibility at the origin and stress also holds for compressive stress. It is therefore expected that a linear relationship between the reciprocal of the Barkhausen voltage and compressive stress should also hold. However, this study focused on developing a linear calibration technique for a stress-depth profiling method used to detect tensile stresses in ferromagnetic structures in order to prevent catastrophic failures. The scope is thus limited to tensile stress, though in future work compressive stresses will be studied.

## V. CONCLUSION

In this work it was shown that the reciprocal of the Barkhausen peak envelope voltage and the reciprocal RMS voltage follow a linear relationship with stress in the elastic region in ASTM A36 steel. This trend has been observed in previous studies [7]–[9], on different types of steel. This stands as an important result, as it provides a solid foundation for developing a method to resolve the stress state of a ferromagnetic material via Barkhausen signal analysis. At present, Barkhausen signal data are calibrated against x-ray diffraction results, which makes the stress evaluation process expensive,

time-consuming, and destructive. However, a linear relationship between stress and a measurable parameter shown here allows for rapid, on-site, in-service, nondestructive testing. Once the strength of relationship between the reciprocal of the Barkhausen peak voltage and engineering stress is obtained, specimens of unknown stress state can be assessed without the need to input x-ray diffraction data. The ability to calibrate against a linear model lends great utility and can serve as a basis for developing a frequency dependent model for the stress-depth profiling of ferromagnetic structures [10].

#### ACKNOWLEDGMENT

The authors would like to thank the Department of Aerospace Engineering at Iowa State University for the use of the Universal Testing Machine in the Strength of Materials Laboratory for the tensile test and Dr. J. A. Schaefer Senior Lecturer in the Department of Aerospace Engineering at Iowa State University for his assistance in conducting the tensile test.

#### REFERENCES

- [1] D. C. Jiles and S. Hariharan, "Interpretation of the magnetization mechanism in terfenol-d using barkhausen pulse-height analysis and irreversible magnetostriction," *J. Appl. Phys.*, vol. 67, no. 9, pp. 5013–5015, 1990.
- [2] R. Ranjan, D. C. Jiles, O. Buck, and R. Thompson, "Grain size measurement using magnetic and acoustic barkhausen noise," *J. Appl. Phys.*, vol. 61, no. 8, pp. 3199–3201, 1987.
- [3] D. C. Jiles, "Dynamics of domain magnetization and the Barkhausen effect," *Czechoslovak J. Phys.*, vol. 50, no. 8, pp. 893–924, 2000.
- [4] D. C. Jiles and L. Suominen, "Effects of surface stress on barkhausen effect emissions: Model predictions and comparison with x-ray diffraction studies," *IEEE Trans. Magn.*, vol. 30, no. 6, pp. 4924–4926, Jun., 1994.
- [5] C. Jagadish, L. Clapham, and D. Atherton, "Influence of uniaxial elastic stress on power spectrum and pulse height distribution of surface Barkhausen noise in pipeline steel," *IEEE Trans. Magn.*, vol. 26, no. 3, pp. 1160–1163, Mar. 2002.
- [6] H. Sakamoto, M. Okada, and M. Homma, "Theoretical analysis of Barkhausen noise in carbon steels," *IEEE Trans. Magn.*, vol. 23, no. 5, pp. 2236–2238, May 1987.
- [7] L. Mierczak, D. C. Jiles, and G. Fantoni, "A new method for evaluation of mechanical stress using the reciprocal amplitude of magnetic barkhausen noise," *IEEE Trans. Magn.*, vol. 47, no. 2, pp. 459–465, Feb. 2011.
- [8] S. Santa-aho, M. Vippola, T. Saarinen, M. Isakov, A. Sorsa, M. Lindgren, L. Kauko, and L. Toivo, "Barkhausen noise characterisation during elastic bending and tensile-compression loading of case-hardened and tempered samples," *J. Mater. Sci.*, vol. 47, no. 17, pp. 6420–6428, 2012.
- [9] P. Garikepati, T. T. Chang, and D. C. Jiles, "Theory of ferromagnetic hysteresis: Evaluation of stress from hysteresis curves," *IEEE Trans. Magn.*, vol. 24, no. 6, pp. 2922–2924, Jun. 1988.
- [10] O. Kypris, I. C. Nlebedim, and D. C. Jiles, "Mapping stress as a function of depth at the surface of steel structures using a specialized magnetic Barkhausen noise technique," *IEEE Trans. Magn.*, vol. 48, no. 11, pp. 4428–4431, Nov. 2012.



# Mapping Stress as a Function of Depth at the Surface of Steel Structures Using a Frequency Dependent Magnetic Barkhausen Noise Technique

O. Kypris<sup>1</sup>, I. C. Nlebedim<sup>2</sup>, and D. C. Jiles<sup>1,2</sup>, *Fellow, IEEE*

<sup>1</sup>Department of Electrical and Computer Engineering, Iowa State University, Ames, IA, 50011 USA

<sup>2</sup>Ames Laboratory, U.S. Department of Energy, Ames, IA, 50011 USA

**Profiling of stress as a function of depth is an important tool for nondestructive evaluation and can be used to prevent catastrophic failures in structures. In this work, the underlying theory of a new model for the depth profiling of stress in ferromagnetic structures based on the magnetic Barkhausen method is investigated and commented upon. In the model, a ferromagnetic structure is divided into layers of different stress states. By analysis of the constituent equations it was found that the measured Barkhausen voltage increases as the frequency span increases, for both the one- and the two layer cases. It was also found that two layers with the same amplitude of Barkhausen emission at the origin can be approximated as one layer, provided that the upper and lower depths, as well as the frequency range are identical.**

**Index Terms**—Magnetic Barkhausen noise, nondestructive evaluation, stress depth profiling.

## I. INTRODUCTION

**B**ARKHAUSEN emissions result from discontinuous, irreversible changes in magnetization. The voltage induced in a coil due to these discontinuities appears as a noise signal, and is termed the Barkhausen effect. It is widely used as a tool in nondestructive evaluation for determining the stress state in the near surface regions of load bearing components. The Barkhausen noise amplitude and spectrum vary depending on the type of ferromagnetic material, the stress state, defect/inclusion sizes and microstructure [1], [2]. In recent years Barkhausen noise has been used for assessing residual stress levels in steel structures [3], [4]. This is particularly useful in applications where ferromagnetic materials, such as steels, are used for load bearing parts. Studies have shown that the process resulting in the emission of magnetic Barkhausen noise is rather complex [5]–[7].

Recently it has been shown that the peak amplitude of the voltage envelope of magnetic Barkhausen noise signals correlated with the stress state of a ferromagnetic material [8]. However, profiling the depth dependence of stress using the magnetic Barkhausen effect still remains a challenge. In previous work, a model for stress depth profiling based on frequency- and depth dependent eddy current damping of Barkhausen emissions was presented, [9]. The present study provides an in-depth theoretical analysis of the model equations, and the experimental procedures required to verify the model in future work. The aim is to develop a method for mapping stress as a function of depth in ferromagnetic structures.

## II. THEORY

### A. Overview of the Model

Assuming plane wave propagation, an electromagnetic emission  $V_{\text{orig}}$  of angular frequency  $\omega$  originating at some depth  $x$

in a material of conductivity  $\sigma$  and permeability  $\mu$  undergoes eddy-current damping, such that the measured voltage at the surface will be [10]

$$V_{\text{meas}}(x, \omega) = V_{\text{orig}}(x, \omega) e^{-\frac{x}{\delta}} \quad (1)$$

To simplify the analysis, the frequency spectrum of each Barkhausen emission is assumed to have only one frequency component. The quantity  $\delta$  is the distance at which an electromagnetic signal is attenuated to  $1/e$  of its original value due to eddy current dissipation.

In order to graphically describe the model, an illustration of the solution of the model equations is presented in Fig. 1. Consider two different emissions of frequency  $f_a = 0.5$  MHz and  $f_b = 0.1$  MHz (frequencies present in a typical Barkhausen noise spectrum), which occur at depth  $x_a$  and  $x_b$  inside a specimen of constant permeability and conductivity. The emission of frequency  $f_a$  will travel a distance  $\delta_a$  before being attenuated to  $1/e$  of its initial amplitude. Its skin depth lies between depths  $x_0$  and  $x_1$ , hence emission  $f_a$  is considered to be present in a Barkhausen measurement band-passed from  $\omega_0$  to  $\omega_1$ . Assuming for the purposes of the analysis that complete attenuation occurs over a propagation depth  $\delta$ , the emission of frequency  $f_b$  will not be present in that measurement. However the emission at frequency  $f_b$  will be present in a measurement band-passed from  $\omega_0$  to  $\omega_2$ .

For a given frequency, emissions originating from regions deeper in the material will be attenuated more than emissions originating from shallower regions. Consequently emissions of relatively high frequency, originating from deep regions of the specimen, do not reach the surface. Hence, it is possible to identify the depth of emission by defining cut-off frequencies for a measurement, which correspond to particular depths. It is important to remember that emissions at frequency  $f_b$  can also originate in the region between  $x_0$  and  $x_1$ . This is because Barkhausen emissions occur at all depths and over a range of different frequencies. Hence, an emission measured at the surface will therefore be a superposition of many different emissions of the same frequency occurring at different depths. As a result, to distinguish between the emissions at different depths

Manuscript received March 02, 2012; revised April 12, 2012; accepted April 17, 2012. Date of current version October 19, 2012. Corresponding author: O. Kypris (e-mail: kypris@iastate.edu).

Color versions of one or more of the figures in this paper are available online at <http://ieeexplore.ieee.org>.

Digital Object Identifier 10.1109/TMAG.2012.2196792



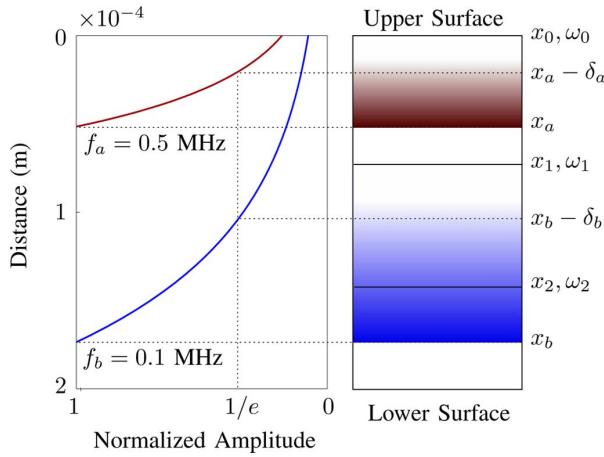


Fig. 1. Emissions of frequency  $f_a = 0.5$  MHz and  $f_b = 0.1$  MHz originating at depths  $x_a$  and  $x_b$  inside a material of constant permeability and conductivity. Attenuation occurs due to the skin effect described in (1). The model assumes a sharp cutoff at  $\delta$ , which allows setting cutoff depths to facilitate the separation of emissions. As long as the skin depth of an emission falls between the upper and lower cutoffs of a layer, it is detected within that layer. Attenuation of the amplitude of emissions is represented by fading colour.

and construct a stress profile, (1) is not sufficient. This has been taken into account in the model, [9].

The basic model considers two consecutive layers which have different values of stress. In each of these layers stress is considered to be homogeneous. Barkhausen measurements at the surface are band-pass filtered to retrieve two signals; one from  $\omega_0$  to  $\omega_1$ , representing emissions from the first layer, and one from  $\omega_0$  to  $\omega_2$  (where  $\omega_2$  is smaller than  $\omega_1$ ), representing emissions from the combined first and second layers. Provided the absolute value of stress in the first layer is known, a set of model equations is used to calculate the stress in the second layer. The signal coming from consecutive layers is found by varying the low frequency cut-off  $\omega_2$  and repeating the procedure. The following sections describe the model equations which apply to a single uniformly stressed layer of material and two uniformly stressed layers of material.

### B. Magnetic Barkhausen Emissions From a Single, Uniformly Stressed Layer

Consider a ferromagnetic slab of finite thickness, relative magnetic permeability  $\mu_r$ , electrical resistivity  $\rho$ , and stress  $\sigma$  as schematically shown in Fig. 2. If Barkhausen emissions of frequency  $\omega_0$  to  $\omega_1$  occur from depth  $x_0$  to depth  $x_1$  into the specimen, and assuming plane wave propagation as well as a white noise spectrum the voltage that is induced in a sense coil located at the surface can be expressed as in (2)

$$\begin{aligned} V_{meas}(x_0, x_1, \omega_0, \omega_1) &= \int_{\omega_1}^{\omega_0} \int_{x_0}^{x_1} V_{orig1} e^{-\alpha x \sqrt{\omega}} dx d\omega \\ &= V_{orig1} f(x_0, x_1, \omega_0, \omega_1) \end{aligned} \quad (2)$$

where  $\alpha = (2\rho/\mu_0\mu_r)^{1/2}$ . The function  $f(x_0, x_1, \omega_0, \omega_1)$  is a generalized attenuation function, the ratio of total measured

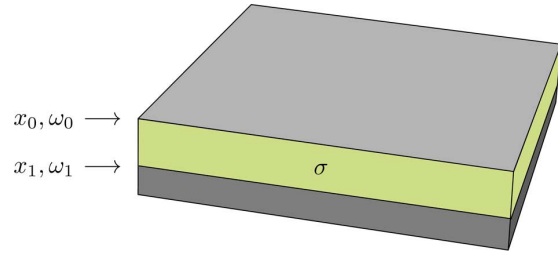


Fig. 2. Layered specimen considered by the model, where layer boundaries correspond to specific frequencies. Stress is denoted by  $\sigma$ .

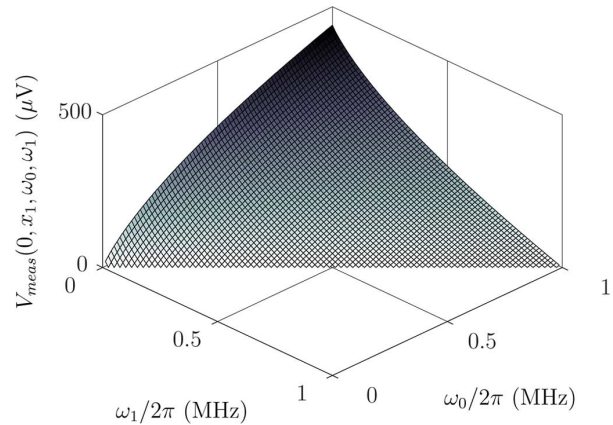


Fig. 3. Measured voltage from one layer plotted as a function of frequencies  $\omega_0$  (upper cutoff) and  $\omega_1$  (lower cutoff). For this study,  $\rho = 8.93 \times 10^{-8}$   $\Omega/m$ ,  $\mu_r = 50$  and  $V_{orig} = 2\mu V$ . Depth  $x_1$  was set to 100  $\mu m$ . Note that when  $\omega_1 > \omega_0$ , there is no detected voltage.

Barkhausen voltage at the surface to the Barkhausen voltage at the point of origin. It is given by

$$\begin{aligned} f(x_0, x_1, \omega_0, \omega_1) &= \frac{2}{\alpha^2} \left[ \frac{1}{x_1} \left( e^{-\alpha x_1 \sqrt{\omega_0}} - e^{-\alpha x_1 \sqrt{\omega_1}} \right) \right. \\ &\quad \left. - \frac{1}{x_0} \left( e^{-\alpha x_0 \sqrt{\omega_0}} - e^{-\alpha x_0 \sqrt{\omega_1}} \right) \right]. \end{aligned} \quad (3)$$

In the limiting case where  $x_0 = 0$  and emissions from the surface to  $x_1$  are considered, the attenuation function becomes

$$\begin{aligned} f(0, x_1, \omega_0, \omega_1) &= \frac{2}{x_1 \alpha^2} [(e^{-x_1 \alpha \sqrt{\omega_0}} - e^{-x_1 \alpha \sqrt{\omega_1}} \\ &\quad + x_1 \alpha (\sqrt{\omega_0} - \sqrt{\omega_1})]. \end{aligned} \quad (4)$$

The above expression is experimentally verifiable when  $x_1$  is equal to the slab thickness. That is, when emissions from all depths are taken into account. In general, when the slab thickness is greater than  $x_1$  the measured signal at the surface will not only represent the emissions occurring within the interval 0 to  $x_1$  but also emissions in the same frequency range originating at depths beyond  $x_1$ .

Fig. 3 is a plot of the voltage given by (4), where  $\mu_r = 50$ ,  $\rho = 8.93 \times 10^{-8}$   $\Omega/m$  and  $V_{orig} = 2\mu V$ . In other words, the average Barkhausen emission in the specimen induces a voltage of 2  $\mu V$  in its immediate vicinity. During its propagation towards the surface, the induced voltage is attenuated exponentially as

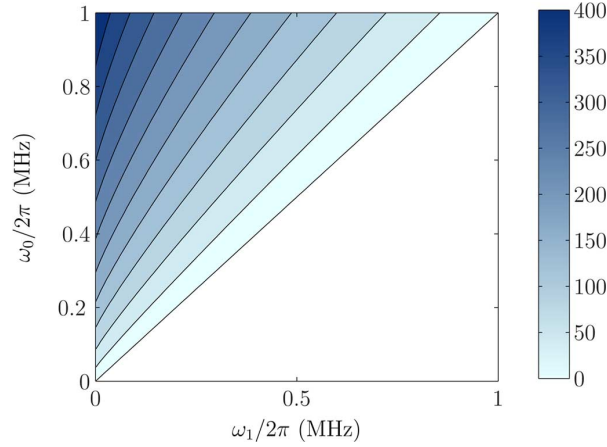


Fig. 4. Contour plot of the measured voltage from one layer, as a function of frequencies  $\omega_0$  (upper cutoff) and  $\omega_1$  (lower cutoff). Voltage values are expressed in  $\mu V$ . Note that when  $\omega_1 > \omega_0$ , there is no detected voltage.

determined by the term  $\alpha$ . For this plot,  $x_1 = 100 \mu m$ , which is also the thickness of the specimen. The frequency cut-offs  $\omega_0/2\pi$  and  $\omega_1/2\pi$  are each varied from 30 kHz to 1 MHz, which correspond to penetration depths  $\delta$  of  $\sim 122 \mu m$  and  $\sim 21 \mu m$  for a material of the given resistivity and permeability. Having established a constant thickness and varying the frequency limits  $\omega_0$  and  $\omega_1$ , a nonlinear trend is apparent.

Fig. 4 is a contour plot of the measured voltage from one layer, plotted as a function of the two cutoff frequencies. It can be seen that the peak voltage is  $\sim 400 \mu V$ . Since  $\omega_1$  and  $\omega_0$  were defined as the lower and upper cutoff frequencies respectively, values of  $V_{meas}$  for which  $\omega_1 > \omega_0$  can be ignored for the purposes of this model. Hence, they were omitted from both plots.

### C. Magnetic Barkhausen Emissions From A Combination of Two Uniformly Stressed Layers

In order to produce a stress depth profile where stress takes on different values with depth, it is necessary to consider the test specimen divided into more than one region, as would be practically expected. A second layer which extends deeper into the specimen has to be considered. However, if the average stresses in the first and second layer are different, the Barkhausen emission amplitudes at their origin will also be different. Then this can be used to determine the difference in stress between the two layers if it is possible to distinguish between emissions from different depths (Fig. 5).

Consequently,  $V_{orig1}$  and  $V_{orig2}$  are defined as the amplitude of emission at the origin for the first and second layer respectively. The expression that takes into account emissions from both is (5)

$$\begin{aligned} V_{meas}(0, x_1, x_2, \omega_0, \omega_1, \omega_2) \\ = V_{meas}(0, x_1, \omega_0, \omega_1) \left( 1 + \frac{f(0, x_1, \omega_1, \omega_2)}{f(0, x_1, \omega_0, \omega_1)} \right) \\ + V_{orig2} f(x_1, x_2, \omega_1, \omega_2). \end{aligned} \quad (5)$$

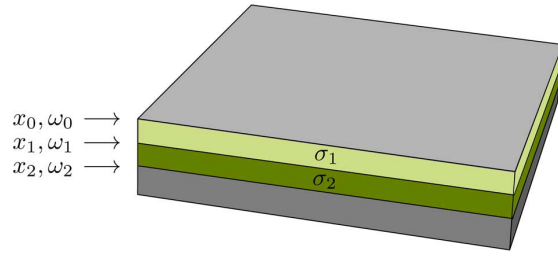


Fig. 5. Layered specimen considered by the model, where layer boundaries correspond to specific frequencies. Stresses in the first and second layer are denoted by  $\sigma_1$  and  $\sigma_2$  respectively.

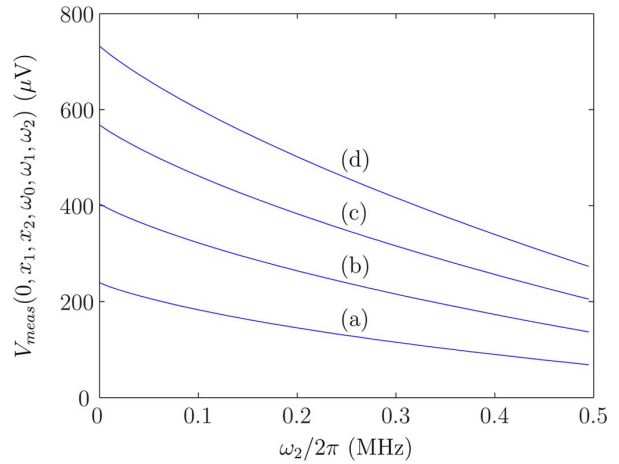


Fig. 6. Measured voltage from two layers plotted as a function of  $\omega_2$ . In this plot,  $\omega_0/2\pi = 1$  MHz,  $\omega_1/2\pi = 0.5$  MHz and  $V_{orig2} = 2 \mu V$ . The value of  $V_{orig1}$  was set to (a)  $1 \mu V$ , (b)  $2 \mu V$ , (c)  $3 \mu V$  and (d)  $4 \mu V$ . The depths were fixed to  $x_1 = 50 \mu m$  and  $x_2 = 100 \mu m$ .

The first term on the right hand side contains the attenuation ratio  $f(0, x_1, \omega_1, \omega_2)/f(0, x_1, \omega_0, \omega_1)$  which normalizes for emissions in the  $\omega_2, \omega_1$  range coming from the first layer. The second term contains the quantity of interest,  $V_{orig2}$  (from which the stress in the second layer can be determined) multiplied by the attenuation function.

To examine the effect of varying  $V_{orig1}$  relative to  $V_{orig2}$ , (5) was plotted for  $V_{orig1}$  at 1, 2, 3 and  $4 \mu V$ , while keeping  $V_{orig2}$  constant at  $2 \mu V$ . In Fig. 6 the measured voltage is plotted as a function of  $\omega_2$ , with  $\omega_1 = 0.5$  MHz and  $\omega_0 = 1$  MHz being held constant. Fig. 6 shows that as the value of  $V_{orig1}$  is increased, there is a corresponding increase in the peak value of the measured voltage. It can be seen that when  $V_{orig1} = V_{orig2} = 2 \mu V$ , the peak voltage is  $\sim 400 \mu V$ .

In Fig. 7, the measured voltage is plotted as a function of  $\omega_2$  and  $\omega_1$ . Having set  $\omega_0 = 1$  MHz, and both  $V_{orig1}$  and  $V_{orig2}$  at  $2 \mu V$ , it can be seen that the effect of varying  $\omega_1$  is not significant and can be ignored in this case. Again, values of  $V_{meas}$  that do

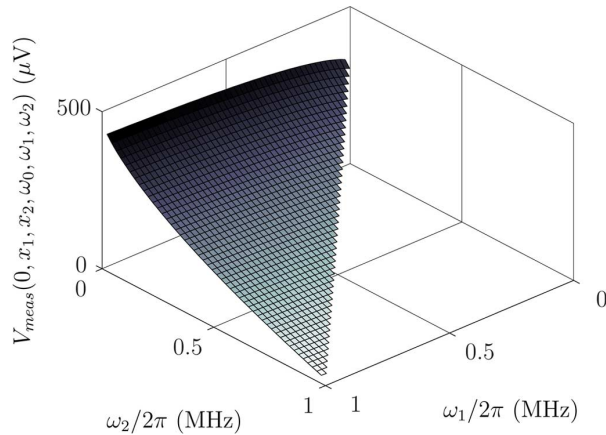


Fig. 7. Measured voltage from two layer plotted as a function of frequencies  $\omega_1$  (intermediate cutoff) and  $\omega_2$  (lower cutoff). In this plot,  $\omega_0/2\pi = 1$  MHz,  $V_{orig1} = V_{orig2} = 2 \mu\text{V}$ . The depths were fixed to  $x_1 = 50 \mu\text{m}$  and  $x_2 = 100 \mu\text{m}$ . Note that when  $\omega_1 < \omega_2$ , there is no detected voltage.

not satisfy the condition  $\omega_2 < \omega_1$  can be ignored, so they were omitted in both plots.

### III. CONCLUSION

In this work, a new model for the depth profiling of stress in ferromagnetic structures was analyzed. It was found that the measured voltage increases as the frequency span increases, for both the one- and the two layer cases. In particular, the peak voltage reaches  $\sim 400 \mu\text{V}$ , for a specimen of  $100 \mu\text{m}$  thickness,  $\mu_r = 50$ ,  $\rho = 8.93 \times 10^{-8} \Omega/m$ , having considered emissions of a frequency range of 30 kHz to 1 MHz. Comparison of the peak voltages of Figs. 4 and 6 yields the observation that when  $V_{orig1} = V_{orig2} = 2 \mu\text{V}$ , and the upper and lower cut-off frequencies and depths are identical, the structure can be considered as only consisting of one layer with  $V_{orig} = 2 \mu\text{V}$ . This result can be further generalized to arrive to the conclusion that when emission amplitudes at the origin of different consecutive layers are identical and the cutoff frequencies are identical, the structure can then be approximated as having a single layer.

The experimental verification of the depth profiling model entails several stages. The reciprocal relationship between peak Barkhausen signal amplitude and stress will be incorporated into the model equations. A steel specimen of known permeability, conductivity, magnetostriction and elasticity will be subjected to four-point bending, such that a linear stress profile is

created along its centerline. A Barkhausen measurement at the surface of the specimen will be bandpass filtered at different frequencies, which correspond to different depths. By keeping  $\omega_1$  constant and varying  $\omega_2$ , one can increase the depth range that can be sampled in the second layer. Provided the stress in the first layer is known, one can determine the stress values at different depths into the specimen from the difference in peak Barkhausen voltage between two layers, and thus construct a stress profile. The resulting plot can then be compared to the result of a solid mechanics simulation carried out using finite element method software.

### ACKNOWLEDGMENT

Research at the Ames Laboratory was supported by the Department of Energy-Basic Energy Sciences (Contract No: DE-AC02-07CH11358).

### REFERENCES

- [1] R. Ranjan, D. C. Jiles, O. Buck, and R. Thompson, "Grain size measurement using magnetic and acoustic Barkhausen noise," *J. Appl. Phys.*, vol. 61, no. 8, pp. 3199–3201, 1987.
- [2] D. C. Jiles and S. Hariharan, "Interpretation of the magnetization mechanism in terfenol-d using Barkhausen pulse-height analysis and irreversible magnetostriction," *J. Appl. Phys.*, vol. 67, no. 9, pp. 5013–5015, 1990.
- [3] D. C. Jiles and L. Suominen, "Effects of surface stress on Barkhausen effect emissions: Model predictions and comparison with x-ray diffraction studies," *IEEE Trans. Magn.*, vol. 30, no. 6, pp. 4924–4926, Nov. 1994.
- [4] C. Jagadish, L. Clapham, and D. Atherton, "Influence of uniaxial elastic stress on power spectrum and pulse height distribution of surface Barkhausen noise in pipeline steel," *IEEE Trans. Magn.*, vol. 26, no. 3, pp. 1160–1163, May 1990.
- [5] B. Alessandro, C. Beatrice, G. Bertotti, and A. Montorsi, "Domain-wall dynamics and Barkhausen effect in metallic ferromagnetic materials. I. Theory," *J. Appl. Phys.*, vol. 68, no. 6, pp. 2901–2907, 1990.
- [6] B. Alessandro, C. Beatrice, G. Bertotti, and A. Montorsi, "Domain-wall dynamics and Barkhausen effect in metallic ferromagnetic materials. II. Experiments," *J. Appl. Phys.*, vol. 68, no. 6, pp. 2908–2915, 1990.
- [7] H. Sakamoto, M. Okada, and M. Homma, "Theoretical analysis of Barkhausen noise in carbon steels," *IEEE Trans. Magn.*, vol. 23, no. 5, pp. 2236–2238, Nov. 1987.
- [8] L. Mierczak, D. C. Jiles, and G. Fantoni, "A new method for evaluation of mechanical stress using the reciprocal amplitude of magnetic Barkhausen noise," *IEEE Trans. Magn.*, vol. 47, no. 2, pp. 459–465, Feb. 2011.
- [9] L. Mierczak, Y. Melikhov, and D. C. Jiles, "Reconstructing residual stress depth profiles using magnetic Barkhausen noise method," presented at the Proc. 55th Conf. Magn. Mater., Atlanta, GA, Nov. 14–18, 2010, poster presentation (FQ-12).
- [10] S. Tiitto and S. Saynajakangas, "Spectral damping in Barkhausen noise," *IEEE Trans. Magn.*, vol. MAG-11, no. 6, pp. 1666–1672, Nov. 1975.

# A New Method for Obtaining Stress-Depth Calibration Profiles for Non-Destructive Evaluation Using a Frequency-Dependent Model of Barkhausen Emissions

O. Kypris<sup>1</sup>, I. C. Nlebedim<sup>1,2</sup>, and D. C. Jiles<sup>1,2</sup>, *Fellow, IEEE*

<sup>1</sup>Department of Electrical and Computer Engineering, Iowa State University, Ames, IA 50011 USA

<sup>2</sup>Ames Laboratory, U.S. Department of Energy, Ames, IA 50011 USA

This study presents the development of a non-destructive method of detecting stress as a function of depth, useful for inspecting steel structures and components without the need to calibrate against x-ray diffraction data. A new frequency-dependent model for Barkhausen emissions based on the attenuation of emission with frequency and distance is used to extract depth-dependent stress information. Controlled, uniform stresses are induced in an ASTM A36 steel specimen, which are then used as a reference to obtain stress-voltage calibration profiles. An inversion process can then be employed to assess specimens of unknown stress states, by using the previously calculated profiles. The slope of the calibration profiles is found to vary with depth, and a simple computer algorithm may be used to extract stresses at different depths by using an averaging method.

**Index Terms**—Barkhausen effect, magnetic Barkhausen noise, non-destructive evaluation, non-destructive testing, stress depth profiling.

## I. INTRODUCTION

NON-DESTRUCTIVE evaluation is a useful tool for the prediction and prevention of component failures. Magnetic non-destructive evaluation has been used for assessing stress levels in steel structures [1] because there is a strong coupling between the magnetic and mechanical properties of ferromagnetic materials. This is particularly important because different types of steels are used in a wide range of applications. When a cyclically varying magnetic field is applied to such materials, discontinuous changes in magnetization result in Barkhausen noise which depends on microstructural conditions such as defect/dislocation density and grain size [2], [3]. Barkhausen noise can then be measured using a search coil placed on the surface of the specimen. This dependence of Barkhausen noise on mechanical and microstructural states can, as a result, be used in non-destructive evaluation of steels because the phenomenon shows great sensitivity to elastic deformation.

Despite the numerous studies on Barkhausen noise in recent years [4]–[6], the complexity of the underlying physical process has prevented the development of an all-inclusive theory. In the field of magnetic non-destructive evaluation, calibration of Barkhausen noise measurement results against x-ray diffraction data is a common practice, especially for the assessment of sub-surface stresses. This reliance on x-ray diffraction data can be in part attributed to the lack of a theoretical explanation for the relationship between stress and a Barkhausen measurement parameter, such as the peak voltage envelope amplitude.

However, in recent work [7] an expression based on a linear relationship between stress and the reciprocal peak voltage envelope amplitude was presented, following a similar trend to that between anhysteretic susceptibility at the origin and stress [8]. This relationship was later verified in different steel compositions [9]. The strength of the relationship between stress  $\sigma$  and  $1/V$  is quantified by a proportionality factor  $b'$ , which is a modified magnetostriction constant, as shown in (1):

$$\frac{1}{V(\sigma_1)} - \frac{1}{V(\sigma_2)} = \frac{3b'(\sigma_1 - \sigma_2)}{\mu_0}, \quad (1)$$

where  $\sigma_1$  and  $\sigma_2$  denote different stress states, such that  $V(\sigma_1)$  and  $V(\sigma_2)$  are the Barkhausen voltages corresponding to stress  $\sigma_1$  and  $\sigma_2$ . This relationship has been used as a basis to develop a model for stress-depth profiling [10], which relies on the eddy-current damping of Barkhausen emissions to identify the amplitude of Barkhausen emissions at particular depths. The model inputs are the analysis depths, the slope and offset of the linear relationship between voltage and stress for each depth range and some experimentally measurable material parameters, such as magnetic permeability and electrical conductivity.

In the present work, an ASTM A36 steel specimen was subjected to uniaxial tension, while its Barkhausen response was measured. The model equations were then applied to the Barkhausen data, in order to calculate the value of the peak Barkhausen voltage envelope amplitude that corresponds to different depth ranges. Using the linear relationship of stress versus reciprocal of the peak Barkhausen voltage envelope amplitude, calibration profiles of slope proportional to  $b'$  corresponding to each depth range were obtained, and it is shown how the slopes and offsets of the calibration profiles vary as different depths are considered. An inversion method for assessing specimens of unknown stress state by using the calibration profiles is proposed, and an equation for calculating stresses at different depths is derived, based on an averaging

Manuscript received November 05, 2012; revised February 15, 2013; accepted February 28, 2013. Date of current version July 15, 2013. Corresponding author: O. Kypris (e-mail: kypris@iastate.edu).

Color versions of one or more of the figures in this paper are available online at <http://ieeexplore.ieee.org>.

Digital Object Identifier 10.1109/TMAG.2013.2251328



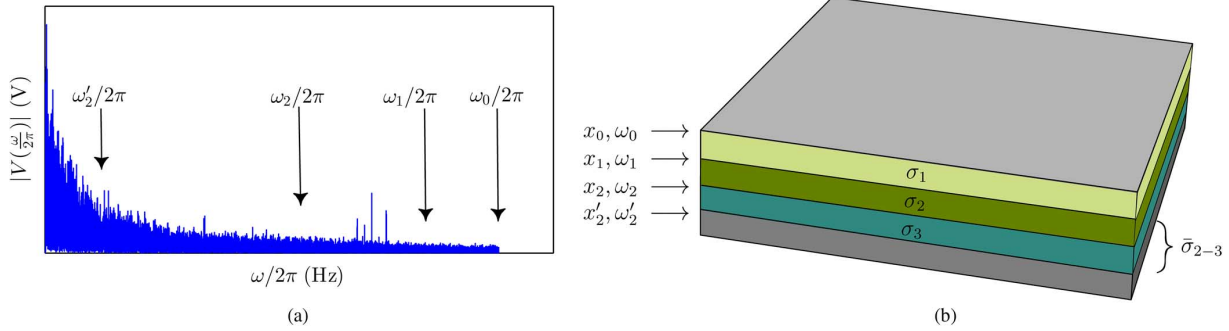


Fig. 1. (a) Typical measured Barkhausen noise spectrum, with  $\omega_0, \omega_1, \omega_2$ , denoting the upper, intermediate and lower cutoff frequencies (*frequencies not to scale*). The  $\omega_2$  limit can be lowered to  $\omega'_2$  in order to sample deeper regions of the specimen. (b) Ferromagnetic specimen divided in three layers of equal volume, where  $\sigma_1, \sigma_2$  and  $\sigma_3$  denote the stress magnitudes in the first, second and third layer respectively. Also  $\bar{\sigma}_{2-3} = (1/2)(\sigma_2 + \sigma_3)$ .

method. Furthermore, the practical limitations of the model implementation are discussed.

## II. THEORY

In previous work [10], the basis of the model comprised of a relationship that quantifies the measured Barkhausen voltage at the surface in terms of the voltage of a single Barkhausen emission  $V_{orig}$  at its origin, such that

$$V_{meas}(x, \omega) = V_{orig}(x, \omega)e^{-\frac{x}{\delta}}, \quad (2)$$

where  $x$  is the depth at which the emission originates. The quantity  $\delta$  is the penetration depth which depends on the angular frequency  $\omega$  of the emission as well as the material permeability  $\mu$  and resistivity  $\rho$ , as shown in (3):

$$\delta = \sqrt{\frac{2\rho}{\omega\mu}}. \quad (3)$$

Consider initially that the specimen has only a single layer, where the measured Barkhausen voltage  $V_{meas}(0, x_1, \omega_0, \omega_1)$  corresponding to the first layer is represented by an integral over all depths from the surface to some depth  $x_1$  and over all frequencies from  $\omega_0$  to  $\omega_1$  [10]. This results in the expression

$$V_{meas}(0, x_1, \omega_0, \omega_1) = V_{orig1}f(0, x_1, \omega_0, \omega_1), \quad (4)$$

where  $V_{orig1}$  is the voltage of a single Barkhausen noise emission in the first layer, assuming, for mathematical tractability, a white Barkhausen emission spectrum at the origin. The term  $f(0, x_1, \omega_0, \omega_1)$  is a special attenuation function for the limiting case where  $x_0 = 0$ . Consider again, the addition of a second layer of material with depth  $x_2$  and thickness  $x_2 - x_1$ . The Barkhausen voltage measured at the surface, emanating from the two combined layers of material can be represented as  $V_{meas}(0, x_1, x_2, \omega_0, \omega_1, \omega_2)$  [10], such that:

$$V_{meas}(0, x_1, x_2, \omega_0, \omega_1, \omega_2) = V_{meas}(0, x_1, \omega_0, \omega_1) \times \left(1 + \frac{f(0, x_1, \omega_1, \omega_2)}{f(0, x_1, \omega_0, \omega_1)}\right) + V_{orig2}f(x_1, x_2, \omega_1, \omega_2) \quad (5)$$

where  $V_{orig2}$  is the voltage of a single Barkhausen emission originating in the second layer. Fig. 1 illustrates the concept of a layered specimen, and how sampling different parts of the Barkhausen frequency spectrum translates into sampling different depth ranges.

Both  $V_{meas}(0, x_1, \omega_0, \omega_1)$  and  $V_{meas}(0, x_1, x_2, \omega_0, \omega_1, \omega_2)$  are experimentally measurable quantities, which correspond to two filtered versions of the measured Barkhausen signal, one band-passed from  $\omega_0$  to  $\omega_1$  and the other band-passed from  $\omega_0$  to  $\omega_2$ , as seen in Fig. 1. However, the voltage emanating from the second layer cannot be directly measured because emissions of the same frequency may occur in different depths, making it impossible to identify the depth of emission simply by filtering the measured signal. Nevertheless, the value of  $V_{orig2}$  can be calculated by subtracting a normalized version of the first layer voltage  $V_{meas}(0, x_1, \omega_0, \omega_1)$  from the combined layer voltage  $V_{meas}(0, x_1, x_2, \omega_0, \omega_1, \omega_2)$  and by solving for  $V_{orig2}$ .

The depth-profiling model considers complete attenuation at the skin depth, such that when the lower cutoff frequency is decreased, more material volume is sampled and more Barkhausen emissions are taken into account. The voltage of a single Barkhausen emission  $V_{orig1}$  can be solved for by rearranging (4), such that:

$$V_{orig1} = \frac{V_{meas}(0, x_1, \omega_0, \omega_1)}{f(0, x_1, \omega_0, \omega_1)}. \quad (6)$$

Similarly, (5) can be rearranged to yield the average amplitude of a Barkhausen emission in the second layer  $V_{orig2}$ , such that

$$V_{orig2} = \frac{1}{f(x_1, x_2, \omega_1, \omega_2)} \left( V_{meas}(0, x_1, x_2, \omega_0, \omega_1, \omega_2) - V_{meas}(0, x_1, \omega_0, \omega_1) \left(1 + \frac{f(0, x_1, \omega_1, \omega_2)}{f(0, x_1, \omega_0, \omega_1)}\right) \right) \quad (7)$$

Once the probing depths and corresponding frequencies are calculated, the attenuation functions can be evaluated, and  $V_{meas}(0, x_1, \omega_0, \omega_1)$  as well as  $V_{meas}(0, x_1, x_2, \omega_0, \omega_1, \omega_2)$  can be obtained by filtering the original Barkhausen signal

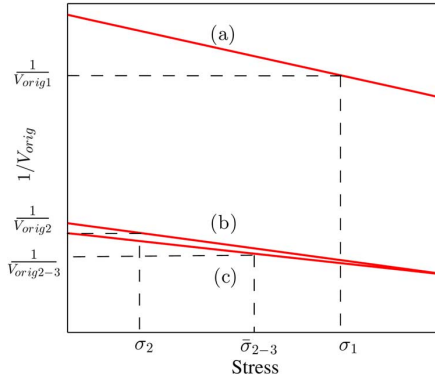


Fig. 2. Conceptual calibration profiles corresponding to specific depths for (a)  $1/V_{orig1}$ , (b)  $1/V_{orig2-3}$ , and (c)  $1/V_{orig2}$ . A specimen of unknown stress state can be assessed by applying (6) and (7), keeping  $\omega_0$ ,  $\omega_1$  and  $\omega_2$  constant with respect to the calibration stage. The reciprocal value of the measured average Barkhausen emission in the first layer  $1/V_{orig1}$  will then lead to a stress  $\sigma_1$ , via the pre-established linear relationship. In a similar manner, the stress  $\sigma_2$  in the second layer, and the average stress  $\bar{\sigma}_{2-3}$  in the combined second and third layer can be found.

accordingly. Thus,  $V_{orig1}$  and  $V_{orig2}$  can be obtained by applying (6) and (7) respectively. These two separate quantities correspond to the first and second layer in the specimen.

The relationship seen in (1) relates the stress state of a layer to the amplitude of the average Barkhausen emission originating in that layer. It should therefore be possible to calibrate against a known stress-voltage relationship, and then use an inversion process to assess samples of unknown stress states.

In order to create a calibration profile it is necessary to start with an unstressed specimen of the material under examination. This will serve as a reference, for which the stress-voltage relationship at different depths is known. By applying a uniform uniaxial tensile stress, measuring the amplitude of Barkhausen emissions, and using (6) and (7),  $1/V_{orig}$  corresponding to each depth range can be plotted versus stress. It is expected that since the stress in the reference specimen is uniform,  $V_{orig1} = V_{orig2} = V_{orig2-3}$ . This will be true provided that treating the Barkhausen frequency spectrum in a piecewise manner, with the skin depth defining the cutoff frequency, is a valid approach. If this assumption is not entirely valid, the calibration curves will not coincide, and will each be characterized by a different offset and slope.

After the calibration profile is created, a specimen of the same composition and unknown stress state can be evaluated. This is done by conducting a Barkhausen measurement and by applying (6) and (7) to compute the Barkhausen peak envelope voltages in the first and second layer. Using the calibration profile, the stress in each layer can subsequently be obtained. By decreasing the lower detection frequency  $\omega_2$  to  $\omega'_2$  in (7), the average stress magnitude  $\bar{\sigma}_{2-3}$  in the combined second and third layer can be determined, provided the calibration profile for  $1/V_{orig2-3}$  exists. Fig. 2 illustrates this concept.

Having  $n$  layers and  $n$  unknown stress magnitudes, the stress-depth profile of the specimen can be deduced by a simple computer algorithm. Provided that layer thicknesses are identical, the average stress in the combined second and third layer can

be denoted as in (8). In the case where the thicknesses are not identical, a weighted average method must be used which is beyond the scope of the present study.

$$\bar{\sigma}_{2-3} = \frac{1}{2}(\sigma_2 + \sigma_3). \quad (8)$$

The stress in the third layer will then be

$$\sigma_3 = 2\bar{\sigma}_{2-3} - \sigma_2. \quad (9)$$

It follows that the stress in the  $n$ th layer can be expressed as

$$\sigma_n = (n-1)\bar{\sigma}_{2-n} - \sum_{i=2}^{n-1} \sigma_i \quad \text{for } n \geq 3, \quad (10)$$

where  $\bar{\sigma}_{2-n}$  is the average stress between the second to  $n$ th layer, and can be found by using the calibration profile for  $1/V_{orig2-n}$ .

### III. EXPERIMENTAL DETERMINATION OF THE CALIBRATION PROFILES

A tensile test specimen of ASTM A36 steel of thickness 6.5 mm, width 12.7 mm and gauge length 26.5 mm was subjected to uniaxial tension in a tensile test machine. The measurement was paused at set intervals, in order to magnetize the specimen and obtain Barkhausen data corresponding to each stress state within the elastic region. The specimen was magnetized with a 100 Hz sinusoidally varying magnetic field of peak amplitude 0.5 kA/m produced by a Barkhausen probe comprising of a magnetizing coil wound around a ferrite C-core electromagnet.

In total, 18 measurements were taken, with 5 trials for each magnitude of stress. A custom Matlab software was written, which filters  $V_{meas}$  accordingly and then solves for the value of  $V_{orig1}$ ,  $V_{orig2}$  and  $V_{orig2-3}$  after having accounted for exponential attenuation of the summed Barkhausen emissions, as shown in (6) and (7). The depths were set to  $x_1 = 60 \mu\text{m}$ ,  $x_2 = 120 \mu\text{m}$ , and  $x'_2 = 180 \mu\text{m}$ , and the corresponding cutoff frequencies  $\omega_1$ ,  $\omega_2$  and  $\omega'_2$  were calculated using values of  $\rho = 0.233 \mu\Omega\text{m}$  and  $\mu_r = 62$ , obtained respectively by dc resistivity and quasi-static hysteresis measurements. The results are plotted as  $1/V_{orig}$  vs. engineering stress in Fig. 3, and Table I lists the value of  $b'$  and the adjusted  $R^2$  goodness of fit ratio for each depth range.

### IV. RESULTS AND DISCUSSION

Fig. 3 shows the reciprocal of the average Barkhausen emission voltage for each layer, plotted against uniaxial engineering stress. The goodness of fit for all measurements indicates a good agreement with the model equation shown in (1). The fact that the calibration profile for  $V_{orig1}$  does not coincide with that of  $V_{orig2}$  and  $V_{orig2-3}$ , possibly indicates that treating the Barkhausen spectrum in a piecewise manner may not be an ideal approach, and future work may show that one needs to alleviate the use of cutoff frequencies in the spectrum to consider it as a whole. It should be noted that the offsets and slopes are also expected to vary with magnetizing frequency. However, this is beyond the scope of the present study.

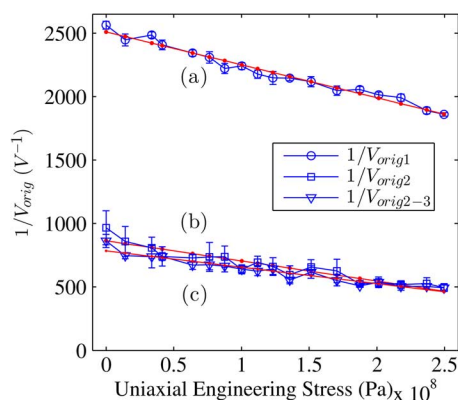


Fig. 3. Experimentally calculated calibration profiles for (a)  $1/V_{orig1}$ , (b)  $1/V_{orig2}$  and (c)  $1/V_{orig2-3}$ , fitted with a linear regression and plotted with 95% confidence intervals. These trends are obtained by filtering the Barkhausen data collected from an ASTM A36 steel specimen under uniaxial tension. In order to produce the calibration profiles, it is assumed that the stress along the measurement direction remains uniform throughout the depth of the specimen. Table I lists the computed calibration profile parameters.

TABLE I  
CALIBRATION PROFILE PARAMETERS

Profile	Depth span ( $\mu\text{m}$ )	$b'$ ( $\text{m s A}^{-1} \text{N}^{-1}$ )	Adj. $R^2$
$\frac{1}{V_{orig1}}$	0-60	$-1.0871 \times 10^{-12}$	0.97031
$\frac{1}{V_{orig2}}$	60-120	$-6.6484 \times 10^{-13}$	0.89073
$\frac{1}{V_{orig2-3}}$	60-180	$-5.3942 \times 10^{-13}$	0.91055

In order to successfully use the calibration profiles to assess the variation of stress with depth for specimens of unknown stress state, certain conditions must be met. Particularly, the measurement parameters for calibration and test specimens must be identical. This includes sensor configuration/geometry, probe-specimen coupling, as well as magnetizing frequency, magnetizing amplitude and sampling frequency. Since the Barkhausen effect is a stochastic process, it is necessary to keep all parameters as constant as possible across measurements.

## V. CONCLUSION

In this work, a method for obtaining calibration profiles for a stress-depth dependence model was proposed. It was found that calibration profiles can be obtained by considering different depth ranges inside a uniformly stressed specimen, and the concept of using an inversion process to assess the stress-depth profile in a test specimen of same material was presented. The calculated profiles do not coincide, indicating that the assumption

of treating the Barkhausen noise frequency spectrum in a piecewise manner may not be entirely valid. A good agreement was established between the linear model of (1) and the Barkhausen data at different depths, which indicates that the linear relationship between the reciprocal of the Barkhausen voltage and stress holds as different portions of the Barkhausen frequency spectrum are considered. It was also shown that the stress in the  $n$ th layer is given by a simple relationship, provided the depth increment is constant. Provided that measurement parameters remain constant throughout the calibration and detection stages, the presented method is intended to alleviate the need for using x-ray diffraction data, as it relies solely on calibrating against known stress values using the reciprocal Barkhausen voltage.

## ACKNOWLEDGMENT

This research was undertaken with support of a Graduate Fellowship for O. Kypris from the Takano Foundation and was also supported by the James and Barbara Palmer Endowment in the Department of Electrical and Computer Engineering at Iowa State University.

## REFERENCES

- [1] D. C. Jiles and L. Suominen, "Effects of surface stress on barkhausen effect emissions: Model predictions and comparison with x-ray diffraction studies," *IEEE Trans. Magn.*, vol. 30, no. 6, pp. 4924–4926, 1994.
- [2] R. Ranjan, D. C. Jiles, O. Buck, and R. Thompson, "Grain size measurement using magnetic and acoustic barkhausen noise," *J. Appl. Phys.*, vol. 61, no. 8, pp. 3199–3201, 1987.
- [3] D. C. Jiles and S. Hariharan, "Interpretation of the magnetization mechanism in ferfenol-d using barkhausen pulse-height analysis and irreversible magnetostriction," *J. Appl. Phys.*, vol. 67, no. 9, pp. 5013–5015, 1990.
- [4] B. Alessandro, C. Beatrice, G. Bertotti, and A. Montorsi, "Domain-wall dynamics and barkhausen effect in metallic ferromagnetic materials. i. theory," *J. Appl. Phys.*, vol. 68, no. 6, pp. 2901–2907, 1990.
- [5] B. Alessandro, C. Beatrice, G. Bertotti, and A. Montorsi, "Domain-wall dynamics and barkhausen effect in metallic ferromagnetic materials. ii. experiments," *J. Appl. Phys.*, vol. 68, no. 6, pp. 2908–2915, 1990.
- [6] H. Sakamoto, M. Okada, and M. Homma, "Theoretical analysis of Barkhausen noise in carbon steels," *IEEE Trans. Magn.*, vol. 23, no. 5, pp. 2236–2238, 1987.
- [7] L. Mierczak, D. C. Jiles, and G. Fantoni, "A new method for evaluation of mechanical stress using the reciprocal amplitude of magnetic barkhausen noise," *IEEE Trans. Magn.*, vol. 47, no. 2, pp. 459–465, 2011.
- [8] P. Garikepati, T. T. Chang, and D. C. Jiles, "Theory of ferromagnetic hysteresis: Evaluation of stress from hysteresis curves," *IEEE Trans. Magn.*, vol. 24, no. 6, pp. 2922–2924, 1988.
- [9] S. Santa-aho, M. Vippola, T. Saarinen, M. Isakov, A. Sorsa, M. Lindgren, L. Kauko, and L. Toivo, "Barkhausen noise characterisation during elastic bending and tensile-compression loading of case-hardened and tempered samples," *J Mater Sci*, vol. 47, no. 17, pp. 6420–6428, 2012.
- [10] O. Kypris, I. C. Nlebedim, and D. C. Jiles, "Mapping stress as a function of depth at the surface of steel structures using a specialized magnetic Barkhausen noise technique," *IEEE Trans. Magn.*, vol. 48, no. 11, pp. 4428–4431, 2012.



## A model for the Barkhausen frequency spectrum as a function of applied stress

O. Kypris, I. C. Nlebedim, and D. C. Jiles

*Department of Electrical and Computer Engineering, Iowa State University, Ames, Iowa 50011, USA*

(Received 6 December 2013; accepted 6 February 2014; published online 25 February 2014)

We derive a two parameter multi-exponential model to describe the frequency spectrum of Barkhausen noise in bulk steel under high excitation rates and applied tensile stress. We show how the amplitude and shape of the frequency spectrum depend on two directly measurable quantities, Barkhausen voltage and effective magnetic permeability, respectively, and how these change with stress. By incorporating frequency and depth dependence components into our model, we provide a framework for identifying stress variations along depth, which can be used for the purposes of non-destructive characterization. © 2014 AIP Publishing LLC. [<http://dx.doi.org/10.1063/1.4866195>]

### I. INTRODUCTION

Discontinuous and irreversible changes in magnetisation can occur when the domain boundaries of a ferromagnet are displaced. The physical mechanisms that govern these discontinuous magnetisation “jumps,” also known as *Barkhausen jumps*, fall into the category of non-linear dynamical systems. Depending on the degree to which the domains are coupled inside the material, displacement of a domain boundary may trigger the displacement of neighbouring domain boundaries, thereby initiating a magnetic avalanche if the externally applied magnetic field is increased slowly. However, inhomogeneities in the lattice tend to pin the domain boundaries to particular locations because it is energetically favourable. This pinning inhibits the domain wall motion, when the applied magnetic field is insufficient to propagate the domain wall past the pinning point. If the strength of coupling between adjacent magnetic domains and the degree of randomness in the pinning potential reach some critical value, the shapes of avalanches with different durations become similar, exemplifying scale invariance.<sup>1–10</sup> This type of behaviour is a result of Brownian correlations in the pinning potential and can be quantified by power-law functions. These dynamics are also reflected in the power spectrum of Barkhausen emissions, which, at the lower end scales as approximately  $1/\omega^2$  in the Alessandro-Beatrice-Bertotti-Montorsi (ABBM) model<sup>11,12</sup> and from  $1/\omega^{1.3}$  to  $1/\omega^2$  in the Random Field Ising (RFI) model, depending on the strength of dipolar interactions.<sup>1,13</sup> The regions in which scale invariance applies, widen when the material is driven at a low field rate, below a critical driving velocity. If the driving velocity  $v$  exceeds the critical value  $v_c$ , continuous motion sets in, and it is no longer possible to distinguish between individual avalanches. The scale of this power-law behaviour depends on the domain wall correlation length  $\zeta$ , which controls the range of interaction between the moving domain wall and the pinning sources. During magnetisation, when the rate of applied magnetic field is increased such that  $\zeta$  becomes negligible, the Brownian correlations in the domain wall motion decrease.<sup>14</sup> As a result, Barkhausen emissions begin resembling uncorrelated Gaussian noise, and

their frequency spectrum can be approximated as flat. Since the amplitude at the origin of emissions becomes frequency independent, the most significant non-linear contribution in the spectrum can be attributed to the exponential attenuation caused by eddy current dissipation. This facilitates the derivation of a model that describes the frequency spectrum of Barkhausen emissions as a function of stress and possibly other microstructural variations.

Consider a ferromagnetic specimen, such as bulk steel, mathematically divided into infinitesimally thin layers along its depth, and consider each layer as a source of Barkhausen emissions. By magnetising the specimen at a fast rate, most of the scaling behaviour is eliminated, giving rise to a approximately flat Barkhausen emission spectrum. This emission spectrum is attenuated by eddy currents as they propagate through the specimen and superimpose at the surface to produce the signal that we measured using an induction sensor.

We have derived a two-parameter multi-exponential model for the Barkhausen spectrum and relate the two parameters to uniform tensile stress, with parameter  $\langle V \rangle$  representing the signal amplitude at the point of origin of emissions, and parameter  $\zeta$  quantifying the rate of decay of the emission spectrum. By that, we show that the previously observed bulk relationship between Barkhausen amplitude and stress<sup>15,16</sup> can also be seen in the frequency domain. This result has practical consequences in the area of non-destructive characterization; it introduces the possibility of predicting stress at specific depths inside a magnetic material, solely by measuring the Barkhausen emissions at the surface and analyzing the results in terms of two parameters. It can prove useful in safety-critical applications such as in the aerospace industry, where component failure can lead to loss of human life.<sup>17</sup>

### II. THEORY

In a specimen of ferromagnetic material that is magnetised by an applied field, magnetic avalanches of various durations occur at many different depths simultaneously. The stochastic process that governs these discontinuous



changes in magnetisation is the *Ohrstein-Uhlenbeck process*, quantified by a *Langevin equation*<sup>18</sup>

$$\frac{dH_p}{d\phi} + \frac{H_p}{\xi} = \frac{dW}{d\phi}, \quad (1)$$

where  $W(\phi)$  is the Wiener-Levy process, and its derivative,  $dW/d\phi$  is the Gaussian white-noise process. The pinning field  $H_p(\phi)$  quantifies the extent to which inhomogeneities in the lattice pin the domain walls to energetically favourable positions. The correlation length  $\xi$  quantifies the range of interaction between the moving domain wall and the pinning sources. The time-domain equivalent of (1) is<sup>18</sup>

$$\frac{dH_p}{dt} + \frac{H_p}{\tau_c} = \frac{dW}{dt}, \quad (2)$$

where  $\tau_c = \xi/(d\phi/dt)$ .

At high magnetization rates (typically  $\geq 100$  Hz),  $\tau_c$  becomes small, such that  $H_p \sim dW/dt$ . This implies that at high magnetization rates the pinning field, and consequently the domain wall velocity are governed by a white-noise process. To further clarify what is meant by high magnetization rates, the dimensionless parameter<sup>18</sup>  $c = \tau f$  is invoked, where  $\tau = GS\mu_{irr}/\rho$  and  $f$  is the frequency of the applied field.  $G$  is a constant equal to 0.1356,  $S$  is the cross-sectional area being magnetized,  $\mu_{irr}$  is the irreversible large-scale permeability, and  $\rho$  is the electrical resistivity of the specimen. The cross-sectional area can be approximated as  $S = \delta w$ , where  $\delta = \sqrt{\rho/(\pi f \mu_{irr})}$  and is the penetration depth at a certain applied field frequency, and  $w$  is the width of the section. By substitution, we yield

$$c = \sqrt{\frac{\mu_{irr} f}{\pi \rho}} G w, \quad (3)$$

which for a typical steel resistivity  $\rho = 2.2 \times 10^{-7} \Omega m$ , quasi-static permeability  $\mu_{irr} = 60 \mu_0$ ,  $w = 10$  mm, and  $f = 100$  Hz, yields  $c \cong 0.14$ . In the limit  $c = 0$  and for low applied field rates<sup>8</sup> (typically in the order of 0.05 Hz), the power spectrum of Barkhausen emissions resembles that of Brownian noise (with  $P(\omega) \sim \omega^{-2}$ ), while for  $c > 0$ , and for higher applied field rates (typically  $\sim 100$ – $1000$  Hz) the power spectrum at the origin of emissions flattens out, and begins to resemble a white noise spectrum.

The resulting electromagnetic emissions, which diverge outwards from the origin of local magnetisation changes, will have the same statistical properties. This allows us to express the Barkhausen signal at the origin  $V(t)$  as Gaussian white noise of zero mean and variance  $\sigma^2$

$$V(t) \sim \mathcal{N}(0, \sigma^2). \quad (4)$$

For steels, the addition of magnetoelastic energy due to stress causes the nucleation of  $180^\circ$  domain walls in the direction of applied stress.<sup>19</sup> In materials with positive magnetostriction, an increase in the number of pinned domain walls (caused by elastic stress) leads to an increase in the variance of the noise, owing to the larger number of Barkhausen events occurring at a given time instant. The

mean remains at zero, since the net magnetization increase in the specimen is ignored.

To examine how the emissions attenuate as they propagate through the material, we take the Fourier transform of the signal  $V(t)$  at the origin. It has been shown previously that the Fourier transform of Gaussian, uncorrelated white noise will have a Rayleigh distributed magnitude. For mathematical tractability and clarity, we only consider the mean magnitude of the Fourier transform  $\langle V \rangle$ , which is proportional to the standard deviation of the noise. As the emissions propagate, attenuation as a function of frequency causes the higher frequency components to dissipate faster (Fig. 1), with the rate of attenuation being exponential, such that the measured frequency spectrum at the surface, due to one emission, is

$$V(\omega) = \langle V \rangle e^{i\phi} e^{-\gamma(\omega)x}, \quad (5)$$

where  $\langle V \rangle$  is the expected magnitude of the Fourier transform at the origin,  $\phi$  is the phase of the emission at the point of origin,  $x$  is the distance from the surface to the point of origin of the emission, and  $\gamma(\omega) = \alpha(\omega) + i\beta(\omega)$  is the propagation constant, a function of angular frequency  $\omega$ . Expression (5) describes the propagation of a plane wave in a conductive medium; the sensor measures the perpendicular component of the flux density, with unit vector  $\hat{x}$  normal to the surface. The coefficient  $\alpha(\omega)$  quantifies the rate of attenuation, while  $\beta(\omega)$  is the phase constant and defines the rate of phase change as the wave propagates. In conductors,  $\alpha = \beta = \sqrt{\omega \mu_{eff}/2\rho}$ , where  $\mu_{eff}$  and  $\rho$  represent the effective magnetic permeability (here, we define the effective magnetic permeability as the effective permeability of the magnetic circuit, which includes the test specimen and sensor apparatus) and the electrical resistivity, respectively. For mathematical tractability, we only consider the magnitude of the term  $e^{-\gamma(\omega)x}$  in (5), and we take the mean of the phase at the origin (the phase of the Fourier transform of uncorrelated Gaussian noise is uniformly distributed between  $-\pi$  and  $\pi$ , with a mean of zero). We can then write the attenuated amplitude of emission as

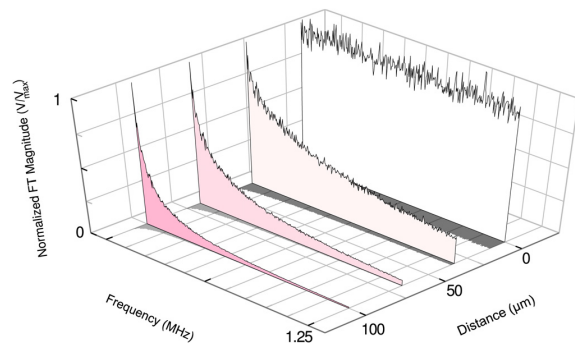


FIG. 1. Effect of eddy current damping on the Barkhausen spectrum. In our model, Barkhausen emissions occurring at an infinitesimally thin region inside a specimen have a white noise frequency spectrum. The energy in emissions is dissipated due to generation of eddy currents, causing the spectrum to become pink as it propagates through the material.

$$V(\omega) = \langle V \rangle e^{-z(\omega)x}. \quad (6)$$

We assume that the variation of  $\rho$  with stress is negligible, thus we only consider  $\mu_{\text{eff}}$  and  $\langle V \rangle$  to be functions of stress. Barkhausen jumps occur everywhere inside the specimen, and every depth  $x$  is the point of origin of a Barkhausen spectrum, of the form (6). Integrating over a range of depths from  $x_0$  to  $x_1$  leads to the following expression for the measured signal at the surface due to all emissions, as a function of frequency  $\omega$  and stress  $\sigma$ :

$$V_{\text{meas}}(\omega, \sigma) = \langle V(\sigma) \rangle \int_0^{x_1} e^{-\sqrt{\frac{\mu_{\text{eff}}(\sigma)}{2\rho}} x} dx, \quad (7)$$

$$= \langle V(\sigma) \rangle \frac{1}{\zeta(\sigma)\sqrt{\omega}} (1 - e^{-\zeta(\sigma)x_1\sqrt{\omega}}), \quad (8)$$

$$= \langle V(\sigma) \rangle f(0, x_1, \zeta(\sigma), \omega), \quad (9)$$

where  $\zeta = \sqrt{\mu_{\text{eff}}/2\rho}$  and is introduced for mathematical tractability. In the above integral, the frequency spectrum of the voltage measured in a coil positioned at the surface is expressed in terms of emissions emanating from a span of depths, or a layer, which can be associated with a mean value of emission amplitude  $\langle V \rangle$  and permeability  $\mu_{\text{eff}}$ .

In previous work, it has been shown that the reciprocal of the peak envelope amplitude of Barkhausen noise in the time domain varies linearly with elastic stress.<sup>15,20</sup> This relationship can be derived from an extension to the theory of ferromagnetic hysteresis.<sup>21</sup> The parameter  $\langle V \rangle$ , being the y-intercept of the frequency spectrum, represents an extrapolated mean value, which is expected to vary with stress, in a way similar to the peak envelope amplitude and RMS. We postulate that  $\langle V \rangle$  follows the same relationship with stress.

### III. MEASUREMENT OF BARKHAUSEN SIGNALS AS A FUNCTION OF APPLIED UNIAXIAL STRESS

In our experiments, we subjected a specimen of A36 steel to uniaxial tensile stress, while measuring the Barkhausen emissions with an induction coil positioned at the surface of the specimen, at an applied field rate of 100 Hz. This frequency also results in higher induced voltage and therefore higher signal to noise ratio. Before fitting our model, the raw measured signal was processed as shown in

Fig. 2. A non-linear least squares algorithm was used to fit the following function to the post-processed frequency spectrum, for different magnitudes of uniform tensile stress:

$$V_{\text{meas}}(\omega) = \langle V \rangle f_s(\omega) f(0, x_{\text{max}}, \zeta, \omega) + \epsilon(\omega), \quad (10)$$

where  $x_{\text{max}}$  represents a maximum detection depth of 100  $\mu\text{m}$ ; over that depth range, the applied field amplitude can be approximated as constant. The function  $f_s(\omega)$  remains invariant with stress and in our experiments decays approximately at the rate of  $\omega^{-0.2}$ . It was heuristically determined by fitting the data in iteration and searching for the decay rate that yielded the best fit. Within the scope of the present study, the physical origin of this power-law decay is not of interest; it can be attributed to either sensor frequency response and/or some residual scaling behaviour. However, it is important to note that it is not found to be a function of stress, while the multiexponential expression contained in  $f(0, x_{\text{max}}, \zeta(\omega))$  is varying with stress. The fitting parameters were  $\langle V \rangle$ ,  $\zeta$  and the constant term  $\epsilon(\omega)$ , which accounts for random Gaussian noise introduced by the measurement.

The parameter  $\langle V \rangle$  is proportional to domain wall velocity, which is further confirmed in the results of Figures 3(a) and 3(b). In the elastic region (region 1), domain wall velocity is increased due to the effect of elastic energy on the lattice which unpins the domain walls. At the onset of the plastic region (region 2), newly introduced dislocations pin domain walls, such that on average domain wall velocity is reduced. Prior to fracture (region 3), domain wall activity has reduced significantly due to the high dislocation density. We apply our linear model of  $1/\langle V \rangle$  vs  $\sigma$  to the elastic region (1) (Fig. 3(b)). This relationship can be derived theoretically, from an extension to the model of ferromagnetic hysteresis.<sup>21</sup> Note that in Figure 3(b), a linear relation may also be used to approximate the relationship between  $1/\langle V \rangle$  and stress in the plastic region.

A decrease of  $\zeta^2$ , and consequently  $\mu_{\text{eff}}$  with stress is seen in Figure 3(b). The fact that this quantity exhibits a constant, linear decrease over both elastic and plastic regions is notable; mainly because this behaviour is not observed in the case of  $1/\langle V \rangle$ , while both  $1/\langle V \rangle$  and  $\zeta$  are intrinsically coupled via the permeability. It is noteworthy that the parameter  $\langle V \rangle$  controls the y-axis intercept of the spectrum. It can be shown that  $V_{\text{meas}} \rightarrow \langle V \rangle x_{\text{max}}$  as  $\omega \rightarrow 0$ , which indicates that the extrapolated value at  $\omega = 0$  will be proportional to

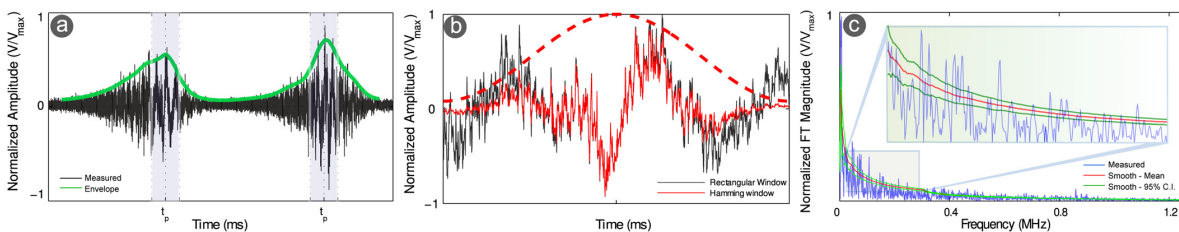


FIG. 2. Analysis of raw Barkhausen signals. (a) From the raw signal, we extracted the regions centered around the peaks, calculated the ensemble average, and (b) applied a Hamming window to reduce spectral leakage. (c) To eliminate low-frequency sensor artifacts, we omitted data below 20 kHz. In order to remove random fluctuations in the spectral amplitude at higher frequencies, the spectrum at each magnitude of stress was smoothed with a moving average over a 10 kHz span. The mean (red) as well as upper and lower 95% confidence bounds (green) were obtained by calculating the ensemble average of 5 measurement trials for each stress. Each trial contained a total of 10 Barkhausen bursts.

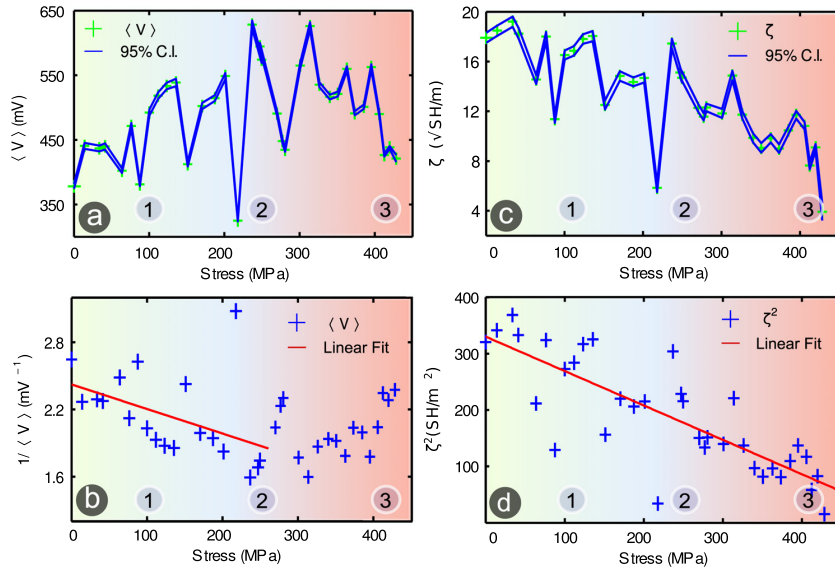


FIG. 3. Results of parameter extraction. Figure 3(a) shows the relationship between the mean voltage at the origin  $\langle V \rangle$  and stress, obtained from a nonlinear least squares fit of our theory to measurement. Regions (1), (2), and (3) indicate the elastic, plastic, and fracture regions. In (b), we plot the reciprocal of  $\langle V \rangle$  for values of stress in the elastic region, which follows a linear relationship with stress. In (c) and (d), parameters  $\zeta$  and  $\zeta^2$  (which is proportional to  $\mu_{\text{eff}}$ ) can be seen to decrease with stress. The upper and lower 95% confidence bounds were calculated using an asymptotic normal distribution for the parameter estimates.

the depth of detection. Parameter  $\zeta$  is responsible for the rate of attenuation with frequency; stress affects both the amplitude and the shape of the spectrum.

#### IV. DISCUSSION

From Fig. 4, we observe that on average, the quality of fit slightly improves with increasing stress, indicating that the white noise assumption becomes increasingly valid with stress.<sup>22</sup> To elaborate on this statement, the mean field theory can be invoked. In ferromagnetic materials, the degree of coupling between neighbouring domains is quantified by the mean field coupling coefficient  $\alpha$ . The energy stored between  $N$  neighbouring domains with magnetisation  $m$  is given by

$$E = -\mathbf{m} \cdot \mu_0 \alpha N \mathbf{m}, \quad (11)$$

where  $\mu_0$  is the permeability of free space. To model inhomogeneities that pin the domain boundary as it moves, a stochastic pinning field  $H_i \sim \mathcal{N}(0, \sigma^2)$  is introduced, such that the energy stored between the domain and the pinning field is

$$E = -\mu_0 \mathbf{m} \cdot \mathbf{H}_i. \quad (12)$$

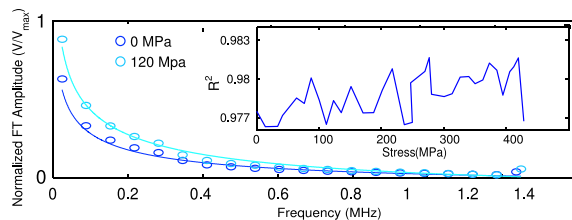


FIG. 4. Fit of (10) to experiment. Our model employs two parameters to describe the Barkhausen spectrum:  $\langle V \rangle$ , which is the mean amplitude of the Barkhausen voltage at the origin of emission and controls the y-intercept of the measured spectrum at the surface, and  $\zeta$ , which is proportional to the square root of effective permeability, and controls the decay of the Barkhausen signal amplitude as it propagates to the surface.

Finally, the magnetostatic energy in the applied field  $H_a$  is represented by

$$E = -\mu_0 \mathbf{m} \cdot \mathbf{H}_a, \quad (13)$$

to yield an expression for the total energy of

$$E = -\mu_0 \mathbf{m} \cdot \mathbf{H}_a - \mathbf{m} \cdot \mu_0 \alpha N \mathbf{m} - \mu_0 \mathbf{m} \cdot \mathbf{H}_i, \quad (14)$$

where the first, second, and third terms represent the magnetostatic (Zeeman), coupling, and pinning energies, respectively. Hysteretic behaviour increases with  $\alpha$ , due to the increased coupling between adjacent domains. This is analogous to the snapping mechanism in brittle materials, in that a single domain wall displacement instigates a large avalanche. In models of ferromagnetic hysteresis, a high value for  $\alpha$  is associated with increased switching behaviour, and high permeabilities at the coercive point, a characteristic of hard ferromagnets. Soft ferromagnets, on the contrary, exhibit lower values of permeability at the coercive point, caused by a smaller exchange coupling.

In the presence of dislocations (which may have similar effect on a propagating domain as impurities) caused by lattice straining, domain coupling decreases even further, making the contribution of  $\alpha$  small enough for the stochastic pinning field term to dominate. Since all other energy terms remain invariant, the free energy term in (14) can be expressed as

$$\Delta E = -\mu_0 \mathbf{m} \cdot \mathbf{H}_i. \quad (15)$$

Thus, under high applied stresses, the dominating mechanism is  $H_i$ , which can be modeled as white noise with frequency spectrum ranging from 20 kHz (approximate lower cutoff frequency of Barkhausen spectrum) to 1.25 MHz (upper cutoff imposed by measurement system). A slight overall increase with stress of the  $R^2$  quality of fit coefficient is observed in Fig. 4. Higher stress in a material of positive

magnetostriction is associated with increased irreversible permeability  $\mu_{irr}$ , which according to (3) will lead to an increase in  $c$ , thus validating our assumption that an increasing  $c$  gives rise to a white noise spectrum at the origin.

## V. CONCLUSION

In the case where stress is invariant along depth, as examined in the present paper, the integral in (9) may be bounded by 0 and  $x_{max}$ . In the case of stress variations with depth, where every volumetric region gives rise to a unique  $V$  and  $\zeta$ , the expression may be split into an arbitrary number of integrals, in order to consider intermediate depth ranges separately. Each volumetric region in the specimen is assumed to give rise to its own Barkhausen spectrum, with all spectra combining at the surface to produce  $V_{meas}$ , such that the combined spectrum is

$$V_{meas}(\omega) = \sum_{i=1}^N \langle V_i \rangle f_s(\omega) f(x_i, x_{i+1}, \zeta_i, \omega) + \epsilon(\omega), \quad (16)$$

where  $N$  denotes the number of depth ranges, or layers. After having fitted the above function to the measured spectrum and obtained  $\langle V \rangle$  and  $\zeta$  for each depth range, they can be compared to reference values given by the controlled uniform stress measurements (Fig. 3). This approach can be used to create stress-depth profiles of magnetic materials for the purposes of non-destructive characterization.

In this work, we derived a model to describe the spectrum of Barkhausen emissions under applied tensile stress, as a function of the Barkhausen amplitude and permeability at the origin of emission. The formulation of the model in terms of depth spans, or layers, opens the possibility of evaluating material properties as a function of depth. Each layer of emissions contributes to the measured spectrum at the surface, such that different stress-depth profiles will result in different combinations of values of parameters observed at the surface. This approach can be used to build sensors that employ the method of Barkhausen spectroscopy as a means for evaluating and characterizing materials non-destructively. In applications where safety is critical, the

former can be used as part of a procedure for detecting and preventing catastrophic failures.

## ACKNOWLEDGMENTS

This research was undertaken with support of a Graduate Fellowship for O. Kypris from the Takano Foundation and was also supported by the James and Barbara Palmer Endowment in the Department of Electrical and Computer Engineering at Iowa State University.

- <sup>1</sup>G. Durin and S. Zapperi, *Phys. Rev. Lett.* **84**, 4705 (2000).
- <sup>2</sup>P. J. Cote and L. V. Meisel, *Phys. Rev. Lett.* **67**, 1334 (1991).
- <sup>3</sup>A. Baldassarri, F. Colaiori, and C. Castellano, *Phys. Rev. Lett.* **90**, 060601 (2003).
- <sup>4</sup>O. Narayan, *Phys. Rev. Lett.* **77**, 3855 (1996).
- <sup>5</sup>E. Puppini, S. Ricci, and L. Callegaro, *Appl. Phys. Lett.* **76**, 2418 (2000).
- <sup>6</sup>E. Puppini, *Phys. Rev. Lett.* **84**, 5415 (2000).
- <sup>7</sup>K.-S. Ryu, H. Akinaga, and S.-C. Shin, *Nat. Phys.* **3**, 547 (2007).
- <sup>8</sup>S. Papanikolaou, F. Bohn, R. L. Sommer, G. Durin, S. Zapperi, and J. P. Sethna, *Nat. Phys.* **7**, 316 (2011).
- <sup>9</sup>A. Schwarz, M. Liebmann, U. Kaiser, R. Wiesendanger, T. Noh, and D. Kim, *Phys. Rev. Lett.* **92**, 077206 (2004).
- <sup>10</sup>D.-H. Kim, S.-B. Choe, and S.-C. Shin, *Phys. Rev. Lett.* **90**, 087203 (2003).
- <sup>11</sup>B. Alessandro, C. Beatrice, G. Bertotti, and A. Montorsi, *J. Appl. Phys.* **68**, 2908 (1990).
- <sup>12</sup>B. Alessandro, C. Beatrice, G. Bertotti, and A. Montorsi, *J. Appl. Phys.* **64**, 5355 (1988).
- <sup>13</sup>F. Colaiori, *Adv. Phys.* **57**, 287 (2008).
- <sup>14</sup>R. White and K. Dahmen, *Phys. Rev. Lett.* **91**, 085702 (2003).
- <sup>15</sup>L. Mierczak, D. C. Jiles, and G. Fantoni, *IEEE Trans. Magn.* **47**, 459 (2011).
- <sup>16</sup>O. Kypris, I. C. Nlebedim, and D. C. Jiles, *IEEE Trans. Magn.* **49**, 4148 (2013).
- <sup>17</sup>S. Findlay and N. Harrison, *Mater. Today* **5**, 18 (2002).
- <sup>18</sup>G. Bertotti, *Hysteresis in Magnetism: For physicists, Materials Scientists and Engineers, Electromagnetism* (Academic Press, San Diego and Calif. [u.a.], 1998).
- <sup>19</sup>C. G. Stefanita, L. Clapham, and D. L. Atherton, *J. Mater. Sci.* **35**, 2675 (2000).
- <sup>20</sup>O. Kypris, I. C. Nlebedim, and D. C. Jiles, *IEEE Trans. Magn.* **49**, 3893 (2013).
- <sup>21</sup>P. Garikepati, T. T. Chang, and D. C. Jiles, *IEEE Trans. Magn.* **24**, 2922 (1988).
- <sup>22</sup>H.-S. Lee, K.-S. Ryu, I.-S. Kang, and S.-C. Shin, *J. Appl. Phys.* **109**, 07E101 (2011).





## Barkhausen spectroscopy: Non-destructive characterization of magnetic materials as a function of depth

O. Kypris,<sup>a)</sup> I. C. Nlebedim, and D. C. Jiles

*Department of Electrical and Computer Engineering, Iowa State University, Ames, Iowa 50011, USA*

(Presented 5 November 2013; received 23 September 2013; accepted 18 October 2013; published online 22 January 2014)

In this study, we conceptually divided a ferromagnetic specimen into layers along its depth. For each layer, we derived a non-linear integral equation that describes the attenuation with frequency and distance of magnetic Barkhausen emissions coming from that layer. We postulate that the Barkhausen spectrum measured at the surface by an induction coil can be expressed as the sum of the individual layer spectra. We show how a non-linear least squares algorithm can be used to recover the properties in individual layers. These are related to stress using an extension to the theory of ferromagnetic hysteresis. We found that the quality of the fit is influenced by the sensitivity of the ferromagnetic material to strain, as well as by the sensor-specimen coupling. The proposed method can be used for the non-destructive characterization of stress as a function of depth in magnetic materials. © 2014 AIP Publishing LLC. [<http://dx.doi.org/10.1063/1.4862095>]

### I. INTRODUCTION

The magnetic Barkhausen noise method is popular for its reliability<sup>1-8</sup> in assessing stress levels in ferromagnetic components when other non-destructive evaluation methods cannot be used to evaluate the specimen under test. The method relies on detecting the magnetic Barkhausen signals, which are electromagnetic noise-like emissions with energy contained mostly in the 20 kHz to 2 MHz range. These emissions are a by-product of discontinuous magnetization changes, which occur when the specimen is subjected to an applied, time-varying magnetic field. The presence of magnetoelastic energy in the lattice, as a result of strain, alters the magnetic permeability and thus the Barkhausen signal. This makes it possible to measure the amplitude of the Barkhausen signals and obtain an estimate of mechanical stress, based on a calibration curve calculated from a series of reference measurements.

Despite the method's success in assessing average stress levels in a structure, there is still a need for the ability to determine depth-specific stress information; this is currently done using a combination of x-ray diffraction and electropolishing, which is, however, destructive. Such an advance would extend the existing Barkhausen technique and thus provide industry with a rapid, non-destructive, cost-effective stress evaluation tool.

In this study, we formulate a system of non-linear integral equations that describe the spectra of Barkhausen signals emanating from different depths inside a specimen. An expression for the resultant signal measured at the surface was derived, and a least-squares fitting algorithm was used to extract stress-related parameters for each depth.

### II. THEORY

Consider a specimen of ferromagnetic material with homogeneous and isotropic resistivity  $\rho$ . Barkhausen emissions occur over the entire volume that is magnetized by an

externally applied magnetic field. They are collectively assumed to have a flat frequency spectrum, such that their average amplitude at the origin  $V_{orig}$  is independent of frequency; this is the white noise assumption. Assuming plane wave propagation, as emissions travel towards the surface, they attenuate as a function of both distance and frequency, such that  $x = \sqrt{2\rho/\omega\mu}$ ; where  $x$  is the distance at which the amplitude reduces to  $1/e$  of its value at the origin,  $\mu$  is the magnetic permeability seen by emissions as they travel towards the surface, and  $\omega$  is the angular frequency. In our treatment, we have ignored the phase of Barkhausen emissions and considered only their magnitude. It is possible to conceptually divide the specimen into layers along its depth, with each layer having a unique value of permeability  $\mu$  and emission amplitude  $V_{orig}$ , associated with a certain magnitude of mechanical stress  $\sigma$  present in that layer. As emissions propagate, they attenuate at a rate unique to each layer (in previous treatments and to simplify the problem, we assumed that permeability remained invariant<sup>1,3</sup>).

#### A. Single emission

It is possible to express the measured emission at the surface, in terms of its amplitude at the origin<sup>1,3</sup>

$$V_{att1}(\omega) = V_{orig1}e^{-\zeta_1 x \sqrt{\omega}}, \quad (1)$$

where  $\zeta_1 = \sqrt{\mu/2\rho}$ . The above emission occurs in the first layer and thus only passes through that layer, attenuating at an exponential rate proportional to  $\zeta_1$ . For an emission originating in the second layer, in a similar manner, one can write

$$\begin{aligned} V_{att2}(\omega) &= V_{orig2}e^{-\zeta_2(x-\Delta x)\sqrt{\omega}}e^{-\zeta_1\Delta x\sqrt{\omega}} \\ &= V_{orig2}e^{-\sqrt{\omega}(\zeta_2(x-\Delta x)+\zeta_1\Delta x)}, \end{aligned} \quad (2)$$

as the emission attenuates at a rate proportional to  $\zeta_2$  while it passes through the second layer. The layer thickness is denoted by  $\Delta x$ .

<sup>a)</sup>Electronic mail: kypris@iastate.edu.

## B. Multiple emissions

Since multiple emissions occur in a layer, by taking the integral over a certain depth range, the combined spectra of all emissions within that range are considered. That gives  $V_{att1}(\omega)$  as the component of the signal detected at the surface<sup>1,3</sup>

$$\begin{aligned} V_{att1}(\omega) &= V_{orig1} \int_{x_0}^{x_1} e^{-\zeta_1 x \sqrt{\omega}} dx \\ &= -\frac{V_{orig1}}{\zeta_1 \sqrt{\omega}} (e^{-\zeta_1 x_1 \sqrt{\omega}} - e^{-\zeta_1 x_0 \sqrt{\omega}}). \end{aligned} \quad (3)$$

Similarly, for emissions originating in the second layer,

$$\begin{aligned} V_{att2}(\omega) &= V_{orig2} \int_{x_1}^{x_2} e^{-\sqrt{\omega}(\zeta_2(x-\Delta x) + \zeta_1 \Delta x)} dx \\ &= -\frac{V_{orig2}}{\zeta_2 \sqrt{\omega}} (e^{-\sqrt{\omega}(\zeta_2 x_2 - (\zeta_2 - \zeta_1) \Delta x)} \\ &\quad - e^{-\sqrt{\omega}(\zeta_2 x_1 - (\zeta_2 - \zeta_1) \Delta x)}). \end{aligned} \quad (4)$$

Uncorrelated white noise has a uniformly distributed phase between  $-\pi$  and  $\pi$ ; we can therefore use the assumption that at the origin the phase is zero (mean value) such that, since dispersive effects are ignored, the resulting phase at the surface is also zero, leading to only constructive interference when all attenuated spectra are summed. By summing the emissions in separate layers, we are also implicitly assume that they are statistically independent. This summation yields the measured spectrum at the surface  $V_{meas}(\omega)$ , such that

$$V_{meas}(\omega) = \sum_i V_{att_i}(\omega), \quad (5)$$

where  $V_{att_i}$  is the Barkhausen signal from the  $i$ th layer. One can retrieve the stress state of the material, by fitting the above expression to Barkhausen spectra measured at the surface of a specimen and extracting the value of stress-related parameters  $\zeta$  and  $V_{orig}$ . With this approach, for  $n$  total layers, one obtains  $2n$  parameters. It is possible to reduce the number of fitting parameters by incorporating a Barkhausen-stress calibration relationship<sup>2,9</sup> into our model for the spectrum.

## C. Reducing the number of fitting parameters

It was shown previously<sup>10</sup> that the reciprocal of the peak differential susceptibility  $1/\chi'$  varies linearly with stress, via the following relation:

$$\frac{1}{\chi'(0)} - \frac{1}{\chi'(\sigma)} = \frac{3b\sigma}{\mu_0}, \quad (6)$$

where  $\sigma$  denotes stress and  $b$  is a magnetostrictive coefficient with units  $\text{m}^2\text{A}^{-2}$ , which connects magnetostriction with magnetization,<sup>11</sup> associated with a quadratic approximation to the  $\lambda - M$  curve, and can be obtained using a quasi-static magnetostriction measurement. The above relation can also be used to relate the reciprocal of the peak Barkhausen voltage to stress,<sup>2</sup> such that

$$\frac{1}{V_{orig}(0)} - \frac{1}{V_{orig}(\sigma)} = \frac{3b'\sigma}{\mu_0}, \quad (7)$$

where  $b'$  is a modified magnetostriction coefficient with units  $\text{m}^2\text{V}^{-1}\text{A}^{-2}$ . Its value depends on the frequency of magnetization, strength of magnetizing field and sensitivity of the Barkhausen probe, and is, thus, not easily determinable. By dividing (6) by (7), we yield

$$\frac{\frac{1}{\chi'(0)} - \frac{1}{\chi'(\sigma)}}{\frac{1}{V_{orig}(0)} - \frac{1}{V_{orig}(\sigma)}} = \frac{b}{b'}. \quad (8)$$

Solution for  $V_{orig}(0)$  yields

$$V_{orig}(\sigma) = -\frac{b}{b'} \frac{1}{\frac{1}{\chi'(0)} - \frac{1}{\chi'(\sigma)} - \frac{b}{b'} \frac{1}{V_{orig}(0)}}, \quad (9)$$

where  $b$ ,  $\chi'(0)$ , and  $V_{orig}(0)$  can be experimentally determined. The differential susceptibility at some value of unknown stress  $\chi'(\sigma)$  is related to  $\mu_r$  and  $\zeta$  such that

$$\chi'(\sigma) \cong \mu_r'(\sigma) = 2\rho\zeta^2(\sigma)/\mu_0. \quad (10)$$

By substituting (9) into (3) and (4) (and consequently (5)), we are reducing the number of fitting parameters from  $2n$  to  $n + 1$ .

## III. SIMULATION OF BARKHAUSEN SPECTRA EMANATING FROM VARIABLE STRESS-DEPTH PROFILES

To establish a relationship between stress and relative permeability, an extension to the theory of ferromagnetic hysteresis<sup>10</sup> was used

$$\mu_r' \cong \chi' = \frac{M_s}{3a - \left( \alpha + \frac{3b(\sigma + \sigma_{offset})}{\mu_0} \right) M_s}, \quad (11)$$

where  $a$  is a parameter which characterizes the shape of the anhysteretic magnetization,  $\alpha$  is a mean field term that quantifies interdomain coupling,  $\sigma$  is the stress present in the sample, and  $M_s$  is the saturation magnetization. Plots of  $\mu_r'$  and its reciprocal versus stress can be seen in Fig. 1.

To simulate non-uniform strain, each layer was assigned a different value of stress, by modulating the value of the differential permeability and thus the parameter  $\zeta$ , which was defined in Sec. III. Different values of stress lead to different y-axis intercepts and spectrum shapes, as shown in Fig. 2. To simulate a practical measurement and thus make the treatment more realistic, Gaussian random noise was added to the simulated spectra. A least squares algorithm was used to obtain the estimates  $\hat{\zeta}_1$  and  $\hat{\zeta}_2$ , from which the stress can be calculated, using the linear relationship shown in Fig. 1.

## IV. DISCUSSION

From the results of Fig. 1, it is evident that tensile stress leads to an increase in the Barkhausen signal amplitude at

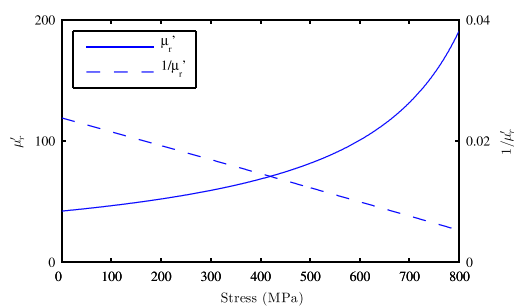


FIG. 1. Calibration relationship, relating relative differential permeability, and its reciprocal to stress. We set  $a = 2019.620 \text{ Am}^{-1}$ ,  $M_s = 2.485 \times 10^5 \text{ Am}^{-1}$ , and  $\alpha = 1.9119 \times 10^{-2}$ , which are typical values for a soft steel. The values of  $b$  and  $\sigma_{\text{offset}}$  were set to  $1 \times 10^{-17} \text{ m}^2 \text{ A}^{-2}$  and  $-800 \text{ MPa}$ , respectively.

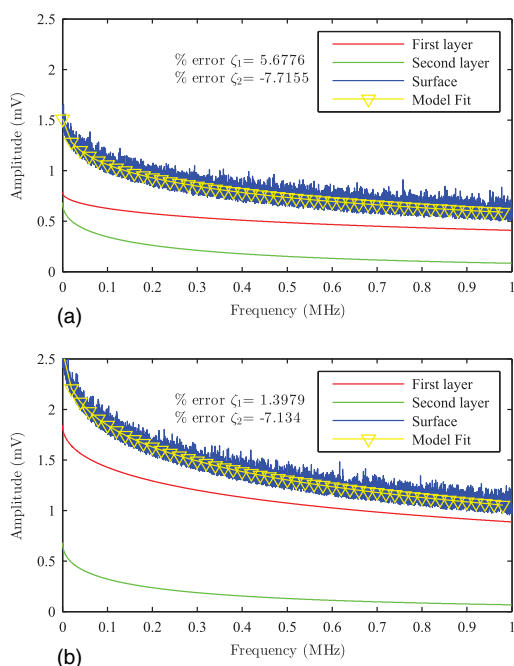


FIG. 2. Least-squares fit to simulated Barkhausen spectra, of the non-linear expression of (5) combined with the relationship in (9), for different stress magnitudes in the first and second layer. The value of  $b'$ , which quantifies the sensitivity of the sensing element, was set to  $1 \times 10^{-22} \text{ m}^2 \text{ V}^{-1} \text{ A}^{-2}$ . The parameters  $\chi'(0) \cong \mu_r'(0)$ ,  $\rho$ , and  $V_{\text{orig}}(0)$  were set to 42, 0.22  $\mu\Omega \text{ m}$ , and 10 V, respectively. The layer thickness  $\Delta x$  was set to 50  $\mu\text{m}$ .

the origin. This is true for steels with positive magnetostriction, while in the case of negative magnetostriction, the converse is true. While the parameter  $b$  solely relies on the magneto-mechanical coupling within the specimen and therefore can be accurately determined via a quasi static magnetostriction measurement,  $b'$  relies also on the probe-specimen coupling and amplification factor of the sensing equipment. The magnetization in a material with a higher value of  $b$  is more sensitive to changes in strain, and, as a result, the Barkhausen amplitude at the origin becomes larger. The amplitude of the signals at their origin also affects the accuracy of the fitting algorithm. It follows that detection of stress becomes easier and more reliable when using a well-coupled, sensitive sensing element on steels with relatively high magnetostriction.

## V. CONCLUSION

In this work, we derive the theoretical framework for a magnetic spectroscopy method that can be used to non-destructively assess the local stress state by separating the Barkhausen signals originating in different regions inside a ferromagnetic specimen. This is particularly useful in aerospace applications where tensile stresses on component surfaces may initiate crack formation, possibly leading to failure and loss of human life.

## ACKNOWLEDGMENTS

This research was undertaken with support of a Graduate Fellowship for O. Kypris from the Takano Foundation and was also supported by the James and Barbara Palmer Endowment in the Department of Electrical and Computer Engineering at Iowa State University.

- <sup>1</sup>O. Kypris, I. C. Nlebedim, and D. C. Jiles, *IEEE Trans. Magn.* **49**, 3893 (2013).
- <sup>2</sup>O. Kypris, I. C. Nlebedim, and D. C. Jiles, *IEEE Trans. Magn.* **49**, 4148 (2013).
- <sup>3</sup>O. Kypris, I. C. Nlebedim, and D. C. Jiles, *IEEE Trans. Magn.* **48**, 4428 (2012).
- <sup>4</sup>K. Mandal, D. Dufour, R. Sabet-Sharghi, B. Sijgers, D. Micke, T. W. Krause, L. Clapham, and D. L. Atherton, *J. Appl. Phys.* **80**, 6391 (1996).
- <sup>5</sup>T. W. Krause, L. Clapham, and D. L. Atherton, *J. Appl. Phys.* **75**, 7983 (1994).
- <sup>6</sup>C. C. H. Lo, E. R. Kinser, and D. C. Jiles, *J. Appl. Phys.* **99**, 08B705 (2006).
- <sup>7</sup>C. Lo, S. J. Lee, L. C. Kerdus, and D. C. Jiles, *J. Appl. Phys.* **91**, 7651 (2002).
- <sup>8</sup>K. Mandal, D. Dufour, T. W. Krause, and D. L. Atherton, *J. Phys. D: Appl. Phys.* **30**, 962 (1997).
- <sup>9</sup>L. Mierczak, D. C. Jiles, and G. Fantoni, *IEEE Trans. Magn.* **47**, 459 (2011).
- <sup>10</sup>P. Garikepati, T. T. Chang, and D. C. Jiles, *IEEE Trans. Magn.* **24**, 2922 (1988).
- <sup>11</sup>M. J. Sablik and D. C. Jiles, *IEEE Trans. Magn.* **29**, 2113 (1993).



## Optimization of sensor design for Barkhausen noise measurement using finite element analysis

N. Prabhu Gaunkar,<sup>a)</sup> O. Kypris, I. C. Nlebedim, and D. C. Jiles

Department of Electrical and Computer Engineering, Iowa State University, Ames, Iowa 50011, USA

(Presented 6 November 2013; received 24 September 2013; accepted 5 November 2013; published online 10 February 2014)

The effects of design parameters for optimizing the performance of sensors for magnetic Barkhausen emission measurement are presented. This study was performed using finite element analysis. The design parameters investigated include core material, core-tip curvature, core length, and pole spacing. Considering a combination of permeability and saturation magnetization, iron was selected as the core material among other materials investigated. Although a flat core-tip would result in higher magnetic flux concentration in the test specimen, a curved core-tip is preferred. The sensor-to-specimen coupling is thereby improved especially for materials with different surface geometries. Smaller pole spacing resulted in higher flux concentration. © 2014 AIP Publishing LLC. [<http://dx.doi.org/10.1063/1.4864438>]

### I. INTRODUCTION

Barkhausen emissions occur due to sudden changes in magnetization within a ferromagnetic material and are obtained with application of a continuously varying magnetic field.<sup>1</sup> The emissions can be measured as induced voltage signals using induction sensors. Due to the strong interrelationship between the magnetic properties and micro-structural features in ferromagnetic materials, Barkhausen effect presents a powerful tool for non-destructively monitoring the condition of such materials. This can be done by correlating the peak amplitude of the voltage pulse obtained during Barkhausen emission measurement with stress.<sup>2,3</sup> For industrial equipment, such monitoring of structural health is essential to avoid failures resulting from micro-structural changes, residual stresses, surface deformations, and micro-cracks generated in operations.

Apart from the stress-state or other micro-structural inhomogeneities in the materials, the detected Barkhausen signal also depends on the magnetizing field produced by the coils, the core geometry, sensor-to-specimen coupling, and spacing between core tips. It is therefore important that the sensor configuration be optimized to improve the sensitivity, reproducibility, and accuracy of the detected Barkhausen signals. In this study, it is shown how the choice of sensor design parameters affects the generation of magnetic fields used to excite Barkhausen emissions in a specimen. Using finite element simulations a method of optimizing these parameters for sensors with C-core geometries with two windings is demonstrated. The choice of performing DC simulations and thus ignoring frequency dependent effects is supported by the fact that typical Barkhausen noise excitation coils operate in the lower quasi-static limit and are thus well described by a DC approach.

### II. THEORY

From Ampere's circuital law, for a magnetic circuit

<sup>a)</sup>Author to whom correspondence should be addressed. Electronic mail: neelampg@iastate.edu.

$$\oint \mathbf{H} \cdot d\ell = NI. \quad (1)$$

Here  $\mathbf{H}$  is the magnetic field strength in the core, generated due to current  $I$  flowing in a coil having  $N$  turns.  $\ell$  is the length of the flux path. The equivalent circuit of the magnetizing unit for this study is shown in Fig. 1(a). The total magnetic field strength due to the two magnetizing coils is taken to be 0.5 kA/m, in line with a previous study<sup>4</sup> on Barkhausen measurement. The two magnetizing coils can be approximated as solenoids of finite lengths. We can therefore find the field intensity along the axis, at a distance  $x$  from the center of the solenoid using the relation<sup>5,6</sup>

$$H = \frac{NI}{L} \left( \frac{L + 2x}{2\sqrt{D^2 + (L + 2x)^2}} + \frac{L - 2x}{2\sqrt{D^2 + (L - 2x)^2}} \right). \quad (2)$$

$D$  is the coil diameter, which for a C-core represents a coil with value shown in Table I.  $L$  is the length of the magnetizing coil. The magnetic field at the off-axis point C, which in this study is the center of the test specimen, is considered to be equivalent to the on-axis field at a distance  $x$  from the center of the coil. This is a valid approximation since the magnetic flux path is curved by the material, thus making it possible to set  $x = ABC$ . Therefore, we use this relationship to approximate the value of the magnetic field at the point marked C. Since the analytical expression is an approximation of the magnetic field at point C, we utilized finite element simulations for improved accuracy.

### III. SIMULATION

Fig. 1(b) shows the geometry of the magnetizing unit. C-core geometry was selected, being a typical geometry for Barkhausen sensors. The number of turns and coil length for the magnetizing coils were calculated using Eq. (2). A DC magnetizing current of 1 A was assumed. The properties and dimensions of the core and the coil are listed in Table I. A finite element simulation was performed using the AC/DC module of COMSOL Multiphysics.



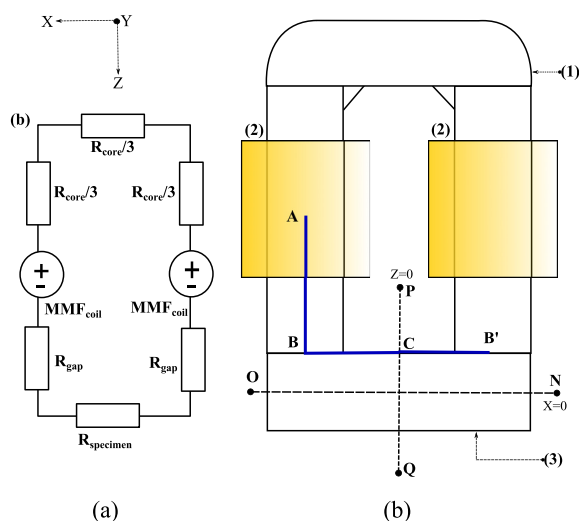


FIG. 1. (a) The equivalent magnetic circuit. (b) Schematic of the magnetizing assembly showing the core material (1), coils (2), and test specimen (3). Line segments NO and PQ represent sections along X and Z direction, respectively.

#### IV. RESULTS AND DISCUSSION

The effects of using different core materials for the magnetizing unit and the variations in the tip-curvature, length and inter-pole spacing of the core-materials have been investigated.

##### A. Effect of core material

Table II shows the core materials investigated including their electrical and magnetic properties. It can be seen in Fig. 2 that the maximum magnetic flux density in the material corresponds to the material with highest permeability. Although permalloy has the highest flux concentration, its

TABLE I. Core and coil dimensions (per pole).

Sensor	Coil	Core
Material	Copper	Variable
Length	8 mm	14 mm
Width	4 mm	3.4 mm
Depth	4 mm	3.4 mm
Number of Turns	32	N/A

TABLE II. Properties of the materials studied for use as the core material of the magnetizing unit.

Material	Electrical Conductivity S/m	Relative Permeability	Relative Permittivity
Air	0	1	1
Iron	1E7	5000 (Ref. 7)	300 (Ref. 8)
78 Permalloy	0.5E7	100000	5000 (Ref. 8)
Electrical Steel	2.12E6	4000	1
Ni-Zn Ferrite	2E-5 (Ref. 9)	1000 (Ref. 10)	14 (Ref. 9)

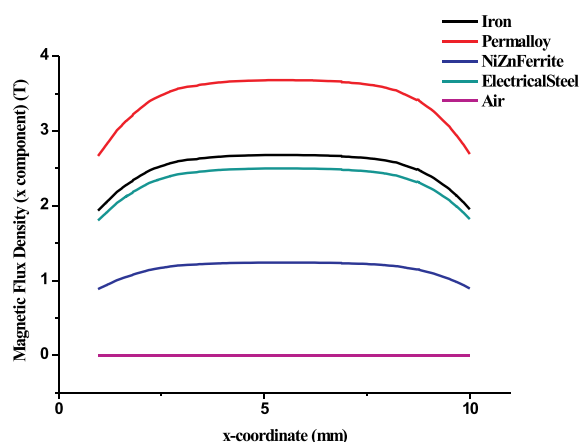


FIG. 2. Effect of material on magnetic flux density. Magnetic flux density was measured between the pole centers along the line segment NO as seen in Fig. 1(b).

saturation magnetization ( $0.86 \times 10^6$  A/m) is almost half of that of iron ( $1.71 \times 10^6$  A/m). Since it is important not to saturate the core material in application, iron was selected as the choice material for the rest of the study.

##### B. Effect of core-tip curvature

The effect of core-tip curvature on the magnetic flux density in the sample is shown in Fig. 3. The curvature of the core-tip is an important parameter to ensure good sensor-to-specimen coupling. Cores with flat, pointed and curved tips were investigated. Fig. 3 shows that the best performance can be obtained using a core-material with a flat tip. Nevertheless, in applications, a curved core-tip helps ensure consistent flux coupling with test specimens of varying surface geometries. Hence the core-tip curvature selected has an arc length of 3.45 mm that is slightly more than the length of a flat tip. Magnetic flux leakage occurs in the region between the core poles resulting in asymmetrical flux density above and below the test specimen.

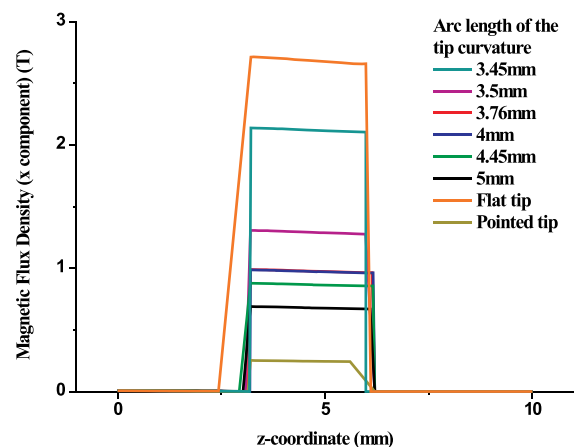


FIG. 3. Effect of tip curvature on the magnetic flux density. Magnetic flux density was measured along the line segment PQ as shown in Fig. 1(b).

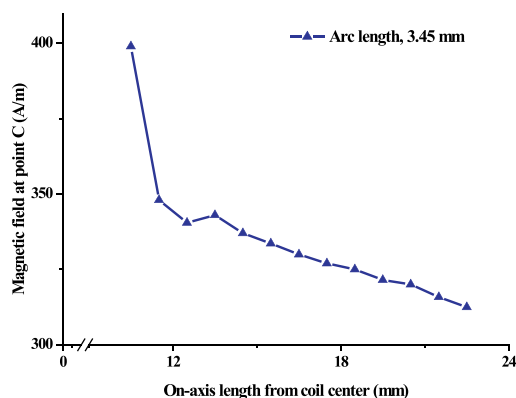


FIG. 4. Effect of core length on magnetic field. The on-axis length from coil center is defined as the length along path ABC, shown in Fig. 1(b). AB varies with increasing length of poles.

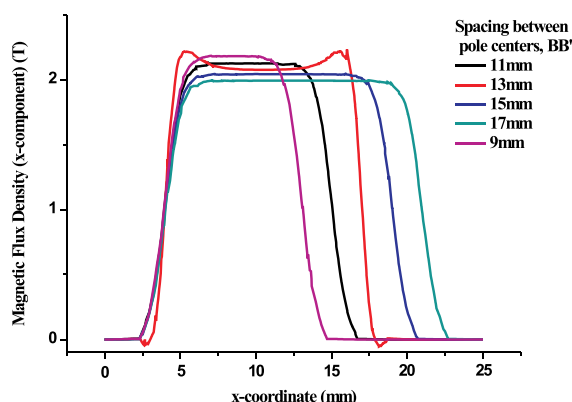


FIG. 5. Effect of pole spacing. The pole spacing was measured along the line segment NO, as shown in Fig. 1(b), where BB' indicates the spacing between the pole centers.

### C. Effect of core length

The effect of path length, ABC, of the core material on the generated magnetic field is shown in Fig. 4. These are obtained using an iron core with an arc length of 3.45 mm. The magnetic field strength decreases with increasing length of the core material. This is an important design consideration especially where varying the sensor size is necessary to test different parts of the same component. The maximum field strengths obtained at point C are in the range 0.31–0.4 kA/m. This is less than the 0.5 kA/m calculated and might be due to flux leakage. The maximum field penetration is obtained with the magnetizing coils are placed at a distance of 0.5 mm (i.e., closest to the test specimen). This was

incorporated into the design to observe the effect of spacing between the poles of the sensor.

### D. Effect of inter-pole spacing

Fig. 5 shows the effect of varying the spacing between the two poles of the sensor. It can be seen that small spacing maximizes the magnetic flux density. In application, however, maximizing the flux density by decreasing the pole spacing should be balanced with the fact that measurement noise increases due to mutual inductance when the pole spacing is reduced. This is important considering that Barkhausen emissions are already noise-like.

## V. CONCLUSIONS

The study carried out on the optimization of the sensor design parameters for Barkhausen emission measurements revealed the following. A sensor constructed with soft iron resulted in high magnetic field penetration into the test specimen. The sensor geometry governed the coupling between the sensor and the test specimen, a flat tip resulting in the best coupling. The sensor design can be further optimized to suit specific applications taking into consideration the parameters analyzed and described in this study.

## ACKNOWLEDGMENTS

This research was funded by the Department of Electrical and Computer Engineering, Iowa State University and the ASNT Fellowship Award.

- <sup>1</sup>A. Dhar and D. Atherton, *IEEE Trans. Magn.* **28**, 3363 (1992).
- <sup>2</sup>O. Kypris, I. C. Nlebedim, and D. C. Jiles, *IEEE Trans. Magn.* **48**, 4428 (2012).
- <sup>3</sup>L. Mierczak, D. C. Jiles, and G. Fantoni, *IEEE Trans. Magn.* **47**, 459 (2011).
- <sup>4</sup>O. Kypris, I. C. Nlebedim, and D. C. Jiles, *IEEE Trans. Magn.* **49**, 4148 (2013).
- <sup>5</sup>D. C. Jiles, *Introduction to Magnetism and Magnetic Materials*, 1st ed. (Chapman and Hall, London and New York, 1991).
- <sup>6</sup>A. E. Umenei, Y. Melikhov, and D. C. Jiles, *IEEE Trans. Magn.* **47**, 734 (2011).
- <sup>7</sup>D. D. L. Chung, *Functional Materials: Electrical, Dielectric, Electromagnetic, Optical and Magnetic Applications (with Companion Solution Manual)*, Engineering Materials for Technological Needs Vol. 2 (World Scientific, Hackensack and New Jersey, London, 2010).
- <sup>8</sup>J. S. Wilson, *Sensor Technology Handbook* (Elsevier, Amsterdam and Boston, 2005).
- <sup>9</sup>A. Goldman, *Modern Ferrite Technology*, 2nd ed. (Springer, New York and NY, 2005).
- <sup>10</sup>S. E. Lyshevski, *Nano- and Micro-Electromechanical Systems: Fundamentals of Nano- and Microengineering*, 2nd ed., Nano- and Microscience, Engineering, Technology, and Medicine Series Vol. 8 (CRC Press, Boca Raton [u.a.], 2005).

# Analysis of Barkhausen Noise Emissions and Magnetic Hysteresis in Multi-Phase Magnetic Materials

Neelam Prabhu Gaunkar, Orfeas Kypris, Ikenna Cajetan Nlebedim, and David C. Jiles, *Fellow, IEEE*

Department of Electrical and Computer Engineering, Iowa State University, Ames, IA 50011 USA

**Ferromagnetic materials occur in single or multi-phase state and furthermore can undergo phase changes during processing or over time during service exposure. These phase changes can be attributed to physical processes or chemical reactions. In this paper, we examine the hysteresis and Barkhausen emission profiles of two-phase magnetic materials. Besides the shape of magnetic hysteresis curves that can reveal the presence of more than one phase, we demonstrate that the Barkhausen noise signatures for two-phase materials form two-peaks in their Barkhausen voltage profile. This can be used as a tool for non-destructive evaluation of ferromagnetic materials in industrial applications.**

**Index Terms**—Barkhausen emission, hysteresis, Jiles–Atherton (J–A) model, multi-phase materials, non-destructive evaluation, two-phase materials.

## I. INTRODUCTION

**H**YSTERESIS is a path-dependent response of a material to an input based on its previous exposure to the input. It is commonly observed in ferromagnetic and ferroelectric materials when they are subjected to external magnetic and electric fields, respectively. Several models [1]–[4] have been proposed to predict the hysteretic behavior of ferromagnetic materials. Of the available empirical models, the Preisach model [2] and Jiles–Atherton (J–A) model [4] are widely used. In this paper, we adopt the J–A model to study hysteresis in two-phase ferromagnetic materials.

The J–A model considers an array of distributed magnetic moments subjected to magnetic field, temperature, and stress. The bulk magnetization of the material is obtained by integrating the distribution of magnetic moments over all the possible orientations. The changes in magnetization can then be subdivided into magnetic domain processes, which contribute to reversible and irreversible changes in magnetization.

Besides magnetic hysteresis curves, magnetic Barkhausen effect (MBE) emissions also represent changes in the magnetization behavior of a material when it is subjected to a continuously varying magnetic field [5]. These emissions can be captured as voltage pulses using a sense coil placed in the vicinity of the test specimen. MBE emissions are related to the interaction of the magnetic domains with the pinning sites during magnetization [6].

Previous studies have extended the J–A model to incorporate anisotropy, magnetoelastic, and thermal effects [7]–[9]. Recently, it has been extended to model the dynamic hysteresis of materials with two ferromagnetic phases [10]. In this paper, we show that the MBE emission and hysteresis behavior for single phase and two-phase materials differ.

Manuscript received March 7, 2014; revised June 25, 2014; accepted June 27, 2014. Date of current version November 18, 2014. Corresponding author: N. P. Gaunkar (e-mail: neelampg@iastate.edu).

Color versions of one or more of the figures in this paper are available online at <http://ieeexplore.ieee.org>.

Digital Object Identifier 10.1109/TMAG.2014.2335204

0018-9464 © 2014 IEEE. Personal use is permitted, but republication/redistribution requires IEEE permission.

See [http://www.ieee.org/publications\\_standards/publications/rights/index.html](http://www.ieee.org/publications_standards/publications/rights/index.html) for more information.

## II. THEORY

### A. Single-Phase and Two-Phase Materials

Single-phase magnetic materials usually exhibit a sigmoid-shaped hysteresis curve over one cycle of applied magnetic field. In contrast, two-phase (or multi-phase) magnetic materials, may exhibit a distorted sigmoidal curve, reflecting the presence of two or more magnetic phases in one hysteresis cycle. One of the phases switches at a lower coercive field and other at a higher coercive field.

An example can be found in composite materials, which are currently finding applications in magnetic sensors/actuators, composite magnetoactive materials, and exchange-spring magnets. A second phase can form within a single-phase matrix material as a result of external stress [11], changes in composition, or sometimes by thermal processing. Fig. 1 shows hysteresis loops corresponding to a single magnetic phase and two-phase magnetic materials. Although studies on models for single phase materials are extensive, there is still a need for a suitable model to properly represent the magnetic hysteresis in multi-phase magnetic materials. A suitable model will be able to predict the magnetic properties and performance of composite magnetic materials.

### B. J–A Model

The J–A model was originally developed for describing the hysteresis behavior of a simple single-phase ferromagnetic material [4]. It uses five physical parameters  $\alpha$ ,  $a$ ,  $k$ ,  $c$ , and  $M_s$  to predict the magnetic hysteresis behavior of materials.  $\alpha$  is the domain coupling coefficient,  $a$  is the domain density coefficient,  $k$  is the pinning coefficient,  $c$  is the reversibility coefficient, and  $M_s$  is the saturation magnetization. The permeability is affected by domain coupling  $\alpha$ , and domain density  $a$ . The pinning parameter  $k$ , is proportional to the density of pinning sites and the energy of pinning sites primarily determines the coercivity. The reversibility factor  $c$ , represents reversible domain wall bowing and rotation. Mathematically, the J–A model describes the hysteresis behavior of magnetic materials by solving the relation in [4]

$$\frac{dM}{dH} = \frac{1}{(1+c)} \frac{M_{an} - M}{\delta k - \alpha(M_{an} - M)} + \frac{c}{(1+c)} \frac{dM_{an}}{dH} \quad (1)$$

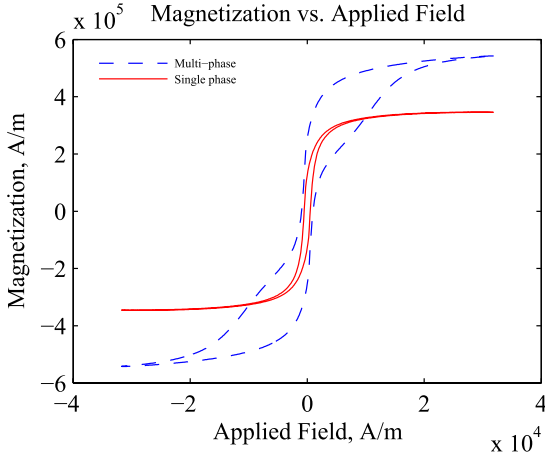


Fig. 1. Hysteresis curves for a single magnetic phase (red-solid curve) and a two-phase magnetic material (blue-dashed curve).

where  $H$  refers to the applied field and  $\delta$  is a directionality parameter, ranging from 1 for the forward magnetization cycle, to  $-1$  for the reverse magnetization cycle,  $M$  refers to the total magnetization, and  $M_{an}$  represents the anhysteretic magnetization.  $M$  can be further subdivided into the irreversible ( $M_{irr}$ ) and reversible magnetization ( $M_{rev}$ ) as in

$$M = M_{irr} + M_{rev}. \quad (2)$$

The reversible magnetization is attributed to domain wall bowing, reversible translation, and reversible rotation, whereas the irreversible magnetization is primarily due to domain wall pinning and irreversible rotation. The anhysteretic magnetization can be described using the Langevin function as described in (3). This relation highlights the dependence of  $M_{an}$  on the saturation magnetization  $M_s$ , the domain density,  $a$  and the effective applied field  $H_e$

$$M_{an} = M_s \left( \coth \frac{H_e}{a} - \frac{a}{H_e} \right). \quad (3)$$

The effective field is considered to be a combination of the applied field  $H$  and the magnetization  $M$  scaled by the coupling parameter  $\alpha$  as follows:

$$H_e = H + \alpha M. \quad (4)$$

In order to model the hysteresis behavior in two-phase materials as shown in Fig. 1, the J-A parameters for each phase are extracted. Using this set of parameters, we reproduce the magnetic hysteresis loop for each phase. For a two-phase material, for example, with a hard and a soft phase that are not coupled as shown in Fig. 1, the two sets of parameters should yield hysteresis loops corresponding to those separate magnetically hard and soft phases. This ability to reproduce the hysteresis loops of constituent phases of a composite or a combined hysteresis loop of the phases present using the plots of the J-A model, presents a viable approach for non-destructive evaluation of the two phase materials.

### C. Stochastic Model for Barkhausen Effect

The stochastic nature of the Barkhausen emissions have been studied in detail [12]–[14]. Although Barkhausen

emissions result from discontinuous magnetization changes inside a material, they can be measured on the surface of a material using an inductive sensor. We use this interesting feature of MBE emission and correlate it to the magnetization response to study the ferromagnetic phases within the material. From Faraday's law of electromagnetic induction, the induced emf,  $V_{emf}$ , sensed by the Barkhausen sensor is proportional to the rate of change of magnetic flux with time  $d\phi/dt$ , which is equivalent to the rate of change of magnetization with time scaled by the area of the pick-up coil and permeability of free space. Alternatively, the sum of the magnetization jumps (jump sum magnetization  $dM_{JS}/dt$ ) due to the irreversible component of magnetization is related to Barkhausen emissions. The relationship between the induced emf, time rate of change of  $M_{JS}$ , and irreversible magnetization component due to an applied magnetic field is shown in (5), where  $dM_{irr}/dH$  is the differential susceptibility and  $dH/dt$  is the time rate of change of the applied magnetic field [15], [16]

$$|V_{emf}| \propto \frac{dM_{JS}}{dt} = \gamma \frac{dM_{irr}}{dH} \frac{dH}{dt} \quad (5)$$

where  $\gamma$  represents the ratio of the discontinuous magnetization  $M_{disc}$  to the irreversible component of magnetization  $M_{irr}$  multiplied by  $N_t$ , the number of Barkhausen events occurring in a given time period  $t$ .  $\langle M_{disc} \rangle$  represents average discontinuous change in magnetization. In this case, it is considered to be an ensemble average. It is also a very small quantity. Numerically

$$\gamma = \frac{d\langle M_{disc} \rangle N_t}{dM_{irr}} = \langle M_{disc} \rangle \frac{dN_t}{dM_{irr}} + N_t \frac{d\langle M_{disc} \rangle}{dM_{irr}}. \quad (6)$$

It was found that the size of the Barkhausen jumps is considered to be weakly related to the irreversible change in magnetization and thus,  $\gamma$  can be approximated to be equal to  $\langle M_{disc} \rangle dN_t/dM_{irr}$ . The random nature of Barkhausen emissions allows the number of events,  $N_t$ , to be described by a recursive relation wherein the number of events is always held to be a positive, non-zero quantity. The increment in the number of events with time is assumed to follow a Poisson distribution [14]. The number of events,  $N_t$  in the time interval  $t$ , is related to the number of events  $N_{t-1}$  in the previous time interval  $t-1$  as seen in

$$N_t = N_{t-1} + \delta_{rand} \sqrt{N_{t-1}} \quad (7)$$

where  $\delta_{rand}$  is a random number lying in the range  $\pm 1.47$ . Originally,  $\delta_{rand}$  was assumed to lie in the range  $\pm 1$ . However, 32% of the time the increment in  $N_t$  should be beyond one standard deviation [14]. Incorporating (5)–(7), we model the Barkhausen activity as described by the relation in [14]

$$\frac{dM_{JS}}{dt} = \frac{dM_{irr}}{dH} \frac{dH}{dt} \langle M_{disc} \rangle \frac{dN_t}{dM_{irr}}. \quad (8)$$

Equation (8) shows that the magnetization jump sum is proportional to the number of Barkhausen activities resulting from discontinuous magnetization process. Equations (1) and (8) form the foundation for the stochastic-hysteretic model for Barkhausen emissions. In the following sections, we extend these relations to describe the Barkhausen noise signals in two-phase magnetic materials.

TABLE I  
EXTRACTED J–A MODEL PARAMETERS FOR  
INDIVIDUAL MEASURED PHASES

J-A parameters	Soft Phase	Hard Phase
Reversibility Parameter, $c$	0.5	0.5
Pinning Parameter, $k$	1437.233	13326.036
Domain Density, $a$	1520.150	23064.293
Saturation Magnetization, Ms	3.801e+05	2.471e+05
Coupling factor, $\alpha$	5.001e-03	2.902e-01

TABLE II  
EXTRACTED J–A MODEL PARAMETERS FOR  
COMBINED MEASURED PHASE

J-A parameters	Soft Phase	Hard Phase
Reversibility Parameter, $c$	0.5	0.5
Pinning Parameter, $k$	1034.851	10348.515
Domain Density, $a$	1411.161	13170.837
Saturation Magnetization, Ms	2.759e+05	3.511e+05
Coupling factor, $\alpha$	6.351e-03	1.905e-01

### III. EXPERIMENTAL DETAILS

Constituent powders, barium hexaferrite ( $\text{BaFe}_{12}\text{O}_{19}$ -hard phase) and cobalt manganese ferrite ( $\text{CoMn}_{0.1}\text{Fe}_{1.9}\text{O}_4$ -soft phase), were first ball-milled and then pressed into 1 in, 0.5 in, and 0.25 in pellets. This was followed by sintering at a temperature of 1200 °C for a duration of 6 h, in air atmosphere. Individual samples of each phase were also prepared. The magnetic hysteresis measurements on the samples were carried out using a hysteresis-graph measurement system.

In order to select appropriate J–A parameters for each phase, we used the optimization function in [10] and [17]. This function allows the estimation of the values of the J–A parameters by selecting a suitable range for each parameter. Table I shows the J–A parameters for two-phase behavior contributed to the composite magnetic hysteresis by the individual phases. A similar procedure was carried out for the barium hexaferrite-cobalt ferrite composite. Table II shows the J–A parameters for this composition. With the exception of the pinning parameter,  $k$ , and domain density,  $a$ , the J–A parameters obtained are approximately in the expected range verified by comparing the values in Tables I and II.

### IV. RESULTS AND DISCUSSION

Fig. 2 shows the microstructure of the two-phase material used in this paper, which comprises of barium hexaferrite ( $\text{BaFe}_{12}\text{O}_{19}$ ), harder phase material, and cobalt manganese ferrite ( $\text{CoMn}_{0.1}\text{Fe}_{1.9}\text{O}_4$ ), a softer phase. A standard ceramic sample preparation process was employed for producing these samples.

Fig. 3 shows three hysteresis plots derived from the  $\text{CoMn}_{0.1}\text{Fe}_{1.9}\text{O}_4$  phase, the  $\text{BaFe}_{12}\text{O}_{19}$  phase, and a composite of both phases. It can be seen that the hysteresis loop for the composite is different from that derived from individual phases, which indicates magnetic coupling between the two phases in the composite. In this work, we have attempted to separate the constituent phases of the two-phase material by using the J–A model and the five physical model parameters. We then characterized the hysteresis behavior using MBE emission profiles.

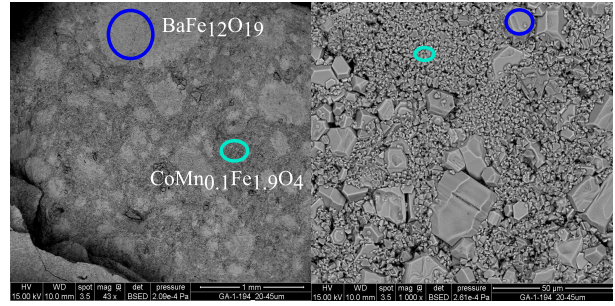


Fig. 2. Microstructure of the two-phase composite sample. White regions: barium hexaferrite (left). Dark regions: cobalt manganese ferrite (left). Microstructure at higher magnification highlighting the two different regions (right).

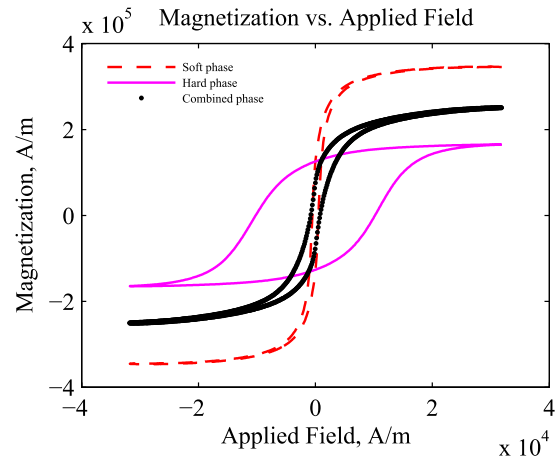


Fig. 3. Hysteresis loops for the measured samples for cobalt-manganese ferrite ( $\text{CoMn}_{0.1}\text{Fe}_{1.9}\text{O}_4$ ) or soft-phase (red-dashed curve). Barium hexaferrite ( $\text{BaFe}_{12}\text{O}_{19}$ ) or hard phase (magenta-solid curve). Combination of barium hexaferrite and cobalt-manganese ferrite (black-dotted curve).

The stochastic model of the Barkhausen effect, as formulated in (8), was utilized to observe the Barkhausen noise profile of the individual phases. For our simulations, we assumed the initial number of Barkhausen events,  $N_i$ , to be 1000. Fig. 4(a) shows the MBE profile obtained for the magnetically softer phase ( $\text{CoMn}_{0.1}\text{Fe}_{1.9}\text{O}_4$ ) followed by that of the magnetically harder phase ( $\text{BaFe}_{12}\text{O}_{19}$ ) in Fig. 4(b). This behavior can be modeled using the relation described in

$$\frac{dM_{JS, \text{total}}}{dt} = \beta_1 \frac{dM_{\text{phase1}}}{dt} + \beta_2 \frac{dM_{\text{phase2}}}{dt} \quad (9)$$

where  $\beta$  indicates the volume fraction.

Since addition of the hysteresis components for individual phases was obtained by linear combination, summation of the MBE was carried out. This operation results in a MBE profile with emergence of secondary peaks as seen in Fig. 4(e). A similar operation was also carried out for the constituent phases. Fig. 4(c) shows the MBE profile for the softer phase that was identified using the J–A model. Fig. 4(d) shows the MBE profile for the harder phase that was identified. The linear superposition of the MBE profiles, Fig. 4(c) and (d), leads to Fig. 4(f). In Fig. 4(e) and (f), we observe two distinct peaks, which indicates the presence of two different ferromagnetic phases within the material. These observations



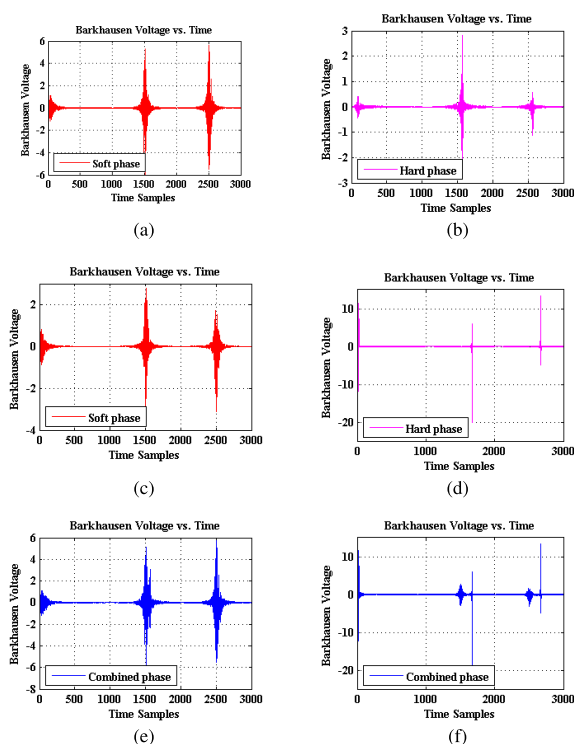


Fig. 4. Barkhausen noise profiles. In each figure, the three voltage bursts correspond to the initial magnetization, reverse magnetization cycle, and forward magnetization cycle. (a) BN profile for the soft phase obtained from measured hysteresis loop using the J–A model parameters. (b) BN profile for the hard phase obtained from measured hysteresis loop using the J–A model parameters. (c) BN profile for soft phase in two-phase material obtained from the hysteresis loop reconstructed using the J–A model parameters. (d) BN profile for hard phase in two-phase material obtained from the hysteresis loop reconstructed using the J–A parameters. (e) Linear superposition of BN (a) and (b). (f) Linear superposition of BN (c) and (d).

lead to the conclusion that the magnetic behavior of two-phase (or multi-phase) composite materials can be characterized from the MBE profiles. To do this, the bounds of the J–A parameters need to be selected appropriately such that the two phases can be effectively separated out. Similar behavior has been observed with changes in local strains, hardness, and composition gradients in ferromagnetic steels [11], [18], [19]. The peak intensity of the normalized Barkhausen voltage is related to the volume fraction of each phase. For our simulations, we assumed that each phase had an equal volume fraction, i.e.,  $\beta$  is equal to 1. Variations in the volume fractions would lead to the reflection of an enhanced or diminished response corresponding to the particular phases. We could further define (9) to include dependence on composition variations, for example, using a scaling factor,  $\beta$ .

## V. CONCLUSION

This paper shows that the J–A theory can be extended to describe the magnetic behavior of two-phase ferromagnetic materials. The J–A model has been applied to analyze the magnetic behavior of the magnetic phases of a two-phase material. The stochastic-hysteretic model for the Barkhausen

effect allowed us to describe the Barkhausen noise profile for single-phase and two-phase materials. Two distinct peaks were observed for composites comprising of different magnetic phases as used in this work. The model can be utilized as a tool for non-destructive evaluation of two-phase ferromagnetic materials for the detection and characterization of constituent phases.

## ACKNOWLEDGMENT

The authors would like to thank Dr. A. Raghunathan, Z. Ding, and H. Xu for their contributions and insightful discussions. This work was supported by the Department of Electrical and Computer Engineering, Iowa State University, Ames, IA, USA.

## REFERENCES

- [1] L. A. L. E. Landau and E. Lifshitz, "On the theory of the dispersion of magnetic permeability in ferromagnetic bodies," *Phys. Zeitschrift Sowjetunion*, vol. 8, no. 153, pp. 153–169, 1935.
- [2] F. Preisach, "Über die magnetische Nachwirkung," *Zeitschrift Phys.*, vol. 94, nos. 5–6, pp. 277–302, 1935.
- [3] E. C. Stoner and E. P. Wohlfarth, "A mechanism of magnetic hysteresis in heterogeneous alloys," *Philosoph. Trans. Roy. Soc. London*, vol. 240, no. 826, pp. 599–642, May 1948.
- [4] D. C. Jiles and D. L. Atherton, "Theory of ferromagnetic hysteresis," *J. Magn. Mater.*, vol. 61, nos. 1–2, pp. 48–60, 1986.
- [5] O. Kypris, I. C. Nlebedim, and D. C. Jiles, "Experimental verification of the linear relationship between stress and the reciprocal of the peak Barkhausen voltage in ASTM A36 steel," *IEEE Trans. Magn.*, vol. 49, no. 7, pp. 4148–4151, Jul. 2013.
- [6] M. Dimian and P. Andrei, *Noise-Driven Phenomena in Hysteretic Systems* (Signals and Communication Technology). New York, NY, USA: Springer-Verlag, 2014.
- [7] M. J. Sablik and D. C. Jiles, "Coupled magnetoelastic theory of magnetic and magnetostrictive hysteresis," *Archives Electr. Eng.*, vol. 60, no. 1, pp. 49–57, Mar. 2011.
- [8] M. J. Sablik and D. C. Jiles, "Coupled magnetoelastic theory of magnetic and magnetostrictive hysteresis," *IEEE Trans. Magn.*, vol. 29, no. 4, pp. 2113–2123, Jul. 1993.
- [9] P. R. Wilson, J. N. Ross, and A. D. Brown, "Simulation of magnetic component models in electric circuits including dynamic thermal effects," *IEEE Trans. Power Electron.*, vol. 17, no. 1, pp. 55–65, Jan. 2002.
- [10] A. Raghunathan, Y. Melikhov, J. E. Snyder, and D. C. Jiles, "Modeling of two-phase magnetic materials based on Jiles–Atherton theory of hysteresis," *J. Magn. Mater.*, vol. 324, no. 1, pp. 20–22, 2012.
- [11] A. Raghunathan, P. Klimczyk, and Y. Melikhov, "Application of Jiles–Atherton model to stress induced magnetic two-phase hysteresis," *IEEE Trans. Magn.*, vol. 49, no. 7, pp. 3187–3190, Jul. 2013.
- [12] B. Alessandro, C. Beatrice, G. Bertotti, and A. Montorsi, "Domain-wall dynamics and Barkhausen effect in metallic ferromagnetic materials. I. Theory," *J. Appl. Phys.*, vol. 68, no. 6, p. 2901, May 1990.
- [13] G. Bertotti and I. D. Mayergoyz, *The Science of Hysteresis*. Amsterdam, The Netherlands: Academic, 2006.
- [14] D. C. Jiles, "Dynamics of domain magnetization and the Barkhausen effect," *Czechoslovak J. Phys.*, vol. 50, no. 8, pp. 893–924, Aug. 2000.
- [15] A. Mitra and D. C. Jiles, "Effects of tensile stress on the magnetic Barkhausen effect in 2605 CO amorphous alloy," *IEEE Trans. Magn.*, vol. 31, no. 6, pp. 4020–4022, Nov. 1995.
- [16] D. C. Jiles, L. B. Sipahi, and G. Williams, "Modeling of micromagnetic Barkhausen activity using a stochastic process extension to the theory of hysteresis," *J. Appl. Phys.*, vol. 73, no. 10, p. 5830, May 1993.
- [17] D. E. Finkel and C. T. Kelley, "Additive scaling and the DIRECT algorithm," *J. Global Optim.*, vol. 36, no. 4, pp. 597–608, Dec. 2006.
- [18] A. Ktena et al., "Barkhausen noise as a microstructure characterization tool," *Phys. B, Condens. Matter*, vol. 435, pp. 109–112, Feb. 2014.
- [19] M. Blaow, J. T. Evans, and B. A. Shaw, "Effect of hardness and composition gradients on Barkhausen emission in case hardened steel," *J. Magn. Mater.*, vol. 303, no. 1, pp. 153–159, Aug. 2006.